Surface engineering of conductive material-based composites for energy applications

by

Miaomiao Zhang

A dissertation submitted to Graduate Faculty of
Auburn University
in partial fulfillment of the
requirements for the Degree of
Doctor of Philosophy

Auburn, Alabama
August 7, 2021

Keywords: conducting polymers, transition metal compounds, energy storage, supercapacitors.

Approved by

Dr. Xinyu Zhang, Chair, Professor, Department of Chemical Engineering
Dr. Dong-Joo Kim, Professor, Department of Materials Engineering
Dr. Siyuan Dai, Assistant Professor, Department of Mechanical Engineering
Dr. Asha-Dee Celestine, Assistant Professor, Department of Aerospace Engineering

Abstract

With the increasing concern on renewable sources (wind, wave and solar), energy storage and power management have become increasingly important topics. Supercapacitors (SCs) with features of ultrahigh power output, excellent cycle life, fast charge/discharge rates and environment-friendly nature have been considered as one kind of promising energy storage devices for meeting the ever-increasing power requirements of energy storage systems. Obviously, the specific capacitances, the energy and power densities and the cycling stability are important parameters for evaluating SCs. Many attempts have been tried to enhance their performance by exploring various kinds of electrode materials. Conducting polymers (CPs) and transition metal (TM)-based materials are two kinds of vital electrode materials for SCs. CPs, also known as synthetic metals, are basically organic polymers with both metallic and semi-metallic features. Polypyrrole (PPy) and polyaniline (PANI) are commonly used CPs electrode materials for SCs, even for flexible SCs, due to their pseudo-capacitive characteristic, easy processible, flexible, and high specific capacitance values. However, the low cycling stability of CPs caused by structure degeneration during the reversable charge/discharge processes becomes a major bottleneck and hinders their further development. TM-based materials, especially the multicomponent metal materials, are another type of excellent electrode material for SCs due to their richer redox-active reactions sites. However, this type of material usually faces conductivity problems. Therefore, trying to solve above mentioned issues is essential for the further development of SCs. My Ph.D. research aimed to find easy

and feasible strategies to design and improve the electrochemical performance of electrode materials. In the whole work, I demonstrated dopants have a great effect on the electrochemical performance of CPs (mainly focus on PPy and PANI)-based electrodes and selecting a suitable dopant can be used as an effective way for enhancing the electrochemical behavior of CPs-based electrode materials. In addition, a high-rate and ultra-stable transition metal phosphide (TMP) electrode (Mn-CoP/Ni nanosheets) was successfully prepared by a facile electrodeposition method. Moreover, a simple and ultra-fast microwave method was successfully used to synthesis the high-performance transition metal sulfide (TMS)-based electrode material (nickel-cobalt sulfide/graphene hybrid material). The outcomes of my Ph.D. research will provide a much easier route in achieving high performance CPs-based and TM-based electrode materials as promising candidates for energy storage application and broaden their practical applications.

Acknowledgments

All of the research work presented here would be impossible to complete without many individuals' help and guidance. Thus, I would like to deeply thank everyone who helped me during my research.

My advisor Dr. Xinyu Zhang would be the first one I would like to thank. I am so thankful for his continuous help. All research work I did at Auburn University are inseparable from his support, guidance, and advice. Our conversations and discussions on all kinds of research opportunities helped me establish my research projects and achieved excellent results. Under his guidance, I learned how to analyze and solve problems at a deeper level.

I am also thankful to thank my committee members: Dr. Dong-Joo Kim, Dr. Tae-Sik Oh, Dr. Asha-Dee Celestine and Dr. Siyuan Dai. Thank for taking time to help me review my work and provide very precious suggestions and valuable feedback and thank for all kinds of help they provide on my research work. I could not complete my graduation so smoothly without their help.

I am also grateful to my collaborators Dr. Ruigang Wang and their students Dr. Zhongqi Liu and Zhen Wei for their help and support on my research work. I am also thankful to the Department of Polymer and Fiber Engineering for providing the welcoming and comfortable study and working environment to conduct this research.

I would like to thank my fellow friends at the Auburn University, especially my group members who inspired me to broaden my research from multiple perspectives. I especially thank Dr. Amit Nautiyal for his help and guidance with my paper works. I am also grateful to Haishun Du for his help in virous kinds of situations and his valuable insights and guidance in every step of my research.

Lastly, I would like to express my deepest gratitude to my family for their countless sacrifices and support over the past years. Thank them enlighten me and encourage me in my helplessness. Moreover, I would like to thank my brother who always stood by me through all my struggles. When I feel lonely and helpless, he is always there, communicating with me and helping me provide valuable suggestions.

Table of Contents

List of Tables

List of Figures

List of Abbreviations

2D	2-dimensional
3D	Three-dimensional
LIBs	Lithium-ion Batteries
SCs	Supercapacitors
SOHIO	Standard Oil of Ohio
NEC	Nippon electric
EDLCs	Electrical double layer capacitors
PCs	Pseudocapacitors
IHP	Inner Helmholtz plane
OHP	Outer Helmholtz plane
CV	Cyclic voltammetry
GCD	Galvanostatic charge-discharge
EIS	Electrochemical impedance spectroscopy
RC	Resistor-capacitor
AC	Activated carbon
CC	Carbon cloth
CNTs	Carbon nanotubes
SWCNTs	Single walled carbon nanotubes
MWCNTs	Multi-walled carbon nanotubes
CPs	Conducting polymers

PPy	Polypyrrole
PANI	Polyaniline
PEDOT	Poly(3,4-ethylenedioxythiophene)
PT	Polythiophene
TMOs	Transition metal oxides
TMPs	Transition metal phosphides
TMSs	Transition metal sulfides
RuO_2	Ruthenium dioxide
MnO_2	Manganese oxide
IrO_2	Iridium oxide
Nb_2O_5	Niobium oxide
V_2O_5	Vanadium pentoxide
Fe_3O_4	Iron oxide
HCl	Hydrochloric acid
$HClO_4$	Perchloric acid
H_2SO_4	Sulfuric acid
p-TSA	p-toluenesulfonic acid
H_3PO_4	Phosphoric acid
PA	Phytic acid
Pt	Platinum

Chapter 1

Introduction

In the past few decades, the global population and the development of global industry experienced rapid growth, which lead to huge consumption of primary energy (including coal, natural gas and oil) [1] and caused serious environmental pollution problem and energy shortage problem[2]. In recent years, many efforts have been done to alleviate these problems. Therefore, more and more sustainable, safe, and environmentally friendly new energy sources such as wind, solar, hydro-electric power, tidal, and geothermal energy have been explored. However, there are some barriers to use these new energy sources stably and efficiently. This is because many of these new energy sources are dynamic resources which are vary with time and geographic conditions. So, energy storage technology has attracted great attention for the utilization of electricity generated from these intermittent renewable sources[3-5]. Energy storage devices are considered as important components for mitigating the environmental problems and energy shortages problems.

Currently, the most effective and practical technologies for energy storage devices including batteries, fuel cells, capacitors and supercapacitors(SCs)[6]. Batteries are a kind of device relying on the transformation of chemical energy into electrical energy. As shown in **Fig. 1.1a**, a battery composed of an anode, a cathode and electrolyte. Like batteries, fuel cells also depend on the chemical reaction for the conversion of chemical energy to electrical energy. The difference is

their energy storage system are separate from the power generator (**Fig. 1.1b**). Fuel cells can be considered as one of the most environmentally friendly energy storage devices due to the non-polluted product of the chemical reaction process. Capacitors store energy by the physical charge separation between two electrodes. A capacitor consists of two parallel conductive plates like metallized plastic film or metal electrodes and separated by an insulating dielectric material. (**Fig. 1.1c**). The energy is stored by the electric field produced via opposite charges when a voltage is applied on the electrodes' surface[7]. In other words, the energy is stored on the surfaces of electrodes and their capacitance is a function of the overlapping surface areas of the electrodes. A supercapacitor consists of two electrodes, a separator and electrolyte solution (**Fig. 1.1d**). The electrodes are made of a high conductive collector and active material. The electrolyte solution used as ions conductor. The separator used to satisfy ions conduction between the electrodes while preventing the electronic conduction caused by physical contact of electrodes[8]. SCs store energy by the separation of chemically charged species at the electrified interface between electrode and electrolyte. When an external power source applied on the electrodes, the different potential generated between electrodes which cause positive and negative charges gather on the surface of the electrodes. These charges remain on the surface of the electrodes, even if electric field is removed, which is known as charged capacitor. During the discharge process, positive and negative charges are released to the connected resistive load completing the transmission of stored energy[9].

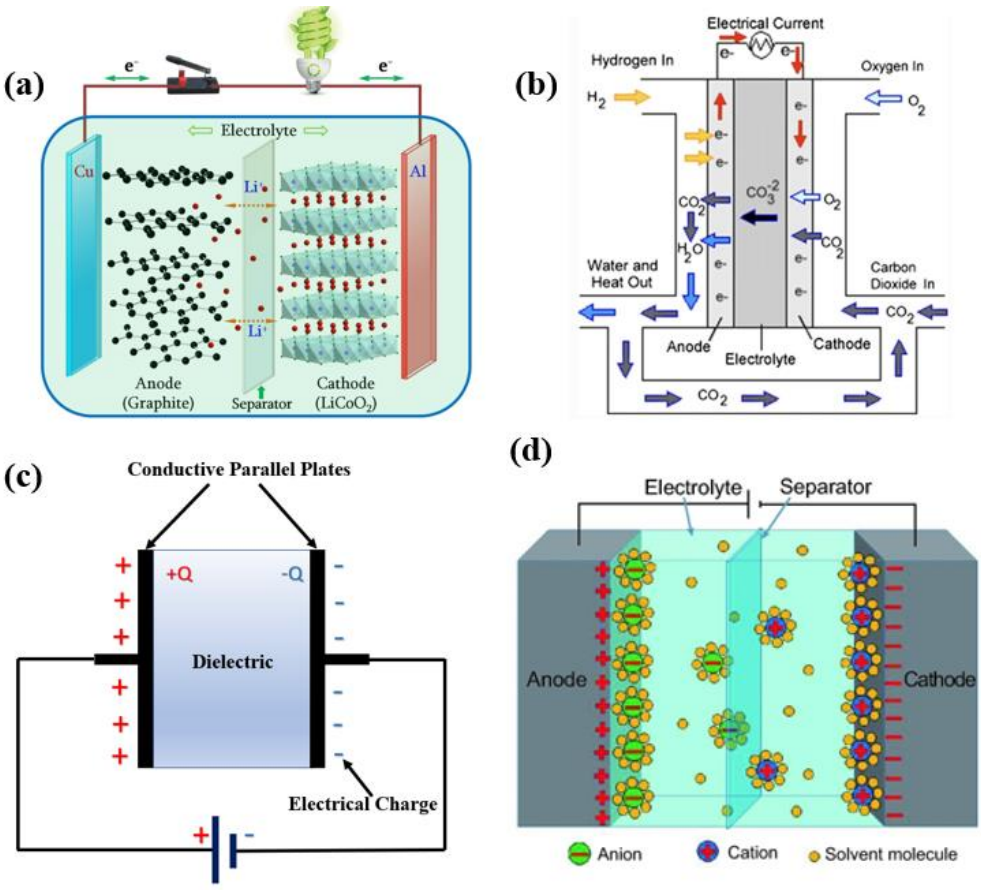

Figure 1. 1 Schematic of the configuration of energy storage devices (a) rechargeable Li-ion batteries; (b) full cells; (c) capacitors;(d) supercapacitors[10-12].

The Ragone plot (**Figure 1.2**) of these basic energy storage devices exhibit that each type of device has a different combination of power density and energy density. Even though the traditional capacitors can be charged faster and provide the highest specific power than batteries, supercapacitors and fuel cells, but their high self-discharge rate and lower energy density properties limits their applications and development. The advantages of high energy efficiency, high specific energy, low noise and the cleanness of energy production make fuel cells becoming one of the most favorable renewable energy sources. But their low power density impedes their performance. Obviously, only supercapacitors and batteries can combine high power density and high energy density together. In the past decades, batteries, especially

lithium-ion batteries (LIBs) have got great successes because of their superior comprehensive battery performance. However, like the previous battery techniques, the development of LIBs met their bottleneck recently[13]. Supercapacitors, as an excellent power sources with wide applications ranging from portable electronics to hybrid vehicles, cranes, trains, elevators and even huge energy-storage systems[4], have been consider as one of the most promising energy storage devices and have attracted worldwide attention.

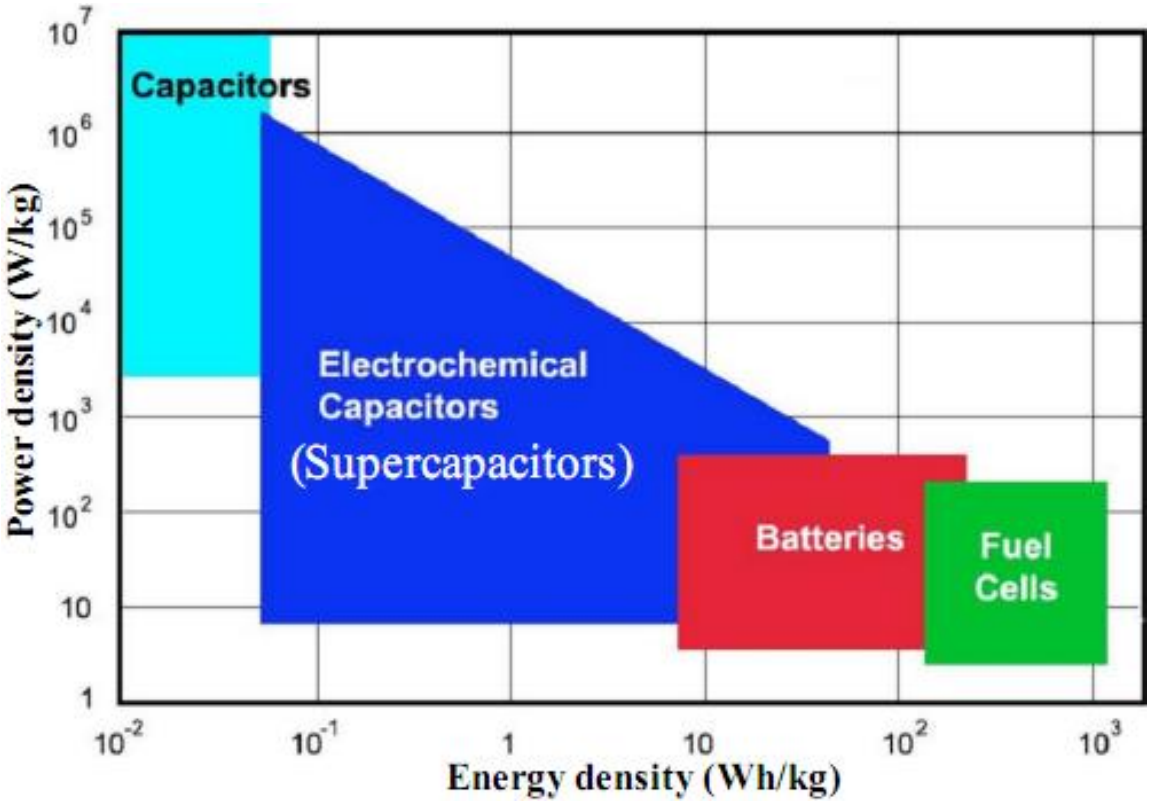

Figure 1. 2 Comparison of Ragone plots for basic electrical energy storage devices[14].

Chapter 2

Background and Literature Survey

Supercapacitors (SCs), also known as ultracapacitors or electrochemical capacitors. The earliest SCs patent was reported and issued in 1957 by Howard Becker[15]. However, this patent did not get enough attention for commercialized. In 1966, an electrolytic capacitor with porous carbon as electrodes and aqueous sulfuric acid solution as electrolyte was developed by Standard Oil of Ohio Company (SOHIO) company[8]. Later, Nippon electric company, NEC (Japan), took over SOHIO and SCs got a rapid development. Until the 1980s, SCs were commercialized by companies like Panasonic, ELNA, and PRI for memory backup and military uses[9]. So far, SCs demonstrate superior performance including excellent reversibility, outstanding power performance, high cyclic stability (>1 000 000 cycles), easily operation, and ease of integration into electronics[16]. Therefore, SCs have been widely used in portable electronics like smartphones, laptops, tablet devices and growing at an exciting rate[9]. In recent years, extensive development in SC technology have been done to satisfy their expanding needs.

2.1 Classification and charge storage mechanisms of supercapacitors

According to the charge storage mechanism, SCs can be classified into electrical double layer capacitors (EDLCs) and pseudocapacitors (PCs) or redox SCs[17]. The capacitances of SCs are mainly depending on the surface reactions of electrode materials. These surface reactions include the electrochemical adsorption or desorption of ions occurring on the interface of electrodes and electrolyte like EDLCs and faradaic redox reactions at the interface of electrodes

and electrolyte in the case of pseudocapacitive materials[9].

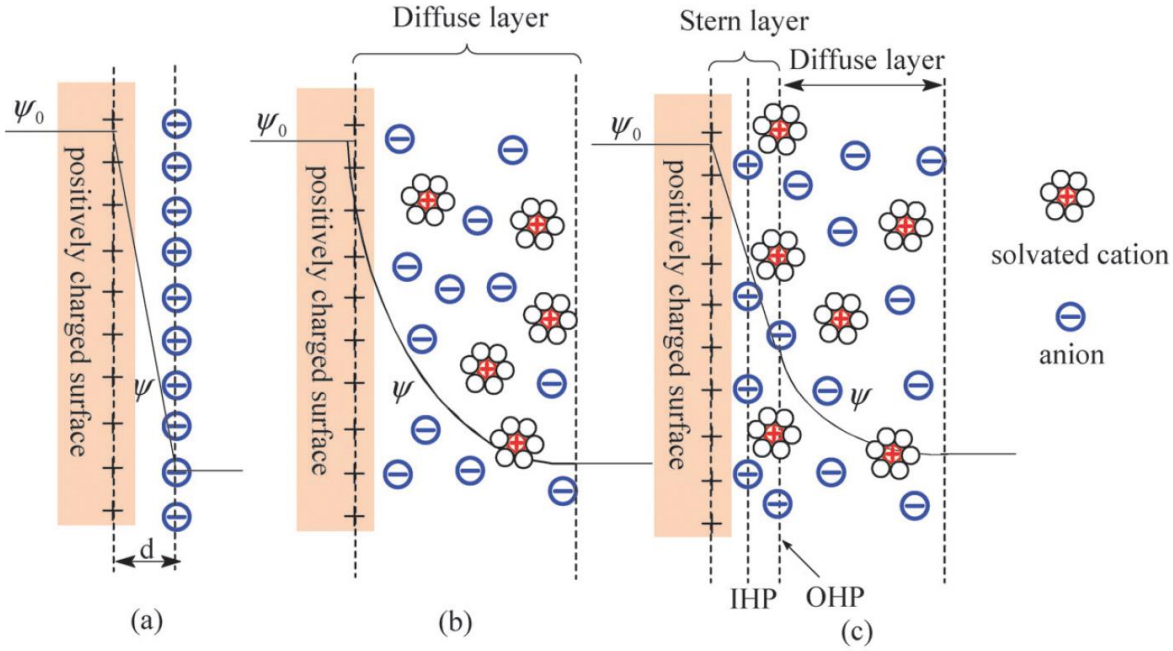

Figure 2. 1 Models for the electrical double layer at a positively charged surface: (a) the Helmholtz model, (b) the Gouy-Chapman model, and (c) the Stern model[18].

EDLCs use high surface area materials like porous carbon as electrodes material and an electrolyte (such as KOH, H_2SO_4, or Na_2CO_3) between the electrodes instead of the dielectric medium used in conventional capacitors. EDLCs can store much more energy than conventional capacitor due to the large surface area of active materials and the atomic range of charge separation distances. The capacitance of EDLCs are usually evaluated in unit of Farads (F), whereas traditional dielectric and electrolytic capacitors are measured by picofarads (pF) and microfarads (μF)[16]. As schematically depicted in **Fig. 2.1a**, the concept for EDLCs was originally proposed and modeled by Helmholtz in the 19th century according to his discovery of opposite charges distribution on colloidal particle interfaces. Based on the Helmholtz double layer model, like two-plate conventional capacitors, two opposite charges layers were formed

at the electrode/electrolyte interfaces and separated by an atomic distance. Later, Gouy and Chapman further modified Helmholtz model into the diffusive layer model by the considering of continuously distribution of electrolyte ions (including cations and anions) in the electrolyte solution (**Fig. 2.1b**)[15]. Because of the inverse relationship between the capacitance of two separated arrays of charges and their separation distance, there would get a very large capacitance value when point-charged ions are close to the electrode surface which lead to an overestimation of the EDLCs capacitance according to Gouy-Chapman model. Then, Stern classified the ion distribution regions as an inner region called the compact layer or Stern layer and a diffuse layer (see **Fig. 2.1c**) by combing the Helmholtz model with the Gouy-Chapman model. Ions (especially hydrated), within the compact layer, have strong adsorption on the electrode. Furthermore, the compact layer is composed of specific adsorbate ions (normally are anions, have no concern with the charge nature of electrode) and nonspecific adsorbate counterions. The specific adsorbate ions and nonspecific adsorbate counterions are distinguished as the inner Helmholtz plane (IHP) and outer Helmholtz plane (OHP). Moreover, the diffusive layer region is defined by the Gouy-Chapman model.

The capacitance for an EDLC (C_{dl}) consists of the compact double layer capacitance (C_H) and the diffusive region capacitance (C_{diff}). So, C_{dl} can be expressed as follows:

$$\frac{1}{C_{dl}} = \frac{1}{C_H} + \frac{1}{C_{diff}}$$

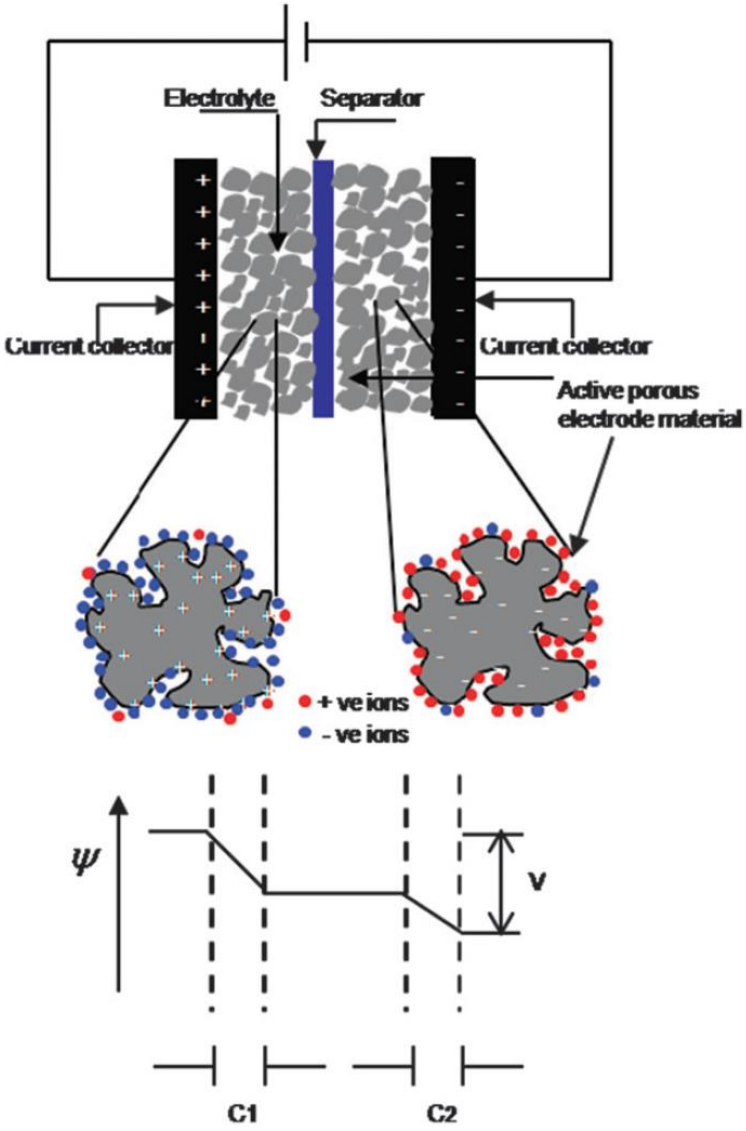

Figure 2. 2 Schematic of EDLCs based on porous electrode materials[15].

The performance of EDLCs at a planar electrode surface can be influenced by the factors like the types of electrolyte ions, the electrical field across the electrode and the chemical affinity between the ions and the electrode[18]. Because of the porous material with a high specific surface area usually used as electrode, the behavior of EDLCs are more complex than at a planar electrode surface due to the transportation of ions in a confined system could be affected some parameters including the spatial constraints of the pores, the tortuous mass transfer path,

the wetting ability of pore surface by the electrolyte and the ohmic resistance connected with the electrolyte[15]. **Fig. 2.2** illustrated the mechanism of EDLCs with porous carbon as electrode. The capacitance of EDLCs can be calculated by the equation used for parallel-plate capacitor[15]:

$$C = \frac{\varepsilon_r \varepsilon_0 \times A}{d}$$

Where ε_r is dielectric constant of the electrolyte; ε_0 represents the vacuum permittivity; A is the ion-accessible electrode surface area; d represents the effective thickness of electrical double layer. According to above mentioned information, EDLCs store energy via the reversible adsorption of electrolyte ions onto the electrode. The charge/discharge mechanism of EDLCs is the ion adsorption and desorption process which means there is no faradaic reaction during this process[9].

In contrast to EDLCs, the charge storage mechanism of pseudocapacitors is based on a Faradaic charge process. When a potential is applied to pseudocapacitor, electrolyte ions would be adsorbed onto the surface or reach the near-surface region of pseudocapacitive electrode, along with fast and reversible redox reactions in these regions. This reaction also involves the passage of charge across the double layer resulting in the generation of faradaic current across the supercapacitor cell. This mechanism is related to the valence state change of the electrode material caused by electron transfer. Ruthenium dioxide (RuO_2), features a high theoretical specific capacitance, wide potential window, high electrochemical reversibility, high specific energy density and long cycle-life, has been widely studied as pseudocapacitor electrode material providing pseudo-capacitive property[19]. Although, faradaic reaction occurs on RuO_2

thin film, its CV curve exhibiting the typical capacitive feature with a close to rectangular shape[20]. Research on RuO_2 has also led to a further understanding of the necessary properties of pseudocapacitor materials. The term pseudocapacitance is formally used to describe the properties of electrode materials which have capacitive electrochemical signatures (such as observed with EDLCs electrode), i.e., exhibiting the linear dependence of the charge stored with the range of the potential window, but the charge storage resulting from charge-transfer faradaic reactions through the double layer[21].

According to Conway et al., there have been identified three kinds of Faradaic mechanisms corresponding to three types of electrochemical capacitive features: (i) underpotential deposition, (ii) redox pseudocapacitance, and (iii) intercalation pseudocapacitance[22-23]. The scheme of these fundamental processes shown in **Figure 2.3**.

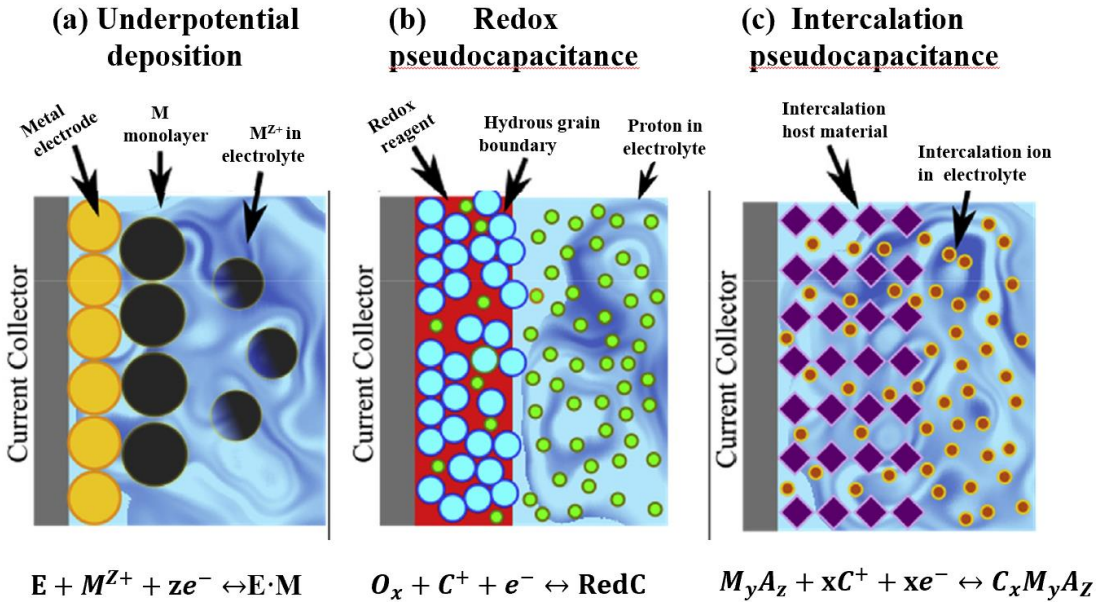

Figure 2. 3 Redox mechanisms for different types of pseudocapacitive electrodes: (a) underpotential deposition, (b) redox pseudocapacitance and (c) intercalation pseudocapacitance[23].

For underpotential deposition, metal cations will electrodeposition and form an adsorbed monolayer on the surface of a dissimilar metal substrate when potentials above the standard redox potential are applied. Additionally, underpotential deposition can be applied to other adsorbed layers, like H from H_3O^+ or H_2O pseudocapacitance[24]. This process can be described by following equation:

$$\mathrm{E} + M^{Z+} + \mathrm{z}e^- \leftrightarrow \mathrm{E{\cdot}M}$$

Where, E represents metal electrode (e.g., Pt, Ru, Rh or Au), M denotes the absorbed atoms (e.g., H or Pd), z is the valence of the absorbed atoms. Even though the good charge and discharge kinetics reversibility is the basic factor for underpotential deposition type pseudocapacitive materials achieving their favorable power densities, the limited operational potential ranges, only 0.3-0.6 V, which relative to capacitance values make their energy density cannot be compared with other pseudocapacitive systems[22].

The redox pseudocapacitance is a typical form of pseudocapacitance which occurs when ions are electrochemically adsorbed onto the surface or near-surface region of electrode materials accompanying faradaic reactions which occur with charge transfer. Transition metal oxides (e.g., RuO_2 and MnO_2) and conducting polymers synthesized by electrochemical methods (e.g., polypyrrole (PPy) and polyaniline (PANI)) are typically used materials for redox pseudocapacitance[24]. These redox pseudocapacitance electrode materials exhibit pseudocapacitance based on fast redox reactions with electron transfer between the oxidized species Ox (e.g., RuO_2, MnO_2, or p-doped conductive polymers) and the reduced species, Red

(e.g., RuOOH, MnOOH, or n-doped conductive polymers). These reactions can be expressed as:

$$O_x + C^+ + e^- \leftrightarrow \mathrm{RedC}$$

where C represent the electrolyte cation C^+ (e.g., H^+, K^+, Na^+). There are no chemical transformation occurs during the charge/discharge process. Nevertheless, the faradaic reactions result in the formation of a reversible functionalized molecular layer on the electrode surface. The potential of the electrode is proportional to the electroactive ions covered electrode surface area and exhibits a linear dependence on the charge. These are completely different features compared with the battery-type redox reactions[24]. The redox pseudocapacitance has excellent capacitance behavior and the maximum capacitance can reach (~5000 F cm^{-3})which is much larger than the maximum achievable theoretical capacitance of a compact high surface area carbon EDLC capacitor (~825 F cm^{-3})[22].

Intercalation pseudocapacitance is another type of faradaic process occurring with the insertion of ions into the tunnels or layers of the redox-active material accompanying a charge-transfer (Faradaic) process but without crystallographic phase changes of the material. This process is different from intercalation process involved in a battery where occurs crystallographic phase transformation during the charge transfer processes[24]. The intercalation of Li^+ ions into host material (e.g., MoS_2, TiS_2, and Nb_2O_5) and the intercalation of H into host, for example, Pd and Pd-Ag alloys are extensively studied intercalation pseudocapacitor system. With the rapid development in 2D materials, transition metal carbides (MXenes) are introduced as peculiar

intercalation host material. The intercalation of ions (e.g., Li^+, Na^+, K^+, Al^{3+}) into Mxene layers becomes a novel way for obtaining high-volume pseudocapacitors. The redox reactions between intercalating ions and host materials of intercalation pseudocapacitance can be illustrated in eq

$$M_yA_z + \mathrm{x}C^+ + \mathrm{x}e^- \leftrightarrow C_xM_yA_Z$$

where M_yA_z denotes the layer-lattice intercalation host material and x represents the transferred electrons number, C^+ is the intercalating ions. In order to maintain electric neutrality, metal valence changes exist in the intercalation process. The electrochemical performance of a cation intercalation pseudocapacitor can be described as "transitional" state of Li-ion batteries and supercapacitors[25]. The capacitor-like electrochemical signatures characterization, such as fast ion transport kinetics, high-rate capability, short charge time, long cycling stability, etc., are main distinguishing features of intercalation pseudocapacitance. However, the battery type materials normally exhibit a lower power density caused by limited solid-state diffusion[22].

Intercalation pseudocapacitive electrode materials have attracted widespread attention due to their superior electrochemical performance (e.g., high capacitance, good rate capability, wide potential window). In order to identify the intrinsic beginning of intercalation pseudocapacitance, researchers have begun to classify these materials as "intrinsic" and "extrinsic" pseudocapacitive materials. For intrinsic pseudocapacitive materials, the crystalline grain sizes or morphologies have no effect on their charge-storage properties. Nevertheless, some battery-type materials (e.g., $LiCoO_2$ and bulk V_2O_5) which only exhibit diffusion-

controlled capacity in their bulk state but can performance the pseudocapacitive behavior with the particle dimensions to nanosizes[20]. Such kind materials are considered as extrinsic pseudocapacitive materials. Hence, even the same type of material, pseudocapacitance or battery-type energy storage characteristics can be imparted according to their particle diameters.

These three faradaic redox mechanisms are on the basis of three different types of physical processes and occur on the corresponding type of material, respectively. Nevertheless, they deliver similar electrochemical signatures because of the similar thermodynamic features, which is, the functional relationship between the electrode potential and the extent of charge resulting from adsorption/desorption processes occurred at the electrode/electrolyte interface or within the inner surface of the hostage material[23]. These processes can be generically represented by eq[20].

$$\mathrm{E} = E^0 - \frac{RT}{nF}\ln\left(\frac{X}{1-X}\right)$$

where E is the electrode potential (V), R is the ideal gas constant (8.314 J mol^{-1} K^{-1}), T is the temperature (K), n is the number of electrons involved in the Faradaic process, F is Faraday constant (96 485 C mol^{-1}), and X is the extent of fractional coverage of the surface or inner structure by the potential determining ionic species. From above equation, a specific (gravimetric) capacitance (C/F g^{-1}) can be defined in regions where the E vs. X plot is linear[23]:

$$\mathrm{C} = \left(\frac{nF}{m}\right)\frac{X}{E}$$

where m is the molecular weight of the electrode material. Because the E vs. X plot is entirely

truly linear as an ideal supercapacitor, so the measured capacitance cannot always constant thus termed as pseudocapacitance.

Even though the above-mentioned thermodynamic analysis is important, we still need to emphasize that the intrinsic kinetic processes associated with the emergence of a pseudocapacitance which are crucial for determining the overall electrochemical performance of the energy storage device. This stems from the fact that faradaic reactions involved in pseudocapacitance are pretty similar with reactions in battery type materials. Some kinetic effects lead to polarization for battery materials also occur in pseudocapacitor materials including: (1) the activation polarization with the concomitant Faradaic charge-transfer processes; (2) the ohmic polarization connected with the electronic and ionic resistance of cell components and the contact resistance of current collector and electrode material; (3) the concentration polarization deriving from mass transport of the electrochemical process. According to these polarization processes, a passivation layer could form at the interface of the active material and electrolyte[22]. For different materials, this passivation layer has different effect on their electrochemical performance since the different reaction rates of the surface, the near-surface, and bulk faraday processes, i.e., faraday reactions occurred on the surface or the near-surface are not limited by the mass transfer of active ionic species, which can severely affected the bulk Faraday process by a slow solid-state diffusion, resulting their high rate capabilities[23].

2.2. Kinetic electrochemical features of SCs.

Various electrochemical characterization methods have been developed and used to evaluate

the electrochemical performance of SCs. Cyclic voltammetry (CV), galvanostatic charge-discharge (GCD), and electrochemical impedance spectroscopy (EIS) techniques are commonly used. Essentially, the three fundamental parameters: voltage, current, and time can be directly measured by these mentioned techniques; other metrics, such as capacitance, operating voltage, equivalent series resistance, the time constant, energy, and power performance of SCs, can be derived from them[16]. The combination of these three testing techniques contributes to obtain a more comprehensive characterization study due to the benefits and drawbacks of each technique which has its own focus and targeted parameters (The merits and demerits of these three techniques are briefly summarized in **Table 2.1.**[15]). For different types of supercapacitors, the different charge storage mechanisms lead to different kinetic behavior during the CV, GCD and EIS tests which will be discussed in the following discussion[24]. Furthermore, these three techniques can be used to evaluate the performance of SCs electrode materials and SCs devices. When reporting the result, a clear distinction has to be made between the performance of the cell or just for its active material, which is a clearly logical practice but usually been ignored. Additionally, technical differences between SCs devices testing and SCs materials testing will be discussed in the following sections.

Table 2. 1 Technical merits and demerits of the CV, GCD, and EIS techniques[15].

S. No	Technique	Merits and demerits
1	CV	**Merits** • Degradation process • Specific capacitance • Differentiate between EDLC and PC **Demerits**

		• Show only kinetic aspects; thermodynamic aspect is neglected
2	GCD	**Merits** • Capacitance • Differentiate between EDLC and PC **Demerits** • Show same triangular shape for all double layer capacitive materials
3	EIS	**Merits** • Separately evaluate various resistances in a system • Specific capacitance evaluation • Differentiate between resistive and inductive nature • Relaxation time for recharging • Degradation behavior **Demerits** • Evaluation at small voltage only • Discrete behavior above 10^6 Hz

Cyclic voltammetry (CV) is a widely used technique to study the electrical performance of supercapacitor electrode materials. In a CV experiment, a linearly changed electric potential will be applied to the system and the produced response current would be recorded. As the applied potential is ramped linearly versus time which means a slanting increased positive voltage sweep firstly reach to the maximum set potential, then the sweep is immediately reversed for discharging until the potential is ramped in the opposite direction to return to the initial potential. Thus, CV measurement was used as an important method for studying the mechanism of supercapacitor electrode materials due to its special testing mechanism allow it provides a species in the forward scan and then probe its fate in the reverse scan within a few seconds. In addition, the specific capacitance and the capacitance stability (retention) as a function of the scan rate and the number of cycles can be evaluated by CV technique.

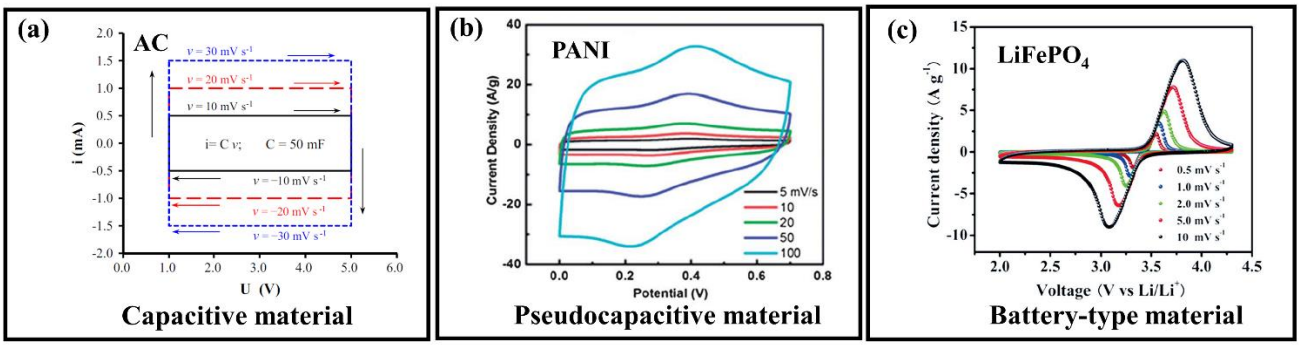

Figure 2. 4 CV curves of different electrode materials. (a) EDLCs (AC). (b) pseudocapacitive electrode (PANI). (c) battery electrode ($LiFePO_4$ vs Li)[24].

During CV testing, the capacitive current i_c of an ideal EDLCs normally follows:

$$i_c = \frac{dQ}{dt} = C\frac{dU}{dt} = Cv$$

Where, C is the capacitance, ν is voltage sweep rate. Here, i_c is potential-independent due to the potential-independent capacitance[26]. Thus, the CV curves of ideal EDLCs have rectangular shapes (**Fig. 2.4a**). On the other hand, for battery-type electrodes, obvious separated peak caused by redox reactions can be observed in CV curves (**Fig. 2.4c**). While the shapes of pseudocapacitors are between these two situations (**Fig. 2.4b**).

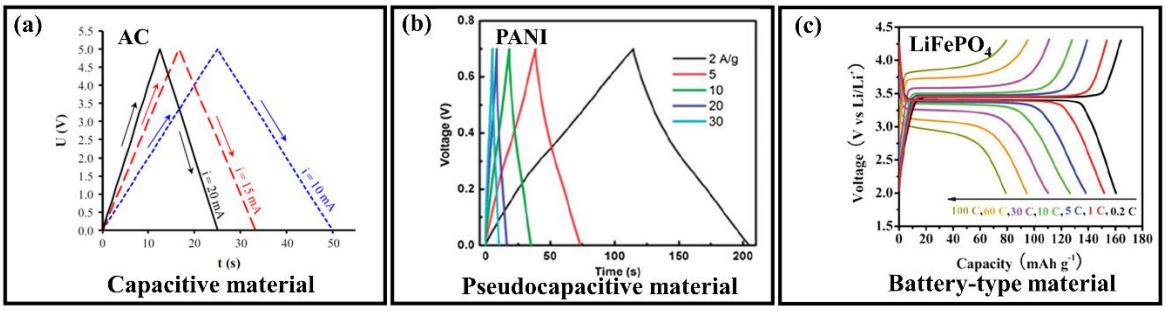

Figure 2. 5 GCD curves of different electrode materials. (a) EDLCs (AC). (b) pseudocapacitive electrode (PANI). (c) battery electrode ($LiFePO_4$ vs Li)[24].

GCD technique is a commonly used method to characterize SCs under direct current. During the test, a constant current with or without dwell time (the time interval between charging and discharging with the peak voltage V_0 kept constant) will be applied to the SC devices or working electrodes for the repeatedly charging and discharging process. The relationship between potential (V) and time (s) is the output. For different types of electrode materials, the GCD curves are also exhibits different shapes. The stored charge q (coulombs) of a capacitor follows:

$$q = C\Delta V$$

Where, C is the capacitance in farads, ΔV is the potential difference in volt.

During the GCD test, both q and V are time-based parameters. By differentiating the equation with time for each side, we obtain:

$$\frac{dq}{dt} = C\frac{dV}{dt}$$

On the other hand:

$$\frac{dq}{dt} = i_{(t)}$$

Thus,

$$dV = \frac{i_{(t)}}{C}dt$$

As GCD was tested under the constant current, $i_{(t)}$ is a constant parameter here.

For EDLCs, the capacitance C is an intrinsic property. Therefore, the profile of the voltage versus time for EDLCs shows a nearly linear shape (**Fig. 2.5a**)[26-27]. For battery-type electrode materials, potential plateaus caused by phase transformations can be clearly observed in GCD curves (**Fig. 2.5c**). While, for pseudocapacitive materials, the GCD curves have deformed linear shape due to the existing of redox reaction (**Fig. 2.5b**).

EIS is a powerful analytical technique to measure the performance of electrochemical cells at different frequency regimes. EIS testing is conducted in an equilibrium state which is different from the CV and GCD tests that constantly disrupt the electrochemical system state according to their dynamic nature. In the EIS test, a small sinusoidal voltage (normally 5 mV or 10 mV) will be superimposed on the steady-state potential (DC potential or open circuit potential) to measure the impedance of the cell as a function of frequency (frequency range normally between 100 kHz and 10 mHz). Normally, the resulting impedance data are represented by Bode plot and Nyquist plot. The Bode plot used to descript the response relationship of the phase angle versus frequency. The Nyquist plot shows the impedance relationship of the imaginary part ($-Z_{im}$) and the real part (Z_{real}) at different frequencies. Z_{real} depends on the resistance of the electrode, the electrolyte, the contacts, and Faradaic resistance; Z_{im} is associated the diffusion of electrolyte[28]. According to the measurement of the response of frequency and impedance, EIS can be used to analysis the charge transfer, mass transport and charge storage mechanisms. In addition, the capacitance, energy, and power properties can be estimate by EIS technique[16].

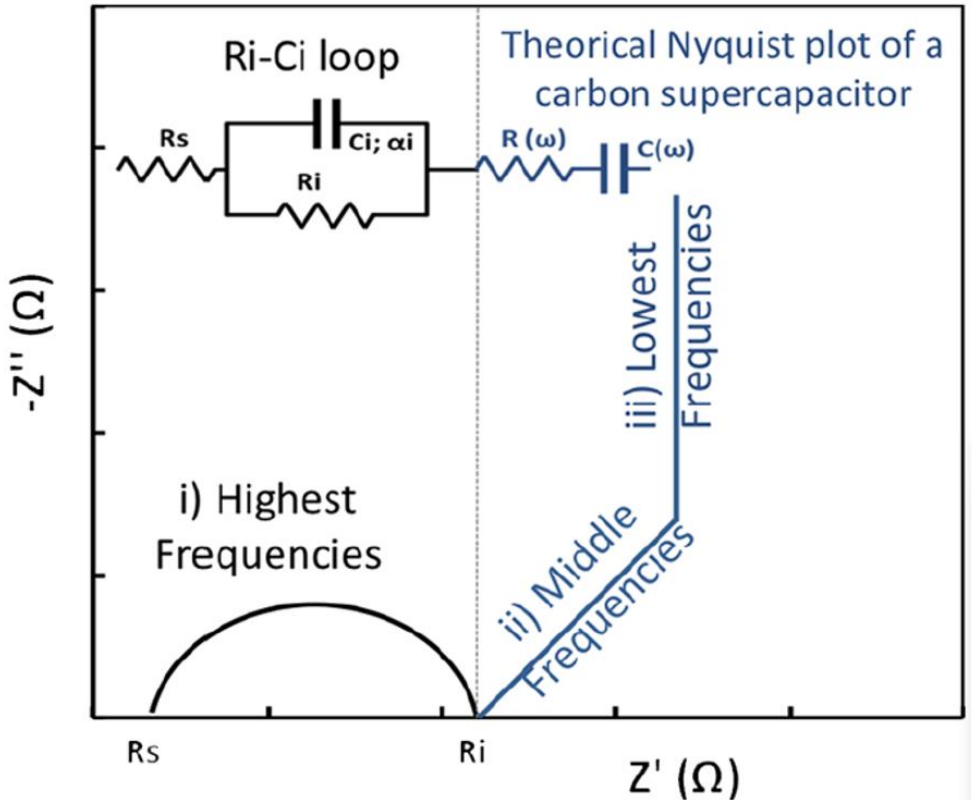

Figure 2. 6 Typical Nyquist plot of a carbon-carbon supercapacitor. It includes high to low frequency behavior of a supercapacitor with the equivalent circuits (R_s is the high frequency resistance, R_i is the resistance of the active material/current collector interface, C_i is the interface capacitance with the dispersion parameter α_i, $R_{(\omega)}$ is a part of the supercapacitor resistance depending on the frequency, and $C_{(\omega)}$ is the supercapacitor cell capacitance)[28].

There are some classic models thoroughly describe the impedance of extensively studied porous electrodes. For example, **Fig. 2.6** shows a typical Nyquist plot and the equivalent circuit of a carbon-carbon supercapacitor[28]. The schematic of Nyquist plot can be divided into three different regions: (i) the semicircle at high frequency, (ii) the 45° line at medium frequency and (iii) the vertical line at low frequency (**Fig. 2.6**). At high frequency, R_s, represents the bulk electrolyte resistance including the ohmic resistance of electrolyte; the intrinsic resistance of the active material and the contact resistance at electrode and current collector interface[29]. The semicircle loop, defined as a resistor-capacitor (RC) circuit (R_i-C_i), is attribute to the charge

transfer resistance and the double-layer capacitance. C_i corresponding to the interfacial capacitance and α_i (the penetrability coefficient: $0 < \alpha_i < 1$) represents the nonideal behavior of C_i. When $R_i \rightarrow \infty$, the interface likes being blocked and the cell plot is same to the ideal supercapacitor (**Fig. 2.6**). Normally, when the conductivity of the electrolyte increased or the interface electrical resistivity of the electrode and current collector decreased, the $R_s + R_i$ decreases[28]. The 45° line at medium frequency is ascribed to the resistance depending on frequency (R_ω) which is related to the diffusion and penetration of electrolyte in the electrode pores. The circuit $R_{sc}(\omega)$-$C(\omega)$ corresponding to the cell behavior at low frequency. $C(\omega)$ corresponding to the cell capacitance. The series resistance of the cell, $R_{sc}(\omega)$, ($R_{sc}(\omega) = R_s + R_i + R_\omega$), depends on the impedance contact. Both $R_{sc}(\omega)$ and $C(\omega)$ are changed with frequency. As illustrated here (Figure 8), the ideal supercapacitor has a vertical tail. Non-vertical slope usually indicates the existing of other processes (besides double-layer formation) including Faraday reactions or diffusion limitation[30]. The cell capacitance $C(\omega)$ can be calculated from the EIS results by following Equation:

$$C(\omega) = C_{real}(\omega) - jC_{im}(\omega) = \frac{-Z_{im}(\omega)}{\omega|Z(\omega)|^2} - j\frac{Z_{real}(\omega)}{\omega|Z(\omega)|^2}$$

where j is the imaginary number; ω is the angular frequency; Z_{real} and C_{real} represent the real part of impedance and capacitance; Z_{im} and C_{im} are the imaginary part of impedance and capacitance.

2.3 Electrodes materials

The electrode materials for supercapacitors should have features including high surface area, high conductivity, good stability, eco-friendly and low cost. A significant number of materials are currently available as electrode materials for supercapacitors mainly including several categories: carbon, transition metal oxides/hydroxides, conductive polymers, transition metal sulfides and composites. Based on the different type of energy storage process of different electrode materials, electrode materials for supercapacitors can be divided into EDLCs electrode materials and pseudocapacitors electrode materials (**Fig. 2.7**).

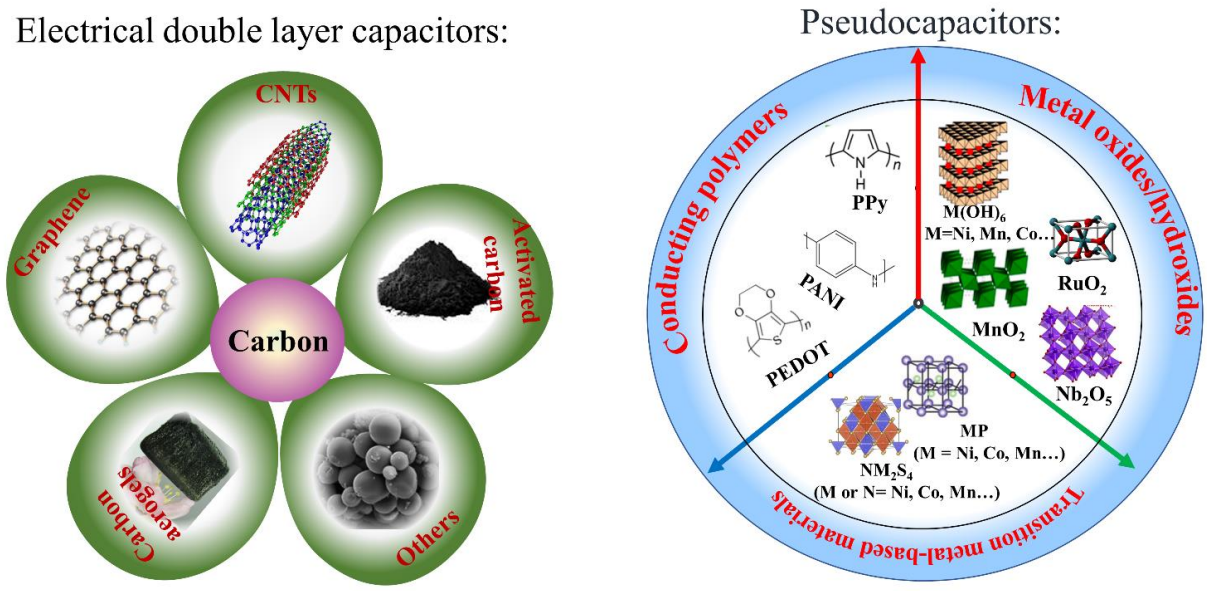

Figure 2. 7 Electrode materials for different type of supercapacitors.

2.3.1 Electrodes materials for EDLCs

Carbon materials with properties such as high conductivity, low cost and high surface area are

developed as electrode materials for EDLCs. The energy storage mechanism of carbon materials electrodes is based on the formed electrochemical double layer by physical separation of electronic charges and ions occurred at the interface between the electrode and electrolyte. Therefore, the capacitance mainly depends on the active surface area of electrode materials. Furthermore, other factors associated with active surface area including the electrical conductivity, surface functionality, pore shape and structure and pore size distribution have great effect on the electrochemical performance of electrode[31]. Methods for improving specific capacitance of carbon materials consist of functionalizing the surface, improving the surface area, adjusting the pore size and distribution. Commonly used carbon materials for EDLCs electrode materials include carbon nanotubes (CNTs), activated carbon, carbon aerogels, graphene etc[24].

Activated carbon (AC) is the firstly selected and the mostly used commercial electrode material for EDLCs electrodes. AC material contains all of the common pore sizes: micropore, mesopore and macropore. Thus, AC can provide large surface area and good electrical properties. AC can be produced from various carbonaceous materials rich in carbon even some agricultural wastes (such as cassava peels, apricot seeds, coconut shell, etc.) by the method of physical activation or chemical activation or a combination of both[32-33]. By adjusting carbon precursors and activation methods, AC with various physiochemical properties can be obtained. Among them, the maximum specific surface area can be as high as 3000m^2 g^{-1}. Additionally, the obtained AC by activation processes has a wide pore size distribution, including micropores (< 2 nm), mesopores (2 - 50 nm) and macropores (> 50 nm)[32].

Practically, the specific capacitance is not entirely dependent on specific surface area of AC. This is because electrolyte ions are too big to enter into some smaller micropores, which means this smaller micropores are not effective during charge accumulation[31]. Thus, many researchers have focused on finding the most suitable pore size for a certain electrolyte ion size. Several researches showed that for the majority of aqueous electrolytes, the pore size of around 0.4 ~ 0.7 nm is best and for organic electrolytes, the most suitable pore size is 0.8 nm[34-35]. Thus, the maximum Cs can be achieved by the coordination between the pore size and the ion size. In addition, the surface functionalization is also an effective method to increase the capacitance of AC and research shows that the existing of the functional groups may help the enhancement of faradaic redox reactions and have a 5 - 10% increasement in Cs[31].

Carbon nanotubes (CNTs) with cylindrical nanostructures have remarkable mechanical and electrical properties and thermal conductivity. The discovery of CNTs has greatly promoted carbon materials science and engineering. Great attention has been focused on exploring CNTs as supercapacitor electrode material based on their super properties and their unique open and available network of mesopores. The mesopores are connect to each other and form a continuous charge distribution in the CNTs which makes more effective use of the accessible specific surface area[36]. This helps the CNTs based electrodes have comparable capacitances performance to some activated carbon electrodes. In addition, the interconnected mesoporous network helps the easily penetrate and diffusion of electrolyte ions which makes CNTs electrode shows lower ESR than AC electrodes[37]. CNTs can be classified as single walled CNTs (SWCNTs) and multi-walled CNTs (MWCNTs). The performance of SWCNTs are

mainly affected by the electrode/electrolyte accessibility and the electrolyte ions size. SWCNTs have great theoretical specific surface area ($1315 m^2 g^{-1}$) that is higher than MWCNTs. The mesopores in MWCNTs make electrolyte ions easily flow across the electrode/electrolyte interface. However, the significant volume change caused by repetitive ions intercalation and depletion leads the decreased mechanical stability of MWCNTs.

Carbon aerogels are made by carbonization of organic aerogels at high temperature or obtained by a frozen-dry process. Basically, Carbon aerogels are composed by a continuous network of carbon nanoparticles with interspersed micropores and mesopores. The concentration of micropores and mesopores can be controlled by the curing and drying methods, the original ingredients and the carbonization conditions. Thus, the nanostructures of carbon aerogels can be designed by adjusting the synthesis conditions. The micropores and mesopores structure provide high surface area and ultra-light properties for carbon aerogels. Combined with their good electrical conductivity, carbon aerogels are typically used electrode materials for EDLCs. In addition, their continuous structures allow carbon aerogels used as binder less electrode material as they can chemically bond with the current collector. Therefore, the carbon aerogels electrodes have lower equivalent series resistance which yield higher power [38].

Graphene, monolayer of graphite, has a two-dimensional (2D) structure with carbon atoms arranged in a regular hexagonal pattern. The study and applications of graphene has enjoyed significant attention since it has been mechanically exfoliated in 2004[39]. Recently, graphene has been considered as one of the important electrode materials for supercapacitor due to its excellent electrical conductivity, large surface area, chemical stability and mechanical

stability[40]. Compared to other carbon materials (e.g., AC, CNTs), graphene, as electrode material, doesn't rely on the distribution of pores[32]. The exposed graphene sheet surfaces and the easily accessible to electrolyte are two important benefits of using graphene as electrode material. The specific surface area of graphene is around 2630 $m^2 g^{-1}$ and the whole efficiency of specific surface area can achieve a capacitance of up to 550 F g^{-1}[41-42]. However, for some bulk graphene, the occurred aggregation and restacking resulting in a much lower specific surface area than the theoretical value. For the maximum utilization of specific surface area and intrinsic surface capacitance of graphene sheet, many efforts have been taken to prevent graphene sheets being aggregated and restacked themselves during the whole synthesis process and the subsequent electrode production procedures. Therefore, producing the curved graphene sheets were considered as a good way as they will not restack face to face[32]. In addition, integrate the single graphene sheet into the bulk graphene material is also considered as an effective approach[40].

2.3.2 Electrode materials for pseudocapacitors

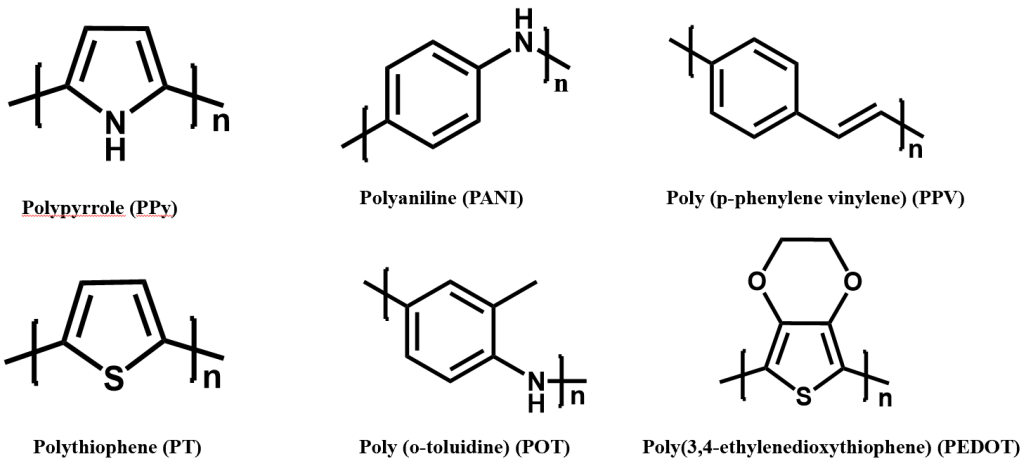

Figure 2. 8 Chemical structures of some representative conducting polymers.

Conducting polymers (CPs) are a subset of a large group of materials called organic polymers which possess semiconducting or conducting properties. CPs consist of alternating single and double bonds which called conjugated double bonds. Each conjugated double bond consists a localized "sigma(σ)" bond and a localized "pi (π)" bond. This special conjugation structure provides the possibility of conducting property for conducting polymers. The first conducting polymer, conducting polyacetylene exhibiting an excellent electrical conductivity of 10 orders of magnitude of (10^3 $S.cm^{-1}$) after it was oxidized by iodine vapor, was discovered in late 1970s by Alan G. MacDiarmid, Hideki Shirakawa and Alan J. Heeger[43]. In the ensuing years, research in this area is continuing to grow with the developing of variety of conducting polymers like polypyrrole (PPy), polyaniline (PANI), poly(3,4-ethylenedioxythiophene) (PEDOT), polythiophene (PT), poly (p-phenylene vinylene) (PPV) etc. (**Fig. 2.8**). Different CPs and their composites have been widely explored as electrodes material for pseudocapacitors due to their good conductivity, the low cost and the easy synthesis property[44]. In most cases, CPs storage energy by the enabling faradaic redox reactions. Unlike carbon materials, which only depends on the surface of electrodes during the whole charging process, CPs charging process happens throughout the bulk of the material. During the redox process, electrolyte ions transfer into and out of the polymer backbones which leading to the increased capacitance due to the happening reactions. However, this process also accompanies by the lower cyclability due to the continuous ion insertion and extraction process destroys the structure of CPs. An idea supercapacitor should combine a high capacitance and a good cycling stability. Thus, many effects have been done to combine this two features in a CP electrode including design different CPs structures which have high surface area available for charging and possess the ability to

withstand the swelling and shrinkage and combine CPs with other materials to make CPs-based composites [45-47].

In 1971, first pseudocapacitance was discovered in ruthenium dioxide (RuO_2) electrode because of the involved faradaic charge-transfer reactions. Since then, more and more transition metal oxides (TMOs) electrodes have been developed for pseudocapacitors, such as manganese oxide (MnO_2), iridium oxide (IrO_2), Niobium oxide (Nb_2O_5), vanadium pentoxide (V_2O_5) and Iron oxide (Fe_3O_4). Among them, RuO_2 and MnO_2 have got the most extensive studied. RuO_2 has metal-type conductivity and reversible redox reactions facilitating ions transfer and capacitance performance. So far, RuO_2 with different nanostructures such as nanoparticles, nanoneedles, nanotubes and nano-porous films have been synthesized as electrodes. Hu et al designed and tailored a 3D nanotubular array of RuO_2. xH_2O which shows a pretty high capacitance value reach to 1300 F g^{-1}[48]. Not only the high capacitance but also its long cycle life, wide voltage window and highly reversible reduction-oxidation reaction make RuO_2 an excellent electrode material. The main disadvantage of RuO_2 is its high cost. Thus, new synthesis methods and composite materials are needed for further development of RuO_2. MnO_2 with good capacitive performance, low cost and environmentally safe properties has been considered as one of the most promising electrode materials for pseudocapacitors[32]. The nanostructured MnO_2 synthesized by different methods got lots interest used in pseudocapacitors[38]. Amorphous nanostructured MnO_2 synthesized under ambient conditions from $KMnO_4$ and ethylene glycol exhibiting a good capacitance of 250 F g^{-1} and a much stability with capacitance retention of 92% after 2000 cycles[49]. Porously assembled 2D

nanosheets of MnO_2 synthesized by exfoliation and flocculation process shows a capacitance around 140-160 F g^{-1} and a stability with capacitance retention ~93-99% after 1000 cycles[50]. Although, many research results exhibit the improved capacitance performance of transition metal oxides with different nanostructures. The poor electrical conductivity and slow ion transfer rate restricting the specific capacitance and charge/discharge ability of the electrode. However, the applications of TMOs are mainly restricted by their poor electrical conductivity and unsatisfactory rate capability because the band gap of TMOs implies the semiconductor properties [63,64]. To meet the requirements of practical applications, a large number of new materials, such as hydroxides, sulfides, selenides and phosphides, have been designed.

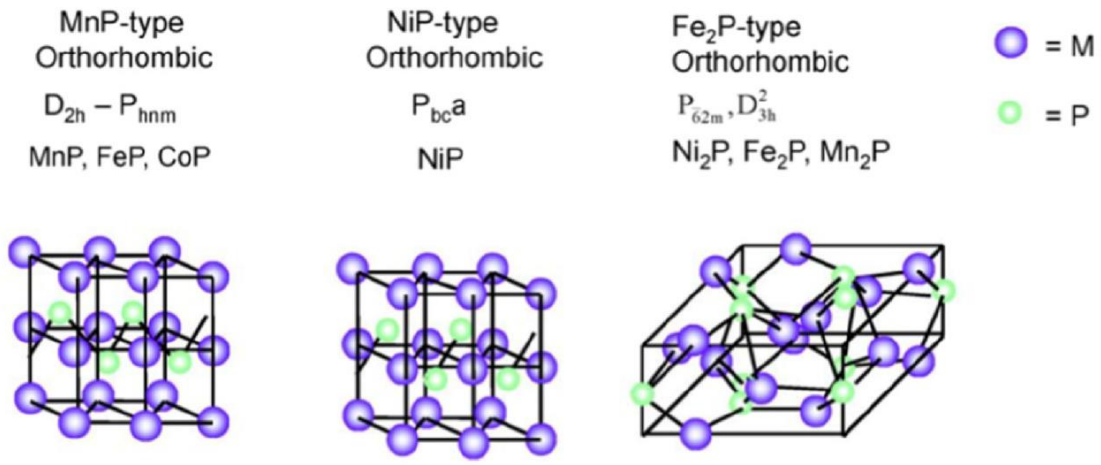

Figure 2. 9 three types of crystal structures for metal phosphides[51].

Transition metal phosphides (TMPs), one transition metal compound formed by a combination of phosphorus with one or several transition metal elements, have been extensively explored and show outstanding performance in electrocatalysts, lithium batteries, and supercapacitor [52-53]. Compared to TMOs, the content of P atoms in TMPs is helpful for enhancing their conductivity due to the lower electronegativity and larger atomic radius of phosphorus in

comparison with oxygen [54]. Thus, TMPs have higher specific capacity, better rate capability than corresponding TMOs. Moreover, TMPs show much stable cycling stability than the common CPs electrodes (e.g. PANI, PPy and their derivatives) as the mechanical degradation of caused by the swelling and shrinking of CPs during the intercalating/deintercalating process. In fact, phosphorus can combine with numerous elements in the periodic table forming a diverse class of phosphides. The high flexibility of phosphorus frameworks allows metal phosphides to have a variety of stoichiometry, various compositions and multitudinous crystal structures. The large atomic radius (0.109 nm) of phosphorus also contributed to the formation of different crystal structures for metal phosphides [55]. **Figure 2.9** gives three examples of crystal structures for metal phosphides. Both MnP-type and NiP-type are the orthorhombic structure and the difference is the phosphorus atoms form chains in MnP-type, while form pairs in NiP-type. The Fe2P-type structure including lots of metal-phosphorus bonds [54]. Affluent metal-metal bonds and metal-phosphorus bonds in these structures make TMPs promising as a class of electrode materials. So far, more and more TMPs have been developed and used as electrodes for energy storage, including Ni_2P, Co_2P, CoP, NiCoP, ZnNiCoP, MnNiCoP, NiCoMoP [56-59].

Transition metal sulfides (TMSs) and their composites are also got tremendous interest as electrode materials for various kinds of energy storage devices including pseudocapacitors, lithium-ion batteries, sodium-ion batteries, and others due to their unique chemical and physical properties, excellent performance, abundance and cost-effectiveness[60]. Compared to metal oxides, oxygen ions are replaced by sulfur ions which have higher electro negativity

contributing to increase the layer spacing and make charge transportation easier thereby preventing the decomposition of the structure and creating more flexible structures[61]. The metal atoms of two-dimensional (2D) layered TMSs (denoted as MS_2, where M = Mo, W, V, Sn, Ti, Zr, etc.) are covalently bonded forming the S-M-S layer and each layer is attracted by van der Waals force[62]. This layered structures of MS_2 make them as idea intercalation host materials for accommodating intercalating ions (e.g., H^+, K^+, Na^+, Li^+, Mg^{2+}) between the interlayer space for the generating of intercalation pseudocapacitance[63]. Compared with metal oxides, research on TMSs as intercalation pseudocapacitors electrodes is relatively limited, and only a few studies have been reported so far. In addition, research shows the intercalation/de-intercalation of ions between S-M-S layers facing the sluggish kinetics. Thus, the conductivity and interlayer space of layered TMSs are two important factors affecting their intercalation pseudocapacitance performance, especially for rate performance. Among 2D TMSs, 1T-MoS_2 and VS_2 with metallic conductivity have been investigated as excellent electrode materials for intercalation pseudocapacitors[64-65]. TMSs of MS_x (M = Ni, Co, Fe, Mn, Cu, etc.) were first explored as cathode and anode materials for LIBs in 1970s[62]. This is because they can react with OH^- in alkaline electrolyte. In the charging process, the low valance transition metals lose electrons and oxidized to a higher valence state while in the discharging process they back to their original state. It means that in each charge and discharge process, the low valance compounds undergo at last once phase change which lead to the battery type charge storage behavior. Thus, they attract great attention as electrodes materials for hybrid SCs. Because after special designing, they can have the capacitor-type material kinetics and show high electrochemical activity owing to the battery charge storage process[63].

Basically, the binary metal sulfides (denoted as AB_2S_4) and ternary metal sulfides (denoted as A_2BCS_4, where A, B, and C are metal centers) exhibit higher electrochemical behavior than single component sulfides. There are mainly two possible reasons: 1) The binary and ternary metal sulfides can provide much richer redox reaction sites which contribute to the increase of faradaic reactions base capacities; 2) The binary and ternary metal sulfides have lower band gap, leading to higher electric conductivity and thus facilitate electronic transmission[66-67]. Consequently, a variety of binary and ternary metal sulfides have been designed and synthesized as electrode material for supercapacitors. Among them, $NiCo_2S_4$, $CuCo_2S_4$, $CoMo_2S_4$ and $ZnCo_2S_4$ are widely studied binary metal sulfides and $ZnCu_2SnS_4$ and $FeCu_2SnS_4$ are widely studied ternary metal sulfides. Although these TMSs materials have high capacitance and excellent rate capabilities, all these goals are hard to obtain simultaneously in one material. Furthermore, the redox reaction occurred at the charge/discharge process would destroy their structures and cause their poor cyclic stability. To solve these problems, many strategies have been developed. Designing and synthesizing TMSs nanostructures with different morphologies is a commonly used method. For example, $NiCo_2S_4$ with different morphologies including zero dimensional (e.g., cubohexaoctahedral nanostructures, hollow microspheres, nanoparticles), two dimensional (e.g., nanorods, nanotubes, nanowires, nanocolumn arrays) and three dimensional (e.g., urchinlike and flowerlike structures) have been studied for SCs and each morphology has its unique advantages[68]. The hybridization of different materials is also act as an effective way. Research shows the adulteration of graphene or graphene derivatives could enhance the electrochemical performance and cycle stability of TMSs. Because the 2D structure of graphene can provide large specific surface area and good

physicochemical stability. Moreover, their porous structures are helpful for the diffusion of electrolyte ions[69]. Thus, TMS/graphene composites have attracted great attention for electrode materials[70-71].

Chapter 3

Polypyrrole film based flexible supercapacitor: mechanistic insight into influence of acid dopants on electrochemical performance

Abstract: The present study is aimed at providing a mechanistic insight into the influence of acid dopants on electrochemical performance of polypyrrole (PPy) film based flexible supercapacitor. PPy films are electrochemically deposited on carbon cloth using different kinds of acid dopants: hydrochloric acid (HCl), perchloric acid ($HClO_4$), sulfuric acid (H_2SO_4), p-toluenesulfonic acid (p-TSA), phosphoric acid (H_3PO_4) and phytic acid (PA). Results show that both the size and the type of dopants have a great influence on the doping level, the mass ratio of counterions, the accessibility of redox sites and the electrochemical performance of PPy film electrodes. Among the obtained electrodes, PPy/HCl exhibits the highest specific capacitance of 960 F g^{-1} at 5 mV s^{-1}, yet with inferior cycling stability. Interestingly, PPy/p-TSA shows the best cycling stability with more than 75% of capacitance retention after 2000 cycles, also with a relatively high specific capacitance (572 F g^{-1} at 5 mV s^{-1}). Moreover, the PPy/p-TSA is used to fabricate a flexible all-solid-state supercapacitor device which exhibits a maximum energy density of 6.2 Wh kg^{-1} and a maximum power density of 2.64 KW kg^{-1}, respectively. Intriguingly, the assembled PPy/p-TSA device exhibits excellent cycling stability with 88% capacitance retention after 6000 cycles. This fundamental study will provide new prospects for developing PPy-based electrode materials for future flexible and wearable supercapacitors.

3.1 Introduction

Supercapacitors, also known as electrochemical capacitors, are energy storage devices that possess superior energy density and power density than conventional capacitors [72]. Their fast delivery rate, lightweight, high power density, reversibility and long cycling stability have made them non-replaceable in a wide variety of applications that require rapid and intense electrical pulses such as portable electronics [73], digital communication [74], uninterruptible power supplies [75], electric hybrid vehicles [76], and pulse laser technique [77], etc. According to the charge storage mechanism, supercapacitors can be classified into electrical double layer capacitors (EDLCs) and pseudocapacitors [17]. For EDLCs, carbonaceous materials with high surface area are usually used as electrodes which store energy by electrosorption of pure electrostatic charge on the porous structures [78-79]. Commonly, EDLCs have high power density and longer life span, but they have low specific capacitance due to the limitation of electrical double layer formed at the electrode/electrolyte interface [80]. Unlike EDLCs, pseudocapacitors use transition metal oxides and conducting polymers as electrode materials, exhibiting 10-100 times higher specific capacitance than EDLCs [81]. This is due to the fast and reversible charge transfer reactions between the electrode and electrolytic ions [82]. Compared with the relatively expensive and hardly processable metal oxides, conducting polymers with many superior properties such as good electric conductivity, easy processability, environmental friendliness and excellent flexibility, have been considered as promising electrode materials for pseudocapacitors, especially for flexible supercapacitor [83].

Polypyrrole (PPy) as one of the most promising conducting polymers exhibits excellent electrical conductivity that can be adjusted according to the usage. The facile interconversion

between redox states, excellent capacitive properties, scalable morphology from few microns to nano level and tunable electrical properties made PPy extensively used in variety of applications such as energy storage devices, sensors, anti-corrosion coatings, EMI shielding, etc. [84-86]. Recently, PPy has drawn considerable interest for the applications of flexible supercapacitors which show great promise in portable and wearable devices [87]. Typically, PPy nanoparticles or films can be prepared by facile chemical or electrochemical polymerization. The strong oxidizing agents such as ammonium persulfate, iron (III) chloride and potassium persulfate are widely used as initiators during the chemical polymerization. However, these oxidizing agents are not only costly but also harmful to human body as they cause irritation to the eyes, skin, lungs, etc. upon contact [88]. Moreover, PPy synthesized via chemical polymerization usually face the challenge of decreased electrical conductivity caused by polymer agglomerations [89]. On the other hand, electrochemical polymerization is a method that requires potential or current to initiate the polymerization process, which is the most common and cost-effective way to synthesize PPy films so far [90]. In addition, the thickness and performance of the binder-free PPy films can be easily controlled by controlling potential or current density. Franciele et al. [91] compared the effects of three different kinds of electropolymerization methods on the supercapacitive behavior of PPy films. The results showed PPy obtained by a potentiostatic method possesses the best performance for supercapacitor application. Based on the above information, potentiostatic polymerization method is applied in the present study for the synthesis of PPy films.

The electrochemical polymerization of PPy film is accompanied by the oxidation reactions of

pyrrole monomer in the presence of doping ions. Doping process is an important process used to improve the conductivity of PPy which carried out by injecting charged species into the conjugated polymer backbone during the synthesis step. Acid dopants have been widely used as oxidizing (p-type) dopants for PPy. The oxidative doping process of PPy can be described as follows[92]: Upon oxidation, a free radical and a positive charge are produced after one electron being removed from the neutral PPy chain. The local resonance of the charge and the radical makes radical and cation coupled with each other accompanied by quinoid-like rings' participation. The combination of a radical and a cation constitutes a polaron. Upon further oxidation, at higher doping levels, pairs of polarons combine with each other resulting in the formation of more energetically favorable bipolarons, and the deformation of benzenoid-to-quinoid in the bipolaron becomes more stronger than that in the polaron. With continuing doping, a continuous bipolaron bands can be formed. For a highly doped PPy, it is conceivable that an overlap between bipolarons occurs, producing partially filled bands and a metallic state with a positive charge and an associated counterion (e.g., Cl^-, SO_4^{2-}). Briefly speaking, dopants are introduced into PPy chain to modify their electrical performance during the doping process. During charging-discharging process, PPy films will undergo redox reaction and changes its redox state (doped and dedoped) when ions are inserted/extracted from the polymer backbone. Thus, the type of dopants used in the polymerization process can influence the electrochemical performance of PPy films when used as a supercapacitor electrode [93]. Several previous studies have shown that the capacitive behavior of PPy can be strongly influenced by the type of dopants. Yong et al. [94] reported that PPy film doped by 0.5 M HNO_3 exhibited good electrochemical properties for supercapacitor applications. The specific capacitance of PPy/0.5

M HNO_3 film can reach up to 596 F g^{-1} at a current density of 5 mA cm^{-2} with 96% of retention after 1000 cycles (50 mV s^{-1}). Lang et al. [95] reported the role of anthraquinone sulfonate dopants for PPy. The results showed that PPy/AQS (9,10-anthraquinone-2-sulfonicacidsodiumsalt) exhibits the highest specific capacitance of 608 F g^{-1} at a scan rate of 5 mV s^{-1}. However, comprehensive study regarding to the influence of acid dopants on electrochemical performance (especially cycling stability) of PPy film-based supercapacitors is currently lacking.

From a mechanistic point of view, the electrochemical performance of PPy films can be influenced by the number of redox sites in the polymer that can be accessed by the ions. More specifically, the polymer-electrolyte interface restricts these ions that can be inserted and removed from the polymer which affects the electrochemical storage capacity of PPy. This storage capacity can be studied by observing the accessibility of the redox sites at the polymer-electrolyte interface. In this work, PPy films were electropolymerized on the carbon cloth substrates by potentiostatic electrochemical techniques (Scheme 1). During the electrochemical deposition process, chlorates (HCl and $HClO_4$), sulfates (H_2SO_4 and p-TSA) and phosphates (H_3PO_4 and PA) were used as dopants. The influence of these dopants on morphology, electrochemical performance and accessibility of redox sites in the polymer was studied in this work. Furthermore, a flexible all-solid-state supercapacitor device was fabricated using PPy/p-TSA films as electrodes and PVA/H_2SO_4 gel as electrolyte to investigate the electrochemical performance of PPy film-based supercapacitor device for practical applications (**Scheme 3.1**).

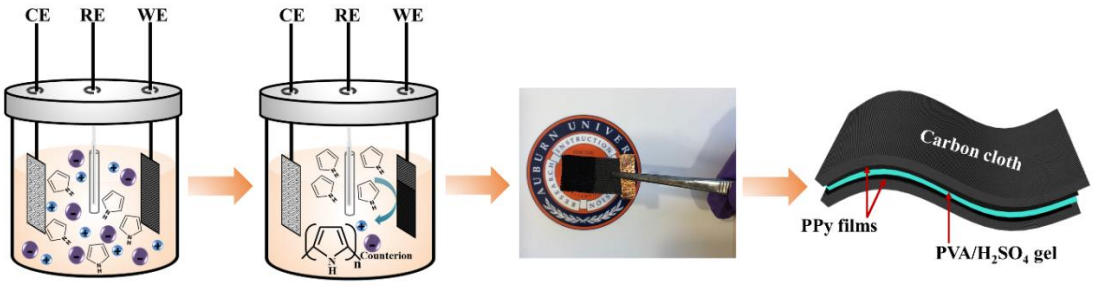

Scheme 3.1 Schematic illustration of the synthesis process of PPy with different dopants and the fabrication of flexible all-solid-state symmetric supercapacitors.

3.2. Experimental

3.2.1. Materials

Hydrochloric acid (HCl) was purchased from BDH chemicals. Perchloric acid ($HClO_4$) was purchased from VWR, USA. Sulfuric acid (H_2SO_4) was purchased from Anachemia. p-toluenesulfonic acid (p-TSA) was purchased from Alfa Aesar, USA. Phosphoric acid (H_3PO_4) was supplied by EM Science. Phytic acid (PA) and pyrrole monomer were purchased from Tokyo Chemical Industry. Acetone and HNO_3 were purchased from VWR, USA. In addition, carbon cloth (CC) (40 cm x 40 cm) was purchased from Fuel Cell Earth LLC, MA. Platinum (Pt) gauze (100 mesh, 99.9% metal basis) was purchased from VWR, USA. All chemicals were used without further treatment or purification.

3.2.2 Electrodeposition of PPy films.

The synthesis of PPy films was carried out by electropolymerization using an electrochemical workstation (CHI 760D). Prior to electrodeposition, CC (1 cm × 2 cm) was cleaned by HNO_3, DI water and acetone, respectively to remove surface contamination and increase the surface wettability of carbon surface followed by vacuum drying at 60°C. The pre-treated CC was used

as substrate for electrodeposition of PPy and only half of the CC was immersed in the electrolyte to obtain an area of 1 cm^2. The single compartment three-electrode system was used, where CC was used as the working electrode, Pt mesh served as the counter electrode and Silver/Silver chloride/KCl (3 M) (Ag/Ag^+, E° = +205 mV vs. SHE) used as the reference electrode. The electrolyte was an aqueous solution containing 0.1 M pyrrole and 0.5 M dopants. The PPy films were obtained by applying constant potential of 0.8V for 5min. After electrodeposition, the PPy coated CC was rinsed by DI water and vacuum dried at 60°C for 24 h. During the electrochemical deposition process, dopants including chlorates (HCl and $HClO_4$), sulfates (H_2SO_4 and p-TSA) and phosphates (H_3PO_4 and PA) were used. The structure of dopants molecules used in this study is shown in Fig. S2. The obtained PPy films are marked as PPy/HCl, PPy/$HClO_4$, PPy/H_2SO_4, PPy/p-TSA, PPy/H_3PO_4, PPy/PA, respectively.

3.2.3 Fabrication of all-solid-state supercapacitor device

The polyvinyl alcohol (PVA)/H_2SO_4 gel electrolyte was prepared as follows: Firstly, 3g H_2SO_4 was added in 30 mL deionized water, then 3 g PVA was added into the H_2SO_4 solution. The obtained mixture was kept at 85 °C under constant stirring until it became clear. Secondly, the prepared PVA/H_2SO_4 gel electrolyte was slowly poured onto two pieces of PPy coated CC (1.5×3 cm^2 with coating area of 1.5×2 cm^2). The two electrodes were left in the fume hood overnight to vaporize the excess water. Finally, two electrodes were gently pressed together, and the all-solid-state supercapacitor device was obtained.

3.2.4 Characterization

The morphology of the PPy films was characterized by using a scanning electron microscope

(SEM, Thermo Scientific Apreo) at 5.0 kV with 10 mm working distance. Fourier Transform Infrared (FTIR) spectra were recorded in a Thermo Nicolet 6700 instrument within frequency range of 4000-500 cm^{-1}. X-ray photoelectron spectroscopy (XPS) was performed with a Kratos Axis DLD spectrometer by Al Kα (hν = 1486.6 eV) radiation under the of 10^{-10} Torr pressure conditions. The carbon peak C 1s (284.8 eV) was used to calibrate the binding energies. The specific surface area and pore size of PPy films were calculated from the nitrogen adsorption-desorption isotherms, which were conducted with a Quantachrome NOVA 2200e, Surface Area and Pore Size Analyzer. All electrochemical measurements were conducted in 1.0 M H_2SO_4 as the supporting electrolyte. Cyclic voltammetry (CV) measurements were performed within a potential range of -0.2 V to +0.8 V with varying scan rate ranges from 5 to 200 mV s^{-1}. Galvanostatic charge-discharge (GCD) measurements were conducted within a potential window of 0 to +0.8 V with different current density (1, 2, 3, 4, 5 and 6 A g^{-1}). Moreover, electrochemical impedance spectroscopy (EIS) measurements were recorded within the frequency range from 100 kHz to 0.01 Hz by applying a 5mV amplitude AC voltage.

For all-solid-state supercapacitor device, the supercapacitive performance was tested in a two electrodes system keeping all conditions and parameters same as mentioned above.

For the three-electrode system, the specific capacitance of PPy films was calculated from CV curves using the following equation:

$$C_{sp} = \frac{\int \mathrm{I}dV}{vm\Delta \mathrm{V}}$$

Where C_{sp} is the specific capacitance based on the mass of electroactive material (F g^{-1}), I is

the response current (A), V is the potential (V), υ is the scan rate (mV s^{-1}), m is the mass of electroactive material (g), ΔV is the potential range (V).

For the symmetric all-solid-state supercapacitor, the specific capacitances based on CV curves can be derived from the capacitance of the device [96]:

$$C_{sp} = 4\frac{\int \mathrm{I}dV}{vm\Delta \mathrm{V}}$$

Where m is the total mass of the active material included in the whole device(g), I, V and υ are same as that in the three-electrode system.

The energy density and power density showed in the Ragone plot can be calculated by the following equations [97], respectively:

$$C_{cell} = \frac{\int \mathrm{I}dV}{vm\Delta \mathrm{V}}$$

$$\mathrm{E} = \frac{1}{2\times 3.6} C_{cell}\Delta V^2$$

$$\mathrm{P} = \frac{3600Ev}{\Delta V}$$

Where C_{cell} is the capacitance of the symmetric solid-state device determined from CV curves (F g^{-1}). I is the applied current density (A), m is the total mass of the active material included in the whole device (g), υ is the scan rate (mV s^{-1}), ΔV is the discharge voltage window (V). E and P represent the energy density (W h kg^{-1}) and power density (W kg^{-1}), respectively.

3.3 Results and Discussions

3.3.1 Morphology

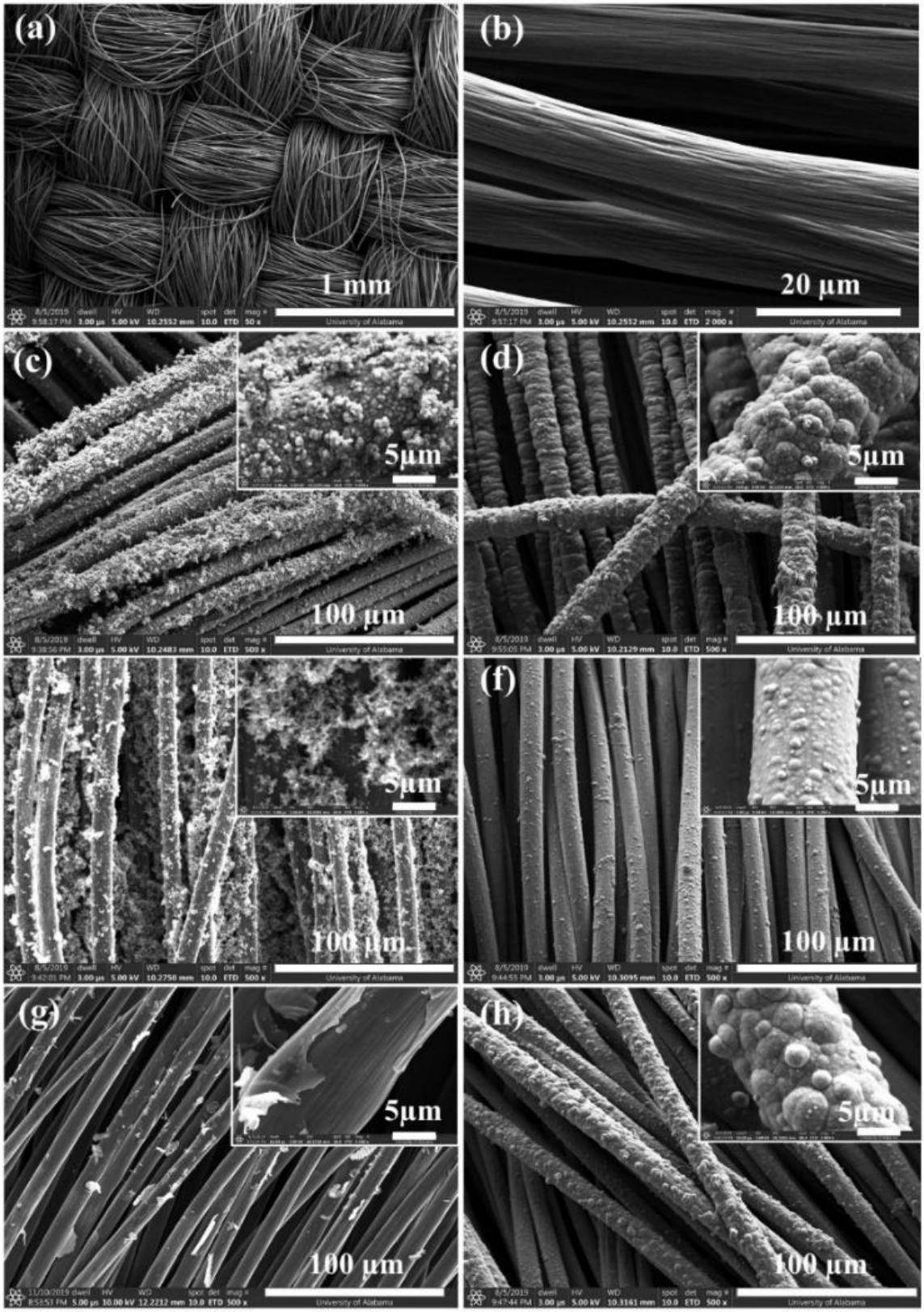

Figure 3. 1 (a-b) SEM images of carbon cloth; SEM images of PPy films: (c) PPy/HCl; (d) PPy/$HClO_4$; (e) PPy/H_2SO_4; (f) PPy/p-TSA; (g) PPy/H_3PO_4 and (h) PPy/PA.

The morphologies and structures of pristine carbon cloth and PPy films doped with different dopants were characterized under the SEM. As shown in **Figs. 3.1a** and **3.1b**, we can see that the pristine CC is consisted of numerous carbon fibers with smooth surface having diameter ~9.5 μm. Moreover, a large number of parallel rough grooves appear on the surface of each carbon fiber, which are suitable for the deposition of PPy that enhances the attachment and adhesion of PPy on the substrate. Furthermore, the high conductivity, good mechanical strength, and excellent flexibility make CC as an ideal substrate for the electrodeposition of PPy. **Figs. 3.1 (c-h)** show the morphologies of PPy films obtained by using different dopants. The morphologies of PPy films exhibit significant differences corresponding to different dopants. Compared to the pristine CC, all the PPy samples are agglomerated with different numbers and sizes of cauliflower-like nodules on the surface, except that PPy/H_3PO_4 shows a compact sheet structure. Interestingly, for the dopants with similar atom types (e.g. HCl and $HClO_4$; H_2SO_4 and p-TSA; H_3PO_4 and PA), the size of PPy nodules doped with bigger molecular volume is much bigger than that of their counterparts doped with smaller molecular volume i.e. PPy/$HClO_4$>PPy/HCl; PPy/H_2SO_4>PPy/p-TSA; PPy/ H_3PO_4>PPy/PA. This is because smaller size dopants result in more compact structures, while bigger size dopants make PPy structures more loosely packed. In order to confirm this conjecture, PPy/H_2SO_4 and PPy/p-TSA were selected as representative examples to compare their specific surface area and pore size by BET analysis. As shown in **Fig. 3.2**, the pore size of PPy/H_2SO_4 and PPy/p-TSA are concentrated at 4.3 nm and 4.9 nm, respectively. The specific surface area of PPy/H_2SO_4 and PPy/p-TSA was calculated to be 29.3 $m^2 g^{-1}$ and 26.3 $m^2 g^{-1}$, respectively. Both the pore size and specific surface area results support our speculation. In addition, it is reported that the specific capacitance of

electrode materials is proportional to their specific surface area [98]. Furthermore, compact structures give smaller and shorter paths for ions transport which could provide better conductivity. Whereas loosely packed structures give bigger and longer paths for ions transport, which would reduce the degree of swelling and shrinking of PPy films during the charge-discharge process. Thus, we can speculate that smaller size dopants could help PPy films have better capacitance behavior and bigger size dopants could help PPy films have better cycling performance.

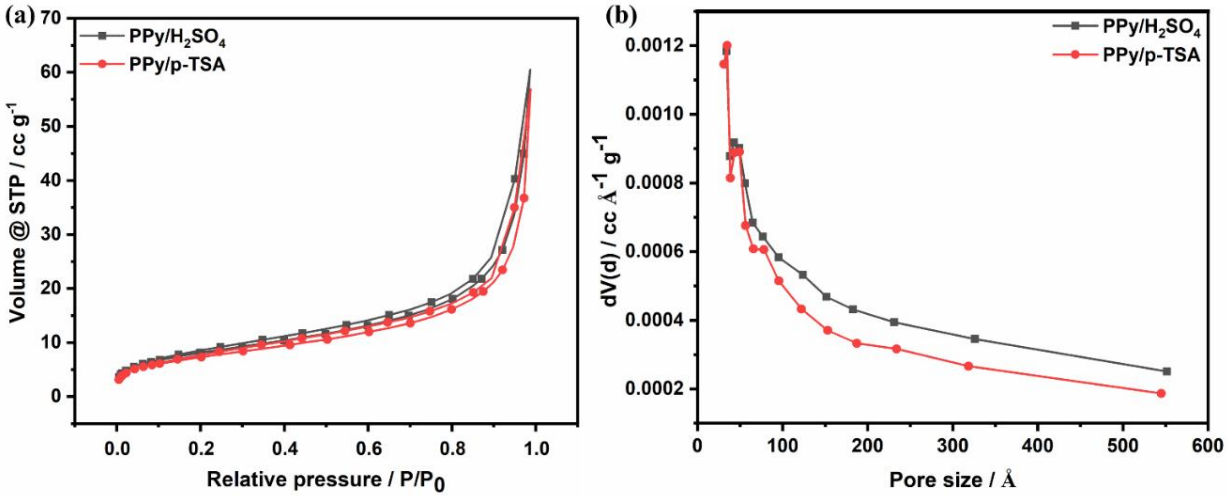

Figure 3. 2 (a) Nitrogen adsorption-desorption isotherm and (b) BJH pore size distribution plots of PPy/H_2SO_4 and PPy/p-TSA.

3.3.2 FTIR Analysis

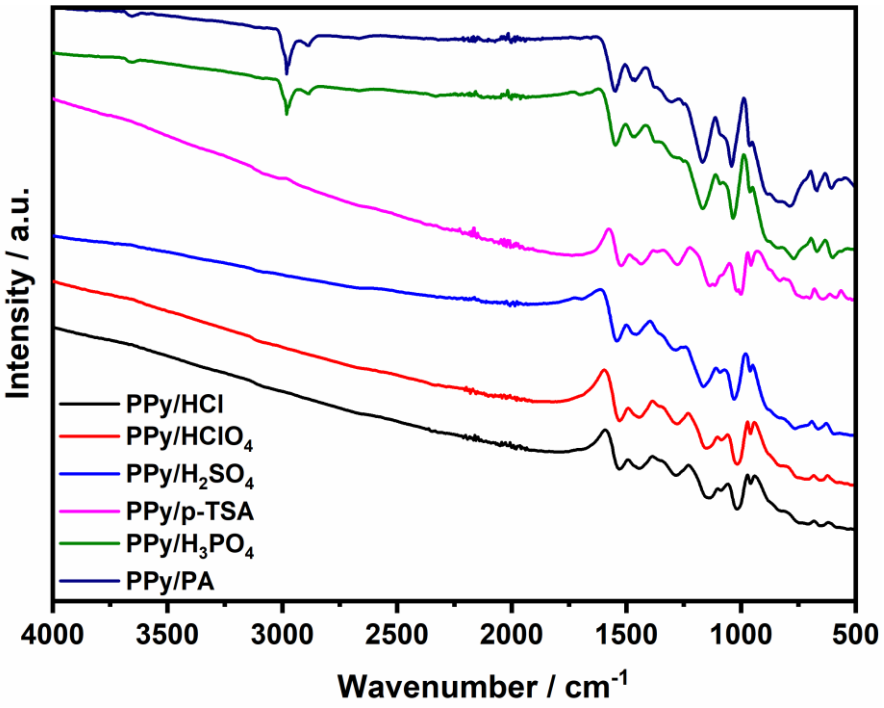

Figure 3. 3 FTIR spectra of PPy films doped with different acid dopants.

Table 3. 1 Summary of FTIR observations for PPy samples under different dopants.

Peak assignment	Peak position (cm^{-1})					
	PPy/HCl	PPy/$HClO_4$	PPy/H_2SO_4	PPy/p-TSA	PPy/H_3PO_4	PPy/PA
Hydroxyl of H_3PO_4 and PA	-	-	-	-	3660	3651
C=C stretching vibrations of pyrrole ring	1530	1536	1541	1521	1548	1547

C-N stretching vibrations of pyrrole ring	1445	1450	1457	1435	1462	1461
C–H or C–N in-plane deformation	1283	1285	1283	1276	1250	1302
P=O bonds	-	-	-	-	1167	1167
S-O bond stretching of SO_3^-	-	-	-	1118	-	-
C–N stretching vibrations	1088	1089	1091	1084	1090	1090
S=O group	-	-	1030	-	-	-
C=C bending	958	960	960	957	960	961

The FTIR spectra of PPy doped by different dopants are presented in **Fig. 3.3**. The spectra exhibit the signature peaks of PPy functional groups and the combinations between PPy and dopants ions (**Table 3.1**). The characteristic peaks around 1541, 1450, 1281, 1090 and 960 cm^{-1} wavenumbers are presented in all PPy samples, which are attributed to the characteristic peaks of PPy (**Fig. 3.4**). The peaks located at 1541 and 1450 cm^{-1} correspond to the C=C and C-N stretching vibrations of pyrrole ring [99]. The week peak at 1281 cm^{-1} is attributed to the C–H or C–N in-plane deformation [100]. The small peak at 1090 cm^{-1} is assigned to the =C–H in-plane

deformation [101]. The peak at 960 cm^{-1} belong to the C=C bending in the plane [102]. The peak at 1137 cm^{-1} of PPy/HCl and the peak at 1160 cm^{-1} of PPy/$HClO_4$ could be due to the presence of counter-ions Cl^- and ClO_4^- from HCl and $HClO_4$ dopants, respectively [103]. For PPy/H_2SO_4, the peak at 1030 cm^{-1} corresponding to asymmetrical stretching of the S=O group confirms the presence of a small amount of H_2SO_4 as dopant [104]. For PPy/p-TSA, a peak located around 1118 cm^{-1} is caused by S-O bond stretching of SO_3^- demonstrating the presence of p-TSA as dopant [105]. For PPy/H_3PO_4 and PPy/PA, the absorption peak approximately 3650 cm^{-1} is assigned to the hydroxyl of H_3PO_4 and PA in functional group region [106-107]. The peak at 1167 cm^{-1} due to the vibration of P=O bonds indicating the present of H_3PO_4 and PA in PPy structures [108]. Based on the above information, we can conclude that dopants with different structures are successfully introduced into PPy.

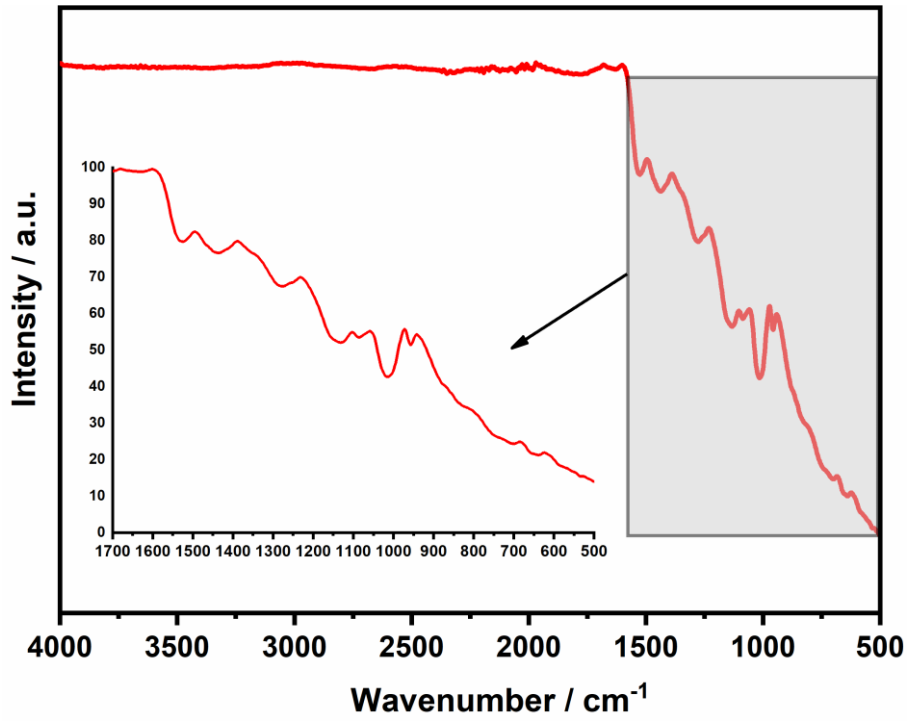

Figure 3. 4 FTIR spectra of PPy film without dopant.

3.3.3. XPS Analysis

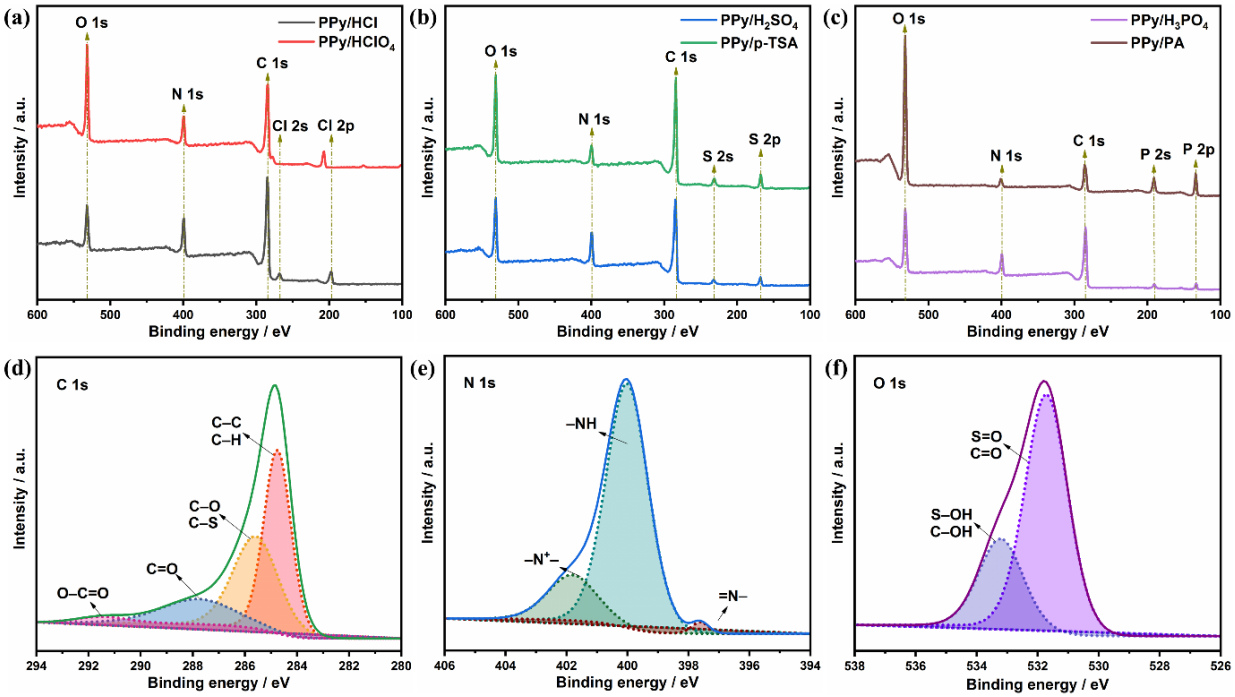

Figure 3. 5 (a-c) XPS survey spectra of PPy films using different dopants: (a) PPy/HCl vs. PPy/$HClO_4$; (b) PPy/H_2SO_4 vs. PPy/p-TSA; (c) PPy/H_3PO_4 vs. PPy/PA; (d-f) Core level photoelectron peaks for the PPy/p-TSA films: (d) C 1s; (e) N 1s; (f) O 1s.

Table 3. 2 Surface chemical composition, doping level and mass ratio of counterions in PPy films doped with different acids.

Samples	C 1s (%)	N 1s (%)	O 1s (%)	X^1 2p (%)	X/N ratio[2]	Counterion mass ratio
PPy/HCl	70.84	13.31	12.47	3.37	0.25	0.12
PPy/$HClO_4$	57.55	13.82	24.91	3.73	0.27	0.29
PPy/H_2SO_4	65.71	12.77	18.64	2.88	0.23	0.25
PPy/p-TSA	65.50	7.68	22.46	4.36	0.57	0.60
PPy/H_3PO_4	60.89	11.12	24.60	3.39	0.31	0.31

PPy/PA	28.54	5.09	54.29	12.09	0.40	0.80

[1] X represents Cl for PPy/HCl and PPy/$HClO_4$, S for PPy/H_2SO_4 and PPy/p-TSA, P for and PPy/PA.

[2] X/N ratio represents the doping level for one pyrrole ring in the PPy chain [109].

Surface chemistry of PPy films doped by different acids was further investigated by XPS analysis. **Figs. 3.5** (a-c) display the XPS survey spectra, and the corresponding surface chemical composition of PPy films are summarized in **Table 3.2.** As show in **Fig. 3.5a**, compared with PPy/HCl, both Cl 2p and Cl 2s core level peaks in PPy/$HClO_4$ shift towards to high binding energy, which is attributed to the high positive oxidation state of Cl atom in ClO_4^-. In addition, much higher amount of O atom can be observed in PPy/$HClO_4$ due to the big differences in the counterion structure of Cl^- and ClO_4^-. Similar phenomena happen to the groups of PPy/H_2SO_4 vs. PPy/p-TSA and PPy/H_3PO_4 vs. PPy/PA, as displayed in **Fig. 3.5b** and **Fig. 3.5c**, respectively. Moreover, as indicated in **Table 3.2**, PPy films doped with bigger molecular volume present higher doping level in the same atom type dopants. Particularly, the doping level of PPy/p-TSA is as high as 0.57. According to the doping level and molecular weight of counterions, we further calculated the mass ratio of counterions in PPy films. For the same atom type dopants, PPy films doped with bigger molecular volume exhibit higher mass ratio of counterions. For different atom type dopants with similar molecular volume, the mass ratio of counterions order appears to be: phosphates > sulfates > chlorates, i.e. PPy/H_3PO_4 > PPy/H_2SO_4 > PPy/HCl; PPy/PA > PPy/p-TSA > PPy/$HClO_4$. Moreover, the PPy/p-TSA film is selected as a representative example to interpret the core level photoelectron peaks in detail. As shown in **Fig. 3.5d**, the C 1s core level peak can be deconvoluted into four components,

among which the peak at 284.8 eV is attributed to C-C and C-H bonds, the peak at 285.6 eV is assigned to C-O and C-S bonds, while the peaks at 287.7 eV and 291.5 eV correspond to C=O and O-C=O bonds, respectively [109]. The N 1s spectrum in **Fig. 3.5e** is deconvoluted into three peaks. Among them, the major peak at 400.0 eV is assigned to neutral nitrogen (-NH) in the pyrrole ring, the lower binding energy tail at 397.7 eV corresponds to imine group (=N-), whereas the peak shifted to the higher binding energy at 401.8 eV is attributed to the positively charged nitrogen ($-N^{+}-$) of polaron and bipolaron species [110]. **Fig. 3.5f** displays the O 1s core level spectrum and its deconvolution. The main peak at 531.7 eV corresponds to S=O and C=O groups, and the peak at 533.2 eV is attributed to S-OH and C-OH bonds [111].

3.3.4 Electrochemical performance

Figs. 3.6 (a-f) show the CV curves of PPy films with different dopants at different scan rates from 5 to 200 mV s^{-1} with the potential range of -0.2-0.8 V. At low scan rates, all of the CV curves appearing distorted symmetrical quasi-rectangular shapes without obvious redox peaks, indicating that over the whole CV process, the charge and discharge process of PPy electrodes were at a pseudo-constant rate (**Fig. 3.7**) [112]. As scan rate increases, the current density increases, and the redox peaks become more obvious. The CV curves deviated from quasi-rectangular like shapes caused by the polarization of the electrodes [113]. This is because the ion concentration at the solid/liquid interface rapidly increases with the increases of the scan rates. At high scan rate, the diffusion rate of electrolyte from the solid/liquid interface to the active site of electrode material cannot match the rate of the electrochemical reaction of electrode materials which leads to the electrolyte enriched at the solid/liquid interface and the polarization performance

of the electrodes. The degree of polarization for PPy films with different dopants is different at higher scan rates. The highly distorted leaf-shaped CV curves presented at 200 mV s^{-1} are attributed to the limited ionic and electronic transport [114]. The different degree of polarization for different PPy films is probably attributed to different doping level and various mass ratio of counterions in different PPy samples, which will affect the ionic diffusion rate during the redox reaction at electrode interface.

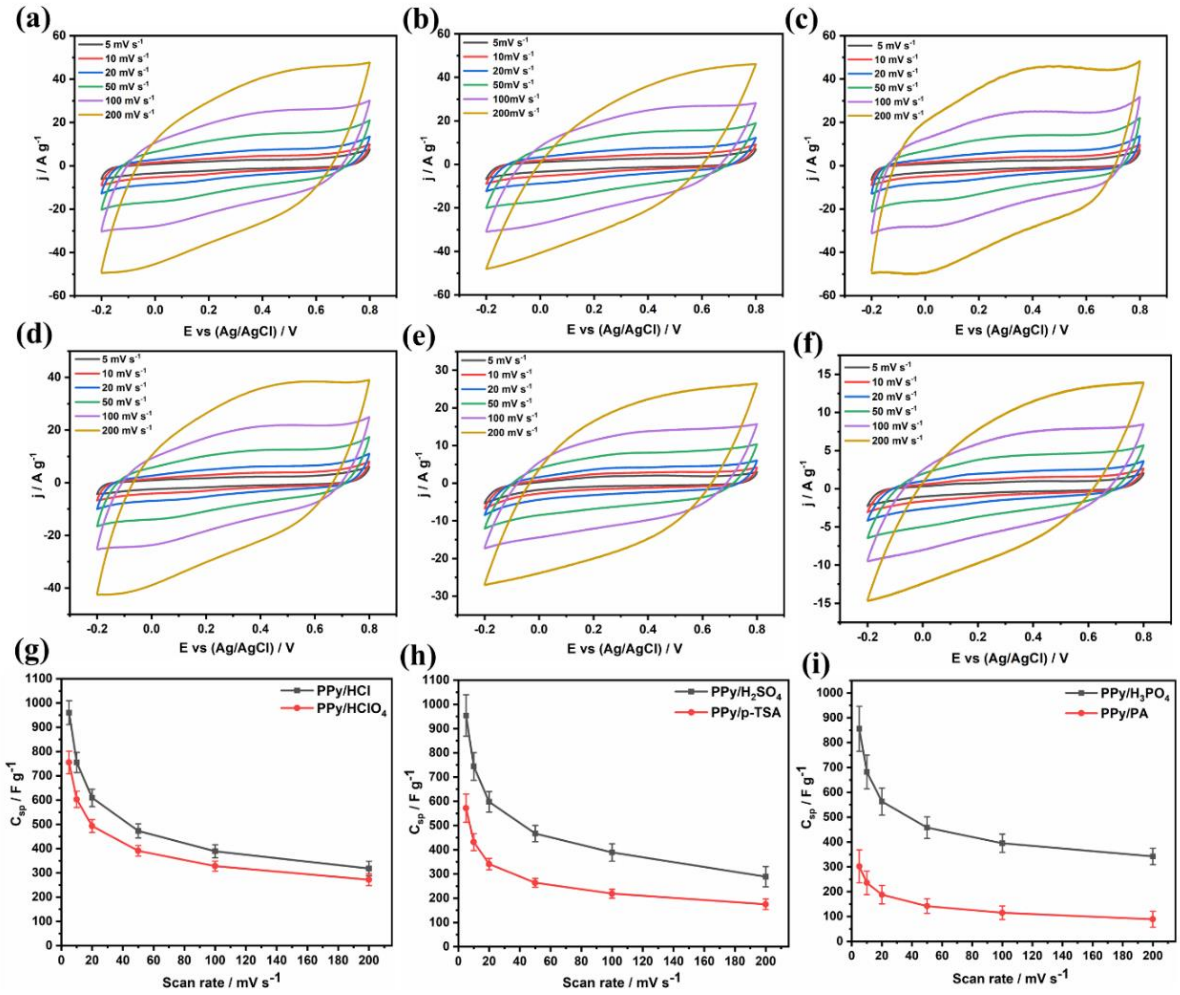

Figure 3. 6 (a-f) Cyclic voltammetric curves of PPy films: (a) PPy/HCl; (b) PPy/H_2SO_4; (c) PPy/H_3PO_4; (d) PPy/$HClO_4$; (e) PPy/p-TSA; (f) PPy/PA; (g-i) Specific capacitance of PPy films for: (g) PPy/HCl and PPy/$HClO_4$; (h) PPy/H_2SO_4 and PPy/p-TSA; (i) PPy/H_3PO_4 and PPy/PA.

Table 3. 3 The specific capacitance of PPy films at different scan rates.

Scan rate	Specific capacitance (F g^{-1})					
($mV \cdot s^{-1}$)	PPy/HCl	PPy/$HClO_4$	PPy/H_2SO_4	PPy/p-TSA	PPy/H_3PO_4	PPy/PA
5	960	755	954	572	856	302
10	755	603	744	432	682	236
20	609	493	598	341	563	188
50	473	391	467	264	458	142
100	389	328	385	219	395	115
200	318	272	289	175	342	89

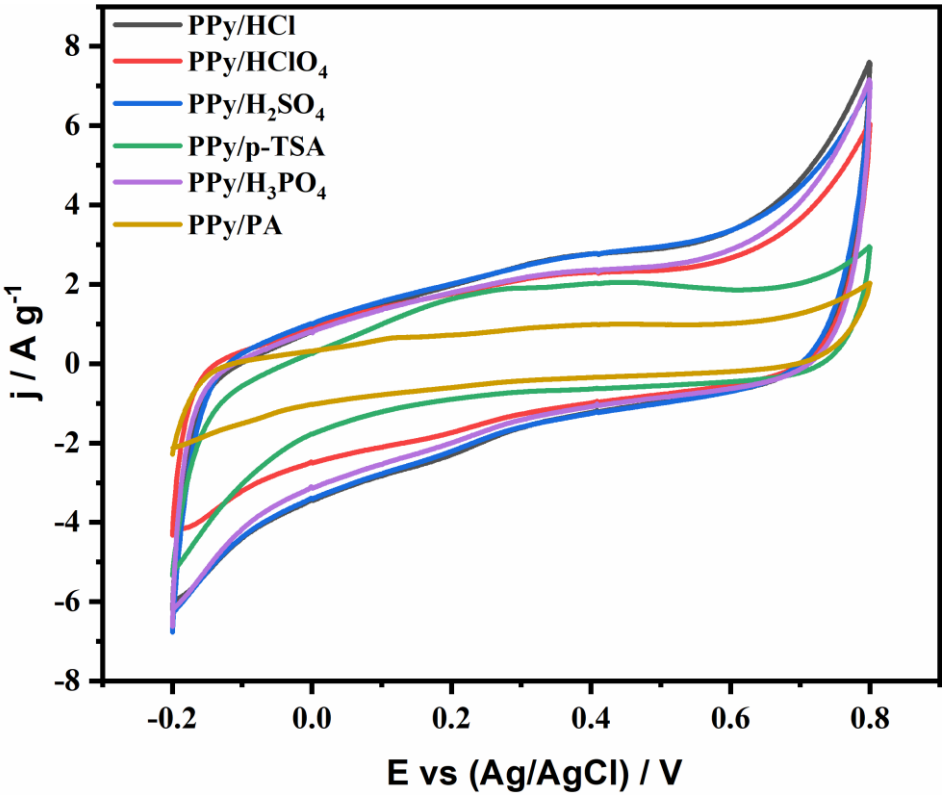

Figure 3. 7 CV curves of PPy with different dopants at 5 mV s^{-1}.

As shown in **Fig. 3.6 (g-i)**, the specific capacitances (C_{sp}) decreases with the scan rates from 5 to 200 mV s^{-1} for all the PPy films electrodes, the detailed C_{sp} values are given in **Table 3.3**. The C_{sp} for PPy films doped by HCl, $HClO_4$, H_2SO_4, p-TSA, H_3PO_4 and PA at the scan rate of 5 mV s^{-1} are 960 F g^{-1}, 755 F g^{-1}, 954 F g^{-1}, 572 F g^{-1}, 856 F g^{-1} and 302 F g^{-1}, respectively. PPy doped by HCl has the highest capacitance. The capacitance of PPy doped by H_2SO_4 and H_3PO_4 do not show a big difference with PPy/HCl which also can be compared by CV curves (**Fig 3.7**) according to the proportional relation between the C_{sp} and the area enclosed by CV curve. Interestingly, it can be observed that for the dopants with similar atom types, the PPy films doped with smaller molecular volume exhibit higher specific capacitance and better rate capability than that doped with bigger molecular volume ($C_{sp\ HCl} > C_{sp\ HClO4}$; $C_{sp\ H2SO4} > C_{sp\ p\text{-}TSA}$; $C_{sp\ H3PO4} > C_{sp\ PA}$). This result is consistent with the inference from SEM (**Fig. 3.1**). Moreover, based on the counterion mass ratio calculated in **Table 3.2**, PPy doped with smaller size dopants shows lower counterion mass ratio than that doped by bigger size dopants. In other words, for the same amount of PPy samples (e.g. 1 gram), PPy films doped with smaller size dopants contains more PPy than their counterparts. Since only PPy contributes to the capacitance, PPy films doped by smaller size dopants exhibit higher specific capacitance than PPy doped by bigger size dopants. For different atom type dopants with similar molecular volume, the specific capacitance order appears to be: chlorates > sulfates > phosphates ($C_{sp\ HCl} > C_{sp\ H2SO4} > C_{sp\ H3PO4}$; $C_{sp\ HClO4} > C_{sp\ p\text{-}TSA} > C_{sp\ PA}$), which is also in line with the mass ratio of counterions (**Table 3.2**). Based on the above discussions, both the types and the sizes of acid dopants play important roles on the electrochemical performance of PPy films.

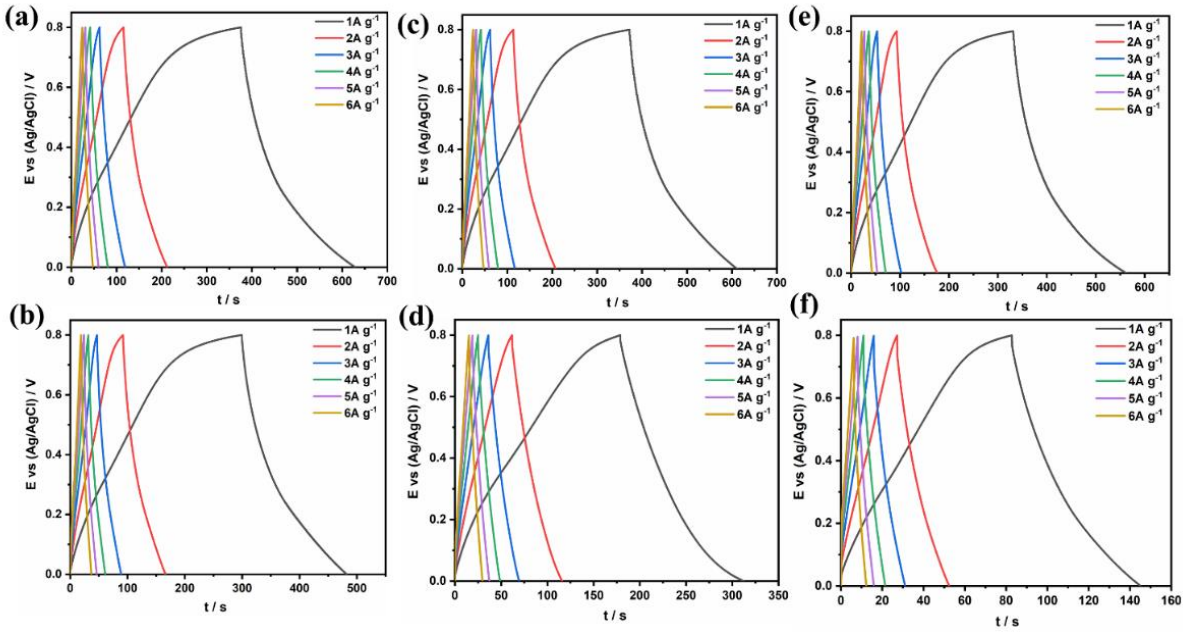

Figure 3. 8 Galvanostatic charge-discharge curves of PPy films at different current densities: (a) PPy/HCl; (b) PPy/$HClO_4$; (c) PPy/H_2SO_4; (d) PPy/p-TSA; (e) PPy/H_3PO_4; (f) PPy/PA.

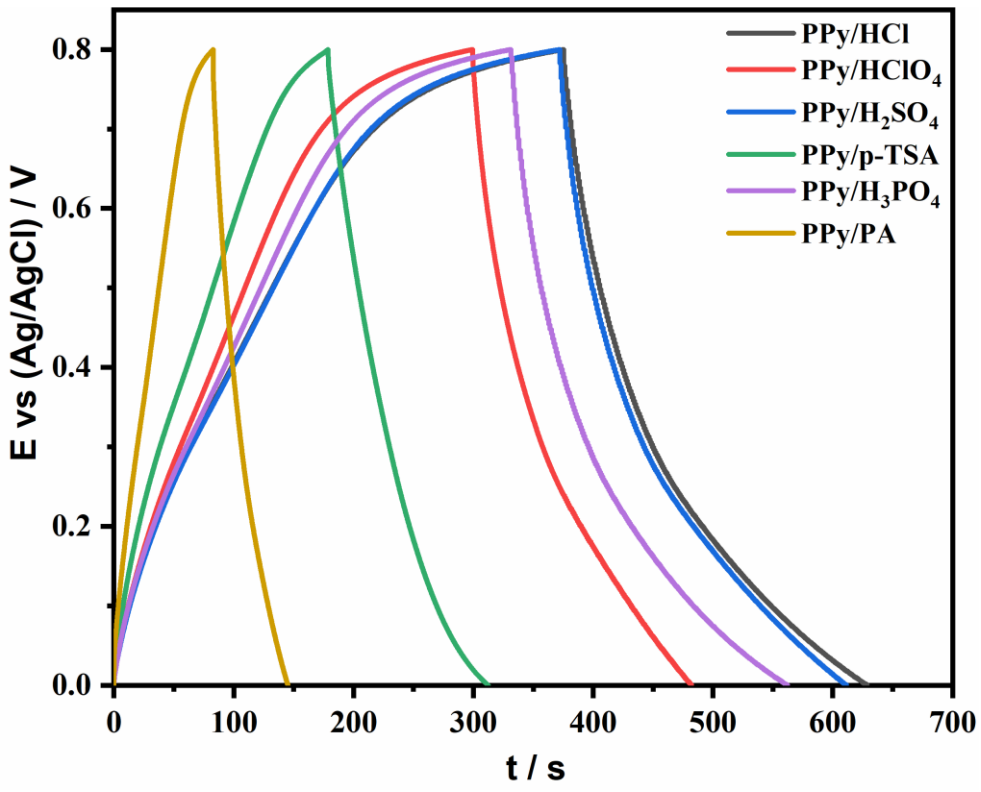

Figure 3. 9 Galvanostatic charge-discharge curves of PPy films with different dopants at 1A g^{-1}.

GCD curves of PPy films with different dopants at different current densities from 1 to 6 $A \cdot g^{-1}$ in the potential range of 0 to 0.8 V are shown in **Fig. 3.8**. All GCD curves display quasi-triangular shapes which indicate the good charge-discharge reversibility of PPy films. A slight asymmetry of GCD curves can be observed at low current density (1A g^{-1}), attributing to the potential dependent redox reactions which is corroborated by the CV results [115-116]. Furthermore, with the increase of current density, the charge-discharge time decrease. This is due to the fact that at high current density, the electrolyte ions cannot enter the internal structure of electrode materials and can only diffuse into the surface of electrode materials [117]. Internal resistance drop (IR drop) can be observed at low current density because of equivalent series resistance occurring at the electrode and electrolyte interface [118]. For similar atom type dopants, the PPy samples doped with bigger dopants show larger IR drop ($IR_{HClO4} > IR_{HCl}$; $IR_{p\text{-}TSA} > IR_{H2SO4}$; $IR_{PA} > IR_{H3PO4}$), indicating higher internal resistance for ions transfer in and out of PPy films. Additionally, the conductivity of PPy films doped with bigger dopants are lower than those doped by smaller dopants, as indicated by the EIS results in **Fig. 3.10**. For similar atom type dopants, the charge-discharge time also reflects the capacitance order of PPy films follows: $C_{sp\ HCl} > C_{sp\ HClO4}$; $C_{sp\ H2SO4} > C_{sp\ p\text{-}TSA}$; $C_{sp\ H3PO4} > C_{sp\ PA}$. When comparing the charge-discharge time at 1A g^{-1} (**Fig 3.9**), PPy doped by HCl shows the longest charge-discharge time which indicates its highest capacitance among all these PPy samples. This result is probably attributed to the fact that PPy/HCl shows the lowest mass ratio of counterion, corresponding to the highest amount of PPy when calculate the specific capacitance based on the same amount of PPy films. For different atom type dopants with similar molecular volume, the charge-discharge time order appears to be: chlorates > sulfates > phosphates ($C_{sp\ HCl} > C_{sp\ H2SO4} > C_{sp\ H3PO4}$; $C_{sp\ HClO4} >$

$C_{sp\ p\text{-}TSA} > C_{sp\ PA}$). Based on the above discussion, the capacitances performance reflected by the GCD curves are consistent with the CV results.

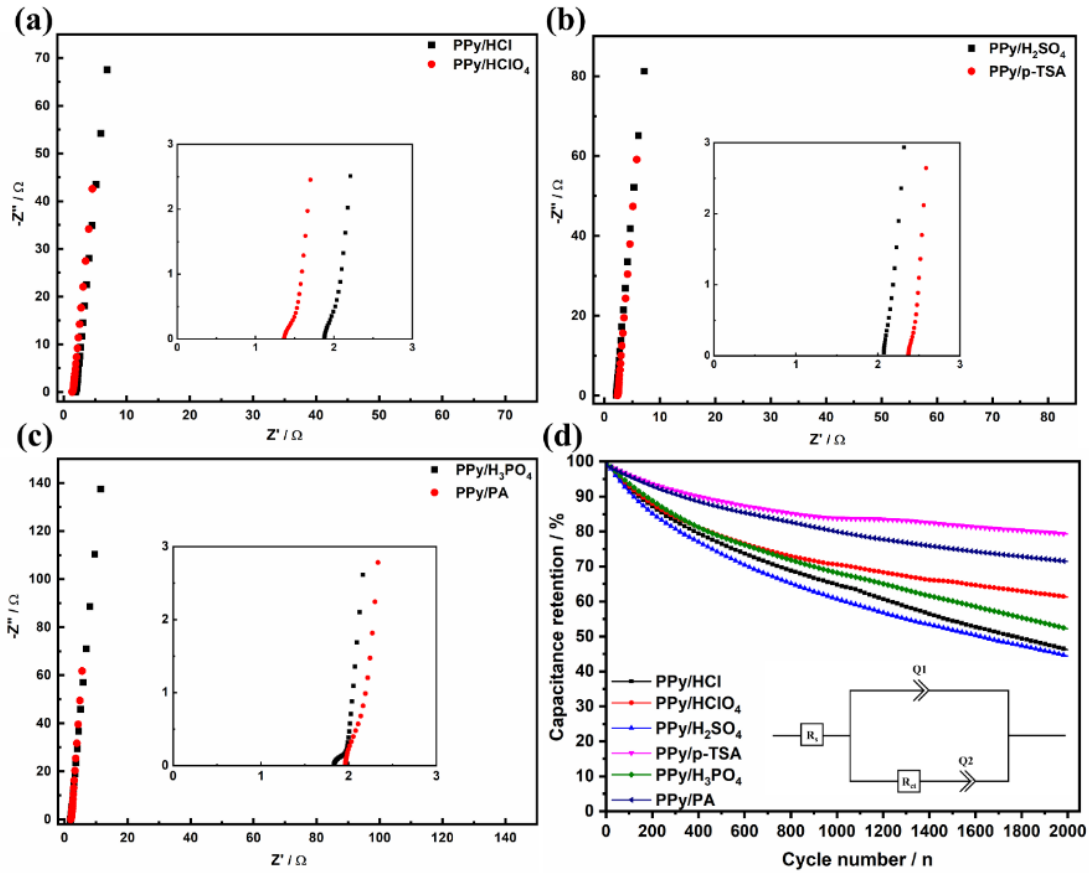

Figure 3. 10 (a-c) Nyquist impedance plots of PPy films: (a) PPy/HCl and PPy/$HClO_4$; (b) PPy/H_2SO_4 and PPy/p-TSA; (c) PPy/H_3PO_4 and PPy/PA. (d) Comparison of cycling stability of PPy films for all the dopants used (The inset image is the equivalent circuit model).

To further comprehensively investigate the charge-discharge and resistance performance for electrolyte ion diffusion in these electrode films, EIS was performed at open circuit potential within the frequency range of 100 kHz to 0.01 Hz. The equivalent circuit model (**Fig. 3.10d insert**) was proposed based on impedance spectra. The ideal capacitor (C) was replaced by constant phase element (Q) to obtain best fitting for the spectra with relative error of $1x10^{-12}$. The Q_1 is associated to electrical double layer forms at electrode/electrolyte interface, and Q_2 is due to

pseudocapacitive behavior of redox PPy. The relation between Q and C can be understood as: $C=Q^n$ where values of n varies between 0 and 1 [119]. For ideal capacitor n=1 whereas for rough or porous electrodes such as conducting polymers, n<1.

The EIS of PPy films with different dopants were collected and plotted as Nyquist plots, as shown in **Fig. 3.10 (a-c)**. All the EIS curves show similar shape with quasi-semicircular parts at high frequency region and near-vertical linear parts at low frequency region. The quasi-semicircular part at high frequency region presents the solution resistance (R_s) reflected by the intercept of the semicircle on x-axis and charge-transfer resistance (R_{ct}) reflected by semicircle diameter [120]. The small real-axis intercept value at high frequency region suggesting low R_s (~ 2 Ω) attributed to the solution resistance used in the experiment for all PPy samples. The inconspicuous semicircles at high frequency region reflecting low R_{ct} and fast faradaic charge transfer process for all the PPy films [121]. The slope at the low frequency suggests the high ion mobility and diffusion in PPy electrodes [122-123]. It can be observed that the plots of the PPy films doped by small molecular dopants in the low frequency region are more vertical than the PPy films doped by big molecular dopants, indicating that the PPy films doped with small dopants shows better capacitance performance. Both are in agreement with the results obtained by CV and GCD curves (**Fig. 3.6 and Fig. 3.8**).

Cycling stability is another important parameter for evaluating the supercapacitor behavior of electrode material for real application. The cycling performance of PPy films was tested by GCD at a current density of 4 A g^{-1} within a potential window of 0-0.8 V for 2000 cycles. For pseudocapacitive polymer materials, like PPy, during repeated charge/discharge process, the

intercalation/deintercalation of ions usually make a large volumetric change for electrode material which causes a structural breakdown and fast decay of capacitive behavior [124-125]. As shown in **Fig. 3.10d**, the capacitance retention of PPy/H_2SO_4 and PPy/HCl decreased significantly and less than 50% of capacitance retention for both two samples due to the structural breakdown. While the PPy/H_3PO_4 and PPy/$HClO_4$ showed better cycling stabilities than above mentioned samples, with more than 50% of capacitance retention for both samples. Notably, PPy/p-TSA and PPy/PA exhibit excellent cycling stability with more than 70% of capacitance retention for more than 2000 cycles. It should be noted that for similar atom type dopants, the PPy films doped with smaller size dopants showed higher capacitance than that when doped with bigger size dopants, however the opposite is true for cycling stability. This result is because smaller size dopants help to creates smaller and shorter paths in PPy structures. The shorter paths help in faster diffusion of ions through the structure thus enhances the capacitance. However, these small paths provided by small size dopants cannot withstand for a sufficiently large number of charge/discharge cycles. In contrast, bigger size dopants create bigger and more loose paths. These bigger and relatively loose PPy structures make the samples more stable for diffusion of ions during charge/discharge process. Moreover, according to the counterion mass ratio listed in **Table 3.2**, PPy films doped with bigger size dopants exhibit much higher mass ratio of counterions than their counterparts doped with small size dopants. This counterions probably benefit the formation of more loosely PPy structure and assist in supporting the structure during charge-discharge cycles, thus leading to better cycling performance.

From the above results, it can be concluded that dopants greatly influence both capacitance and cycling performance of PPy films. PPy/HCl exhibits the highest capacitance performance (960 F g^{-1}), but with inferior cycling stability. On the other hand, PPy/p-TSA shows the best cycling performance with a capacitance retention rate for more than 75% after 2000 cycles and still with a relatively high capacitance of 572 F g^{-1}. These values of PPy/p-TSA are comparable to and even higher than the most of previously reported PPy based supercapacitors (see **Table 3.4**).

Table 3. 4 Comparison of specific capacitance among some previously reported PPy based supercapacitors.

Material	Specific capacitance	Scan rate	Capacitance retention (cycle)	Ref.
PPy coated on stainless steel	254 F g^{-1}	2 mV s^{-1}	-	[126]
PPy coated on CC	166 F g^{-1}	5 mV s^{-1}	-	[91]
PPy coated on stainless steel	343 F g^{-1}	2 mV s^{-1}	85% (1000)	[127]
PPy coated on nylon lycra fabric	123 F g^{-1}	10 mV s^{-1}	55% (500)	[128]
PPy/lignosulfonate coated cotton fabrics	304 F g^{-1}	0.1 A g^{-1}	76% (300)	[129]
PPy covered MnO_2	141.6 F g^{-1}	2 mA cm^{-2}	49.6% (500)	[130]
PPy-bacterial cellulose membranes	459.5 F g^{-1}	0.16 A g^{-1}	70.3% (50)	[131]

PPy Coated Carbon Nanotube electrode	220 F g^{-1}	2 mV s^{-1}	83.1% (1000)	[132]
PPy/HCl coated on CC	960 F g^{-1}	5 mV s^{-1}	46% (2000)	This work
PPy/p-TSA coated on CC	572 F g^{-1}	5 mV s^{-1}	79% (2000)	This work

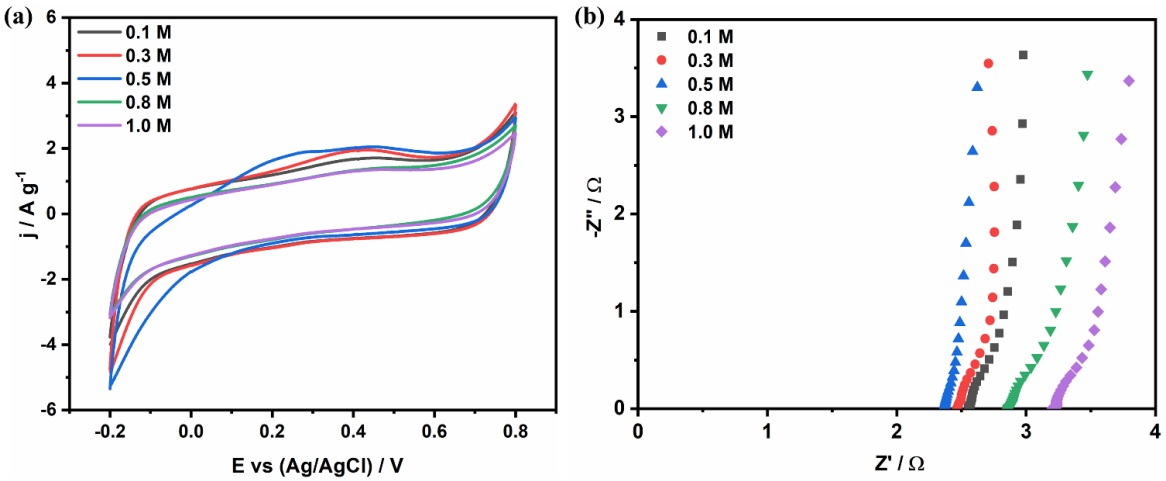

Figure 3. 11 (a) CV curves of PPy/p-TSA with different p-TSA concentrations at 5 mV s^{-1}; (b) Nyquist impedance plots of PPy/p-TSA with different p-TSA concentrations.

Table 3. 5 The specific capacitance of PPy/p-TSA different p-TSA concentrations at 5 mV s^{-1}.

Concentration of p-TSA (mol L^{-1})	0.1	0.3	0.5	0.8	1.0
Specific capacitance (F g^{-1})	509	542	572	403	389

PPy/p-TSA was chosen as a representative sample to further investigate the effect of dopant concentration on the capacitance performance by changing p-TSA concentration during the synthesis of PPy/p-TSA. The CV measurement (**Fig. 3.11a**) was used to evaluate the

electrochemical performance of PPy/p-TSA at different dopant concentration. By comparing the calculated capacitance (**Table 3.5**) based on CV curves, we can clearly see that the capacitance of PPy/p-TSA firstly increased with the increase of p-TSA concentration until the p-TSA concentration reached 0.5 mol L^{-1}. Then, the capacitance of PPy/p-TSA decreased with continuously increase of p-TSA concentration. The above results can be interpreted according to the doping process of PPy: Initially, the doping level of PPy increased with the increase of dopant concentration until the optimal dopant concentration (0.5 mol L^{-1}) is reached, resulting in the increase in electrical conductivity, which helps to enhance the electrochemical performance of PPy. To confirm this inference, EIS was further carried out. As shown in **Fig 3.11b**, PPy/p-TSA at the optimal dopant concentration (0.5 mol L^{-1}) shows the lowest R_s and R_{ct}, corresponding to the best electrical conductivity. However, with further increasing of dopant concentration, excess dopant ions appear in the solution and surround around PPy which impede the contact of PPy with electrolyte, thus leading to the blocked ion transmission and decreased capacitance behavior.

Table 3. 6 Total charge accumulated during electropolymerization, maximum charge that can be produced during reduction of the PPy films and number of redox sites available in the PPy films.

Charge	**HCl**	**$HClO_4$**	**H_2SO_4**	**p-TSA**	**H_3PO_4**	**PA**
Q_t (C)	5.92	7.04	5.66	3.81	3.47	4.62
Q_{max} (C)	0.82	0.98	0.79	0.53	0.48	0.64

Inspired by the mechanistic interpretation of charge storage in PPy membranes proposed by Northcutt and Sundaresan [133], we further calculated the accessibility of redox sites on the PPy

films to interpret the mechanism of charge storage with different dopants. The maximum number of redox sites in a doped PPy film can be calculated by the charge accumulated during the electropolymerization, is given by:

$$N_r = \frac{Q_t}{nF}$$

Where Nr is maximum number of redox sites (mol) in the synthesized polymer, Q_t is total charge consumed during electropolymerization of the polymer (**Table 3.6**), n (= 2.3) is number of electrons transferred per pyrrole monomer [134] and F is faraday constant.

If the number of electrons produced when a cation is inserted into a PPy is represented by z (where z =1 for H^+), the maximum charge produced from reversible cation insertion (Q_{max}) is calculated following:

$$Q_{max} = N_r F z = \frac{Q_t z}{n}$$

The accessibility of redox sites is given by:

$$A = \frac{Q_c}{Q_{max}}$$

Where A is accessibility coefficient, charge (Q_c) is the charge that was produced during the discharge or reduction process.

Table 3. 7 Accessible coefficient of the PPy films varies with scan rates for all the dopants used.

Scan rates (mV s^{-1})	HCl	$HClO_4$	H_2SO_4	p-TSA	H_3PO_4	PA
5	0.2779	0.2957	0.2427	0.3194	0.2586	0.2959
10	0.2183	0.2496	0.1953	0.2409	0.2083	0.2389
20	0.1782	0.2109	0.1603	0.1923	0.1733	0.1943
50	0.1409	0.1715	0.1261	0.1473	0.1419	0.1493
100	0.1180	0.1454	0.1033	0.1225	0.1233	0.1216
200	0.0964	0.1220	0.0775	0.0973	0.1070	0.0941

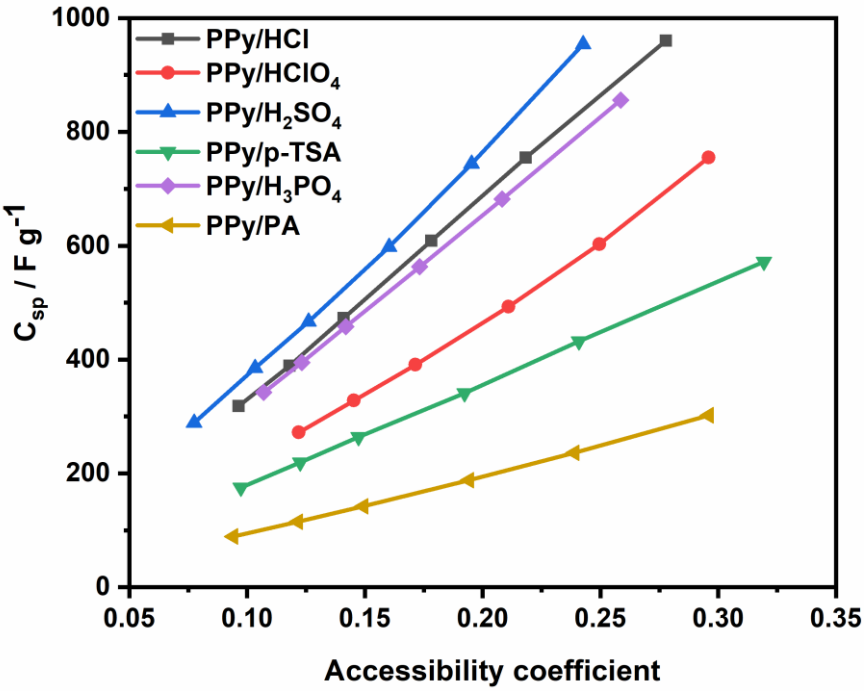

Figure 3. 12 Specific capacitance relation with accessible coefficient for all the dopants used in the study.

Fig. 3.12 showed the relationship of accessibility of redox sites and specific capacitance of PPy films. **Table 3.7** summarized the accessible coefficient of the PPy films varies with scan rates

for all the dopants. From **Fig. 3.12** and **Table 3.7**, we can clearly see that the number of accessible redox sites influences the capacitance of PPy films. A higher accessibility coefficient at lower scan rate leads to a higher specific capacitance. This is due to the redox sites are not easily accessible due to diffusion of protons at higher scan rates. These results are in agreement with decrease in peak currents with increase in scan rates for each dopant used in this study. As we can see in the SEM images (**Fig. 3.1**), the smaller size dopants yield in compact PPy structure that makes it difficult to access the redox sites. This is the reason for that maximum accessible coefficients for smaller size dopants (e.g. HCl, H_2SO_4 and H_3PO_4) are all below 0.28. Although these small size acids doped PPy films have smaller accessible coefficients, they exhibit higher specific capacitance than their counterparts. For example, PPy/HCl exhibits the highest specific capacitance at 5 mV s^{-1}, even though with a modest accessible coefficient. This phenomenon is probably due to the compact structure and the highest mass ratio of PPy play more important roles than accessible coefficients on the specific capacitance. On the other hand, bigger size dopants result in open structure that help in more accessibility of redox sites. This can be observed in $HClO_4$, p-TSA and PA doped PPy films where around 30% of redox sites are accessible. Notably, PPy/p-TSA exhibits the maximum accessible coefficient of nearly 0.32, which means 32% of redox sites are accessible. It is worth noting that the accessible coefficient is positively correlated with the cycling performance of PPy films with an exception of PPy/H_3PO_4, as indicated in **Table 3.7** and **Fig. 3.10d**. As shown in **Fig. 3.1**, the PPy/H_3PO_4 shows a compact sheet structure other than the cauliflower-like nodules structure for PPy/HCl. The compact structure of PPy/H_3PO_4 may be the reason caused its lower accessible coefficient than that of PPy/HCl. However, this compact sheet structure may be more stable during

charge/discharge process, resulting in better cycling stability than PPy/HCl. Considering the best cycling stability and relatively high capacitance, PPy/p-TSA was chosen to fabricate all-solid-state supercapacitor devices for further investigation of their practical application.

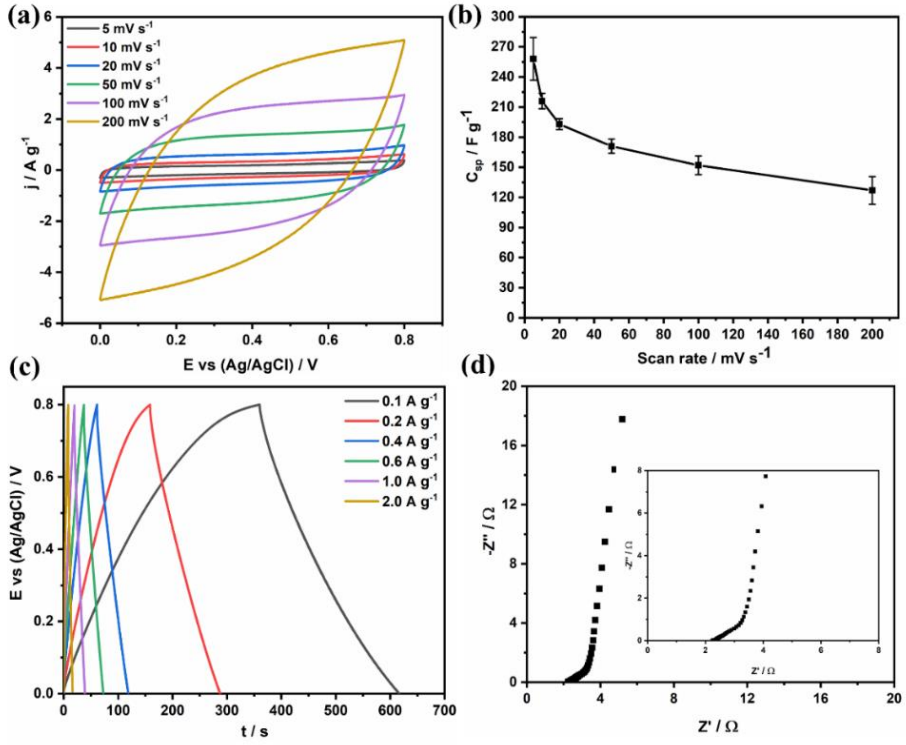

Figure 3. 13 Electrochemical performance of PPy/p-TSA solid-state device: (a) CV curves at different scan rates; (b) Specific capacitances at different scan rates; (c) GCD curves at different current densities; (d) Nyquist plots.

To further investigate the performance of PPy/p-TSA electrode for practical applications. An all-solid-state symmetric supercapacitor was fabricated by using two PPy/p-TSA coated films as flexible electrodes and PVA/H_2SO_4 gel as an electrolyte. For comparison, PPy/PA and PPy/$HClO_4$ all-solid-state devices were also made by using the same procedure. **Fig. 3.13** show the electrochemical performance of PPy/p-TSA device. From **Fig. 3.13a**, it is clear to see the increment of current with the increase of the scan rate, which indicates the ideal capacitive and

fast charge-discharge performance of PPy/p-TSA electrode. In addition, all CV curves present nearly rectangular shape, indicating good rate capability of the PPy/p-TSA device. **Fig. 3.13b** shows the plot of specific capacitance at different scan rate of the PPy/p-TSA device. The highest C_{sp} (280 F g^{-1}) is obtained at the scan rate of 5 mV s^{-1}. **Fig. 3.13c** exhibits the GCD curves at different current densities in the range of 0.1-2 A g^{-1} and all the GCD curves are quasi-triangle shapes, suggesting excellent electrochemical performance. Moreover, the IR drop remains constant with the increase of current density. This result is due to the high conductivity and low charge-transfer resistance, as indicted in the EIS curve (**Fig. 3.13d**) [135].

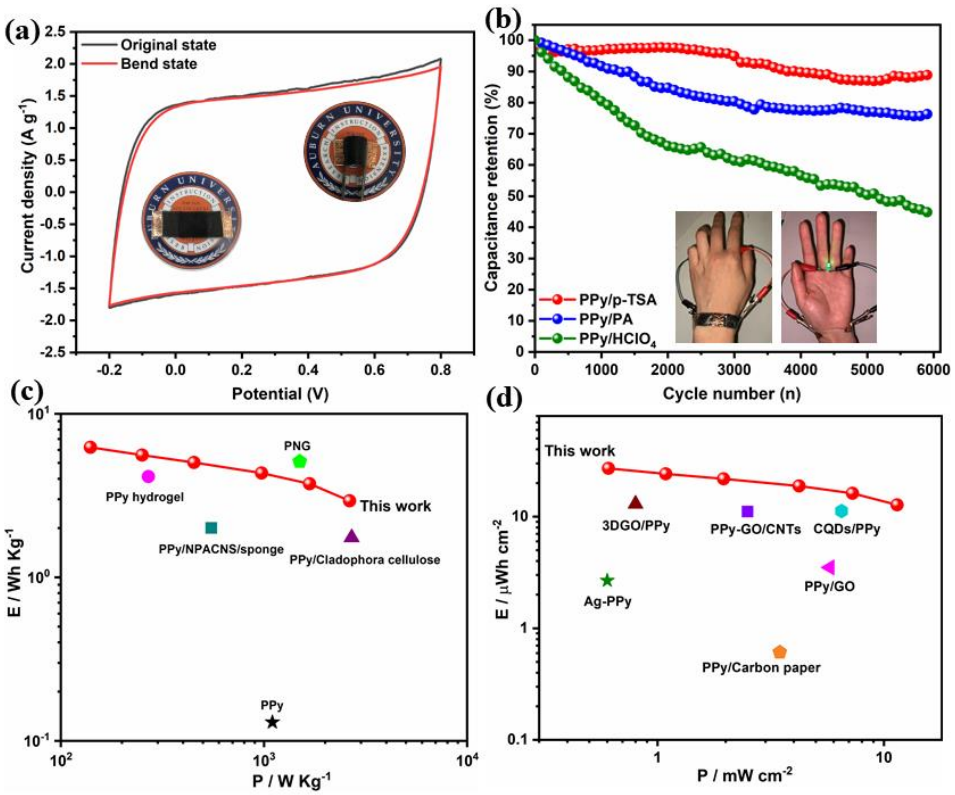

Figure 3. 14 (a) CV curves at original and bend states of the PPy/p-TSA device; (b) Cycling performance of PPy/p-TSA, PPy/PA and PPy/$HClO_4$ devices at 0.5A g^{-1}, A picture showing that a LED lightened by three solid-state PPy/p-TSA device in series (insert); (c) Ragone plots of the solid-state devices on the basis of the total mass of the active material; (d) Ragone plots of the solid-state devices on the basis of the geometric area of the device.

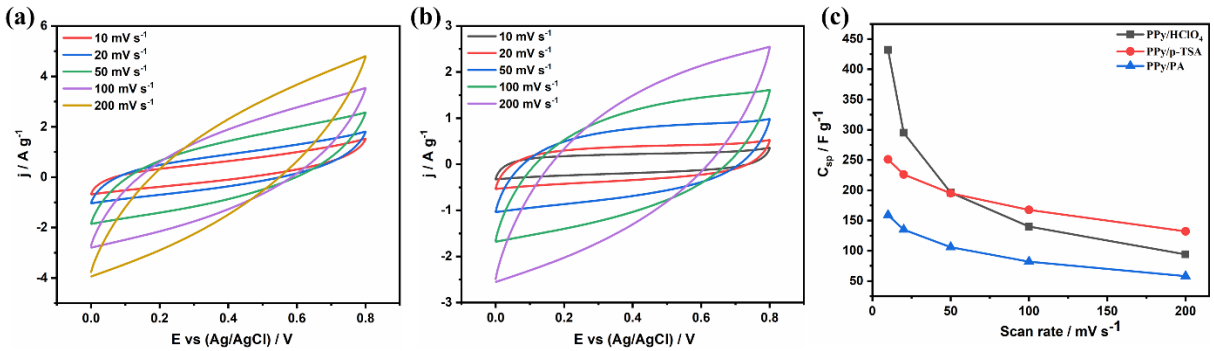

Figure 3. 15 (a) CV curves of PPy/$HClO_4$ device at different scan rate; (b) CV curves of PPy/PA device at different scan rate; (c) Specific capacitances of PPy/$HClO_4$, PPy/p-TSA and PPy/PA devices at different scan rates (10-200 mV s^{-1}).

The flexibility of the as-fabricated PPy/p-TSA all-solid-state device was investigated by measuring the corresponding CV curves at original and bend state (180°). The CV curve in bending state is similar to that of original, indicating the excellent stability of the fabricated device (**Fig. 3.14a**). Furthermore, the comparison of cycling performance of PPy/p-TSA, PPy/PA and PPy/$HClO_4$ devices (**Fig. 3.14b**) indicates that the PPy/p-TSA device exhibits the best cycling stability with a capacitance retention around 88% after 6000 GCD cycles. While the PPy/PA device and PPy/$HClO_4$ device show the capacitance retention around 77% and 44%, respectively, after 6000 cycles. The cycling performance of these three devices is consistent with the results tested in the three-electrode system. Compared to the cycling performance of PPy/p-TSA tested in the three electrodes system (**Fig. 3.10d**), the enhanced cycling performance of PPy/p-TSA device is mainly because the fact that solid electrolyte could hold the active materials very well and avoid falling off during the repeated charging/discharging (electron insertion/extraction) process. It should be noted that there is an initial small drop appeared in capacitance of PPy/p-TSA device for first hundred cycles because of the presence of benzene ring in dopants structure that are preventing the access of redox

sites. After the activation process, the redox sites become accessible during charge-discharge process. The capacitance starts to increase for next couple hundred cycles, which indicate an increasing accessibility of redox sites in the PPy/p-TSA. In contrast, the capacitance decreases dramatically for the first 2000 cycles for both the PPy/$HClO_4$ and PPy/PA devices. This phenomenon is probably due to the fact that the PPy backbone doped by $HClO_4$ and PA was destroyed by ions insertion and extraction, while p-TSA could protect the PPy backbone to some extent. In addition, **Fig. 3.15** compares the specific capacitance as different scan rate for these three devices. Even though the PPy/$HClO_4$ device exhibits the highest specific capacitance at low scan rate (e.g. 5 and 10 mV s^{-1}), the capacitance decreases rapidly with the increase of the scan rate and its capacitance become lower than PPy/p-TSA device when scan rate is higher than 50 mV s^{-1}. For PPy/PA, it shows the lowest specific capacitance even though with relatively good cycling stability. Based on above results, PPy/p-TSA is the best one for solid-state supercapacitor with both good capacitance behavior and excellent cycling stability. The inset of **Fig. 3.14b** displays an example for the practice applicability of PPy/p-TSA devices, where three arbitrary PPy/p-TSA devices are connected in series providing enough charge to light a LED, and the devices are flexible and wearable, demonstrating the attractive practical application of PPy/p-TSA devices.

Energy density and power density are important factors for evaluating the performance of solid-state supercapacitor devices. The Ragone plot of the PPy/p-TSA device (energy density vs. power density) based on the total mass of the active material is shown in **Fig. 3.14c**. The results indicate that the PPy/p-TSA device can deliver an energy density of 6.2 Wh kg^{-1} at a power

density of 140 W kg^{-1} and it still maintains an energy density of 2.9 Wh·kg^{-1} at a power density of 2640 W kg^{-1}. These values are higher than some previously reported PPy based symmetric supercapacitors such as the PPy films (0.13Wh kg^{-1} at 1100 W kg^{-1}) [136], PPy hydrogels (4.13 Wh kg^{-1} at 270 W kg^{-1}) [137], PPy/Cladophora nanocellulose (1.75 Wh kg^{-1} at 2700 W kg^{-1}) [138], PPy/NPACNS/sponge (2 Wh kg^{-1} at 550 W kg^{-1}) [139]. Also, the energy density of PPy/p-TSA device is comparable to some PPy based composite symmetric supercapacitors such as PPy-Nanocellulose-Graphene oxide (PNG) paper (5.1 Wh kg^{-1} at 1500 W kg^{-1}) [140].

The relationship between energy density and power density based on the geometric area of the device is shown in **Fig. 3.14d**. It is evident that the assembled PPy/p-TSA device exhibits the highest energy density of 27.0 µWh cm^{-2} with a power density of 0.6 mW·cm^{-2} and maintains 12.7 µWh cm^{-2} at a higher power density of 11.4 mW cm^{-2}. This obtained values are higher than that of previously reported values such as PPy/GO (3.51 µWh cm^{-2} at 5.763 mW cm^{-2}) [141], Ag/PPy (2.67 µWh cm^{-2} at 0.6 mW cm^{-2}) [142], 3D GO/PPy (13 µWh cm^{-2} at 0.8 mW cm^{-2}) [143], CQDs/PPy (11.2 µWh cm^{-2} at 6.5 mW cm^{-2}) [144], PPy-GO/CNTs (11.1 µWh cm^{-2} at 2.5 mW cm^{-2}) [145] and PPy/Carbon paper (0.61 µWh cm^{-2} at 3.47 mW cm^{-2}) [89]. From the comparison with the previous results for PPy based supercapacitors, the obtained PPy/p-TSA films in the current work show great practical application potential in flexible and wearable supercapacitors.

3.4 Conclusion

In summary, we studied the influence of six commonly used acid dopants on the electrochemical behavior of PPy films as the flexible electrode material. We found the type and size of the dopants significantly influence the electrochemical performance of the PPy

films. Among the six acid dopants used in this study, PPy/p-TSA films have the largest number of accessible redox sites with the accessible coefficient of 0.32, showing the best cycling stability (more than 75% capacitance retention after 2000 cycles), as well as a relatively high capacitance (572 F g^{-1} at 5 mV s^{-1}). In addition, PPy/p-TSA all-solid-state devices were fabricated to evaluate their practical applications. It was found that the PPy/p-TSA devices exhibited high energy density and power density which surpass most of pure PPy based supercapacitors and are even comparable with some PPy composite supercapacitors. More importantly, the PPy/p-TSA devices exhibited excellent cycling stability with 88% capacitance retention after 6000 cycles. Thus, PPy/p-TSA could be promising electrode materials for flexible supercapacitors. This work lays the foundation in promoting PPy-based electrode materials for flexible supercapacitor devices and lead to in-depth studies of fundamental and applied sciences and technologies therein.

Chapter 4

Electropolymerization of polyaniline as high-performance binder free electrodes for flexible supercapacitor

Abstract: Polyaniline (PANI), as one of the most promising electrode materials for flexible supercapacitors, facing the problems of limited capacitive properties and poor cycling stability. Herein, we demonstrate that dopants have a great effect on the electrochemical performance of PANI and selecting a suitable dopant can be used as an effective way for enhancing the electrochemical behavior of PANI electrode. All PANI electrodes were synthesized by electropolymerization method using hydrochloric acid (HCl), perchloric acid ($HClO_4$), sulfuric acid (H_2SO_4), p-toluenesulfonic acid (p-TSA), phosphoric acid (H_3PO_4) and phytic acid (PA) as dopants, respectively. The influence of dopants on morphology, doping level, redox sites accessibility and electrochemical performance of PANI electrodes were studied systematically. The results show that, PANI/$HClO_4$ has the best capacitive behavior with a maximum specific capacity of 1341 C g^{-1} at 5 mV s^{-1} along with a 57 % capacity retention after 2000 cycles. Moreover, PANI/p-TSA shows the best cycling stability with 70% of capacity retention after 2000 cycles accompanied with a relatively high specific capacity (722 C g^{-1} at 5 mV s^{-1}). Furthermore, PANI/$HClO_4$ and PANI/p-TSA were used as electrodes for the fabrication of flexible all-solid-state symmetric supercapacitors. Results indicate that PANI/$HClO_4$ device has higher energy density (12.57 Wh kg^{-1} at 283 W kg^{-1}) than that of PANI/p-TSA (8.86 Wh kg^{-1} at 199 W kg^{-1}). In contrast, PANI/p-TSA device with a capacity retention over 80% after

3000 cycles has better stability than PANI/$HClO_4$ device which maintain 73% capacity after 3000 cycles. This fundamental study provides a much easier route in achieving high performance flexible PANI-based electrodes and opens new opportunities for facilitating PANI-based electrodes as promising candidates for wearable electronics.

4.1 Introduction

Rapid development of flexible and portable electronics such as bendable displays, wearable devices and implantable medical devices used in daily life have attracted increasing attention by consumers and researchers in recent years [146-147]. It is necessary to maintain a stable power and energy supply even in the case of mechanical deformation including twisting and bending or even stretching for flexible power electronic equipment [148]. In a variety of flexible electrochemical energy storage and conversion devices, flexible all-solid-state supercapacitors (SCs) have been considered as one of the most promising candidates due to their flexibility, high power density, moderate energy density, light weight, fast charge/discharge rate, long cycle life, wide operating temperature range and safe handling [149-150]. For conventional SCs, device design is limited because of the inflexibility of electrodes which are normally fabricated by coating the active materials onto metallic current collectors with conductive binders. The utilization of metallic current collectors and conductive binders leading to the low gravimetric capacity, inflexibility and low ion penetration that caused by the current collectors and aggregations of active material [146]. While the high capacity and flexibility are required for flexible SCs, exploring right electrode materials and selecting suitable current collector substrates are essential for fabricating flexible SCs.

Polyaniline (PANI), as a typical conducting polymer, has been considered as one of the most suitable electrode materials for flexible SCs. This is due to its numerous advantages such as high theoretical capacity, high and tunable conductivity, fast reversible electrochemical behavior, low cost and excellent environmental stability [151-153]. Despite the above-mentioned advantages, PANI suffers from limited capacity property and poor cycling stability due to its compactness that leads to the low accessible surface areas and volume changes during the repeating charge/discharge processes [152]. Many attempts have been done to enhance its performance. For instance, compounding PANI with other materials (e.g., carbon-based materials, metal oxides and metal-organic framework materials) has been used as a common way. The synergistic effect of PANI and these materials can help to improve capacity, rate capability and cycling stability of the compounded electrode materials [154-156]. Moreover, synthesizing PANI with nanostructures (e.g., nanowires, nanotubes, nanofibers) is another approach to enhance its performance [157-159]. Several methods have been developed to synthesis nanostructured PANI such as electrospinning, dilute polymerization, stepwise electrochemical deposition, seeding and template synthesis. Even though these strategies can effectively improve electrochemical performance of PANI based electrode materials, the utilization of hazardous materials, harsh experimental conditions, complicated multiple-step process, high cost or time-consuming removal of templates during the synthesis process limit their practical applications [160]. The one-step electrochemical polymerization is considered as one of the most promising method for the synthesis of flexible PANI electrodes due to its easy, fast, cost-effective, binder-free and environmental-friendly properties [161].

The charging/discharging process of PANI based electrode material is a typical doping/dedoping process accompanied by ion exchange between the polymer and the electrolyte [162-163]. Consequently, the dopants used during the polymerization process will have a significant impact on the electrochemical properties of PANI electrodes. Previous studies have suggested that utilizing dopants with different chemical structures could change PANI properties such as surface morphology, solubility and conductivity [164-165]. However, to the best knowledge of authors, there is no research suggesting the influence of dopants on the electrochemical performance of PANI as flexible SCs electrodes. Therefore, investigating the influence of dopants on the electrochemical performance of PANI is necessary for further enhancing the electrochemical performance of PANI-based electrode materials and promoting their further development as the electrode materials for flexible SCs.

In this work, binder free PANI flexible electrodes were synthesized via one-step electropolymerization approach. During the polymerization process, chlorates (HCl and $HClO_4$), sulfates (H_2SO_4 and p-TSA) and phosphates (H_3PO_4 and PA) were used as dopants, respectively, (the chemical structures of dopant molecules were shown in Fig. S1). We studied the influence of these dopants on morphology, doping level, accessibility of redox sites, capacity performance and cycle stability of PANI. Moreover, all-solid-state flexible symmetric supercapacitor devices were fabricated to study the performance of PANI electrodes in the device.

4.2. Experimental

4.2.1. Materials

Carbon cloth (CC) (40 cm x 40 cm) was supplied by Fuel Cell Earth. Aniline monomer and Phytic acid were purchased from Tokyo Chemical Industry. Hydrochloric acid was supplied by BDH chemicals. Sulfuric acid was obtained from Anachemia. p-toluenesulfonic acid was purchased from Alfa Aesar. Phosphoric acid was purchased from EM Science. Perchloric acid, nitric acid and acetone were purchased from VWR, USA. All chemicals were used without further treatment or purification.

4.2.2 Preparation of PANI flexible electrodes.

PANI flexible electrodes were prepared by electropolymerization method using potentiostatic technique on an electrochemical workstation (CHI 760D). Firstly, CC (1 cm × 2 cm) was cleaned by HNO_3, DI water and acetone, followed by vacuum drying at 60°C to remove all the impurities and enhance its surface wettability. The electrochemical polymerization process was performed in a standard three-electrode cell with Pt mesh as counter electrode, Ag/AgCl (E° = +205 mV vs. SHE) as reference electrode and the pre-treated CC with a 1 cm^2 immersion area as working electrode. The electrolyte solution is composed of 0.1 M aniline and 0.5 M acid dopant. The dopants including chlorates (HCl and $HClO_4$), sulfates (H_2SO_4 and p-TSA) and phosphates (H_3PO_4 and PA) were used in this study. The PANI flexible electrodes were obtained by applying 1.0 V constant potential for 5 min. The obtained electrodes were rinsed by DI water then dried in vacuum at 60°C. The PANI synthesized under different dopants are marked as PANI/HCl, PANI/$HClO_4$, PANI/H_2SO_4, PANI/p-TSA, PANI/H_3PO_4, PANI/PA, respectively.

4.2.3 Fabrication of symmetric all-solid-state supercapacitor device

The PVA/H_2SO_4 gel electrolyte was prepared by dissolving 3 g PVA in the solution of 30 mL deionized water and 3 g H_2SO_4. The obtained mixture was heated to 85 °C with constant stirring until it became clear. Subsequently, two pieces of PANI flexible electrodes were immersed in the PVA/H_2SO_4 solution, then the electrodes were dried in the fume hood overnight to vaporize excess water. Finally, the symmetric all solid-state supercapacitor device was assembled by stacking two electrodes together.

4.2.4 Material Characterization

The morphological difference of PANI synthesized with different dopants were characterized by scanning electron microscope (SEM) using a Thermo Scientific Apreo FE-SEM. Fourier Transform Infrared (FTIR) spectra analysis were carried out within frequency range of 2500 - 500 cm^{-1} by a Thermo Nicolet 6700 instrument. X-ray photoelectron spectroscopy (XPS) were measured by a Kratos Axis DLD spectrometer with a monochromatic Al Kα X-ray source under 10^{-10} Torr ultra-high vacuum conditions. The binding energies of all spectra were calibrated by the carbon peak C 1s (284.8 eV) before the XPS data analysis.

4.2.5 Electrochemical characterizations

Electrochemical measurements were performed on a CHI 760D electrochemical analyzer. The electrochemical performance of PANI electrodes were evaluated by cyclic voltammetry (CV), galvanostatic charge/discharge (GCD) and electrochemical impedance spectra (EIS) with 1.0 M H_2SO_4 as the supporting electrolyte. The CV measurements were tested at varying scan rate ranges from 5 to 200 mV s^{-1} within a potential range of - 0.2 V to + 0.8 V. GCD measurements were recorded at a potential window of 0 to + 0.8 V at varying current density (1, 2, 3, 4, 5 and

6 A g^{-1}). The EIS tests carried out by applying a 5mV amplitude AC voltage at open circuit potential within the frequency range of 100 kHz to 0.01 Hz.

The symmetric all-solid-state supercapacitor devices were tested in a two electrodes system with CV tested within a potential range of 0 V to + 0.8 V and GCD recorded at a potential window of 0 to + 0.8 V at varying current density varying from 0.1 A g^{-1} to 2.0 A g^{-1}.

The specific capacity of PANI electrodes tested in three-electrode system can be calculated by using the following equation according to CV curves:

$$C_s = \frac{\int \mathrm{I} dV}{m\nu}$$

Where C_s (C g^{-1}) is the electroactive material mass based specific capacity, I (A) is the current, V (V) is the potential window, m (g) is the mass of electroactive material, υ (mV s^{-1}) is the scan rate.

The capacitance of PANI symmetric all-solid-state supercapacitor device can be calculated based on CV curves according to the following equation:

$$C_{cell} = \frac{\int \mathrm{I} dV}{m\nu\Delta\mathrm{V}}$$

Where m (g) is the mass of the active material in device, ΔV (V) is the potential range, other parameters are same as described in three-electrode system equation.

The energy density and power density of PANI symmetric all-solid-state supercapacitor device were calculated by the following equations [97], respectively:

$$\mathrm{E} = \frac{1}{2 \times 3.6} C_{cell} \Delta V^2$$

$$P = \frac{3600Ev}{\Delta V}$$

Where E (Wh kg^{-1}) and P (W kg^{-1}) corresponding to energy density and power density, respectively; m (g) is the mass of active material in the device, I (A) is the current, υ (mV s^{-1}) is the scan rate, ΔV (V) is the discharge voltage window.

4.3 Results and Discussions

4.3.1 Morphology

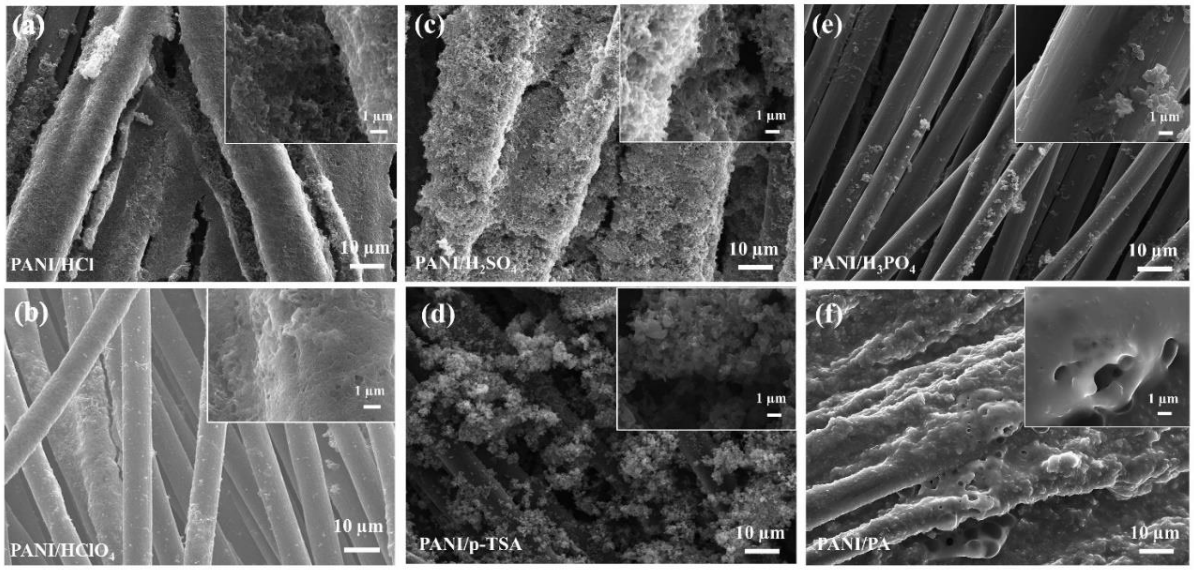

Figure 4. 1 SEM images of PANI films: (a) PANI/HCl; (b) PANI/$HClO_4$; (c) PANI/H_2SO_4; (d) PANI/p-TSA; (e) PANI/H_3PO_4 and (f) PANI/PA. (inset: zoomed image of corresponding sample)

Figure 4.1 shows SEM images of PANI synthesized under different dopants. From a general view, all PANI samples can be uniformly covered on the surface of carbon cloth compared with pristine carbon cloth (**Fig. 3.1b**). It is clear to see that the dopant type has a significant influence on PANI morphologies. The chlorates doped PANI samples **(Figs. 4.1a** and **4.1b**)

have relatively smooth surfaces and both have the formicary-like porous interior structure. While the PANI/HCl (**Fig. 4.1a**) is more loosely packed than PANI/$HClO_4$. Thus, the PANI/HCl has more holes and presented much higher coverage volume than PANI/$HClO_4$. The cracking of the PANI/HCl coating further confirmed its loosely packed structure. The tightly packaged formicary-like structure makes PANI/$HClO_4$ exhibiting a coating layer structure with several randomly distributed particles on it. The sulfates (**Fig. 4.1c** and **Fig. 4.1d**) doped PANI showed cauliflower like morphology. It is clear to see that PANI/H_2SO_4 has smaller floweret size than those of PANI/p-TSA. This makes PANI/H_2SO_4 more evenly distributed and more porous coating. There is a significant difference in phosphates doped PANI (Fig. **4.1e** and **Fig. 4.1f**), the PANI/H_3PO_4 (**Fig. 4.1e**) has a very thin and smooth film structure which very uniform coating with small particles cling to the surface. While PANI/PA is made up by the stacking of particles. The coating of PANI/PA looks smooth, stick and compact. The viscous nature of PA makes PANI looks like glued together. Moreover, the bubbles-like structure and holes can be observed in PANI/PA. Furthermore, by comparing the magnified SEM images, it is not hard to see that for PANI doped by similar type of dopants, the large size dopants lead to a more compact morphologies than PANI doped by small size dopants. This can be explained as the large counter ions are easier to entangle together which makes the polymerized aniline entangles with each other and clumps together during the polymerization process and resulting in the more stacked compact and smooth morphologies [166]. The unevenly covering of PANI/p-TSA and PANI/PA on CC are because p-TSA and PA dopants have larger size than other dopants which leads to the greater degree of winding and pulling. While, for PANI doped by different types of dopants, we can see that the dopants type

plays an important effect not only on the morphology shape but also on the roughness of PANI. Obviously, the sulfates doped PANI samples have the roughest surface and the chlorates doped PANI show a little bit higher roughness than phosphates doped PANI samples. The different morphology, porosity and roughness of electropolymerized PANI samples will provide different electroactive surface area and different kind of pathway for electron/ion transport [167]. Thus, the accessibility of electrolyte ions to interior sites of PANI and the electrochemical performance of PANI samples will be greatly affected by their morphological structures.

4.3.2 FTIR characterization

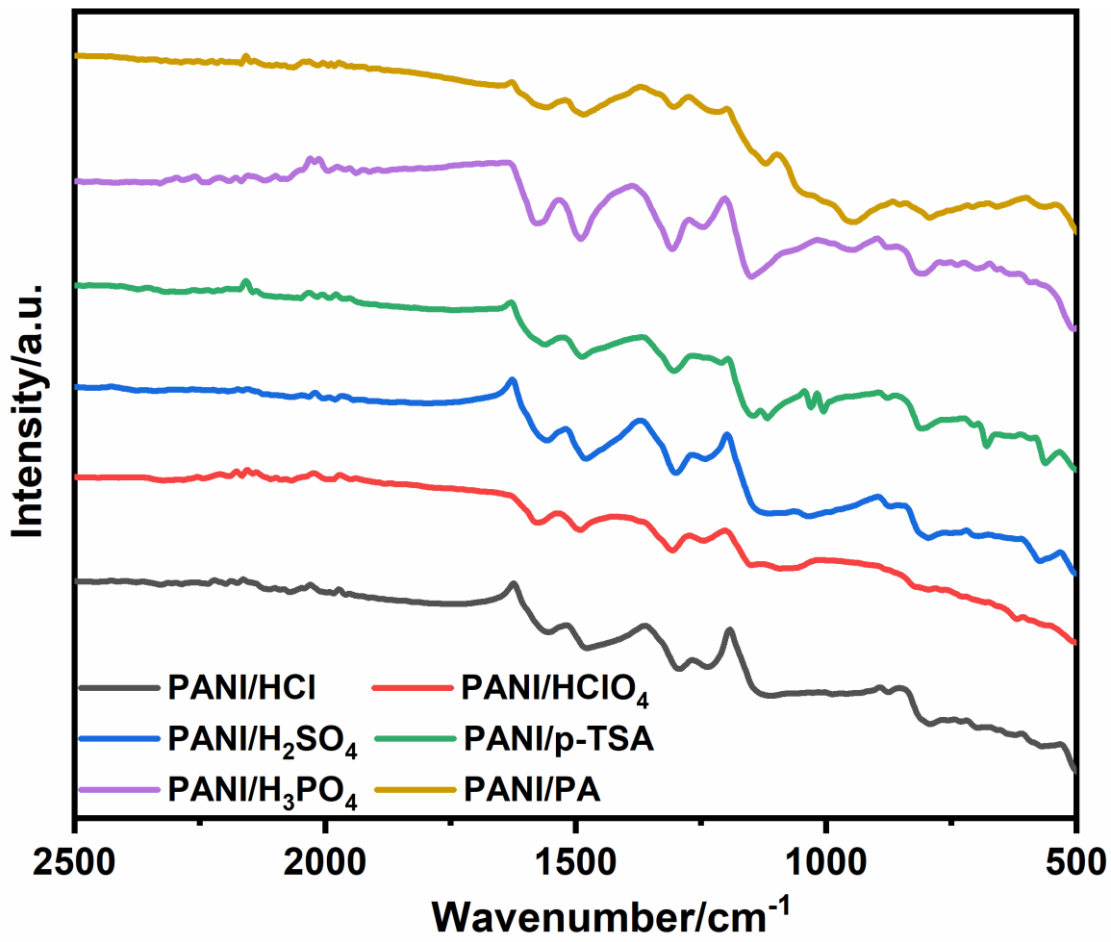

Figure 4. 2 FTIR spectra of PANI films doped with different acid dopants.

The chemical structures of PANI electrodes were investigated by using FTIR spectroscopy. **Fig. 4.2** shows the FTIR spectra of PANI electrodes synthesized under different dopants. The summary of FTIR observations was listed in **Table 4.1**. The peaks at 1560, 1485, 1300, 1240, 795 and 505 cm^{-1} are the characteristic peaks of PANI presented in all PANI electrodes samples. The peaks located at1560 cm^{-1} demonstrated the existence of quinoid rings (Q) caused by the N=Q=N stretching vibration. The peaks at 1485 cm^{-1} was due to the N-B-N stretching mode (N means benzenoid ring) in PANI [168]. The peaks near 1300 cm^{-1} was owning to the C-N-C stretching vibration [169]. The peak appeared at 1240 cm^{-1} was attributed to C-N stretching of the aromatic amine [170-171]. The peaks near 795 cm^{-1} and 505 cm^{-1} were related to the out-of-plane bending vibrations of C-H and C-C in benzenoid units [105, 172-173]. The small peaks at 697 cm^{-1} and 624 cm^{-1} in PANI/HCl were assigned to out of plain bend of C-Cl aromatics [174]. For PANI/$HClO_4$, the small peaks at 1092 cm^{-1} and 619 cm^{-1} were due to the ClO_4^- vibrations [175]. The absorption peaks near 1115 cm^{-1} and 1030 cm^{-1} appeared in H_2SO_4 and p-TSA doped PANI. The peaks of 1115 cm^{-1} were caused by S-O bond stretching of SO_3^- and the peaks at 1030 cm^{-1} were due to the asymmetrical stretching of the S=O group [104-105]. The PA doped PANI has characteristic absorptions at approximately1655 cm^{-1} which corresponding to HPO_4^{2-} characteristic bands of PA [106]. The peaks near 1176 cm^{-1} (1149 cm^{-1} in PANI/H_3PO_4 and 1216 cm^{-1} in PANI/PA) were caused P=O bonds [108]. The peak at 947 cm^{-1} in PANI/H_3PO_4 and 946 cm^{-1} in PANI/PA were due to symmetrical vibration of P-O-C [173]. According to the discussed results, for each PANI sample, the dopant ions were all successfully introduced in to PANI structure during the synthesis process.

Table 4. 1 Summary of FTIR observations for PANI electrodes polymerized with different dopants.

Peak assignment	Peak position (cm^{-1})					
	PANI/HCl	PANI/$HClO_4$	PANI/H_2SO_4	PANI/p-TSA	PANI/H_3PO_4	PANI/PA
HPO_4^{2-} characteristic bands	-	-	-	-	-	1655
N=Q=N stretching vibration	1551	1576	1557	1561	1577	1558
N-B-N stretching	1472	1490	1479	1486	1489	1484
C-N-C stretching	1291	1306	1300	1303	1307	1304
C-N stretching of an aromatic amine	1231	1244	1242	1209	1246	-
P=O bonds	-	-	-	-	1149	1216
S-O bond	-	-	1114	1117	-	-

stretching of SO_3^-						
ClO_4^- vibration	-	1092	-	-	-	-
S=O group	-	-	1035	1030	-	-
P-O-C vibration	-	-	-	-	947	946
C-H out-of-plane bending vibrations in benzenoid units	794	795	796	810	807	793
C-Cl out of plain bend	697	-	-	-	-	-
C-Cl out of plain bend	624	-	-	-	-	-
ClO_4^- vibration	-	619	-	-	-	-
C-C out-of-plane bending vibrations in benzenoid units	497	498	501	499	505	477

4.3.3 XPS Analysis

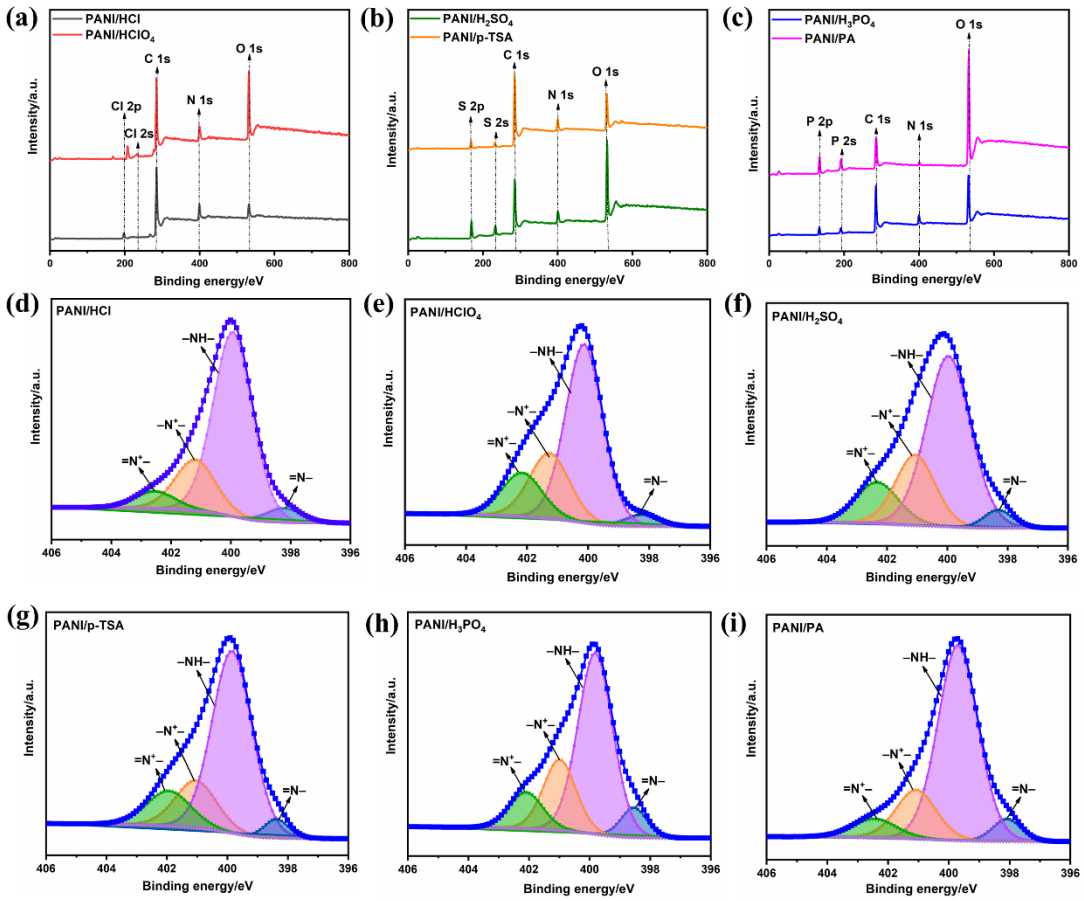

Figure 4. 3 (a-c) XPS survey spectra of PANI electrodes: (a) Chlorates doped PANI electrodes (PANI/HCl vs. PANI/$HClO_4$); (b) Sulfates doped PANI electrodes (PANI/H_2SO_4 vs. PANI/p-TSA); (c) Phosphates doped PANI electrodes (PANI/H_3PO_4 vs. PANI/PA); (d-i) N1s XPS core level spectra of (d) PANI/HCl, (e) PANI/$HClO_4$, (f) PANI/H_2SO_4, (g) PANI/p-TSA, (h) PANI/H_3PO_4, (i) PANI/PA.

Additionally, XPS spectra were performed to evaluate the surface element compositions and quantitatively understand the oxidation state and doping level of PANI samples. **Fig. 4.3 (a-c)** showed the comparison of XPS survey spectra of all PANI electrodes. The C, N, O elements are present in all PANI electrodes. Moreover, Cl, S, P elements are respectively present in chlorates, sulfates and phosphates doped PANI electrodes which further confirms the successfully introduction of dopant ions into PANI chain. Compared to PANI/HCl, the Cl 2p core level peak of PANI/$HClO_4$ shows a higher binding energy which is due to the high positive

oxidation state of Cl atom in ClO_4^-. For chlorates doped PANI, a much higher O 1s peak intensity can be observed in $HClO_4$ which is caused by the big differences in the counterion structure of Cl^- and ClO_4^-. Similarly, the higher O 1s peak intensity in PANI/p-TSA than PANI/H_2SO_4 and PANI/PA than PANI/H_3PO_4 were observed for sulfates and phosphates doped PANI, respectively.

Fig. 4.3 (d-i) show the N 1 s XPS spectra of PANI electrodes. All these N 1 s spectra can be deconvoluted into four peaks corresponding to four different nitrogen atoms connection modes in PANI. These including the quinonoid imine (=N-) structure (398.5 ± 0.4 eV), the benzenoid amine (-NH-) structure (399.5 ± 0.4 eV), the protonated amine ($-N^+-$) structure (400.8 ± 0.4 eV) and the protonated imine ($=N^+-$) structure (402.2 ± 0.4 eV), respectively [176-177]. The ratio of four nitrogen constituents to total nitrogen content of PANI electrodes were calculated and summarized in **Table 4.2**. The pretty low unprotonated imine (=N-) content, the high content of protonated amine ($-N^+-$) and protonated imine ($=N^+-$) indicates all PANI electrodes were successfully doped [177]. The doping level which expressed as the proportion of all positively charged nitrogen (N^+) species to the total nitrogen content was quantified in **Table 4.2** [178]. Interestingly, we found that both size and type of dopants have obvious effects on the doping level of PANI. For sulfates and phosphates doped PANI, when we compare the doping level of PANI doped by similar size dopants, we found that PANI doped by small size dopants have higher doping level than PANI doped by big size dopants, i.e., the doping level of 36.22% for PANI/H_2SO_4 is higher than the doping level of 31.26% for PANI/p-TSA and the doping level of 33.42% for PANI/H_3PO_4 is higher than the doping level of 28.57% for PANI/PA. This result

can be explained from the following two aspects: (1) the big size dopants could generate large steric hindrance, which prevents more counterions from doping into the PANI structure. (2) from the SEM results, the PANI doped by big size dopants have more compact and smooth structures which are difficult for the counterions accompanied by solvent molecules in the electrolyte insert into the structures due to the high resistance and the limited free volume [179]. Moreover, we can see for similar size dopant, the sulfates doped PANI exhibit higher doping level than phosphates doped PANI which are due to the more loose and rough structures of sulfates doped PANI (**Fig. 4.1**) and this makes it easier for counterions enter into the structures of PANI. However, for chlorates doped PANI, other factors exceed the influence of morphological structure on their doing level. Thus, we see that the doping level of PANI/$HClO_4$ (38.48%) is higher than PANI/HCl (26.26%). The doping level of PANI/HCl is even lower than sulfates and phosphates doped PANI. This may be attributed to two reasons: first, compared to sulfates and phosphates, HCl is a volatile acid with higher instability which might reduce the doping quantity to a certain extent; second, sulfates and phosphates are polyacid and sulfonation or phosphating could occur on PANI, which could not only displace the aromatic protons, but also cause the self-doped process and increase the number of ammonium protons [180-181]. The high doping level of PANI/$HClO_4$ might be due to the dopant of $HClO_4$ leads to a very low growth rate of PANI which makes the insertion process of counterions into PANI structure easier [182]. Furthermore, it is easier to form a higher fraction of the conducting emeraldine salt phase in PANI/$HClO_4$ [183]. The above factors combine to make the highest doping level for PANI/$HClO_4$. The electrical conductivity and electrochemical performance of PANI samples will be connected to their doping levels.

Table 4. 2 Nitrogen species ratio to total nitrogen content, doping level of PANI electrodes.

Samples	-N= (%)	-NH- (%)	$-N^+-$ (%)	$-N^+=$ (%)	Doping level (%)
PANI/HCl	4.79	68.94	19.67	6.59	26.26
PANI/$HClO_4$	3.38	58.13	23.02	15.47	38.49
PANI/H_2SO_4	4.00	59.78	22.22	14.00	36.22
PANI/p-TSA	4.00	64.74	17.43	13.83	31.26
PANI/H_3PO_4	7.26	59.32	21.83	11.59	33.42
PANI/PA	5.29	66.14	21.71	6.86	28.57

4.3.4 Electrochemical performance

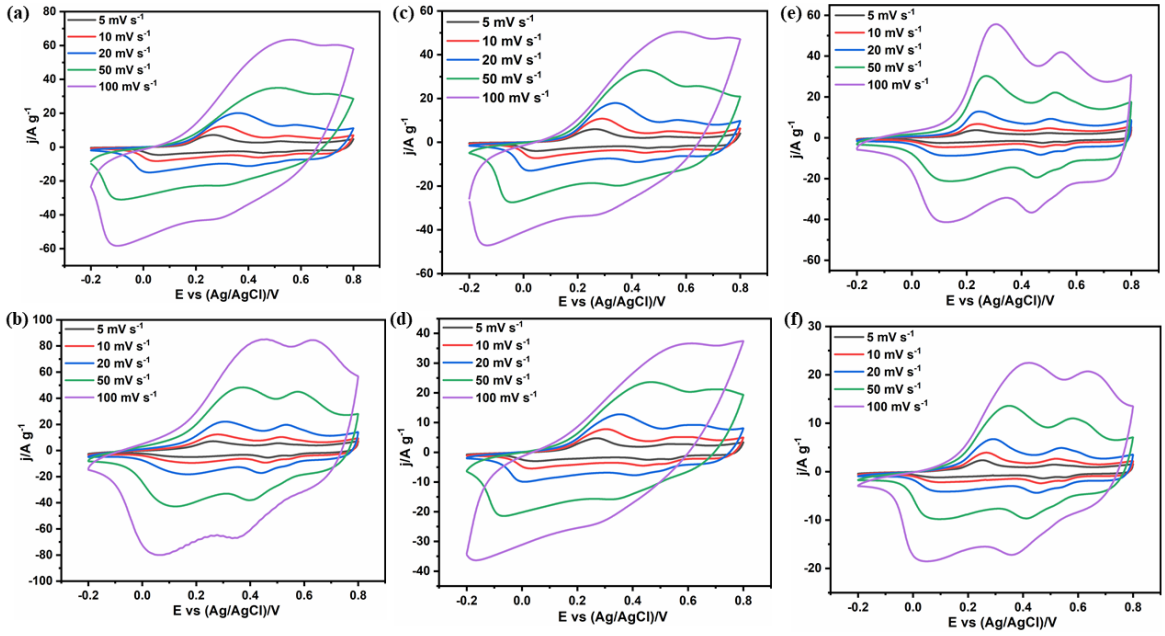

Figure 4. 4 (a-f) Cyclic voltammetric curves of PANI films: (a) PANI/HCl; (b) PANI/$HClO_4$; (c) PANI/H_2SO_4; (d) PANI/p-TSA; (e) PANI/H_3PO_4 and (f) PANI/PA.

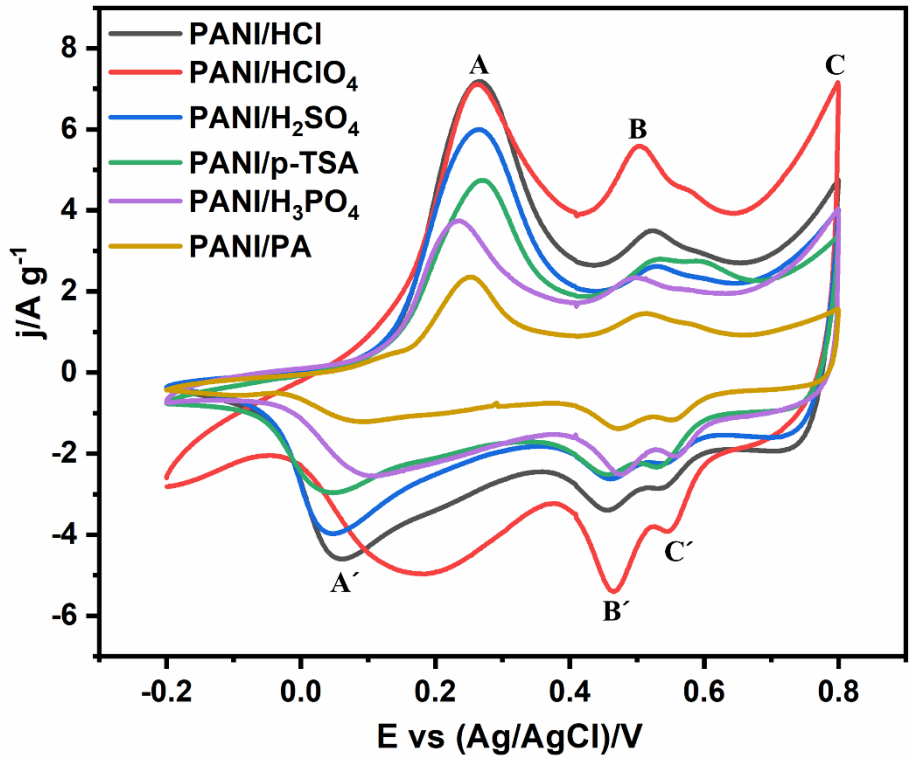

Figure 4. 5 Cyclic voltammetric curves of PANI films at a scan rate of 5 mV s^{-1}.

Electrochemical measurements were carried out to study the effect of dopants on electrochemical behavior of PANI. **Fig. 4.4** shows the CV curves of PANI samples. Three pairs of redox peaks (A/A´, B/B´ and C/C´) can be observed at a low scan rate of 5 mV s^{-1} (**Fig. 4.5**). The A/A´ peaks are associated with the transformation between the fully reduced leucoemeraldine state to the partly oxidized emeraldine state. The B/B´ peaks are attributed to the intermediates of the hydroquinone/benzoquinone redox reaction and the by-products. The C/C´ peaks correspond to the redox transition of the partly oxidized emeraldine state to the fully oxidized pernigraniline state [184-185]. Apparently, the current responses of PANI samples synthesized under different dopants exhibit clear difference which demonstrates the great influence of counter ions. The different current responses are mainly attributed to the different

anion mobility and conductivity of the electrodes [186]. The highest currents were found in PANI/$HClO_4$ which mainly ascribe to its highest doping level, excellent conductivity and relatively small concentrations size. The PANI/HCl even with low doping level also shows very high current which is due to the smallest concentrations size facilitating the anion mobility and remedied its conductivity effect. For sulfates and phosphates doped PANI samples, PANI obtained under small size dopants (PANI/H_2SO_4 and PANI/H_3PO_4) have smaller concentrations size, more porous structure and higher doping level than PANI obtained under big size dopants (PANI/p-TSA and PANI/PA). All these features are conducive to the transmission of electrolyte ions and the increase in response current. Thus, the response currents in CV curves follow the sequence of PANI/H_2SO_4 > PANI/p-TSA, PANI/H_3PO_4 > PANI/PA. In addition, the lowest current response and peaks shift of phosphates doped PANI samples should be due to the more oxidation state of PANI resulted from phosphates dopants [186-187]. The positively shift reduction peak of A′ in PANI/$HClO_4$ might be associated with the high production of intermediates during the hydroquinone/benzoquinone redox reaction and the by-products [188].

For all PANI samples, the areas enclosed by the CV curves are increase with the increase of scan rates. While it can be also observed that with the increase of scan rates, the shapes of CV curves deviated from their shapes at low scan rates with changes in peak height, positive shift in the oxidation peaks potential and negative shift in the reduction peaks potential. These changes mainly attributed to the resistance of the electrode [189-190]. Thus, the deformation degrees of CV curves for PANI samples can be well explained by their doping level. For chlorates doped PANI samples, PANI/HCl shows a more obvious deformation in CV curves

compared to PANI/$HClO_4$. This is because the lower doping level of PANI/HCl corresponds to lower electrical conductivity and higher resistance which reduces the ions transmission rates and leading to high degree of CV curves deformation at high scan rate. Compared to chlorates doped PANI samples, the sulfates and phosphates doped PANI samples exhibit relatively smaller differences in doping level. Therefore, the differences in CV curves deformation of sulfates and phosphates doped PANI samples are smaller than chlorates doped PANI samples at high scan rates. Moreover, the peaks shift and the reduction of redox peaks intensity in PANI/p-TSA and PANI/PA samples are more obvious compared to PANI/SA and PANI/H_3PO_4, respectively, which are caused by the relatively low doping level and high resistance of PANI/p-TSA and PANI/PA.

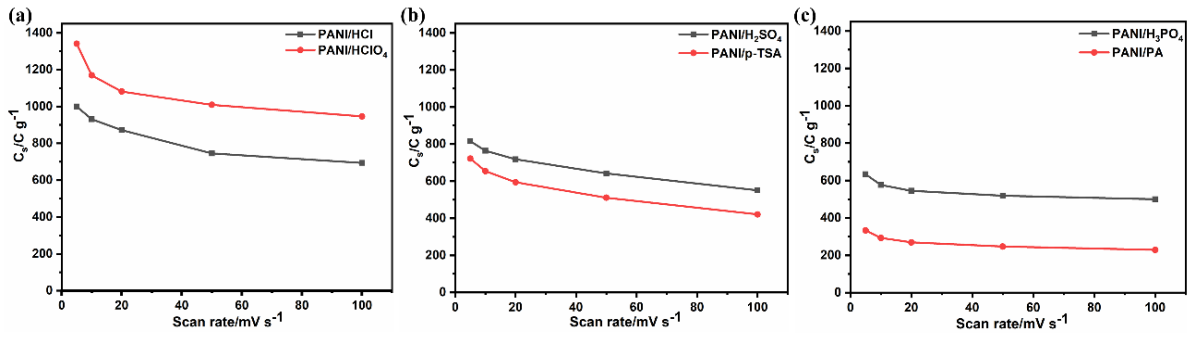

Figure 4. 6 Specific capacity of PANI films by CV curves for: (a) chlorates; (b) sulfates; (c) phosphates.

The C_s of the electrode materials can be calculated by the integral area of CV curves [184]. The relationship between C_s and scan rates of PANI samples were plotted in **Fig. 4.6**. The maximum C_s for each PANI sample can be obtained at a scan rate of 5 mV s^{-1} with the C_s value of 1000 C g^{-1}, 1341 C g^{-1}, 816 C g^{-1}, 722 C g^{-1}, 634 C g^{-1} and 333 C g^{-1}, respectively, for PANI doped by HCl, $HClO_4$, H_2SO_4, p-TSA, H_3PO_4 and PA. Obviously, PANI/$HClO_4$ shows the best

capacity performance among these six samples which is consistent with its highest doping level and electric conductivity [160]. The C_s performance for each dopant is consistent with the results discussed in the CV curves. For sulfates and phosphates acid dopants, the C_s value of PANI doped by smaller size dopants are higher than PANI doped by bigger size dopants (C_s PANI/H_2SO_4 > C_s PANI/p-TSA; C_s PANI/H_3PO_4 > C_s PANI/PA) while this is opposite for chlorates doped PANI (C_s PANI/HCl < C_s PANI/$HClO_4$). These results are in line with their doping level calculated in **Table 4.2**. Thus, doping level should be considered as the first reason for above results. For similar type of dopants, the higher doping level results in higher electrical conductivity which is beneficial to promote the electron transfer process and thus help to increase their capacity properties. Moreover, the difference in morphology should be considered as the second important factor. For sulfates and phosphates doped PANI samples, the big size dopants doped PANI samples have relatively compact, smooth and stick structures (**Fig. 4.1**) which not only decrease electroactive surface area but also increase the resistance of ions transmission resulting in low capacities. While for chlorates doped PANI, even though the large size $HClO_4$ dopant does not provide PANI/$HClO_4$ the same loose and porous structure as PANI/HCl (**Fig. 4.1**), its excellent conductivity remedies this and endows the excellent capacity for PANI/$HClO_4$. Similarly, the loose and porous structure of PANI/HCl (**Fig. 4.1**) providing high electroactive surface area and low ions transmission resistance which remedies its difference in conductivity and provides good capacity for PANI/HCl. Another interesting thing is that the capacity of different type dopants following the order of C_s PANI/chlorates > C_s PANI/sulfates > C_s PANI/phosphates. This result further illustrates the combined effect of the doping level and morphology features and confirms the influence of dopant types on

capacitance performance of PANI.

Fig. 4.7 shows the GCD curves of PANI samples at different current densities. All the GCD curves are almost symmetrically shaped, revealing all PANI samples have superior electrochemical reversibility and excellent coulombic efficiency [191-192]. Their deviation from linearity curves are caused by the redox transitions of polyaniline that matches the redox peaks in CV curves demonsting their pseudocapacitve behavior [193]. The discharge time reveals the energy storage property of electrode material. Evidently, PANI/$HClO_4$ has longest discharge time corresponding to its best electrochemical capacity characteristic. Similarly to the CV results, the discharge times for sulfates and phosphates doped PANI show that PANI doped by smaller size dopants have longer discharge time than PANI doped by bigger size dopants and this is opposite for PANI doped by chlorates which further certifying the capacity performance mentioned in CV results (C_s PANI/H_2SO_4 > C_s PANI/p-TSA; C_s PANI/H_3PO_4 > C_s PANI/PA; C_s PANI/HCl < C_s PANI/$HClO_4$). Moreover, the discharge time of PANI doped by chlorates are longer than PANI doped by sulfates which are longer than PANI doped by phosphates. These further confirmed the capacity property of the three types of dopants follows: C_s PANI/chlorates > C_s PANI/sulfates > C_s PANI/phosphates.

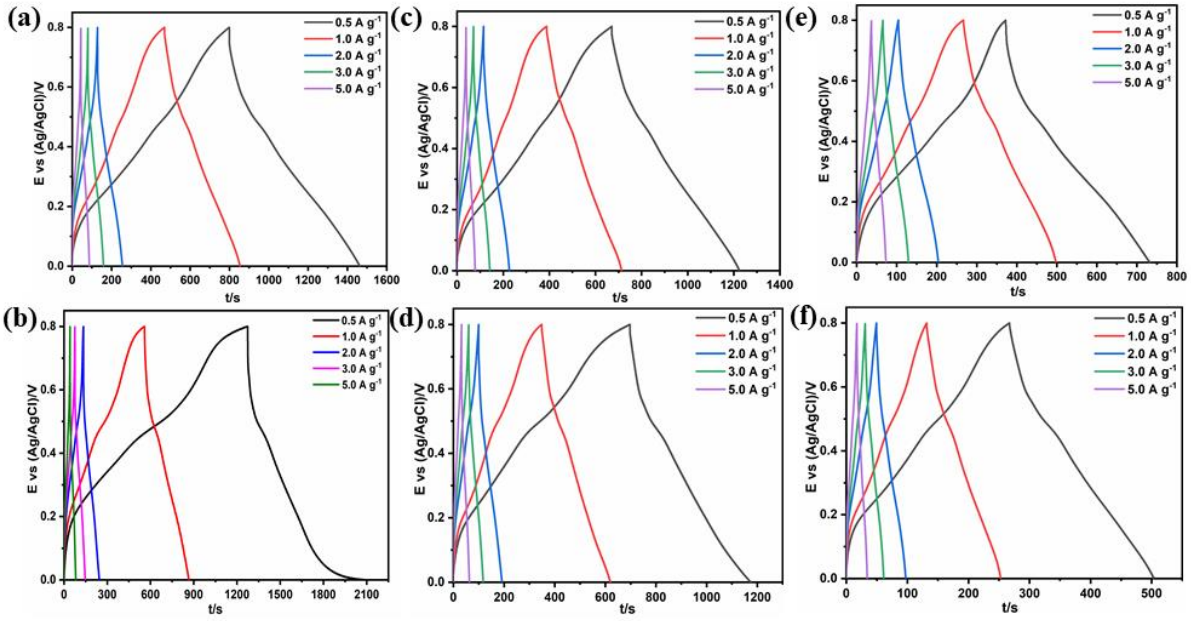

Figure 4. 7 Galvanostatic charge-discharge (GCD) curves of PANI electrodes at different current densities: (a) PANI/HCl; (b) PANI/$HClO_4$; (c) PANI/H_2SO_4; (d) PANI/p-TSA; (e) PANI/H_3PO_4 and (f) PANI/PA.

The redox sites accessibility of PANI electrodes were calculated based on the charge storage interpretation mechanistic [133]. The number of redox sites (Nr, mol) in synthesized PANI can be calculated with equation:

$$N_r = \frac{Q_t}{nF}$$

Where, Q_t is the total consumed charge of PANI during the electropolymerization process, n (= 2.3) is number of electrons transferred per aniline monomer and F is faraday constant.

The maximum charge generated from anion exchange (Q_{max}) can be calculated with the flooowing equation, if z (where z =1 for H^+) is used to represent the number of electrons produced during this process:

$$Q_{max} = N_r F z = \frac{Q_t z}{n}$$

Thus, the accessibility coefficient (A) is:

$$\mathrm{A} = \frac{\mathrm{Q_c}}{\mathrm{Q_{max}}}$$

Where Q_c is the charge accumulated in the PANI electrodes during the reversible CV process.

The relationship between scan rates and accessible coefficient for PANI samples were ploted in **Fig. 4.8**. According to these plots, the accessinbility coefficient number is associated with the capacity performance of PANI electrodes. Evidently, the availability of active redox sites decreasse with the scan rates increase. This is consistent with the decrease in specific capacity as the scan rates increase. $HClO_4$ doped PANI has the maximum redox sites at a scan rate of 5 mV s^{-1} which further expalins its best capacity behavior. Both the capacity performance for similar types of dopants (C_s PANI/HCl < C_s PANI/$HClO_4$; C_s PANI/H_2SO_4 > C_s PANI/p-TSA; C_s PANI/H_3PO_4 > C_s PANI/PA) and for different type dopants (C_s PANI/chlorates > C_s PANI/sulfates > C_s PANI/phosphates) mentioned in previous results are in good agreement with the relationship accessible coefficient and scan rates.

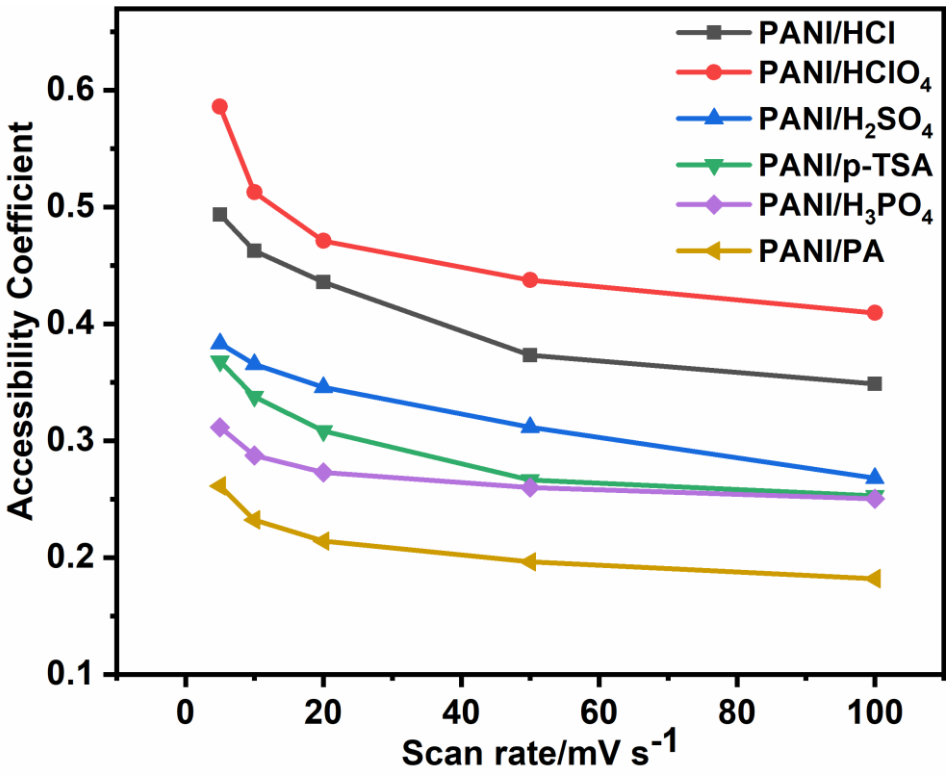

Figure 4. 8 Relationship between scan rates and accessible coefficient for PANI samples.

Electrochemical impedance spectroscopy (EIS) is considered as a most common way to investigate the change at the electrode surface and to characterize the capacitive behavior [194]. **Figure 4.9 a-c** represents the Nyquist plots of PANI samples obtained at open circuit potential with 5 mV amplitude within frequency range of 100kHz-10mHz. The typical impedance spectra contain two regions: one is high-frequency region, represented as small semicircle. The real axis intercept of this small semicircle is used to evaluate the internal resistance (R_s) consists of electrolyte ions resistance, intrinsic resistance of electrode materials and contact resistance at electrode/electrolyte interface [195]. The radius of semicircle represents the the charge transfer resistance (R_{ct}) and electrode conductivity of a electrode material [196]. The low frequency region represented by near vertical line shows the capacitive behavior of the electrode [197]. The low R_s (less than 4 Ω) revealing small electrolyte resistance or internal resistance of each PANI sample

[198]. The semicircles at high frequency region are almost invisible indicates the very low R_{ct} and fast faradaic charge transfer process in PANI samples [121]. At low frequency, the slope of vertical line in PANI/$HClO_4$ is steeper than PANI/HCl suggesting PANI/$HClO_4$ has a better capacity behavior than PANI/HCl (C_s PANI/$HClO_4$ > C_s PANI/HCl) [199]. In contrast to chlorates, the sulfates and phosphates doped PANI have steeper slope for PANI doped by smaller size dopants indicating better capacity property of the PANI doped with smaller size dopants. These results are in agreement with our CV and GCD curves (**Fig. 4.4 & Fig. 4.7**).

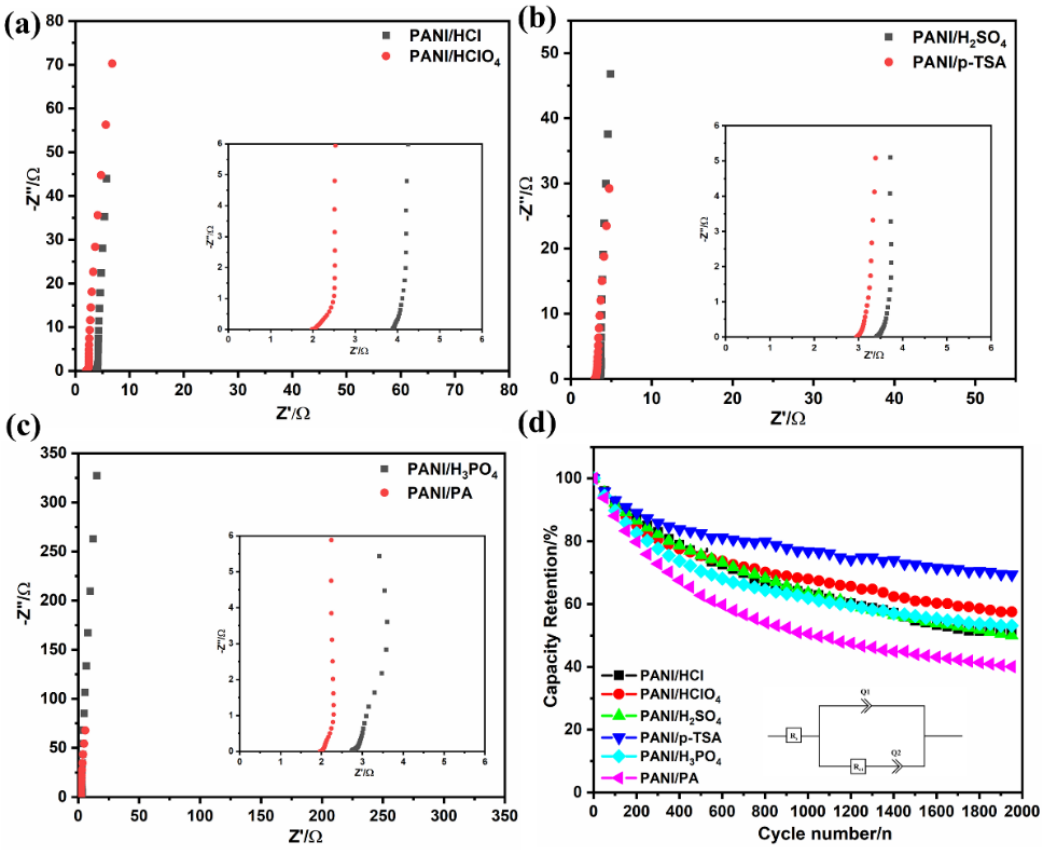

Figure 4. 9 (a-c) Nyquist impedance plots of PANI electrodes with different dopants: (a) chlorates; (b) sulfates; (c) phosphates; (d) Cycling stability of PANI samples (The inset image is equivalent circuit model for PANI electrodes).

It is worth noting that the long-term stability is an important parameter for supercapacitors. The cycling performance of PANI under different dopants were investigated by repeating the galvanostatic charge/discharge test at a current density of 4 A g^{-1} within a potential window of 0 - 0.8 V. As shown in **Fig. 4.9d**, for all PANI samples, the specific capacity decreased to varying degrees at the initial stage. The decrease of capacity is due to the damaged structures caused by the repeated intercalation/deintercalation of ions during the charge/discharge process [200]. In these samples, PANI/p-TSA exhibits the best cycling behavior with a capacity rentention around 70% after 2000 cycles which should be attribuated to the pi-pi stacking of benzene in the structure enhanced the structural stability. PANI/$HClO_4$ also exhibits good cycling stability with approximately 60% retention after 2000 cycles. PANI/HCl, PANI/H_2SO_4 and PANI/H_3PO_4 have similar stability performance with the retained capacity around 50% of their initial value. While PANI/PA shows the worst cycle stability 39.6% retention after 2000 cycles. As shown in **Table 4.3**, both the energy storage capacity and the cycling performance of PANI doped by p-TSA and $HClO_4$ exhibit comparable and even higher results than most of the published works.

Table 4. 3 Comparison of specific capacity and cycling performance among some previously reported PANI based supercapacitors.

Material	Specific capacitance	Scan rate	Capacitance retention (cycle)	Ref.
PANI nanoparticles	115 C g^{-1}	1 mV s^{-1}	-	[201]
PANI/carbon aerogel	710.7 C g^{-1}	1 mV s^{-1}	57% (1000)	[202]
3D PANI	416 C g^{-1}	0.5 A g^{-1}	57% (2000)	[203]
Graphene/PANI	957.1 C g^{-1}	2 mV s^{-1}	90% (1000)	[204]
sulfonated graphene /PANI nanofiber	962 C g^{-1}	2 mV s^{-1}	78% (1000)	[205]
PANI/CNFs	758 C g^{-1}	1 A g^{-1}	85% (1000)	[206]
PANI-N,S-GQDs/CeO_2	189 C g^{-1}	1 A g^{-1}	75% (1000)	[207]
PANI/$HClO_4$ coated on CC	1342 C g^{-1}	5 mV s^{-1}	57% (2000)	This work
PANI/p-TSA coated on CC	722 C g^{-1}	5 mV s^{-1}	70% (2000)	This work

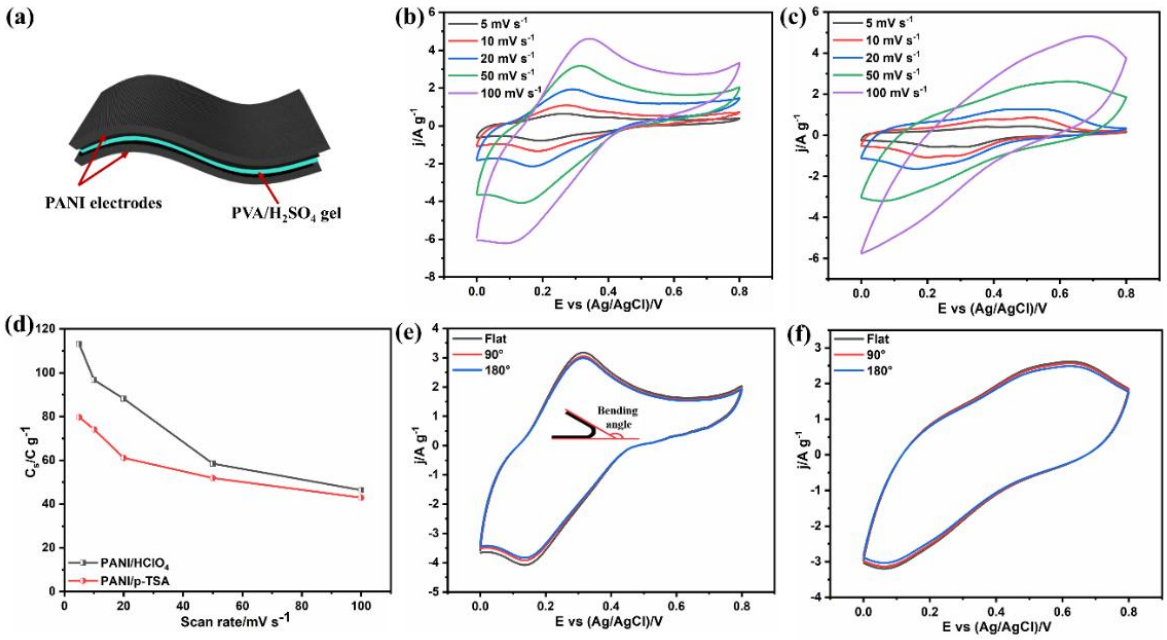

Figure 4. 10 (a) Schematic illustration of flexible PANI symmetric devices; (b) CV curves of the PANI/$HClO_4$ device; (c) CV curves of the PANI/p-TSA device; (d) Comparison of device capacity between PANI/$HClO_4$ and PANI/p-TSA at different scan rates; (e) CV curves of PANI/$HClO_4$ device (50 mV s^{-1}) at different bending states; (f) CV curves of PANI/p-TSA device (50 mV s^{-1}) at different bending angle.

To demonstrate the practical application of PANI electrodes, the solid-state symmetric supercapacitor devices were fabricated by using two same electrodes as positive and negative electrodes, and PVA/H_2SO_4 gel as solid electrolyte, as shown schematically in **Fig. 4.10a**. Considering the electrochemical performance of PANI samples tested in the three-electrode system, $HClO_4$ and p-TSA doped PANI were chosen as electrode materials for fabricating the solid-state symmetric supercapacitor devices, respectively. **Fig. 4.10 b-c** showed the CV performance of PANI/$HClO_4$ and PANI/p-TSA devices at scan rates range from 5 to 100 mV s^{-1} within operating voltage window of 0 - 0.8 V. For these two devices, the redox peaks can be clearly seen at lower scan rate (5 and10 mV s^{-1}). While at higher scan rates, the response currents increase along with shape changes due to the difference between the electrolyte

diffusion and the electrode material reaction rate. The different deformation of CV curves between PANI/$HClO_4$ and PANI/p-TSA devices is related to their doping level and electric conductivity properties. The capacities of these devices were calculated and shown in **Fig. 4.10d**. The device fabricated using PANI/$HClO_4$ shows higher capacity than PANI/p-TSA, which is consistent with the results obtained in the three-electrode system. The CV curves obtained at different bending angles were compared to evaluate the application of devices for flexible and wearable electronics devices. The overlap CV curves at different bending angles of both the devices indicate the high flexibility of PANI-based supercapacitors (**Fig. 4.10e - f**).

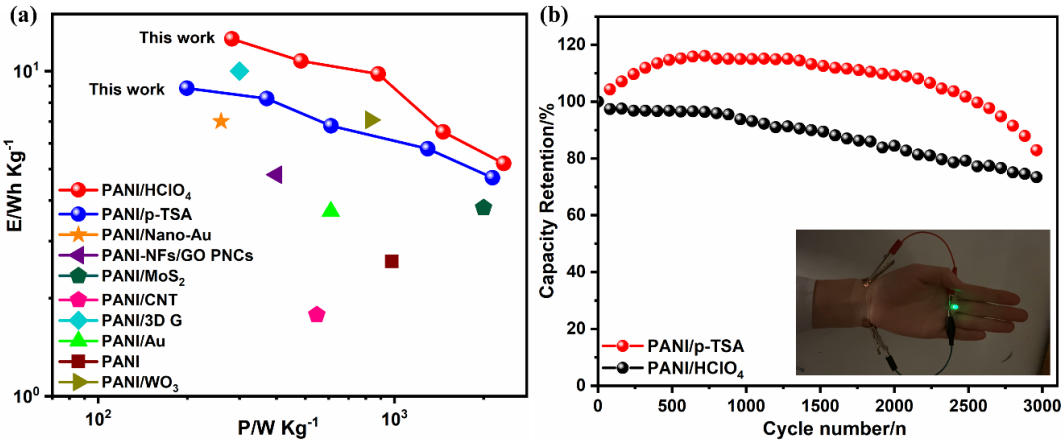

Figure 4. 11 (a) Ragone plots of the solid-state devices on the basis of the total mass of the active material, the comparison of energy and power densities of PANI-based devices: PANI/Nano-Au [208], PANI-NFs/GO PNCs [209], PANI/MoS_2 [210], PANI/CNT [211], PANI/3D G [212], PANI/Au [213], PANI [214], PANI/WO_3 [214]; (b) Cycling performance of PANI/p-TSA and PANI/$HClO_4$ devices at 0.5A g^{-1}, A picture shows a LED can be lightened by flexible PANI devices (insert).

The power density and energy density are two important parameters for the assessment of a supercapacitor device. **Fig. 4.11a** shows the Ragone plots of the devices, the device made by PANI/$HClO_4$ electrodes has higher power density and energy density than PANI/p-TSA device.

The highest energy density delivered by PANI/$HClO_4$ device is 12.57 Wh kg^{-1} at the power density of 283 W kg^{-1}. The highest energy density delivered by PANI/p-TSA is 8.86 Wh kg^{-1} at the power density of 199 W kg^{-1}. Both devices exhibit much higher power and energy densities than those of recently reported PANI-based devices. As shown in inset of **Fig. 4.11b**, this devices can be used as flexible energy sources for powering LED light. Long cycling stability was performed on both these devices by GCD at a current density of 0.5 A g^{-1}. As shown in **Fig. 4.11b**, the cycling stability result of all solid state supercapacitor devices is consistent with the result tested in three-electrode system. PANI/p-TSA shows better cycling stability than PANI/$HClO_4$. The capacity of the devices fabricated by PANI/p-TSA and PANI/$HClO_4$ can be retained over 80% and 73% of their initial capacity after 3000 cycles, respectively. The initial increase in specific capacity retantation of PANI/p-TSA device is because the PANI/p-TSA has an stacked structure as shown in SEM (**Fig. 4.1**). This stacked structure would impede the electrolyte ions into the inner part of the electrode material at beginning. With the repeated charge/discharge process, the electrolyte ions can diffused into the inner structure easier and can permeate into a more internal structure. The specific capacity of this device would increase with more and more sites can be achived by electrolyte ions then it will decrease by the structural degradation after a certain cycles. This phenomenon was not found in the three-electrode test result because the diffusion rate of solution electrolyte is much faster than solid state electrolyte and the electrode materials would more likely to fall off in solution electrolyte. The higher capacity retention of solid state devices compared to sigle electrode tested in the three-electrode systerm is also mainly because the solid electrolyte could hold the active materials well and prevent them shedding during the repeated

charging/discharging (electron insertion/extraction) process.

4.4 Conclusion

In summary, we demonstrated dopants have a great influence on the electrochemical performance of PANI. Thus, the electrochemical behavior of PANI can be enhanced by selecting a suitable dopant during the synthesis process. Six kinds of commonly used dopants were studied here. Different dopants generated different morphology, doping level, redox sites accessibility and electrochemical performance for PANI. Among them, $HClO_4$ doped PANI has the best energy storage property with a specific capacity of 1341 C g^{-1} at 5 mV s^{-1} along with a 57% capacity retention rate after 2000 cycling test. P-TSA doped PANI shows the best cycling stability with 70% of capacity retention after 2000 cycles, also with a relatively high specific capacity (722 F g^{-1} at 5 mV s^{-1}). Then, PANI/$HClO_4$ and PANI/p-TSA were used to fabricate flexible all-solid-state symmetric supercapacitors. Both obtained devices have excellent flexibility. PANI/$HClO_4$ device delivers the maximum energy density of 12.57 Wh kg^{-1} at the power density of 283 W kg^{-1} and good cycling stability with capacity retention of 73% after 3000 cycles. PANI/p-TSA device has the best cycling stability with a capacity retention over 80% after 3000 cycles and relative high energy density of 8.86 Wh kg^{-1} at the power density of 199 W kg^{-1}. The strategical design synthesis of PANI provides a much easier route in achieving high performance flexible PANI-based electrode materials and makes PANI as promising candidates for wearable electronics.

Chapter 5

Facile electrodeposition of Mn-CoP nanosheets on Ni foam as high-rate and ultra-stable electrode for supercapacitors

Abstract: As the combined merits of structures and compositions could generate a great effect on the electrochemical performance of electrode materials, we synthesized manganese doped cobalt phosphide nanosheets supported on Ni foam (Mn-CoP/NF) by a simple and effective electrodeposition method. The synergistic effect between Mn and Co ions provides mixed valence states and adjust the bandgap for accelerating the high redox reaction kinetics and improving the electron mobility and electrical conductivity. Meanwhile, the nanosheets structure provides rich electroactive sites and excellent structural stability for facilitating the electron transfer and resisting structural damage. As expected, the obtained Mn-CoP/NF electrode shows a high specific capacitance (716 F g^{-1} at 0.5 A g^{-1}), high-rate performance (77.4 % capacitance retention with the current density increases from 1 to 10 A g^{-1}) and an ultra-stable cycling stability (capacitance retention of 89.0 % after 20,000 cycles). Moreover, the fabricated Mn-CoP/NF//AC asymmetric supercapacitor (ASC) delivers a high energy density of 19.13 Wh kg^{-1} at a power density of 400 W kg^{-1} with a super cycling stability (capacitance retention of 87.7 % after 20,000 cycles). Furthermore, two ASC devices can be used to light a LED for 6 mins demonstrating its promising practical applications.

5.1 Introduction

Supercapacitors (SCs) have been identified as one kind of the most promising energy storage candidate due to their rapid charge-discharge rates, high power density, and long cycle life [200, 215-216]. These advantages make them propitious to bridge the energy/power gaps between batteries and dielectric capacitors. However, the intrinsically lower energy density of SCs becomes a major challenge, which impedes their practical applications [58]. According to the energy density computational equation: $E=0.5\ CV^2$, the energy density (E) of SCs is mainly determined by the specific capacitance (C) and the operating voltage window (V) [217]. Thus, two effective ways are commonly used to enhance the energy density of SCs: (i) improving the specific capacitance by designing electrode materials with high redox activities. (ii) expanding the operating voltage by fabricating asymmetrical supercapacitor (ASC) with two electrodes worked in different voltage windows. Many efforts have been made to improve the specific capacitance of electrode materials, and a variety of novel materials have been developed in recent years [218-221]. Among them, transition metal compounds with the advantages of high theoretical capacity, rich redox activity abundant natural resources and environmental friendliness have been extensively explored as promising electrode materials [222]. Transition metal compounds store electrical energy mainly by reversible faradaic reactions, and their electrochemical properties can be optimized by tuning their redox active reaction centers and band gaps. Previous research works have demonstrated that transition metal compounds like transition metal oxides and hydroxides can enhance the specific capacitance and energy capacity compared to some traditional electrode materials. This is because transition metal compounds have high theoretical capacity, rich redox activity [223]. However, metal oxides and

hydroxides normally have poor electrical conductivity that affects the charge transport process and restrict the rate performance.

Recently, transition metal phosphides (TMPs) have been considered as promising electrode materials for SCs due to their superior redox activity, high conductivity, thermal stability, metalloid properties and eco-friendly. For example, Zhou's group has proved the enhanced supercapacitor performance of TMPs (e.g., Ni_2P, Co_2P) than their transition metal oxides and hydroxides (e.g., NiO, $Ni(OH)_2$ and Co(OH)) [56]. Therefore, many TMPs have been developed as electrodes for SCs including nickel phosphides [224], cobalt phosphides [225], copper phosphide [226], molybdenum phosphide [227], and iron phosphide [228]. Particularly, cobalt phosphides with superior electric conductivity and metalloid properties have attracted great attention for a range of energy storage applications [229]. For examples, Hu et al. synthesized highly conductive CoP by solid-state synthetic routes. The obtained CoP shows excellent electrochemical performance with a high specific capacitance of 447.5 F g^{-1} at 1 A g^{-1} [230]. While the cobalt phosphides as one kind of solitary TMPs electrodes are still facing the challenge due to rapid oxidation of phosphorus, irreversibility of the faradic reaction and poor structural stability resulting in their poor rate capability and cycling stability [58, 231]. Introducing hetero-metal ions has been considered as an very effective way to ameliorate the above-mentioned problems [232]. For instance, Jin et al. reported the NiCoP microflowers synthesized by a simple low-temperature phosphorization process, which exhibited higher electrochemical performance than monometallic phosphides of CoxP microflowers [57]. More recently, Lei et al. prepared multicomponent transition-metal phosphides of ZnNiCoP on Ni foam. This metal-rich

phosphide achieved a high specific capacity of 1111 C g^{-1} at 10 A g^{-1} [58].These improved electrochemical performance can be attributed to: (i) the introduced hetero-metal ions help promote high redox reaction kinetics; (ii) the introduced hetero-metal ions can adjust the bandgap which is helpful for improving the electron mobility and electrical conductivity; (iii) the formed multicomponent metal materials might have mixed valence states at the multi-metal centers and the synergistic combination of different metals could contribute to the enhancement of electrochemical performance [231]. Thus, choosing proper hetero-metal elements is important for improving the electrochemical performance of cobalt phosphides electrodes. Encouraged by recent studies, manganese (Mn) could be considered as a viable candidate due to its high theoretical capacitance, rich oxidation states (ranging from +2 to +7), naturally abundant, high electrical conductivity, low cost and environmentally friendly properties [59].

Hydrothermal method is the most commonly used way to prepare TMPs electrodes. However, the hydrothermal synthesis processes usually involve two or more steps, which are completed, time-consuming and energy-intensive [233]. Therefore, it is better to explore a simple and effective method for the synthesis of TMPs based electrodes. Currently, electrochemical deposition has been reported as a competitive technique for the facial preparation of TMPs. For instance, Song et al. reported the synthesis of $NiCo_xP_y$ nanosheets on substrate of carbon cloth by a one-step electrodeposition in 5 minutes [234]. Compared with the traditionally synthetic methods, electrodeposition method can provide an easier, faster and more cost-effective way under a more moderate condition.

On account of the above considerations, we synthesized manganese doped cobalt phosphide

nanosheets on Ni foam (Mn-CoP/NF) via a simple and effective electrodeposition method. The electrodeposition method allows in-situ deposition of Mn-CoP on NF and realizes the preparation of Mn-CoP/NF binder-free electrode. Omitting the use of polymer binders and carbon additives could be helpful to have better conductivity, expose more active sites and provide a strong structure. Moreover, the combination of the synergistic effect between Mn and Co ions and the interconnected nanosheets structure are all conducive to the capacitance behavior and cycle stability of electrode. Therefore, the prepared Mn-CoP/NF electrode achieves a high specific capacity of 716 F g^{-1} at 0.5 A g^{-1} with stable cycling stability of 89.0 % after 20,000 cycles. Upon its use as an anode for asymmetric supercapacitor (ASC), an excellent energy density (19.13 Wh kg^{-1} at a power density of 400 W kg^{-1}) and superior cycling stability (87.7 % capacity retention after 20,000 cycles) can also be achieved.

5.2 Experimental

5.2.1 Synthesis procedure

Initially, a few pieces of nickel foams (2 cm × 1 cm) were ultrasonically cleaned with 3.0 M HCl, ethanol and DI water in turn to remove surface impurities. The Mn-CoP were grown on Ni foam via a facial electrodeposition method. The electrodeposition process was conducted in a three-electrode configuration with Ni foam as working electrode, Hg/HgO as reference electrode and a platinum mesh as counter electrode. The electrolyte solution for the electrodeposition process was prepared by mixing 10 mM $Mn(NO_3)_2 \cdot 4H_2O$, 20 mM $Co(NO_3)_2 \cdot 6H_2O$, 30 mM urea and 0.5 M $NaH_2PO_2 \cdot H_2O$. A constant potential of -1.5V was implemented to the three-electrode system to “grow” the Mn-CoP anchored NF. In order to

investigate the potential effect, different potentials (-1.3 V, -1.5 V and -1.7 V) were used during the electrodeposition process. The Mn-CoP/NF obtained at -1.3V, and -1.7V were referred to Mn-CoP/NF-1.3 and Mn-CoP/NF-1.7, respectively. The MnP/NF and CoP/NF were prepared at a constant potential of -1.5 V with the similar process but without adding $Co(NO_3)_2 \cdot 6H_2O$ or $Mn(NO_3)_2 \cdot 4H_2O$ in the electrolyte solution, respectively.

5.2.2 Materials characterization

The field emission scanning electron microscope (FE-SEM, Thermo Scientific Apreo) and transmission electron microscope (TEM, FEI Tecnai F20) were used to characterize the morphologies, sizes and atomic-level structures of the fabricated electrodes. Both electron microscopes were equipped with a dispersive X-ray spectrometer (EDX, EDAX Inc.) for chemical composition analysis. A powder X-ray diffractometer (XRD) (Philips X'Pert MPD) with Cu Kα radiation (λ = 1.5405 Å) was used to study the crystal phases of the as-prepared samples. The X-ray photoelectron spectroscopy (XPS) conducted on a Kratos Axis Ultra DLD spectrometer with Al Kα X-ray source was utilized to determine the elemental compositions and chemical valence states on the surface of the prepared electrodes. The binding energy scale was calibrated with respect to the C 1s peak at 284.8 eV.

5.2.3 Electrochemical measurements

All electrochemical measurements were performed on a CHI 760D electrochemical analyzer at room temperature. The electrochemical performance of the prepared electrodes was firstly tested in three-electrode cell with Hg/HgO and platinum mesh as reference electrode and counter electrode, respectively. 3.0 M KOH was used as aqueous electrolyte during the test.

The Cyclic voltammetry (CV) tests were carried out within the potential window between 0 V to + 0.6 V at virous scanning rates range from 5 to 100 mV s^{-1}. The Galvanostatic charge/discharge (GCD) measurements were conducted in the potential range of 0 to + 0.5 V with different current densities range from to 0.5 to 10 A g^{-1}. The electrochemical impedance spectroscopy (EIS) measurements were recorded at a sinusoidal perturbation of 5 mV in the frequency range of 100 kHz and 0.01 Hz with an open-circuit potential.

The specific capacity (C_s, F g^{-1}) of electrodes can be obtained by GCD results according to the following equation:

$$C_s = \frac{I\Delta t}{m\Delta V}$$

Where, I (A), Δt (s), m (g) and ΔV (V) refer to the response current, discharge time, active material weight and working voltage window, respectively.

Prior to the fabrication of the ASC, the mass ratio of the positive (Mn-CoP/NF) and negative (AC) electrodes were determined by to the following equation:

$$\frac{m_+}{m_-} = \frac{C_-\Delta V_-}{C_+\Delta V_+}$$

where, m, C and ΔV are the loading mass (g), specific capacitance and working voltage range of the electrodes. + and – are used to mark the positive electrode and negative electrode, respectively.

For the two-electrode ASC cell, CV and GCD results were recorded in the potential window of

0 - 1.6 V. The specific capacitance (C_{cell}), energy density (E, Wh kg^{-1}) and power density (P, W kg^{-1}) of the two-electrode ASC were calculated through following equations:

$$C_{cell} = \frac{I'\Delta t'}{m'\Delta V'}$$

$$E = \frac{C_{cell} \times (\Delta V')^2}{2 \times 3.6}$$

$$P = \frac{3600 \times E}{\Delta t'}$$

Where, I', m', Δt' and ΔV' are the response current, active material weight, discharge time and working voltage window of the ASC, respectively.

5.3 Results and discussions

5.3.1 Fabrication and structural investigation

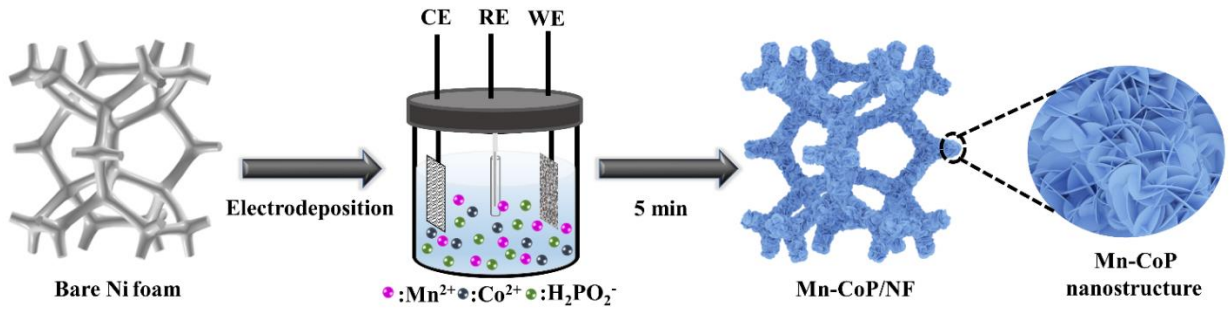

Scheme 5.1. Schematic illustration of the synthesis process of Mn-CoP/NF.

The Mn-CoP/NF was synthesized by a facile, one-step electrodeposition method with $Co(NO_3)_2 \cdot 6H_2O$, $Mn(NO_3)_2 \cdot 4H_2O$ and $NaH_2PO_2 \cdot H_2O$ as precursors. The synthesis process is graphically illustrated in **Scheme 5.1**. The porous Ni foam with high electrical conductivity

and large surface area was selected as substrate. The deposition process contains three procedures. Firstly, the Co/Mn cations went through the diffusion layer leading to the loosen of the salvation sheath. Secondly, electrons were transferred and collected on Ni foam. Finally, the cations incorporation occurred at more energetically stable sites [59]. Apparently, during the electrodeposition process, the applied potential acted as a driving force to propel the Co^{2+} and Mn^{2+} cations transfer to the Ni foam. The nanosheets structure could be formed in a certain time with the directional migration of these ions [235]. A large amount of nanosheets interspersed with each other and tightly attached on the surface of the Ni foam. To confirm the growth of Mn-CoP on Ni foam, different characterizations have been conducted.

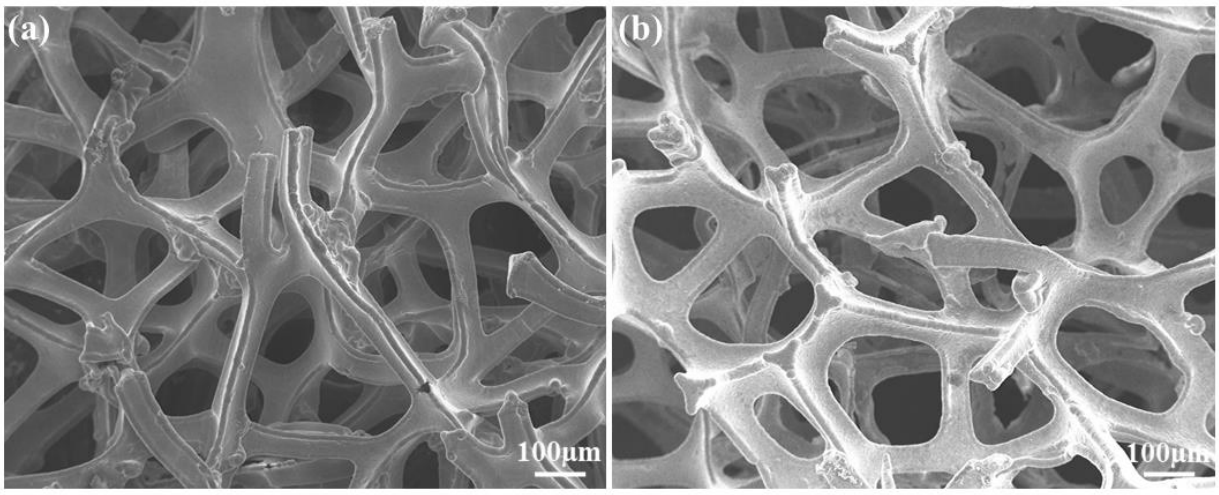

Figure 5. 1 SEM images of Ni foam and Mn-CoP/NF.

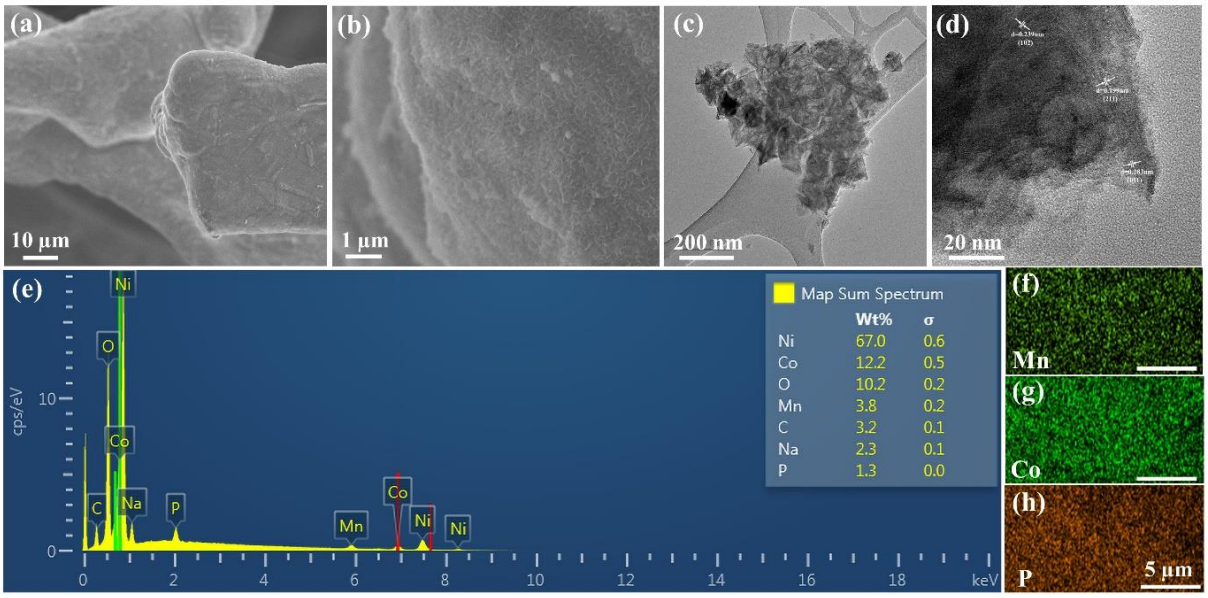

Figure 5. 2 (a-b) SEM images of Mn-CoP/NF at different magnifications; (c) TEM and (d) HRTEM images of Mn-CoP; (e) EDX spectrum of Mn-CoP/NF; (f-h) EDX elemental mapping of Mn, Co and P, the scale bar is 5µm.

The surface comparison between the pure Ni foam and Mn-CoP/NF (**Fig. 5.1)** demonstrates the Ni foam can be uniformly and tightly covered by the Mn-CoP layer. **Fig. 5.2 (a-b)** exhibits the magnified SEM image of Mn-CoP/NF. It is evident that the Mn-CoP film are uniformly and firmly covered on the surface of Ni foam (**Fig. 5.2a**). From **Fig. 5.2b** and TEM image of Mn-CoP (**Fig. 5.2c**, Mn-CoP was peeled off from Ni foam substrate by ultrasonication) the Mn-CoP exhibits a 2D petal piece-like nanosheets morphology and these Mn-CoP nanosheets have nano-scale size and smooth surface. The Mn-CoP nanosheets are interlinked with adjacent nanosheets and vertically anchored on the surface of Ni foam. These interconnected nanosheets not only provide abundant accessible surface for the ion diffusion in electrolyte but also provide the well connection for the high-efficiency electronic transmission. Moreover, rich void space exists among the interlinked nanosheets structure which could play a good buffering effect to resist the structural damage by alleviating the volume changes of the electrode during the

repeated electrochemical reactions. On account of above discussion, it is inferred that this nanosheets structure could provide excellent capacitance behavior and cycle stability simultaneously. The HRTEM image of the Mn-CoP nanosheets was shown in **Fig. 5.2d**. The lattice fringe spacings of 0.199, 0.238 and 0.283 nm corresponding to the (211), (102), and (011) lattice planes of the CoP. EDX analysis was used to investigate the elemental composition and distribution of Mn-CoP/NF electrode. As shown in **Fig. 5.2e**, the high Ni content comes from Ni foam substrate. The detected Co, Mn, P elements combined with the HRTEM results indicating the successfully synthesize of Mn-CoP. In addition, the homogeneous distribution of Mn, Co and P elements can be validated by the EDX mapping of **Fig. 5.2 f-h**.

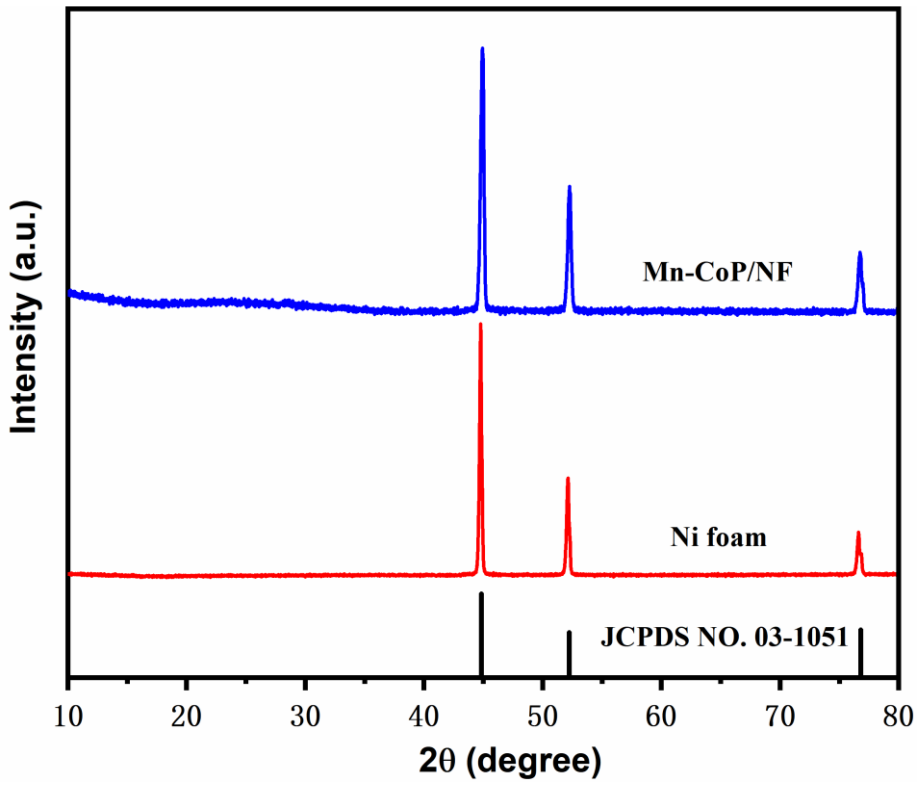

Figure 5. 3 XRD patterns of Mn-CoP/NF and Ni foam.

XRD test was applied to further analyze the phase structure of as-prepared material. As depicted in **Fig. 5.3**, the XRD spectrum of Mn-CoP/NF shows three strong diffraction peaks at 44.8°, 52.2° and 76.8°, which also present in the Ni foam spectrum. These three peaks can be identified as the (111), (200) and (220) planes of metallic nickel (PDF#03-1051, Cubic), respectively. No apparent crystalline phases corresponding to the MnCoP or CoP can be observed, which is possibly due to the low thickness of the Mn-CoP film on Ni foam[236-237].

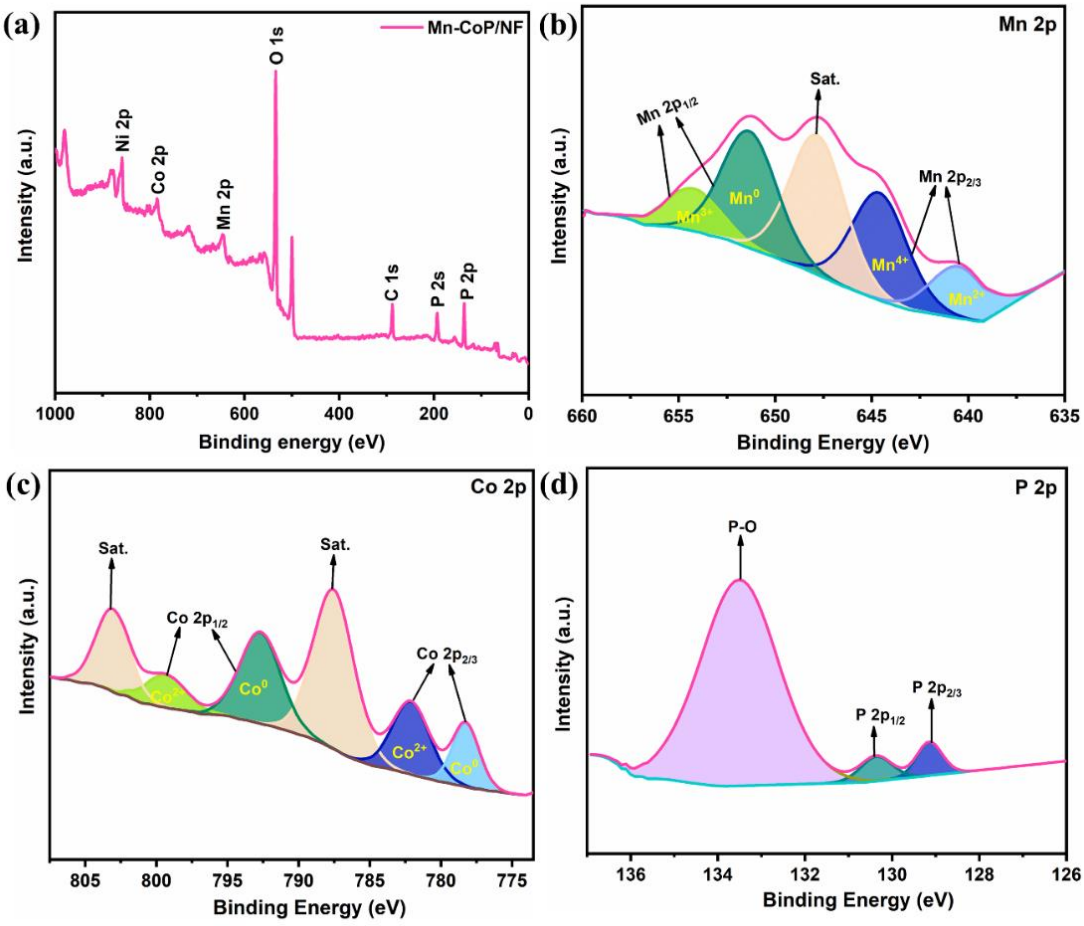

Figure 5. 4 (a) XPS survey spectrum of Mn-CoP/NF, (b-d) high-resolution XPS spectra of: Mn 2p, Co 2p and P 2p.

X-ray photoelectron spectroscopy (XPS) was performed to further investigate the chemical

composition and the superficial chemical state of Mn-CoP/NF. The elements of Mn, Co, P, Ni, C and O can be clearly observed from the XPS survey spectrum (**Fig. 5.4a**), which is in accordance with the EDX spectrum results. The C element signal presented in this pattern arises from the superficial contamination while the O element signal presumably due to the surface oxidation of the sample in the air, which is commonly reported in the literatures [236]. **Fig. 5.4b** shows the high-resolution Mn 2p spectrum. The Mn $2p_{3/2}$ core level region contains two predominant peaks located at 640.2 and 644.5 eV, which are assigned to Mn^{2+} and Mn^{4+}, respectively [238-239]. The peak appeared at 647.7 eV is indexed to the satellite peak (indicated as "sat.") [240]. Another two peaks located at 651.2 and 654.1 eV are assigned to Mn^0 and Mn^{3+} of Mn $2p_{1/2}$ spectrum, respectively [241]. As shown in **Fig. 5.4c**, the ranges of 778.0 - 788.0 eV and 793.0 - 805.0 eV in high-resolution Co 2p spectrum might be assigned to Co $2p_{3/2}$ and Co $2p_{1/2}$, respectively [239]. In the Co $2p_{3/2}$ region, three peaks assigned to Co^0, Co^{2+} and a sat. can be observed at 778.2 eV, 782.1 eV and 787.5 eV, respectively [242-243]. In the Co $2p_{1/2}$ region, other three peaks ascribed to Co^0, Co^{2+} and a sat. appear at 792.7 eV, 799.3 eV and 803.1 eV, respectively [243-245]. In the P 2p spectrum (**Fig. 5.4d**), the two peaks at 129.1 and 130.3 eV are attributed to P $2p_{3/2}$ and P $2p_{1/2}$, respectively, which are assigned to reduced phosphorus in the form of metal phosphides [239, 246]. In addition, the broader peak at 134.0 eV is assigned to the oxidized P species [244]. The peaks at 778.2 and 129.1 eV for Co and P are consistent with the binding energy (BE) of the Co-P bond in CoP [239, 247]. The P $2p_{1/2}$ located at 130.3 eV is slightly negatively shifted compared to the BE of P $2p_{1/2}$ (130.4) eV in CoP, which might be ascribed to Mn doping [248]. Therefore, the XPS results further indicated the successful formation of Mn-CoP on NF.

5.3.2 Electrochemical performance

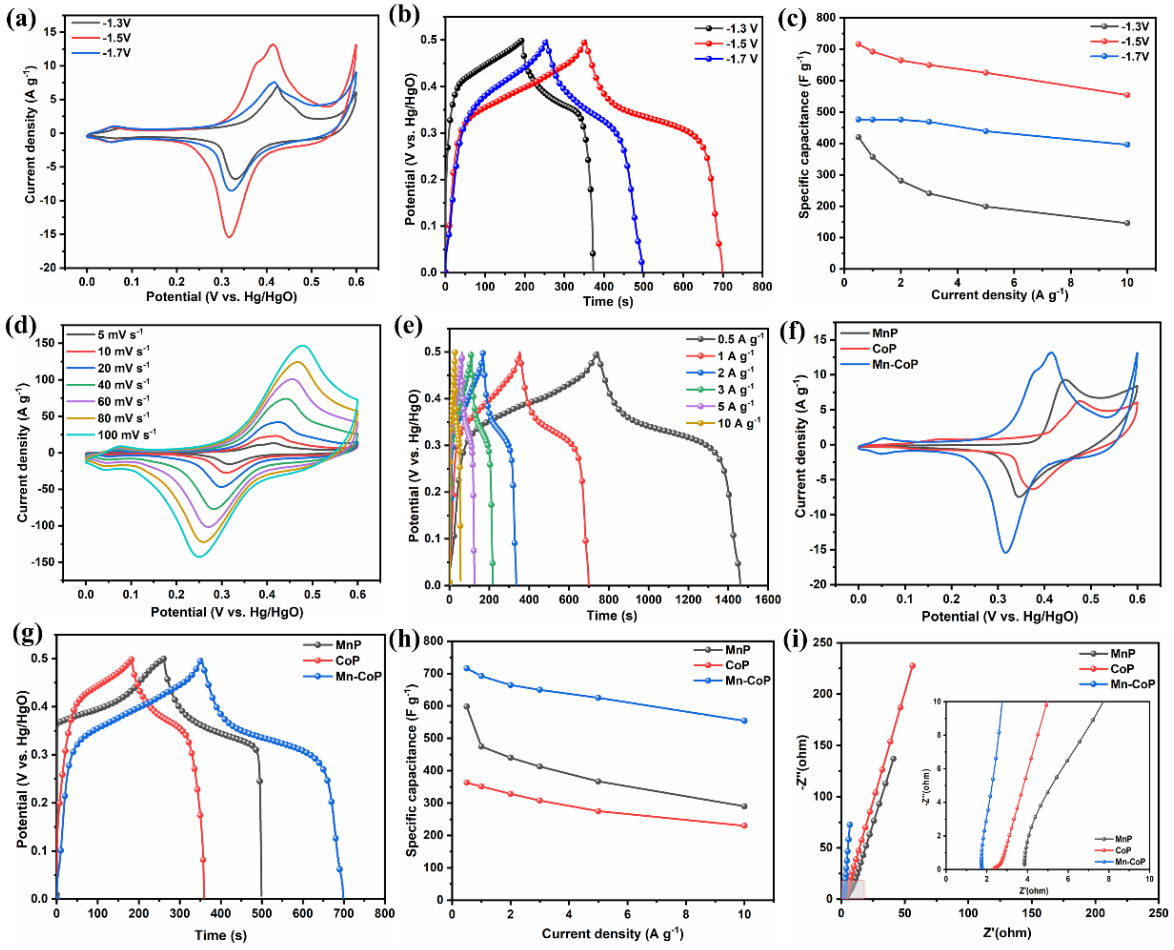

Figure 5. 5 (a-c) CV curves at 5 mV s^{-1}, GCD curves at 1 A g^{-1}, and e C_s at different current density of Mn-CoP/NF-1.3, Mn-CoP/NF and Mn-CoP/NF-1.7. (d) CV curves of Mn-CoP/NF at different scan rates. (e) GCD curves of Mn-CoP/NF at different current densities. (f-i) CV curves at 5 mV s^{-1}, GCD curves at 1 A g^{-1}, C_s at different current density, and Nyquist plots of MnP/NF, CoP/NF and Mn-CoP/NF.

The electrochemical performance of prepared electrodes was investigated via a typical three-electrode system with 3.0 M KOH as electrolyte. Firstly, we studied the influence of deposition voltages on the electrochemical performance of the electrodes. **Fig. 5.5a** compared the CV curves of electrodes prepared at different electrodeposition voltages. Obviously, at the same scan rate, the three electrodes have different current responses. As the enclosed areas of CV

curves are proportional to their capacitances, the Mn-CoP/NF exhibits the best capacitance performance revealing the optimal deposition voltage is -1.5V [247]. In **Fig. 5.5b**, the electrode prepared at -1.5V shows the longest charge/discharge time, which is consistent with CV result. The calculated specific capacitances at different current densities (**Fig. 5.5c**) further confirmed the optimal deposition voltage of -1.5V. Thus, in the follow study, the deposition voltage was fixed at -1.5V. **Fig. 5.5d** shows the CV curves of Mn-CoP/NF electrode at various scan rates from 5 mV s^{-1} to 100 mV s^{-1}. All the CV curves have similar shapes revealing the high reversable redox reactions and high-rate capability of the electrode. As the scan rates increase, the response current becomes more significant and the oxidation/deoxidization peaks shift to a higher/lower potential positions, which are due to the fast interfacial rate kinetics and the internal resistance of the electrode [249-250]. The obvious redox peaks observed in CV curves indicating the pseudocapacitive behavior of the Mn-CoP/NF electrode [232]. The redox reactions are mainly relevant to the reaction between the OH anions in the alkaline electrolyte and the transition metal ions from the fabricated phosphide materials. More specifically, these redox reactions come from the redox transitions of Co^{2+}/Co^{3+}, Co^{3+}/Co^{4+} [59]. The involved redox reactions could be expressed by the following equations:

$$Co^{\delta+} + 2OH^- \rightarrow Co(OH)_2 + (2-\delta)e^-$$

$$Co(OH)_2 + OH^- \rightleftarrows CoOH + H_2O + e^-$$

$$CoOOH + OH^- = CoO_2 + H_2O + e^-$$

While different from cobalt which adopt faradaic battery-type behavior, manganese stores

energy through the intrinsic pseudocapacitive-type mechanism with the redox transitions of Mn^{2+}/Mn^{3+} and Mn^{3+}/Mn^{4+} [59, 251]. In order to further evaluate the electrochemical performance of Mn-CoP/NF electrode, the GCD curves at different current densities from 0.5 A g^{-1} to 10 A g^{-1} were collected in **Fig. 5.5e**. The clear plateaus can be observed on the GCD curves, which is due to the pseudocapacitive behavior of the electrode [231]. The good symmetrical shape of all GCD curves indicates the excellent reversible redox capacities of the electrode [247]. The charge/discharge time decreases with the enhancement of current density revealing the specific capacitance decreases with the increase of current density (**Fig. 5.5c**). From **Fig. 5.5c**, the maximum specific capacitance of Mn-CoP/NF electrode achieves 716 F g^{-1} at the current density of 0.5A g^{-1}. With the scan rate increases to 1, 2, 3, 5, 8, 10 A g^{-1}, the specific capacitance of Mn-Co-P/NF electrode decreases to 692, 664, 650, 625 and 554 F g^{-1}, respectively. The specific capacitance retention of Mn-CoP/NF electrode can maintain over 77.37% of the initial specific capacitance with the current density increasing from 1 to 10 A g^{-1} which demonstrates an excellent rate capability of the electrode [252].

The electrochemical performance comparison between MnP/NF, CoP/NF and Mn-CoP/NF electrodes was also studied under the same testing conditions. **Fig. 5.5f** compared the CV curves of MnP/NF, CoP/NF and Mn-CoP/NF electrodes at a scan rate of 5 mV s^{-1}. The obvious redox peaks associated with the redox reactions between the OH anions and metal ions can be observed on each CV curve, revealing the pseudocapacitance characteristic of three electrodes. Among the three electrodes, the CV curve of Mn-CoP/NF electrode has the largest enclosed area, indicating its best capacitance property. **Fig. 5.5g** compared the GCD curves of MnP/NF,

CoP/NF and Mn-CoP/NF electrodes at the current density of 1 A g^{-1}. All of the GCD curves show obvious plateaus indicating the pseudocapacitance features of the electrodes. The Mn-CoP/NF electrode has longer charge/discharge time than other two electrodes, which further indicated its best specific capacitance. **Fig. 5.5h** compared the calculated specific capacitance of MnP/NF, CoP/NF and Mn-CoP/NF electrodes at different current densities. Obviously, the capacitance of Mn-CoP/NF electrode is higher than those of MnP/NF and CoP/NF electrodes. This result demonstrates that the introduction of hetero-metal ions can effectively enhance the electrochemical performance of the single component metal phosphides of MnP/NF and CoP/NF.

EIS measurements were carried out to further testify the performance of the Mn-CoP/NF electrode. **Fig. 5.5i** shows the EIS curves of the MnP/NF, CoP/NF and Mn-CoP/NF electrodes (the illustration gives the magnified image of the high-frequency region). The EIS curves are consisted of discrete semicircles in the high frequency region and nearly vertical lines in the low-frequency region [231]. The intersections of the high frequency region with the X-axis presents the equivalent series resistance (R_s) which composed by several different resistances, including ionic resistance of the electrolyte, the inherent resistance of the electrode active material and the interface resistance of electrode active material and substrate [247, 253]. The diameters of semicircles reflect the charge transfer resistance (R_{ct}) and it can be used to analyze the charge transfer kinetics [59]. The slopes of the straight lines represent the ion diffusion resistance (R_w) revealing the diffusion and transport kinetics of electrolyte ions in the electrodes [222]. From the magnified illustration, no obvious semi-circles can be detected in the

high frequency regions, suggesting all the electrodes have very low charge transfer resistance. In addition, it can be observed that the Mn-CoP/NF electrode exhibits lower R_{ct} than the other two electrodes, which means the Mn-CoP/NF has better electronic conductivity than the MnP/NF and CoP/NF electrodes. The improved electronic conductivity of Mn-CoP/NF is mainly attributed to the introduction of Mn. The introduced hetero-metal ions make the composite have two different kinds of energy band structures and abundant heterointerfaces, both of which are helpful for the formation of a built-in electric field at the hetero interfaces, resulting in the improvement of electron mobility and electrical conductivity [222, 231]. Additionally, the Mn-CoP/NF electrode has lower R_s value than those of the MnP/NF and CoP/NF electrodes. This is because the better electronic conductivity of Mn-CoP/NF is helpful for the reduction of its R_s. Moreover, the unique structure of Mn-CoP/NF could provide abundant open channels and interconnected nanosheets surfaces which are helpful for electrolyte contact and diffusion. In addition, the slope of Mn-CoP/NF in the low-frequency region is larger than those of MnP/NF and CoP/NF, revealing its lower R_w. This phenomenon might be due to the existing of rich open channels and the high activity of the metal phosphides [252]. Thus, the Mn-CoP/NF electrode exhibited favorable reaction kinetics, enhanced conductivity, lower diffusion resistance and improved electrochemical performance than the single component metal phosphides of MnP/NF and CoP/NF. All of these discussions correspond well with the CV and GCD results.

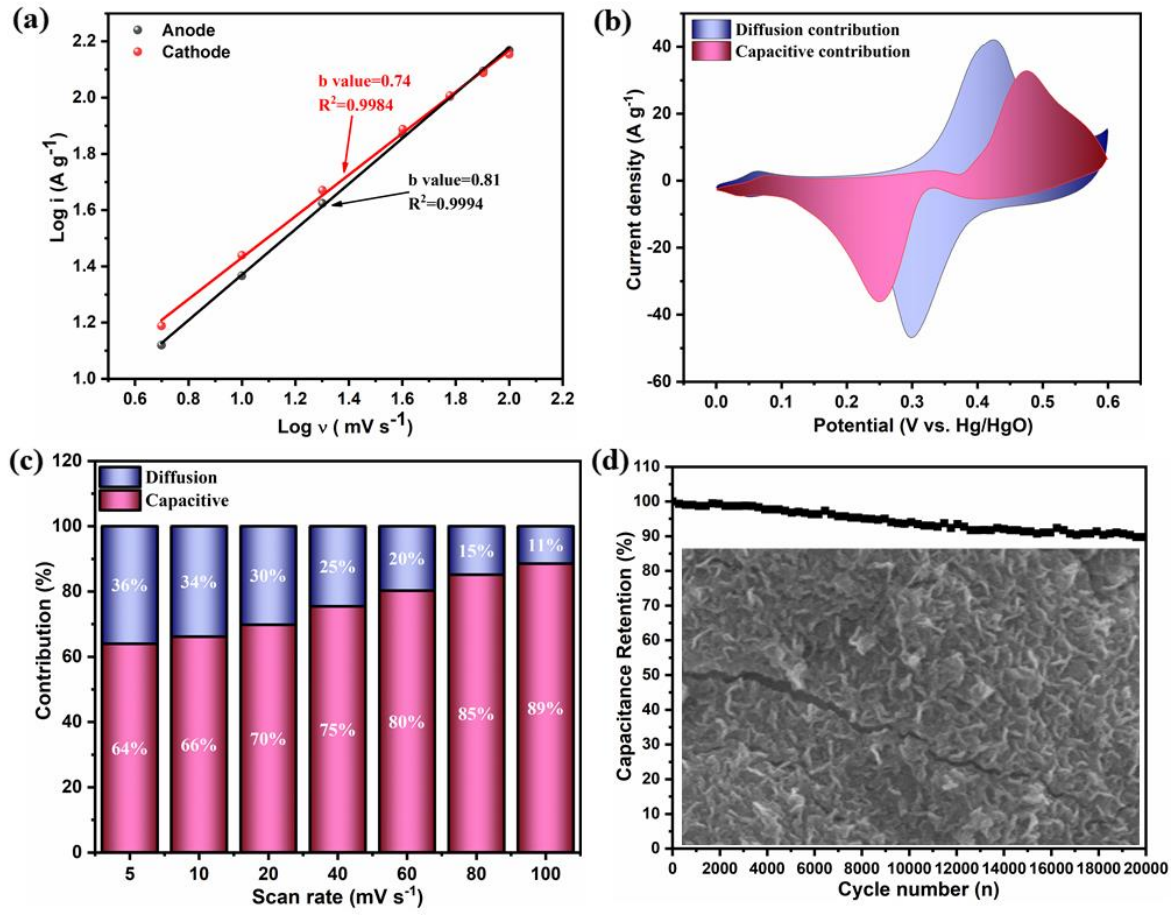

Figure 5. 6 (a) Relationship of log (peak current) versus log (sweep rate) to determine b values. (b) CV plots showing capacitive contribution and diffusion contribution at 20 mV s^{-1}. (c) A bar graph showing contribution ratio of capacitive-controlled and diffusion-controlled capacitance at different scan rates. (d) Long-term cycling stability test of Mn-CoP/NF at 10 A g^{-1}, inset is the SEM image after cycling test.

To better understand the charge storage mechanism of Mn-CoP/NF, the kinetics were analyzed according to the CV measurements (**Fig. 5.5d**). In general, the peak currents (i) and the scan rates (υ) of the CV curves obey a power-law relationship which can be expressed as the following equation [254-255]:

$$i = a\upsilon^b$$

Where i and υ correspond to the peak current and the relevant scan rate, respectively. a and b

are constants. The b-value can be calculated from the slop of the linear relationship between log (*i*) and log (υ). Typically, b = 1 reveals a surface capacitive contribution dominant process, b = 0.5 indicates a typical diffusion-dominated course [256]. As shown in **Fig. 5.6a**, the b value of the Mn-Co-P/NF electrode for anodic and cathodic peaks were calculated to be 0.81 and 0.74, respectively. The calculated b values are between 0.5 and 1.0 indicating the existence of both diffusion-controlled and capacitive-controlled processes with a high ratio of the capacitive contribution processes in the system [257-258].

The ratios of diffusion-controlled and capacitive-controlled capacitive contribution could be quantitatively studied according to Dunn's method. In this method, the current of a CV curve at a given voltage (*i*(V)) can be expressed as:

$$i(\mathrm{V}) = k_1\upsilon + k_2\upsilon^{1/2}$$

This formula can be modified as:

$$i(V)/\upsilon^{1/2} = k_1\upsilon^{1/2} + k_2$$

where k_1 and k_2 are constants that can be determined by the slope and the intercept value of $i(\mathrm{V})/\upsilon^{1/2}$ versus $\upsilon^{1/2}$ plot, respectively. $k_1\upsilon$ represents the capacitive current and $k_2\upsilon^{1/2}$ corresponds to diffusion-controlled current. Thus, with the calculated k_1 value, the capacitive current $i_c(\mathrm{V}) = k_1\upsilon$ can be separated from the total measured current. **Fig. 5.6b** shows comparison of the capacitive contribution (70%) and diffusion contribution (30%) of the Mn-CoP/NF electrode at a scan rate of 20 mV s^{-1}. Similarly, the percentage of capacitive

contribution and diffusion contribution at different scan rates were calculated and summarized in **Fig. 5.6c**. It can be observed that the capacitive contribution was 64% at 5 mV s^{-1} and increased to 89% with the scan rate increases to 100 mV s^{-1}. The enhanced capacitive contribution can be attributed to the shorter ion diffusion length, improved electrical conductivity and rapid electron transfer that provided by the unique structure and the introduced Mn of Mn-CoP/NF [254, 259-260]. Additionally, the high ratios of capacitive contribution at high scan rates further confirms the superior rate performance of Mn-CoP/NF[222].

The cycling stability of Mn-CoP/NF was tested in a three-electrode system at 10 A g^{-1} (**Fig. 5.6d**). The slight decrease of specific capacitance can be observed during the cycling test. The decreased capacity should be due to the volume shrinkage and expansion caused by the repeated redox reactions during the continuous charge and discharge process [261]. Moreover, the increased inner resistance of the testing system resulted from long cycles also lead to the decline of the capacity retention [262]. After 20,000 cycles, the capacity retention can maintain 89.0 % of initial specific capacitance, revealing the excellent cycling stability of the electrode. From the SEM image in the illustration, the structure of Mn-CoP/NF electrode can be well-maintained even after 20,000 cycles, demonstrating its high structure stability. The superior cycling performance of Mn-CoP/NF electrode should be related to its nanosheets structure which has high mechanical stability and strong adhesion on Ni foam substrate. The Mn-CoP/NF nanosheets electrode has rich void space between the interconnected nanosheets that could buffer and balance the volume changes during the cycling process. Based on above

discussion, both the specific capacitance and the cycling performance of Mn-CoP/NF are comparable to or even better than some other reported metal phosphide electrodes (**Table 5.1)**.

Table 5. 1 Specific capacity and cycling performance comparison of Mn-CoP/NF to other reported works.

Material	Structure	Specific capacitance	Retention (cycle)	Ref.
NiCoP/CNF	Nanoparticles	333 F g^{-1} at 2 A g^{-1}	80% (6000)	[263]
CoP	Nanoparticles	286 F g^{-1} at 0.5 A g^{-1}	98.5 % (5000)	[182]
Co-doped $Ni_{11}(HPO_3)_8(OH)_6$	Bouquet-like	751.5 F g^{-1} at 0.5 A g^{-1}	94% (5000)	[221]
CoP/Graphene hydrogel	Nanoparticles	335 F g^{-1} at 5 mV s^{-1}	94.1% (10,000)	[264]
NiP	Nanoporous sphericals	265 F g^{-1} at 20 mV s^{-1}	97 % (1000)	[265]
NiFeP@$NiCo_2S_4$/CC	Nanosheets arrays	874.4 C g^{-1} at 1 A g^{-1}	85.6%(5000)	[222]

CoP	Microcubes	560 F g^{-1} at 1 A g^{-1}	91.2% (10,000)	[229]
FeP	Nanotube arrays	191.2 F g^{-1} at 1 mA cm^{-2}	41% (5000)	[228]
NiCoP/CC	Nanosheets	1143 F g^{-1} at 1 A g^{-1}	74.5 % (5000)	[252]
MnP	Nanorods	269 F g^{-1} at 5mV s^{-1}	-	[251]
Mn-CoP/NF	Nanosheets	716 F g^{-1} at 0.5 A g^{-1}	89.0% (20,000)	This work

In order to further investigate the potential applications of the Mn-CoP/NF electrode under practical conditions, an aqueous ASC was assembled by employing the prepared Mn-CoP/NF and AC as the positive and the negative electrodes, respectively. The CV curves of Mn-CoP/NF and AC electrodes tested in a three-electrode system with a scan rate of 20 mV s^{-1} were shown in **Fig. 5.7a**. The working potentials of Mn-CoP/NF (0 - 0.6 V) and AC (-1.0 - 0 V) reveals the operating voltage window of assembled ASC can be extended to 1.6 V. To further confirm the appropriate operating voltage window of the Mn-CoP/NF//AC ASC, CV and GCD tests within a series of voltage windows were conducted at a scan rate of 50 mV s^{-1} and a current density of 1A g^{-1}, respectively (**Fig. 5.7b & c**). According to **Fig. 5.7b & c**, the shape of the CV and GCD curves at the voltage range of 0 - 1.6 V does not deform appreciably indicating 1.6 V can be selected as a good operating voltage window for Mn-CoP/NF//AC ASC. Therefore, the voltage range of 0 - 1.6 V was selected to investigate the electrochemical performance of the

ASC. **Fig. 5.7d** shows the CV curves of Mn-CoP/NF//AC ASC at different scan rates of 5 - 100 mV s^{-1} within the working voltage rang of 0 - 1.6 V. Apparently, the redox peaks and the quasi-rectangular feature can be observed in all CV profiles indicating the combination of both pseudocapacitive and electric double-layer capacitive characteristics of Mn-CoP/NF//AC ASC. The well-maintained shape of CV curves at high scan rates indicates the fast charge/discharge properties and excellent rate performance of the Mn-CoP/NF//AC ASC [58, 222]. **Fig. 5.7e** presents the GCD curves of the fabricated ASC at various current density of 0.5 to 10 A g^{-1} within the working voltage rang of 0 - 1.6 V. The nonlinear shapes of GCD curves at low scan rates further indicate the combination of pseudocapacitive and electric double-layer capacitive characteristics of the ASC, which matches the above CV results. The almost symmetric shapes and low IR drops reveal the highly reversible electrochemical reactions and high electrical conductivity of the electrode material. The relationship of specific capacitances versus scan rates of the ASC was plotted in **Fig. 5.7f**. The ASC displays a specific capacity of 54 F g^{-1} at current densities of 0.5 A g^{-1}, and even at a high current density of 10 A g^{-1}, the capacitance values maintained at 23 F g^{-1}. These specific capacitance values are comparable with or even higher than some previously reported results for ASCs [179, 266].

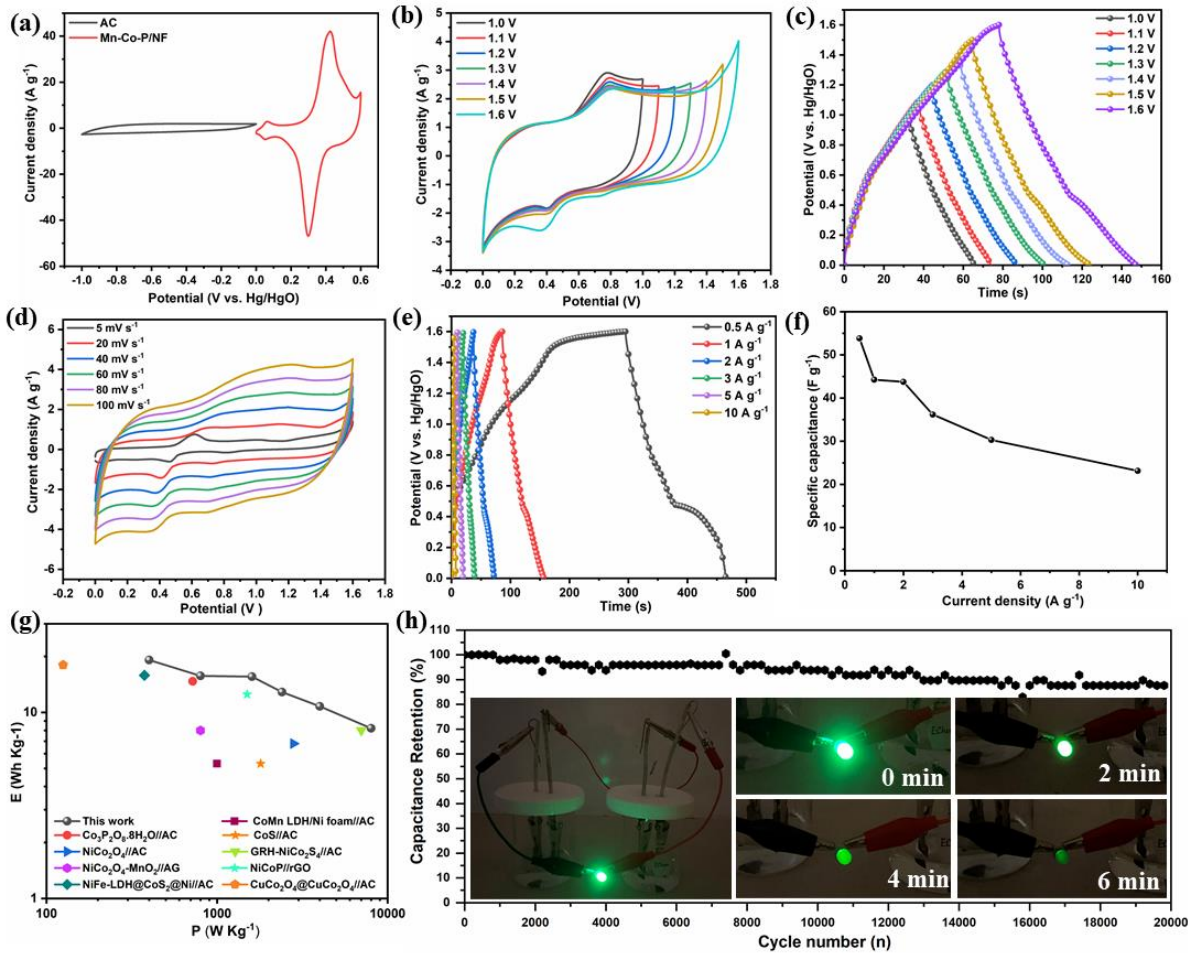

Figure 5. 7 (a) CV curves of AC and Mn-CoP/NF electrodes at 20 mV s^{-1} in a three-electrode system; (b) CV curves of Mn-CoP/NF//AC in various voltage windows at 50 mV s^{-1}; (c) GCD curves of Mn-CoP/NF//AC in various voltage windows at 1A g^{-1}; (d) CV curves of Mn-CoP/NF//AC at different scan rates; (e) GCD curves of Mn-CoP/NF//AC at different current densities; (f) Specific capacitances of Mn-CoP/NF//AC at different current densities; (g) Ragone plot of Mn-CoP/NF//AC and a comparison of energy densities and power densities with other reported works; (h) cycling stability test of Mn-CoP/NF//AC ASC at 10 A g^{-1}; inset is the photographs of a LED light powered by two tandem Mn-CoP/NF//AC ASC at different time.

The Ragone plot of Mn-CoP/NF//AC ASC and a comparison with other recently reported ASC devices were depicted in **Fig. 5.7g**. The Mn-CoP/NF//AC ASC device shows a high energy density of 19.13 Wh kg^{-1} at a power density of 400 W kg^{-1}. Even at an extremely high power density of 8000 W kg^{-1}, the energy density still retained 8.22 Wh kg^{-1}. Obviously, these values

are superior to those of $Co_3P_2O_8 \cdot 8H_2O$//AC [267], $NiCo_2O_4$//AC [268], $NiCo_2O_4$-MnO_2//AG [218], NiFe-LDH@CoS_2@Ni//AC [219], CoMn LDH/Ni foam//AC [269], CoS//AC [270], GRH-$NiCo_2S_4$//AC [271], NiCoP//rGO [252], $CuCo_2O_4$@$CuCo_2O_4$//AC [272] ASC devices. To further investigate the durability of Mn-Co-P/NF//AC ASC, the cycling stability was tested by GCD at 10 A g^{-1} (**Fig. 5.7h**). After 20,000 cycles, the Mn-CoP/NF//AC ASC can maintain 87.7% of the initial capacitance. The result is similar to the capacitance retention obtained in three-electrode system, which further confirmed the excellent cycling stability of Mn-CoP/NF. Intriguingly, as shown in the illustration of **Fig. 5.7h**, the green LED can be easily lighted by two tandem Mn-CoP/NF//AC ASC for 6 mins indicating its great promise in practical applications.

5.4 Conclusions

In summary, the Mn-CoP nanosheets on Ni foam (Mn-CoP/NF) was successfully synthesized by a simple and effective electrodeposition method. The electrochemical performance of the electrodes was optimized based on the deposition voltages and compositions. The best performing electrode exhibits excellent specific capacitance (716 F g^{-1} at 0.5 A g^{-1}), high-rate performance (77.4% capacitance retention with the current density increases from 1 to 10 A g-1) and superior cycling stability (capacitance retention of 89.0 % after 20,000 cycles). The ASC device based on the Mn-CoP/NF//AC shows prominent energy and power density (19.13 Wh kg^{-1} at a power density of 400 W kg^{-1}) as well as a remarkable cyclic stability of 87.7% capacitance retention after 20,000 cycles. The excellent electrochemical performance of Mn-CoP/NF electrode mainly benefiting from the combination of the following factors: the binder-

free in-situ deposition preparation method, the interconnected Mn-CoP nanosheets structure and the synergistic effect between Mn and Co ions. Therefore, the prepared Mn-CoP/NF could be used as a promising candidate for energy storage devices.

Chapter 6

Ultra-fast microwave synthesis of nickel-cobalt sulfide/graphene hybrid electrodes for high-performance asymmetrical supercapacitors

Abstract: Nickel-cobalt sulfides (NCSs) with rich redox-active sites and remarkable theoretical capacity have been regarded as promising electrode materials for supercapacitors. Various approaches have been developed for the synthesis of NCSs based electrode materials. However, most of these methods require complex steps, high energy consumption and time-consuming processes resulting in safety, cost and chemical contamination problems. Herein, we demonstrated a one-step and ultra-fast microwave approach for the synthesis of NCS/graphene composites in a single minute. The prepared NCS/graphene composites can be used as high-performance electrode materials for supercapacitors with a high specific capacitance of 710 F g^{-1} at a current density of 0.5 A g^{-1} and a prominent cycling stability with a specific capacitance retention rate of 75% even after 10,000 cycles. In addition, a high-performance asymmetric supercapacitor (ASC) was assembled by using NCS/graphene composite as positive electrode and activated carbon as negative electrode. The fabricated ASC can deliver a high energy density of 30.29 W h kg^{-1} at a power density of 400 W kg^{-1} and exhibit excellent cycling stability with a capacitance retention of 112% after 10,000 cycles. These impressive results demonstrated that the microwave synthesis can be used as a highly efficient and ultra-fast approach for the preparation of high-performance NCSs based electrode materials.

6.1 Introduction

In recent years, the environmental deterioration and the huge depletion of fossil fuels have expedited the development of clean and renewable energy sources [273]. Electrochemical energy storage devices are essential for the development of renewable energy system, due to the fact that most of the renewable energy sources (i.e., solar, wind, and hydro energy etc.) are intermittent [274]. Supercapacitors (SCs), as one type of promising electrochemical energy storage devices, have attracted great attention according to their low cost, fast charge/discharge rate, high power density, wide working temperature range and excellent cycling stability [275-277]. However, the relatively low energy density of SCs becomes a barrier hindering their widespread applications in reality [278]. Thus, it is a great challenge for SCs to achieve enhanced energy density without sacrifice of power density and cycling performance. Depending on the energy density calculation equation: $E = \frac{1}{2}CV^2$, the energy density of SCs can be improved by expanding the working voltage window (V) of the cells and/or enhancing the specific capacitance of electrode materials [279-280]. Normally, choosing the proper electrolyte is considered as one effective way to enlarge the operating voltage window. However, the voltage expansion range is limited in aqueous electrolytes due to the water decomposition reaction that occurs over 1.23 V [279]. Hence, some organic and ionic-liquid electrolytes were selected to increase voltage window up to 3 V and 5 V, respectively [281]. Nevertheless, most of organic and ionic-liquid electrolytes face the challenges of high cost, environmental pollution and poor ionic conductivity etc. [282]. At present, designing asymmetric supercapacitors (ASCs) with aqueous electrolytes has been considered as a promising strategy to enhance the energy density of SCs. ASCs are generally fabricated by using two different kinds of electrodes that work in

different potential windows. Consequently, ASCs can combine the working voltage windows of these two electrodes achieving the enlarged operating voltage of the whole device. Evidently, the selection of appropriate electrode materials plays a vital role for developing high-performance ASCs [22, 283-284].

Transition metal sulfides (TMSs) have been intensively studied as promising electrode materials due to their high theoretical specific capacitance, excellent cycling stability, high energy density, admirable conductivity and low cost [285-286]. Several TMSs have been explored as electrode in SCs such as MnS, CoS, MoS_2, CuS, FeS_2, NiS etc. [287-288]. However, it is still challenging for TMSs to meet the practical application requirements in terms of specific capacitance, energy density, and cyclic stability. Compared to the monometallic sulfides, the mixed metal sulfides, especially the nickel-cobalt sulfides (NCSs), exhibit higher specific capacitance and cycling stability due to their richer redox-active reactions sites and higher electronic conductivity [273]. As a result, NCSs with remarkable theoretical capacity have been regarded as promising electrode materials [289]. Nevertheless, many research results reported the poor cycling stability and a much lower specific capacitance of NCSs than their theoretical capacitance [274-275, 290]. Many attempts have been tried to address this issue. For example, combining NCSs with carbonaceous materials like graphene [291], porous carbons [292], carbon nanotubes (CNTs) [293] and carbon nanofibers [294], to form a composite has proven to be an effective strategy to solve the above issues due to the enhanced electrical conductivity and faster charge transfer rate of carbon-based materials. Among these carbonaceous materials, graphene has been regarded as one of the most promising substrates for the growth of NCSs

due to its excellent conductivity, large surface area, long-term stability and great processing flexibility [295]. Several research studies have demonstrated the enhanced electrochemical performance of the NCSs/graphene composites. For example, Zhai et al. [291] developed a new NCS/graphene heterostructure which exhibited high specific capacitance and superior capacitance retention. Gao et al. [295] successfully prepared a novel NCS/graphene composites which revealed much higher specific capacitance (nearly twice) and better cycling stability than single NCS electrode.

According to the literature, various approaches can be used for the preparation of NCS/graphene hybrid materials especially through hydrothermal and solvothermal methods. However, most of these methods require complex steps, high energy consumption and time-consuming procedures. Some safety and chemical contamination problems are also accompanied by these synthesis processes. For instance, Wang et al. [296] synthesized NCS/reduced graphene oxide composite by several complex steps and the whole process cost around 2 days. Dong et al. [297] prepared NCS/graphene via a two-step hydrothermal method which involves high energy consumption and tedious process. Zhai et al. [291] prepared NCS/graphene by conversion of MOF precursor into NCS on electrochemically exfoliated graphene. Organic reagents were used during this synthesis process that are harmful for human body and environment. Therefore, a facile and efficient technique is highly desired for the synthesis of NCS/graphene composites to further expand their practical applications. Fortunately, the microwave method can be used as an effective approach to overcome some of these drawbacks due to its rapid heating, fast reaction rate, high product yield, favorable

product purity and/or phase homogeneity, excellent reproducibility, expanded reaction conditions and high efficient energy transformation [298-299]. During a typical microwave synthesis, a closed-vessel container will be placed into the microwave oven, the inside materials owning dielectric property and molecular dipole moment will rotate and migrate under microwave irradiation. By absorbing microwave, the system can get an extremely localized high temperature in several seconds. The generated heat will support the reaction in the container system and the reaction rate can be enhanced with increase of collision that occurred between reactants within a confined space [298, 300]. According to this, microwave method has been reported as a simple and fast technique for the synthesis of some transition metal-based electrode materials [72, 301].

In this work, a one-step and ultra-fast microwave method was demonstrated for the first time to synthesize NCS/graphene hybrid material in a quick reaction time (60 s), and the synthesis process is illustrated in **Scheme 6.1**. The obtained NCS/graphene composites were used to successfully fabricate the high-performance ASCs with high energy density and power density, as well as excellent cycling stability.

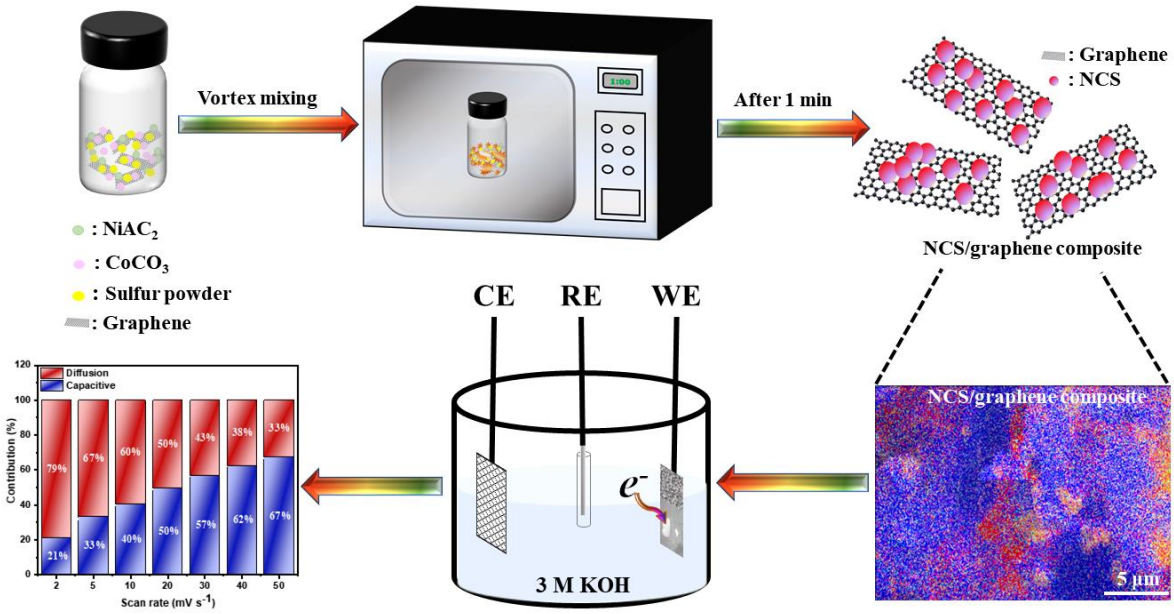

Scheme 6.1. Schematic diagram of the one-step microwave synthesis of NCS/graphene composites as hybrid supercapacitor electrode materials.

6.2 Experimental

6.2.1. Materials

Nickel (II) acetate ($Ni(CH_3CO_2)_2{\cdot}4H_2O$) and sulfur powders were purchased from Alfa Aesar. Cobalt (II) carbonate ($CoCO_3$) was purchased from Fisher Scientific. Graphene substrate was obtained from Magnolia Ridge Inc. All chemicals purchased were used without further treatment or purification. For electrochemical characterizations, the silver/silver chloride reference electrode was obtained from Hach. Platinum (Pt) mesh was obtained from Alfa Aesar.

6.2.2 Synthesis of NCS/graphene composites

The NCS/graphene composites were prepared by an ultrafast microwave solid-state method by using $Ni(CH_3CO_2)_2{\cdot}4H_2O$ as Ni source, $CoCO_3$ as Co source and sulfur powder as S source. In

a typical experiment, $Ni(CH_3CO_2)_2 \cdot 4H_2O$ (25 mg), $CoCO_3$ (25 mg), Sulfur powder (10 mg) and graphene (60 mg) (weight ratio of NCS precursor to graphene is 1:1) were filled into a glass vial and mixed them uniformly by a vortex mixer (2000 rpm). Then, the obtained mixture was heated by a microwave oven (frequency 2.45 GHz, power 1000 W) for 60 s. In the whole system, graphene was used as microwave energy susceptor to supply the heat needed for the decomposition of Ni $(CH_3CO_2)_2 \cdot 4H_2O$ and $CoCO_3$ to NiO and CoO, then converted to NCS and evenly dispersed on the surface of graphene substrate. Other constituents came out by gaseous forms. After this quick microwave irradiation process, the final product of NCS/graphene composite can be obtained. A series of NCS/graphene composites synthesized under different ratios of NCS precursor to graphene, different microwave powers and irradiate times (listed in **Table 6.1**) were also successfully prepared for comparison.

Table 6. 1 Reaction conditions for the synthesis of NCS/graphene composites

Sample	$Ni(CH_3CO_2)_2 \cdot 4H_2O$ (g)	$CoCO_3$ (g)	Sulfur (g)	Graphene (g)	NCS/graphene ratio	Microwave power (W)	Irradiation time (s)
S1	25	25	10	30	2:1	1000	60
S2	25	25	10	60	1:1	1000	60
S3	25	25	10	120	1:2	1000	60
S4	25	25	10	60	1:1	500	60
S5	25	25	10	60	1:1	700	60
S6	25	25	10	60	1:1	1250	60

S7	25	25	10	60	1:1	1000	30
S8	25	25	10	60	1:1	1000	90

6.2.3 Materials characterization

The morphological features of NCS/graphene samples were observed by field-emission scanning electron microscopy (FE-SEM, Thermo Scientific Apreo). The lattice parameters were measured by high resolution transmission electron microscopy (HRTEM, FEI Tecnai F20). The elemental composition was detected by energy dispersive X-ray spectrometer (EDS, EDAX Inc.). The crystal structures of samples were characterized by powder X-ray diffraction (XRD) with a Philips X'Pert MPD diffractometer at condition of Cu Kα radiation (λ = 1.5405 Å) from 10^o to 80^o of the 2θ angle with a step size of 0.2°/min.

6.2.4 Fabrication of ASC

In order to evaluate the device performance of NCS/graphene as electrode material for supercapacitors, an asymmetric supercapacitor (ASC) was assembled by using NCS/graphene as positive electrode, activated carbon (AC) as negative electrode and 3.0 M KOH as electrolyte. The mass ratio of the positive and negative electrodes can be determined according to the charge balance theory ($q^+ = q^-$). Thus, prior to the fabrication of the ASC, the masses of NCS/graphene and AC were balanced according to the following equation:

$$\frac{m_+}{m_-} = \frac{C_- \Delta V_-}{C_+ \Delta V_+}$$

where, m_+ and m_- correspond to the loading mass (g) of the NCS/graphene and AC, respectively. C_+ and C_- represent the specific capacitance of NCS/graphene and AC electrodes. ΔV_+ and ΔV_- are the working voltage range of NCS/graphene and AC electrodes.

6.2.5 Electrochemical measurements

NCS/graphene electrodes were prepared by using Ni foam as current collector. Prior to prepare electrodes, Ni foams (1 cm × 2 cm) were treated by 3.0 M HCl solution under sonication for 10 min, then sonicated in ethanol for 15 min, respectively, to remove the oxide layer. In the following step, the pretreated Ni foams were rinsed with copious DI water and dried in a vacuum oven at 60 °C. The NCS/graphene electrodes were prepared by coating the treated Ni foams (coating area:1 cm × 1 cm) with the homogeneous paste of the NCS/graphene materials and Nafion (5 wt%) binder followed by drying in a vacuum oven at 60 °C. The electrochemical measurements of all the electrode materials were executed on a CHI 760D electrochemical analyzer. A typical three-electrode configuration with NCS/graphene as working electrode, Hg/HgO as counter electrode and Pt as reference electrode was used during the test. Cyclic voltammetry (CV), galvanostatic charge/discharge (GCD) and electrochemical impedance spectroscopy (EIS) tests were carried out with 3.0 M KOH as electrolyte. The CV tests were performed at a voltage range of 0 V to + 0.6 V with scanning rates range from 2 to 50 mV s^{-1}. The GCD tests were conducted at a voltage range of 0 to + 0.5 V at varying current density from to 0.5 to 4 A g^{-1}. The EIS analysis was recorded within the frequency range between 100 kHz and 0.01 Hz at a 5mV amplitude AC voltage. The specific capacity (C_s, F g^{-1}) of electrodes can be evaluated by using the following equation:

$$C_s = \frac{I\Delta t}{m\Delta V}$$

Where, I (A) is the response current, m (g) is the active material of electrode, Δt (s) is the discharge time and ΔV (V) is the working voltage window.

In the two-electrode ASC system, CV and GCD measurements were recorded at the voltage window of 0 - 1.6 V. The specific capacitance (C_{cell}), energy density (E, Wh kg^{-1}) and power density (P, W kg^{-1}) of the fabricated ASC can be calculated according to the following equations:

$$C_{cell} = \frac{I'\Delta t'}{m'\Delta V'}$$

$$E = \frac{C_{cell} \times (\Delta V')^2}{2 \times 3.6}$$

$$P = \frac{3600 \times E}{\Delta t'}$$

Where, I' is the response current of the ASC, m' is the active materials mass of NCS/graphene and AC electrodes, Δt' is the discharge time of the ASC and ΔV' is the working voltage window of the ASC.

6.3 Results and discussions

6.3.1 Fabrication and structural investigation

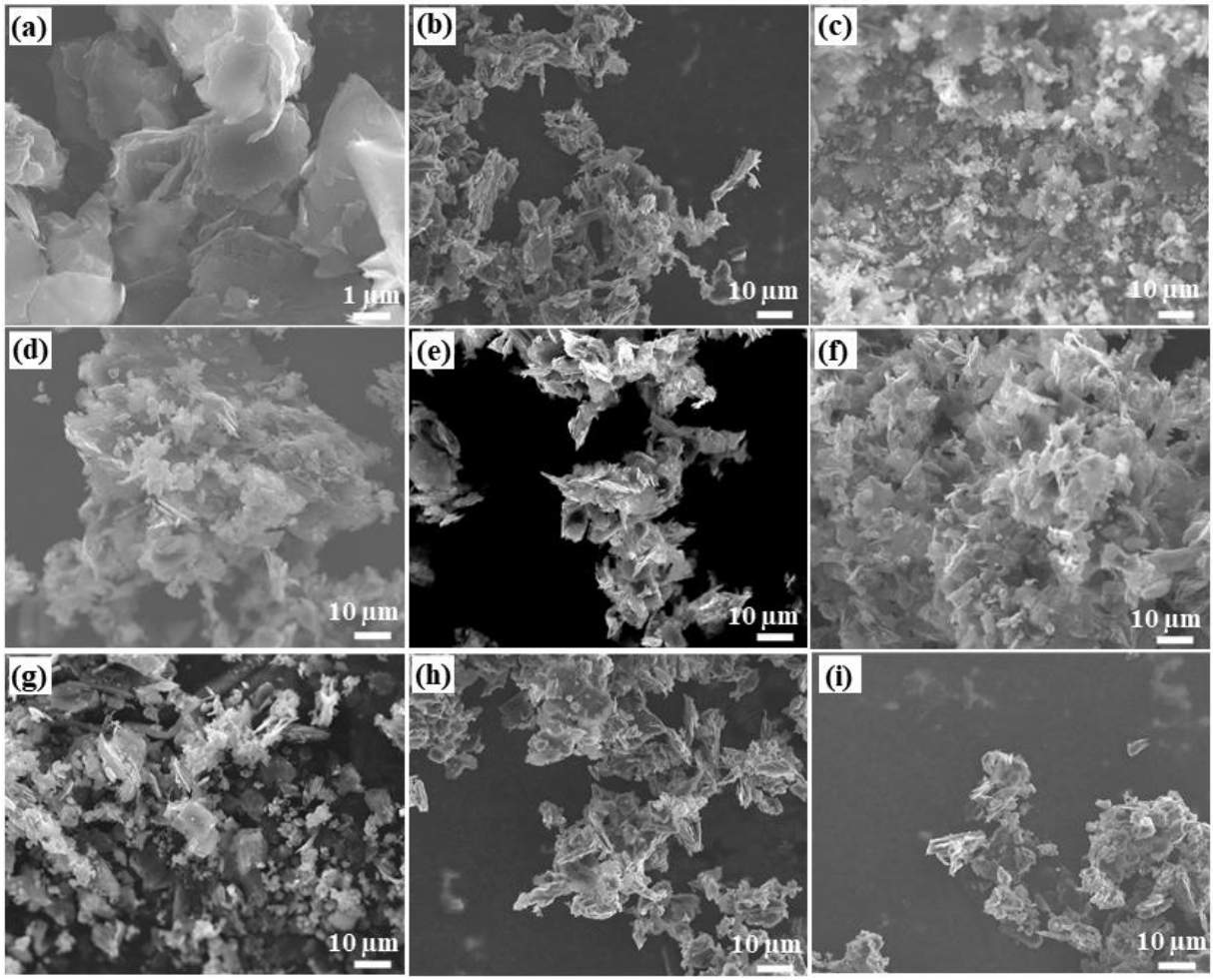

Figure 6. 1 (a) SEM image of pure graphene; (b-i) SEM images of NCS/graphene composites listed in Table 1: (b) sample 1, (c) sample 2, (d) sample 3, (e) sample 4, (f) sample 5, (g) sample 6, (h) sample 7, and (i) sample 8.

The morphologies and microstructural features of NCS/graphene samples prepared at different reaction conditions including different feeding mass ratio of NCS precursor to graphene, different microwave power and different reaction time were characterized by FE-SEM. As shown in **Fig. 6.1**, compared with pure graphene (**Fig. 6.1a**) which has flake-like structure, the obtained NCS species have particle-like structures. For all the NCS/graphene composites, the graphene sheets were decorated with different densities of NCS particles which demonstrated the successful growth of NCS compounds on graphene flakes. In these composites, the

graphene flakes with high surface area and high electrical conductivity are coalesce and/or overlap with each other, forming an interconnected conductive network. This special conductive network not only provides good mechanical properties for the composite but also ensures the well connection between NCS particles and facilitates the electron transfer for achieving high capacitive performance [301]. **Figs. 6.1(b-d)** compared the effect of NCS precursor to graphene mass ratio on the morphology of the obtained composites. Obviously, different amounts of graphene feeding caused different content of NCS particles formed on graphene substrate. This is because the conductive graphene acts as microwave susceptor to provide heat to convert precursors into NCS during the synthesis process. Thus, too little amount of graphene cannot supply enough heat to generate enough NCS (**Fig. 6.1b**) while too much of graphene could generate excess NCS and lead to aggregation (**Fig. 6.1d**). Herein, the NCS precursor to graphene mass ratio at 1:1 is the best for generating the optimum amount of NCS that is uniformly dispersed on graphene surface (**Fig. 6.1c**). **Figs. 6.1(c, e, f, g)** compared the effect of microwave power on the morphology of the composites. It can be clearly seen that the amount produced of NCS increased with the increase of microwave power. The low microwave power (e.g., 500W, 700 W) cannot supply enough heat to generate optimum amount of NCS (**Figs. 6.1(e, f)**) while the aggregation happened with too high microwave power (**Fig. 6.1g)**. As a result, the microwave power at 1000W is the optimal choice for this system (**Fig. 6.1c**). **Figs. 6.1(c, h, i)** compared the effect of microwave irradiation time on the morphology of the synthesized composites. Apparently, different microwave irradiation time resulted in different amount of NCS formed in the composites. Too short microwave irradiation time and too long microwave irradiation time are both not favorable for generating the optimum amount

of NCS and affect the uniform combination of NSC and graphene. As shown in **Fig. 6.1c**, 60 s microwave irradiation can be considered as the optimal time for achieving suitable amount of NCS uniformly dispersing on the graphene surface. By this systematic study, uniform NCS particles could be introduced on the graphene substrate under optimized reaction conditions i.e., NCS/graphene mass ratio at 1:1, microwave power at 1000W, and irradiation time of 60 s.

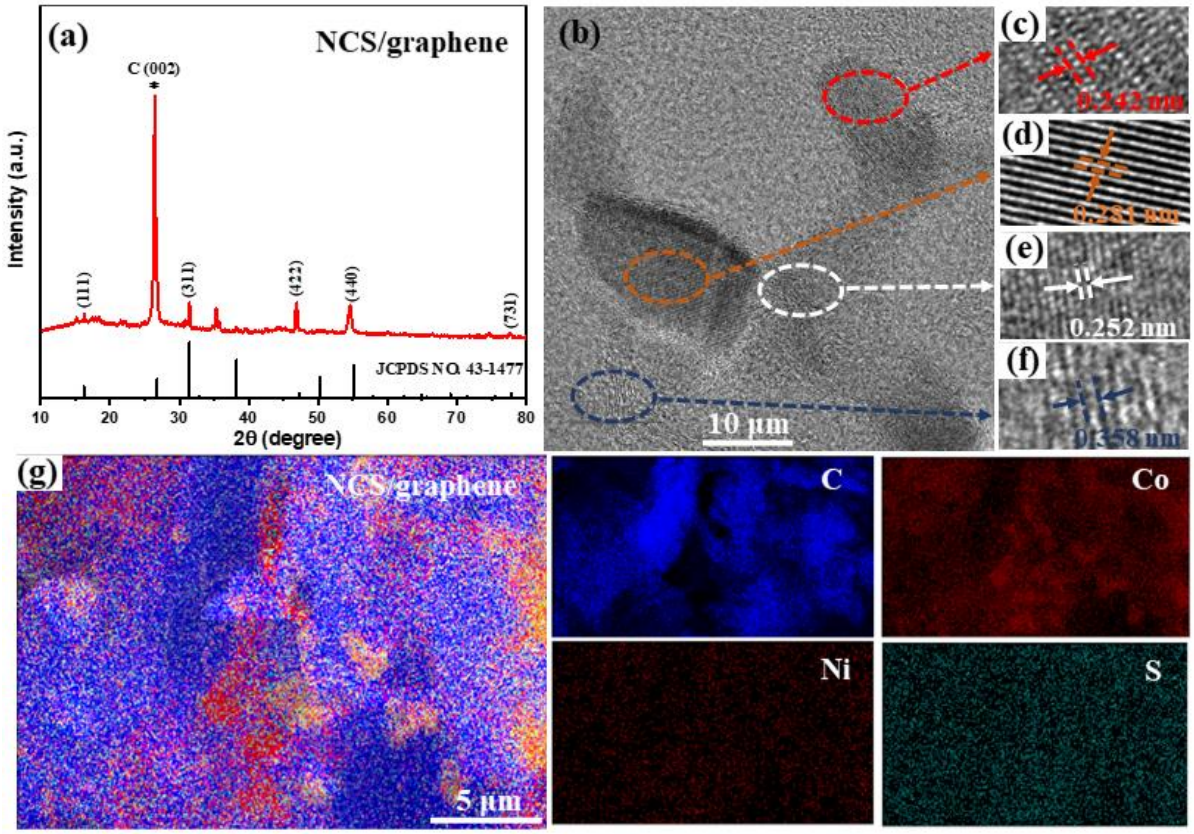

Figure 6. 2 (a) XRD pattern of NCS/graphene composite (S2); (b) HR-TEM images of NCS/graphene composite (S2); (c-f) Interlayer spacings of NCS and graphene; (g) EDS elemental mapping images of carbon (C), nickel (Ni), cobalt (Co), sulfur (S) elements of the optimized NCS/graphene composite (S2).

The crystalline structure of the optimized NCS/graphene composite (S2) was further analyzed by XRD, and the obtained XRD pattern was shown in **Fig. 6.2a**. The strong peak at 2θ = 26.5° can be assigned to the (002) plane of graphite layers in graphene [302-303]. The diffraction peaks

at 2θ = 16.3°, 31.4°, 47.4°, 55.1°, 77.8° can be well assigned to the (111), (311), (422), (440) and (731) planes of the $NiCo_2S_4$ (JCPDS No. 43-1477) [304-305]. Besides, the diffraction peak at 2θ = 35.3° corresponds well with the (101) phase of hexagonal CoS (JCPDS No. 65-3418) [306]. The microstructure and crystallinity of NCS/graphene composite were further characterized by high-resolution TEM. As shown in **Fig. 6.2b**, the HR-TEM image exhibits the conspicuous difference between NCS and graphene through their well-resolved lattice fringes and individual interplanar spacings. The interplanar spacings of 0.242 nm (**Fig. 6.2c**) and 0.281 nm (**Fig. 6.2d**) correspond to the (111) and (311) planes of the $NiCo_2S_4$ cubic phase, respectively [271, 273]. The interplanar distance of 0.252 nm (**Fig. 6.2e**) can be attributed to the (100) plane of the CoS phase [305-306]. The lattice fringe with the interplanar spacing of 0.358 nm (**Fig. 6.2f**) was assigned to the (002) plane of hexagonal graphitic carbon [301, 303]. The HRTEM results are consistent well with the XRD results. The EDS elemental mappings were performed to confirm the elements distribution of the as-prepared NCS/graphene composite. The corresponding color maps (**Fig. 6.2g**) demonstrate the uniform distribution of C, Ni, Co, and S elements throughout the NCS/graphene composite.

6.3.2 Electrochemical performance

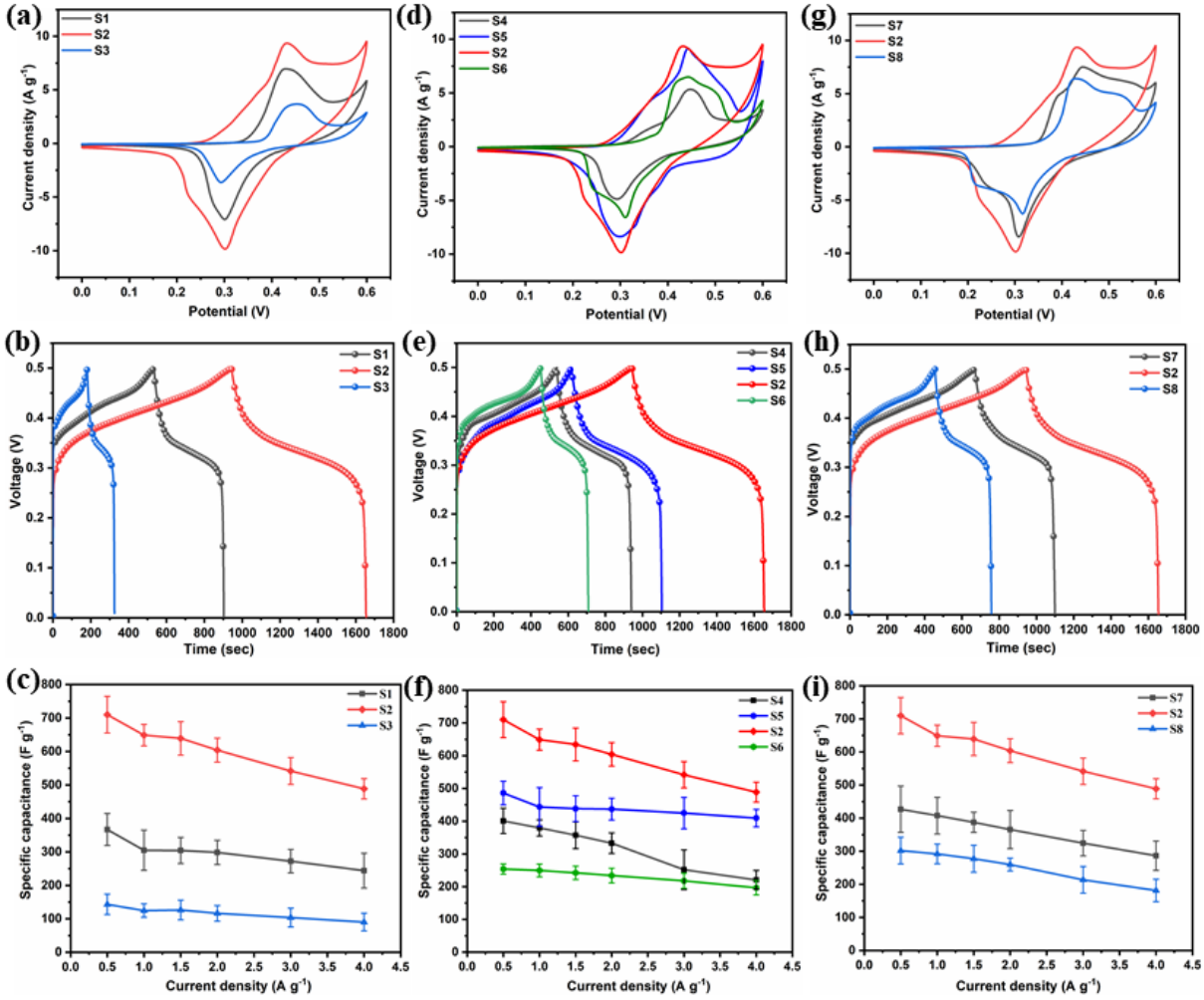

Figure 6. 3 Electrochemical performance of NCS/graphene composites prepared at different NCS precursor to graphene mass ratio (a-c); different microwave power (d-f); different microwave irradiation time (g-i). Note: for all the samples, the CV curves were obtained at 10 mV s^{-1}, and the GCD curves were collected at 0.5 A g^{-1}.

The effects of experimental conditions on electrochemical performance of NCS/graphene samples were measured by performing CV and GCD measurements in a three-electrode cell with 3.0 M KOH as electrolyte. **Figs. 6.3(a-c)** compared the electrochemical performance of NCS/graphene samples prepared at different NCS precursor to graphene mass ratios. For the three samples, the CV curves exhibit different current responses at the same scan rate. The NCS/graphene composite obtained at 1:1 ratio has the highest current response and the largest

CV enclosed area, indicating its best electrochemical performance. The GCD curves in **Fig. 6.3b** show that the order of charge/discharge time is consistent with the order of current response in CV curves of **Fig. 6.3a**. The calculated specific capacitances of NCS/graphene samples in **Fig. 6.3c** clearly show the effect of graphene loading amount on the electrochemical properties of these NCS/graphene composites. Apparently, the NCS/graphene composite obtained at 1:1 ratio of NCS precursor to graphene has the best capacitance behavior which is consistent with the results discussed in CV and GCD curves. This is because graphene acts as substrate for absorbing the microwave energy and converting it to heat energy during the microwave irradiation process. The generated heat energy can trigger the NCS precursor transformed into NCS dispersed on surface of graphene substrate and released other constituents in gaseous forms. Thus, insufficient amount of graphene cannot generate enough heat energy for the NCS transformation process, leading to the relatively low capacitance performance of obtained composite. While too much graphene might generate excess NCS for the whole system and some of NCS stacked together, as verified in **Fig. 6.1d**. The agglomeration would hinder the infiltration of electrolyte and increase charge transfer resistance, leading to the reduced capacitance. From the above results, we demonstrated the best ratio of NCS precursor to graphene for preparing NCS/graphene sample is 1:1. **Figs. 6.3(d-f)** investigated the effects of microwave powers on the electrochemical performance of NCS/graphene samples. From **Fig. 6.3d**, we can see the response current densities of NCS/graphene composites synthesized at different microwave power initially increase with the increase of microwave power until the microwave power surpasses 1000W. As indicted in **Fig. 6.3e**, the charge/discharge times show a similar trend. The calculated specific capacitance in

Fig. 6.3f exhibits the consistent results with CV and GCD data which further confirmed the optimal microwave power is 1000W for achieving the optimal NCS/graphene composite. This result is because, in the early stage, the amount of NCS increased with the increase of microwave power resulting in the enhancement of capacitances. When the power is too high, the excessively produced NCS will pile on top of the composites (**Fig. 6.1g**), and this agglomeration caused the decrease in capacitance performance. The influence of microwave irradiation time on electrochemical performance of NCS/graphene samples was finally studied, and the electrochemical measurement results are presented in **Figs. 6.3(g-i)**. From the CV and GCD curves, it is not hard to see that the NCS/graphene sample prepared with 60 s microwave irradiation time has the highest current response, the largest CV enclosed area and the longest charge/discharge time, indicating its highest specific capacitance. This result was mainly caused by the amount of NCS produced during the microwave irradiation process. More specifically, the relatively short irradiation time (30 s) would produce less amount of NCS, while a relatively long time (90 s) could generate too much NCS and cause agglomeration, both of which are not beneficial to the electrochemical performance. According to above discussion, the optimum experimental conditions for the synthesis of NCS/graphene composite involve a 1:1 feeding mass ratio of NCS precursor to graphene with a 1000W microwave power and a 60 s irradiation time. The maximum specific capacitance of NCS/graphene synthesized at the optimum experimental conditions can reach up to 710 F g^{-1} at the current density of 0.5 A g^{-1}.

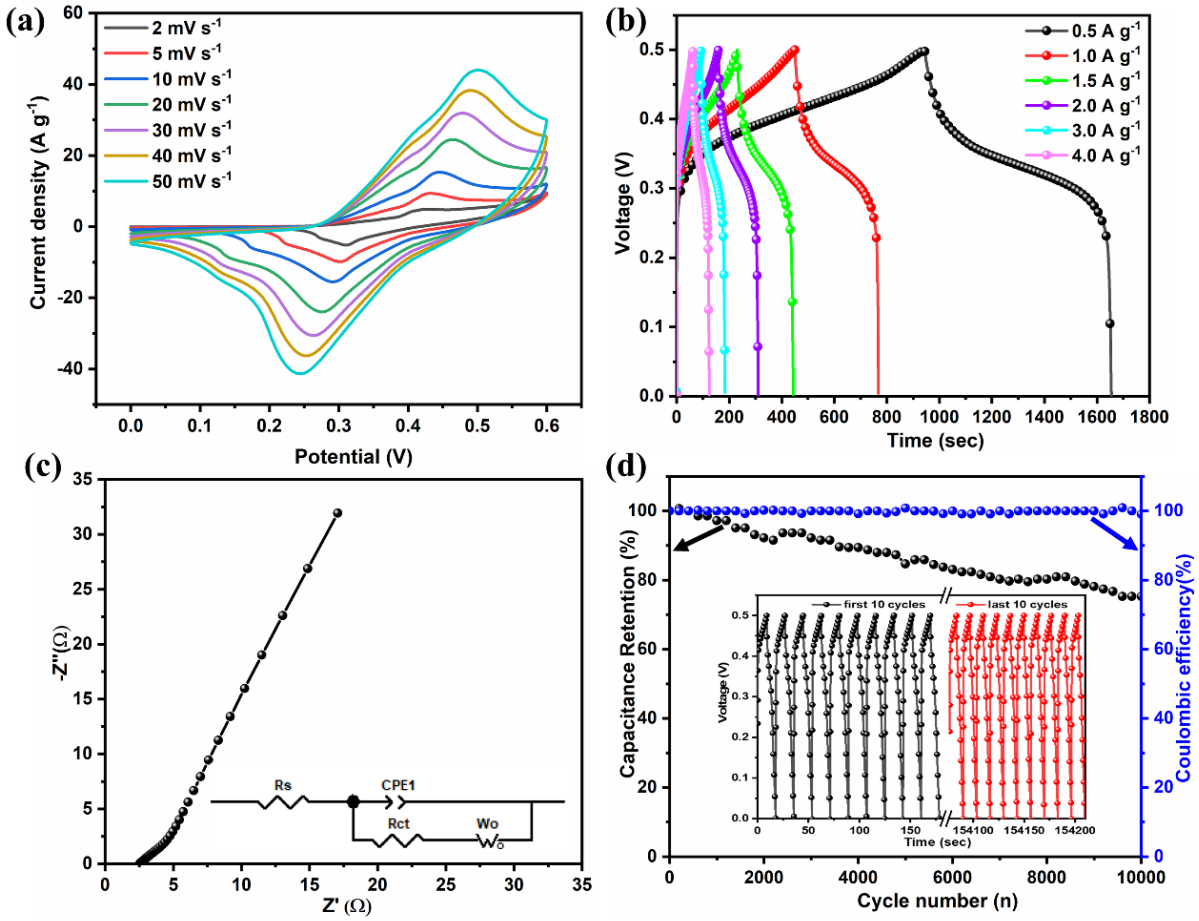

Figure 6. 4 Electrochemical performance of NCS/graphene composite prepared at the optimum experimental conditions (S2). (a) CV curves at different scan rates; (b) GCD curves at different current density; (c) Nyquist plot at open circuit potential (the inset illustration is the equivalent circuit). (d) Cycling stability and Coulombic efficiency versus cycle number.

The electrochemical characteristics of the optimized NCS/graphene composites (S2) were comprehensively evaluated *via* a three-electrode cell using 3.0 M KOH as electrolyte. **Fig. 6.4a** shows the CV curves of NCS/graphene electrode at scan rates ranging from 2 mVs^{-1} to 50 mV s^{-1}. Obviously, a pair of redox peaks can be clearly observed in these CV curves indicating the energy storage mechanism mainly depends on the redox reactions. Both the $NiCo_2S_4$ cubic phase and CoS phase in NCS/graphene electrode are electroactive species and contribute to energy storage in the alkaline electrolyte. The redox peaks in the CV curves can be generally

ascribed to the reversible redox reactions of Ni^{2+}/Ni^{3+}, Co^{2+}/Co^{3+} and Co^{3+}/Co^{4+}, and these redox reactions can be described by the following equations [291, 307] :

$$NiCo_2S_4 + OH \rightarrow NiS_{4-4x}OH + 2CoS_{2x}OH + e^-$$

$$CoS_{2x}OH + OH \rightarrow CoS_{2x}O + H_2O + e^-$$

$$CoS_{2X} + OH \rightarrow CoS_{2x}OH + e^-$$

$$NiS_{4-4x} + OH \rightarrow NiS_{4-4x}OH + e^-$$

$$CoS + OH^- \rightarrow CoSOH + e^-$$

$$CoSOH + OH^- \rightarrow CoSO + H_2O + e^-$$

Furthermore, the response currents and integral area of the CV curves increased with the increase of the scan rates accompanied by slightly positive and negative shifts of the anodic and cathodic peaks, respectively, which were due to the polarization caused by the existence of internal resistance (IR) [291]. GCD technique has been demonstrated as a superlative procedure to evaluate the specific capacity of the electrode. The GCD curves collected at current densities ranging from 0.5 A g^{-1} to 4 A g^{-1} were presented in **Fig. 6.4b**. Apparently, the GCD curves show a non-linear charging/discharging process and the clearly observed voltage plateaus certifying the pseudocapacitive feature. The results from GCD are in line with the CV analysis results. The specific capacitance values of NCS/graphene electrode calculated according to GCD curves are summarized in **Fig. 6.3c** and the gained results could have 710, 649, 639, 604, 542

and 489 F g^{-1} at current densities of 0.5, 1, 1.5, 2, 3 and 4 A g^{-1}, respectively. EIS measurement can be used to probe the ion and electron transport properties and to analyze the electrochemical reaction kinetics of the electrode materials. The Nyquist plot and its fitted equivalent circuit are shown in **Fig. 6.4c**. In the high frequency range, the intercept at the real axis is related to the electrolyte solution resistance (R_s). The R_s value is determined by a combined resistance including the electronic resistivity from working electrode and the ionic resistance from the electrolyte. Here, the R_s value was observed to be 2.54 Ω indicating the excellent specific capacity and extraordinary conductivity of the electrode [308]. The charge-transfer resistance (R_{ct}) of electrode can be taken from the semicircle at the high frequency range. The almost invisible semicircle and small R_{ct} value (0.20 Ω) reveal the fast charge transfer property. The straight slopping line in low-frequency region manifests the mass transfer of ions at the interface of electrode material/electrolyte [308-309]. The long-term cycling stability of the NCS/graphene electrode was tested by a continuous 10000 galvanostatic charge/discharge cycles. As shown in **Fig. 6.4d**, the decreased capacitance retention during the cycling test might be due to the consumption of the active sites in the electrode material caused by the repeating redox reactions and the structural destruction of the electrode material. After 10,000 cycles, the capacitance retention maintained as 75 % of the original specific capacitance verifies superior cyclic durability. In addition, the columbic efficiency maintained around 100 % during the whole cycling process. The first and last ten charge/discharge cycles (inset in **Fig. 6.4d**) were almost symmetric as well as being similar. Both results further confirmed the remarkable reversibility and structural stability of the electrode material [266]. Based on the above discussion, the NCS/graphene composites can be used as excellent electrode materials for supercapacitors.

Both the specific capacitance and the cycling stability are comparable to some other published nickel-cobalt sulfides-based electrodes synthesized *via* tedious steps (**Table 6.2**). The excellent electrochemical properties of NCS/graphene composites are attributed to the synergistic effect of uniformly distributed NCS particles and graphene substrates, in which the graphene provided a large contact surface area and high electrical conductivity, also worked as the conductive medium to connect the NCS particles well and allow the facile ion diffusion, ensuring the efficient participation of NCS particles in the charge-discharge process.

Table 6. 2 A comparison of specific capacity and cycling performance of nickel-cobalt sulfides-based electrodes reported previously and this work.

Material	Synthesized method	Specific capacitance	Retention (cycle)	Ref.
$Ni_{3x}Co_{3-3x}S_4$@carbon	Two-step hydrothermal	696 F g^{-1} at 1 A g^{-1}	73 % (2000)	[310]

$NiCo_2S_4$/Carbon	Carbonization and hydrothermal	747 F g^{-1} at 1 A g^{-1}	89.65%(5000)	[311]
Activated carbon/$NiCo_2S_4$	Carbonization and hydrothermal	605.2 F g^{-1} at 0.5 A g^{-1}	91.3% (5000)	[312]
$(CoNi)O_xS_y$	Hydrothermal	592 F g^{-1} at 0.5 A g^{-1}	95.8% (2000)	[313]
$NiCo_2S_4$/Carbon Aerogel	Carbonization and hydrothermal	603 F g^{-1} at 50 mV s^{-1}	90% (5000)	[314]
$NiCo_2S_4$ Nanoplates	Template-directed hydrothermal	437 F g^{-1} at 1 A g^{-1}	81% (1000)	[315]
Ni-Co-S/Co-S	Hydrothermal and electrodeposition	8.47 F cm^{-2} at 5mV s^{-1}	75% (1800)	[316]
GQDs/$NiCo_2S_4$	Two-step hydrothermal	678 F g^{-1} at 0.2 A g^{-1}	94% (5000)	[317]
NCS/graphene	One-step microwave	710 F g^{-1} at 0.5 A g^{-1}	75% (10000)	This work

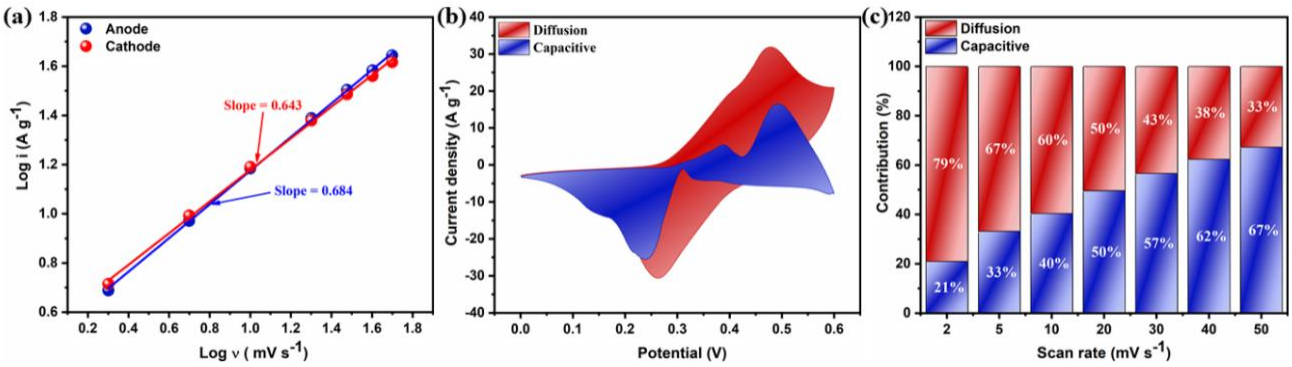

Figure 6. 5 (a) Calculating of b values by log (*i*) versus log (υ) plots at anodic and cathodic peaks; (b) Capacitive contribution (blue region) of NCS/graphene composite (S2) at 30 mV s^{-1}; (c) Capacitive (blue region) and diffusive (red region) contributions of NCS/graphene composite (S2) at different scan rates.

To further study the detailed energy storage behavior of NCS/graphene electrode, the kinetics were investigated by the analysis of CV curves collected at different scan rates (**Fig. 6.4a**). Generally, the relationship between the peak currents (*i*) and scan rates (υ) in CV curves obeys the following equation:

$$i = a\upsilon^b$$

Where *i* is the peak current, υ is the relevant scan rate, and a and b are empirical parameters. According to previous studies, b = 1 indicates an ideal capacitive-controlled process, b = 0.5 indicates a typical ionic diffusion-controlled process and the b value between 0.5 and 1 implies both diffusion-controlled and capacitive-controlled processes existed in the system [254, 259]. From **Fig. 6.5a**, by plotting log (*i*) vs. log (υ), the b values of anodic peaks and cathodic peaks can be obtained as 0.643 and 0.684, respectively, demonstrating the existence of both

capacitive and diffusion-controlled behavior in the NCS/graphene composite [318]. In the CV curves, the current at a certain potential (i(V)) can be expressed as:

$$i(\mathrm{V}) = k_1\upsilon + k_2\upsilon^{1/2}$$

where k_1 and k_2 are constants. $k_1\upsilon$ indicates the capacitive effects and $k_2\upsilon^{1/2}$ corresponds to the diffusion contributions at fixed potentials. By dividing by $\upsilon^{1/2}$ at both sides, above equation can be changed into:

$$i(V)/\upsilon^{1/2} = k_1\upsilon^{1/2} + k_2$$

Then, k_1 and k_2 correspond to the slope and the intercept value of i(V)/$\upsilon^{1/2}$ versus $\upsilon^{1/2}$ plot, respectively. According to above analysis, capacitive contribution part and diffusion contribution part can be quantitatively determined [26]. **Fig. 6.5b** shows the comparison of capacitive current (blue area) and the total current response obtained at a scan rate of 30 mV s^{-1}. It can be seen the capacitive contribution accounts for 57%. Similarly, the capacitive to diffusion contribution ratios at different scan rates were differentiated and summarized in **Fig. 6.5c**. It can be found that the capacitive contribution increases with the increase of the scan rates, a capacitive contribution of 67% can be reached at 50 mV s^{-1}. The enhanced capacitive contribution should be associated with the changed particle size and conductive matrix as reported [20, 259]. This feature might be attributed to the high-rate and long-term cycling performance of the NCS/graphene composite, as proved in the previous study [254].

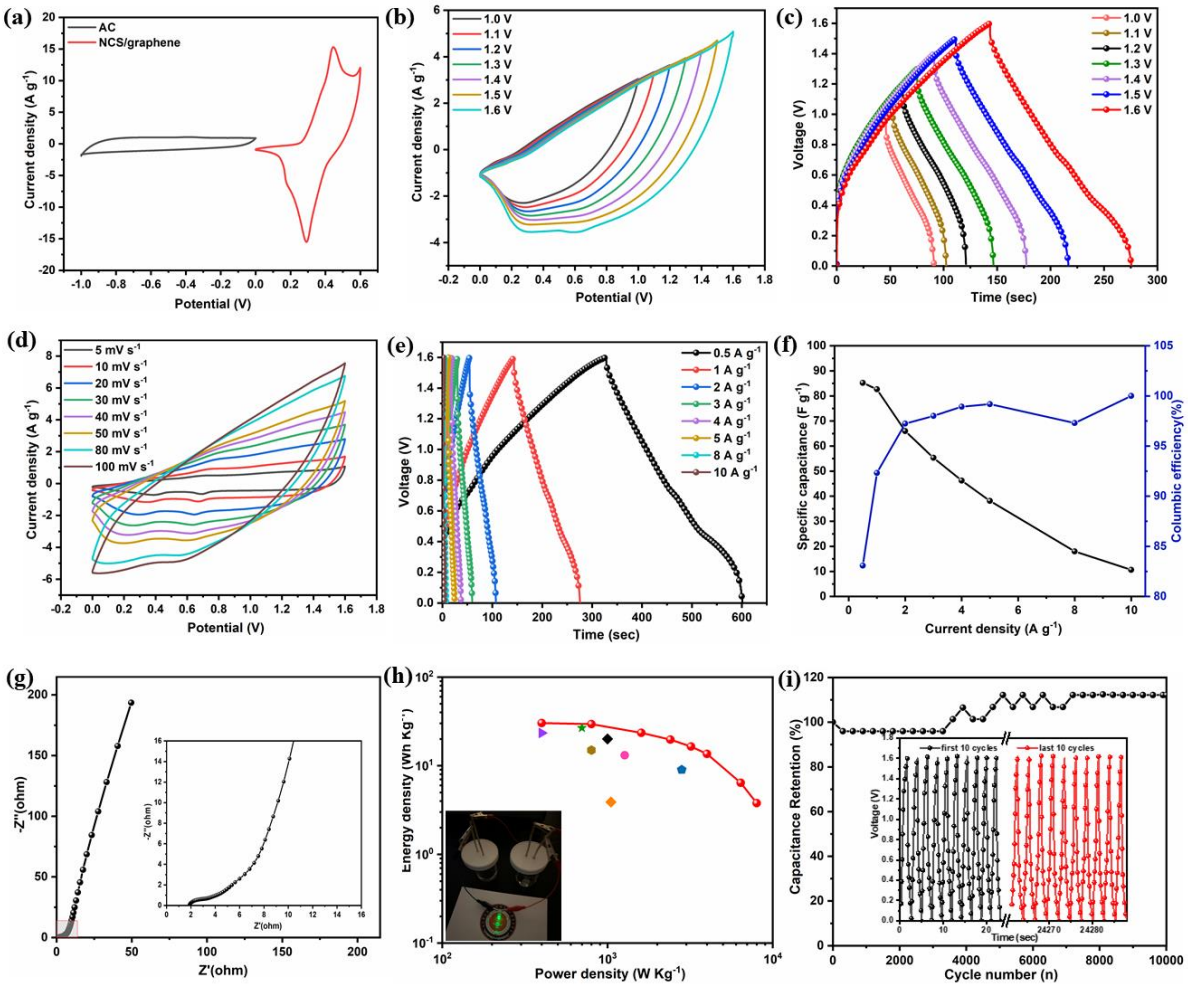

Figure 6. 6 (a) CV curves of NCS/graphene and AC electrodes tested in three-electrode system with a scan rate of 10 mV s^{-1}; (b) CV curves of the NCS/graphene//AC ASC at different voltage windows with a scan rate of 50 mV s^{-1}; (c) GCD curves of the NCS/graphene//AC ASC in various voltage windows at a current density of 1 A g^{-1}; (d) CV curves of NCS/graphene//AC ASC at various scan rates within the voltage window of 0 - 1.6 V; (e) GCD curves of NCS/graphene//AC ASC at different current densities between the voltage window of 0 - 1.6 V; (f) the specific capacitances and coulombic efficiencies of the ASC at different current densities; (g) the Nyquist plot of the ASC; (h) the Ragone plot of the NCS/graphene//AC ASC; (i) the cycling stability and coulombic efficiency of the NCS/graphene//AC ASC at a current density of 10 A g^{-1}.

With a view to better investigate the synthesized NCS/graphene composites for practical application, an ASC was assembled in 3.0 M KOH electrolyte by applying NCS/graphene composite as the positive electrode and AC as the negative electrode. **Fig. 6.6a** shows the CV

curves of NCS/graphene composite and AC electrodes at a scan rate of 10 mV s^{-1} measured in the typical three-electrode system, respectively. It can be seen that the CV curve of AC electrode exhibits quasi-rectangular shape and the NCS/graphene electrode shows obvious redox peaks corresponding to their EDLC and pseudocapacitive charge storage mechanisms, respectively. Moreover, the operating voltage range of AC electrode and NCS/graphene electrode are identified as -1.0 to 0 V and 0 to 0.6 V, respectively, indicating the operating voltage window of NCS/graphene//AC ASC can be extended to be 1.6 V. A series of CV and GCD measurements were carried out to NCS/graphene//AC ASC to evaluate its electrochemical performance. **Figs. 6.6b** and 6.**6c** show the CV and GCD curves of NCS/graphene//AC ASC at potential windows from 0 - 1.0 V to 0 - 1.6 V. Both CV and GCD results indicate the ASC has a stable working potential window up to 1.6 V, corresponding well to the result of **Fig. 6.6a**. Thus, the 0 - 1.6 V voltage window was chosen for the electrochemical measurements of the ASC. **Fig. 6.6d** presents the CV curves of NCS/graphene//AC ASC at virous scan rates from 5 - 100 mV s^{-1} in the potential range of 0 to 1.6 V. The redox peaks and the quasi-rectangular feature can be seen at low scan rates, demonstrating both pseudo-capacitance and electric double layer capacitance contribute to the charge storage process of the ASC. **Fig. 6.6e** shows the GCD curves of NCS/graphene//AC ASC at different current densities from 0.5 - 10 A g^{-1} in the potential range of 0 to 1.6 V. The almost symmetrical shapes and low IR drops indicate the perfect reversibility and low internal resistance of the ASC [319]. The calculated specific capacitances and coulombic efficiencies of the ASC at different current densities are shown in **Fig. 6.6f**. The maximum specific capacitance can reach to 85 F g^{-1} at a current density of 0.5 A g^{-1} and the coulombic efficiency

can maintain over 83% at different current densities, demonstrating the excellent capacitive performance of the ASC. **Fig. 6.6g** displayed the Nyquist impedance plot of the ASC. From the magnified inset image, the small value of real axis intercepts and diameter of semicircle in the high-frequency region correspond to the low R_s (1.84 Ω) and R_{ct} (1.92 Ω), suggesting the rapid ions transfer rate. The vertically inclined line at low frequency region indicates the fast ion diffusion and capacitive properties of the ASC.

Energy density and power density are essential parameters for the evaluation of ASCs. The Ragone plot of the NCS/graphene//AC ASC is in **Fig. 6.6h**. The maximum energy density of the NCS/graphene//AC ASC can reach 30.29 W h kg^{-1} at a power density of 400 W kg^{-1}. Such excellent energy and power density property of NCS/graphene//AC ASC is superior to many other reported NCS-based ASCs, such as hierarchical flower-like $NiCo_2S_4$@polyaniline//AC (20 W h kg^{-1} at 1000 W kg^{-1}) [274], 3D self-supported coralline-like $CuCo_2S_4$@$NiCo_2S_4$//AC (23.4 W h kg^{-1} at 400 W kg^{-1}) [279], graphitized rice husk carbon (GRH) - $NiCo_2S_4$//AC (9 Wh kg^{-1} at 2812 W kg^{-1}) [271], $NiCo_2S_4$ nanoparticles//activated balsam pear pulp (3.9 W h kg^{-1} at 1050 W kg^{-1}) [320], $NiCo_2S_4$ NSs/P-g-C_3N_4//AC(15 W h kg^{-1} at 800 W kg^{-1}) [321], core-shell $NiCo_2S_4$//C (13.1 Wh kg^{-1} at 1270 W kg^{-1}) [322], $NiCo_2S_4$@NiO NWAs//AC (26.67 Wh kg^{-1} at 700 W kg^{-1})[323]. As shown in the inset of **Fig. 6.6h**, two of the series connected NCS/graphene//AC ASC devices can be used as the power supply to light the LED bulb, demonstrating its great potential in practical applications.

The cycling stability and columbic efficiency of the ASC are shown in **Fig. 6.6i**. After 10,000 cycles, the specific capacitance increased to 112% of the initial value demonstrating the

excellent stability of this ASC. As shown in the inset of **Fig. 6.6i**, the last ten charge/discharge cycles show a little bit longer charge/discharge time and have no obvious deformation when compared to the first ten cycles, verifying its excellent electrochemical stability. As the strong cycling stability of AC electrodes has been known, the outstanding cycling stability of the ASC should be due to the high stability of the NCS/graphene electrode and the shallow discharge process of the battery-type NCS/graphene electrode in this ASC setup [271]. Based on above discussion, the superior electrochemical performance of the NCS/graphene electrode might be mainly attributed to: 1) the highly conductive graphene substrates in this positive electrode composite worked as conductive medium, made these NCS particles well connected, and allowed facile ion diffusion which guarantees the efficient participation of each NCS particle in the redox reaction process; 2) the high strength and stable graphene substrates can also act as holder to support the NCS particles in a more stable state. Considering the high energy density and excellent cycling stability, the NCS/graphene//AC ASC shows great potential to be used for practical energy storage applications.

6.4 Conclusions

In summary, we successfully developed an ultra-fast and one-step microwave method for the synthesis of high-performance NCS/graphene hybrid material in a single minute. The effect of synthesis conditions including feeding mass ratio of NCS precursor to graphene, microwave power and irradiation time on the morphology, crystalline structures and electrochemical performance of the as-prepared NCS/graphene composites were systematically investigated. The results showed that the optimal NCS/graphene composite can be prepared by at 1000W

microwave power in 60 s irradiation time with a 1:1 feeding mass ratio of NCS precursor to graphene. The optimized NCS/graphene composite can be used as an excellent electrode material for supercapacitors which exhibited a high specific capacitance of 710 g^{-1} at 0.5 A g^{-1} and good cycling stability (75 % capacitance retention after 10,000 cycles). Moreover, a high-performance asymmetric supercapacitor was assembled by using NCS/graphene composite as positive electrode and AC as negative electrode which can be reversibly charged and discharged at an extended potential window of 1.6 V. Importantly, the NCS/graphene//AC ASC can deliver a high energy density of 30.29 W h kg^{-1} at a power density of 400 W kg^{-1}. Intriguingly, the specific capacitance retention rate of the ASC can achieve at 112% after 10,000 continuous charge/discharge cycles. Therefore, this work demonstrates a simple and ultrafast one-step microwave synthesis method to construct the uniformly distributed NCS/graphene composites as promising electrode materials for high-performance asymmetrical supercapacitors.

Chapter 7

Conclusions and outlook

High-performance supercapacitors with fast charging rate, high power density and energy density, long cycle life and enhanced safety and efficiency are crucial for the energy storage applications. However, the currently commercialized supercapacitors with limited capacitance, energy density and cycling durability cannot satisfy the increasing requirement. Thus, many researchers have focused on enhancing the electrochemical performance of supercapacitors by preparing various kinds of electrode materials through different methods. Under this situation, my research work is devoted to finding facile and effective ways to improve the electrochemical performance of electrode materials by different methods.

Conducting polymers with many superior features have been considered as promising electrode materials for pseudocapacitors. However, the poor cycling stability of conducting polymers caused by the structural damage during the repeating charge/discharge processes impedes their further application. As the charge/discharge process is a typical doping/dedoping process for conducting polymers-based electrode materials. The dopants used during the polymerization process could have a great effect on the electrochemical properties of conducting polymers-based electrodes. Thus, we investigated the influence of several commonly used acid dopants (HCl, $HClO_4$, H_2SO_4, p-TSA, H_3PO_4 and PA) on the electrochemical performance of widely studied conductive polymers: PPy and PANI. The results show that different dopants could have different effects on the capacitance and cycle performance for PPy and PANI electrodes.

Interestingly, for PPy and PANI electrodes, the dopant of p-TSA could provide the best cycling stability and with relatively high specific capacitances and both can be used as electrodes for flexible supercapacitor. This enhanced cycling stability might be due to the presence of aromatic ring in p-TSA dopant could form π- π stacking within the molecule along the polymer chain obtaining the most stable structures. These fundamental studies supplied a simple way to get conducting polymers-based electrodes with excellent capacitance and superior cycling stabilities. Based on the outcomes of above study, we can expand this method to other commonly used conductive polymer materials, such as PEDOT and PPV. Hopefully, more and more high-performance conducting polymers and their composites electrodes can be prepared by this simple method in the future.

In addition to conductive polymers, transition metal compounds are regarded as one of the important electrode materials, especially transition metal sulfides and transition metal phosphides. As the commonly used synthetic methods of transition metal compounds are complex and time-consuming. Therefore, we tried two different simple methods for the preparation of transition metal phosphide (Mn-CoP) and transition metal sulfide composites (NCS/graphene) electrodes, respectively. The Mn-CoP nanosheets electrode was successfully synthesized by a simple in-situ electrodeposition method and the NCS/graphene hybrid material was successfully prepared through a simple microwave method. Both transition metal-based electrodes can be used as high-performance anode electrodes for asymmetric supercapacitor. I hope the research results could provide a meaningful reference for the synthesis of transition metal-based electrode materials in the future.

Reference:

1. Aziz, M. M. A.; Kassim, K. A.; Shokravi, Z.; Jakarni, F. M.; Liu, H. Y.; Zaini, N.; Tan, L. S.; Islam, A. B. M. S.; Shokravi, H., Two-stage cultivation strategy for simultaneous increases in growth rate and lipid content of microalgae: A review. *Renew. Sust. Energ. Rev.* **2020,** *119*, 109621.
2. Okolie, J. A.; Nanda, S.; Dalai, A. K.; Berruti, F.; Kozinski, J. A., A review on subcritical and supercritical water gasification of biogenic, polymeric and petroleum wastes to hydrogen-rich synthesis gas. *Renew. Sust. Energ. Rev.* **2020,** *119*, 109546.
3. Bruce, P. G.; Freunberger, S. A.; Hardwick, L. J.; Tarascon, J. M., Li-O_2 and Li-S batteries with high energy storage. *Nat. Mater.* **2011,** *11* (1), 19-29.
4. Wang, X.; Chen, Y.; Schmidt, O. G.; Yan, C., Engineered nanomembranes for smart energy storage devices. *Chem. Soc. Rev.* **2016,** *45* (5), 1308-30.
5. Díaz-González, F.; Sumper, A.; Gomis-Bellmunt, O.; Villafáfila-Robles, R., A review of energy storage technologies for wind power applications. *Renew. Sust. Energ. Rev.* **2012,** *16* (4), 2154-2171.
6. Balogun, M.-S.; Qiu, W.; Wang, W.; Fang, P.; Lu, X.; Tong, Y., Recent advances in metal nitrides as high-performance electrode materials for energy storage devices. *J. Mater. Chem. A* **2015,** *3* (4), 1364-1387.
7. Luo, X.; Wang, J.; Dooner, M.; Clarke, J., Overview of current development in electrical energy storage technologies and the application potential in power system operation. *Appl. Energy* **2015,** *137*, 511-536.
8. Zhang, L. L.; Gu, Y.; Zhao, X. S., Advanced porous carbon electrodes for electrochemical capacitors. *J. Mater. Chem. A* **2013,** *1* (33), 9395.
9. Divya, M. L.; Natarajan, S.; Lee, Y. S.; Aravindan, V., Biomass-Derived Carbon: A value-added journey towards constructing high-energy supercapacitors in an asymmetric fashion. *ChemSusChem* **2019,** *12* (19), 4353-4382.
10. Liu, C.; Neale, Z. G.; Cao, G., Understanding electrochemical potentials of cathode materials in rechargeable batteries. *Mater. Today* **2016,** *19* (2), 109-123.
11. Hamideh Vaghari, H. J.-M., Aydin Berenjian and Navideh Anarjan, Recent advances in application of chitosan in fuel cells. *Sustain. Chem. Process* **2013,** *1*, 16.
12. Chen, X.; Paul, R.; Dai, L., Carbon-based supercapacitors for efficient energy storage. *Natl. Sci. Rev.* **2017,** *4* (3), 453-489.
13. Song, Z.; Zhou, H., Towards sustainable and versatile energy storage devices: an overview of organic electrode materials. *Energy Environ. Sci.* **2013,** *6* (8), 2280.
14. Zhu, A. L.; Wilkinson, D. P.; Zhang, X.; Xing, Y.; Rozhin, A. G.; Kulinich, S. A., Zinc regeneration in rechargeable zinc-air fuel cells-A review. *J. Energy Storage* **2016,** *8*, 35-50.
15. Raza, W.; Ali, F.; Raza, N.; Luo, Y.; Kim, K.-H.; Yang, J.; Kumar, S.; Mehmood, A.; Kwon, E. E., Recent advancements in supercapacitor technology. *Nano Energy* **2018,** *52*, 441-473.
16. Zhang, S.; Pan, N., Supercapacitors Performance Evaluation. *Adv. Energy Mater.* **2015,** *5* (6), 1401401.
17. Hu, P.; Zhao, D.; Liu, H.; Chen, K.; Wu, X., Engineering PPy decorated $MnCo_2O_4$ urchins

for quasi-solid-state hybrid capacitors. *CrystEngComm* **2019,** *21* (10), 1600-1606.
18. Zhang, L. L.; Zhao, X. S., Carbon-based materials as supercapacitor electrodes. *Chem. Soc. Rev.* **2009,** *38* (9), 2520-31.
19. Lee, B. J.; Sivakkumar, S. R.; Ko, J. M.; Kim, J. H.; Jo, S. M.; Kim, D. Y., Carbon nanofibre/hydrous RuO2 nanocomposite electrodes for supercapacitors. *J. Power Sources* **2007,** *168* (2), 546-552.
20. Augustyn, V.; Simon, P.; Dunn, B., Pseudocapacitive oxide materials for high-rate electrochemical energy storage. *Energy Environ. Sci.* **2014,** *7* (5), 1597.
21. Thierry Brousse, D. B. e., and Jeffrey W. Long, To be or not to be pseudocapacitive? *J. Electrochem. Soc.* **2015,** *162* (5), A5185-A5189.
22. Shao, Y.; El-Kady, M. F.; Sun, J.; Li, Y.; Zhang, Q.; Zhu, M.; Wang, H.; Dunn, B.; Kaner, R. B., Design and mechanisms of asymmetric supercapacitors. *Chem. Rev.* **2018,** *118* (18), 9233-9280.
23. Da Silva, L. M.; Cesar, R.; Moreira, C. M. R.; Santos, J. H. M.; De Souza, L. G.; Pires, B. M.; Vicentini, R.; Nunes, W.; Zanin, H., Reviewing the fundamentals of supercapacitors and the difficulties involving the analysis of the electrochemical findings obtained for porous electrode materials. *Energy Storage Mater.* **2019**.
24. Liu, J.; Wang, J.; Xu, C.; Jiang, H.; Li, C.; Zhang, L.; Lin, J.; Shen, Z. X., Advanced energy storage devices: basic principles, analytical methods, and rational materials design. *Adv. Sci.* **2018,** *5* (1), 1700322.
25. Augustyn, V.; Come, J.; Lowe, M. A.; Kim, J. W.; Taberna, P. L.; Tolbert, S. H.; Abruna, H. D.; Simon, P.; Dunn, B., High-rate electrochemical energy storage through Li^+ intercalation pseudocapacitance. *Nat. Mater.* **2013,** *12* (6), 518-22.
26. Huang, H.; Niederberger, M., Towards fast-charging technologies in Li(+)/Na(+) storage: from the perspectives of pseudocapacitive materials and non-aqueous hybrid capacitors. *Nanoscale* **2019,** *11* (41), 19225-19240.
27. Noori, A.; El-Kady, M. F.; Rahmanifar, M. S.; Kaner, R. B.; Mousavi, M. F., Towards establishing standard performance metrics for batteries, supercapacitors and beyond. *Chem. Soc. Rev.* **2019,** *48* (5), 1272-1341.
28. Rocha, V. G.; Garcia-Tunon, E.; Botas, C.; Markoulidis, F.; Feilden, E.; D'Elia, E.; Ni, N.; Shaffer, M.; Saiz, E., Multimaterial 3D printing of graphene-based electrodes for electrochemical energy storage using thermoresponsive inks. *ACS Appl. Mater. Interfaces* **2017,** *9* (42), 37136-37145.
29. J. Gamby, P. L. T., P. Simon, J.F. Fauvarque, M. Chesneau, Studies and characterisations of various activated carbons used for carbon/carbon supercapacitors. *J. Power Sources* **2001,** *101*, 109-116.
30. Yau-Ren Nian, H. T., Influence of surface oxides on the impedance behavior of carbonbased electrochemical capacitors. J. Electroanal. Chem. **2003,** *540*, 119-127.
31. Poonam; Sharma, K.; Arora, A.; Tripathi, S. K., Review of supercapacitors: Materials and devices. *J. Energy Storage* **2019,** *21*, 801-825.
32. S. Iro, Z., A brief review on electrode materials for supercapacitor. *Int. J. Electrochem. Sci.* **2016**, 10628-10643.
33. Miller, E. E.; Hua, Y.; Tezel, F. H., Materials for energy storage: review of electrode

materials and methods of increasing capacitance for supercapacitors. *J. Energy Storage* **2018,** *20*, 30-40.
34. Raymundo-Piñero, E.; Kierzek, K.; Machnikowski, J.; Béguin, F., Relationship between the nanoporous texture of activated carbons and their capacitance properties in different electrolytes. *Carbon* **2006,** *44* (12), 2498-2507.
35. Gregory Salitra, A. S., Linoam Eliad, Yair Cohen, and Doron Aurbach, Carbon electrodes for double-layer capacitors: relations between ion and pore dimensions. *J. Electrochem. Soc.* **2000,** *147*, 2486-2493.
36. Frackowiak, E.; Metenier, K.; Bertagna, V.; Beguin, F., Supercapacitor electrodes from multiwalled carbon nanotubes. *Appl. Phys. Lett.* **2000,** *77* (15), 2421-2423.
37. Kay Hyeok An, W. S. K., Young Soo Park, Jeong-Mi Moon, Dong Jae Bae, Seong Chu Lim, Young Seak Lee, and Young Hee Lee, Electrochemical properties of high-power supercapacitors using single-walled carbon nanotube electrodes. *Adv. Funct. Mater.* **2001,** *11*, 387-392.
38. Vangari, M.; Pryor, T.; Jiang, L., Supercapacitors: review of materials and fabrication methods. *J. Energy Eng.* **2013,** *139* (2), 72-79.
39. K. S. Novoselov, A. K. G., S. V. Morozov, D. Jiang, Y. Zhang,S. V. Dubonos, V. Grigorieva, A. A. Firsov, Electric field effect in atomically thin carbon films. *Science* **2004,** *306*, 666-669.
40. Ma, Y.; Chang, H.; Zhang, M.; Chen, Y., Graphene-based materials for lithium-ion hybrid supercapacitors. *Adv. Mater.* **2015,** *27* (36), 5296-308.
41. Liu, C.; Yu, Z.; Neff, D.; Zhamu, A.; Jang, B. Z., Graphene-based supercapacitor with an ultrahigh energy density. *Nano Lett.* **2010,** *10* (12), 4863-8.
42. Tae Young Kim, H. W. L., Meryl Stoller, Daniel R. Dreyer, Rodney S. Ruoff, and Kwang S. Suh, High-Performance Supercapacitors Based on Poly(ionic liquid)-Modified Graphene Electrodes. *ACS Nano* **2011,** *5*, 436-442.
43. Hideki S., Edwin J. L., Alan G. M., Chwan K. C., Alan J. H., Synthesis of electrically conducting organic polymers : halogen derivatives of polyacetylene, (CH)x. *J. Chem. Soc., Chem. Commun.* **1977**, 578-580.
44. Meng, Q.; Cai, K.; Chen, Y.; Chen, L., Research progress on conducting polymer based supercapacitor electrode materials. *Nano Energy* **2017,** *36*, 268-285.
45. Xia, C.; Chen, W.; Wang, X.; Hedhili, M. N.; Wei, N.; Alshareef, H. N., Highly stable supercapacitors with conducting polymer core-shell electrodes for energy storage applications. *Adv. Energy Mater.* **2015,** *5* (8), 1401805.
46. Wang, M.; Xu, Y. X., Design and construction of three-dimensional graphene/conducting polymer for supercapacitors. *Chin. Chem. Lett.* **2016,** *27* (8), 1437-1444.
47. Baker, C. O.; Huang, X.; Nelson, W.; Kaner, R. B., Polyaniline nanofibers: broadening applications for conducting polymers. *Chem. Soc. Rev.* **2017,** *46* (5), 1510-1525.
48. Hu C., Chang K., Lin M., Wu Y., Design and tailoring of the nanotubular arrayed architecture of hydrous RuO_2 for next generation supercapacitors. *Nano Lett.* **2006,** *6*, 2690-2695.
49. Ragupathy P., Campet G., Vasan H., Hwang S., Choy J., Munichandraiah N., Remarkable capacity retention of nanostructured manganese oxide upon cycling as an electrode material for supercapacitor. *J. Phys. Chem. C* **2009,** *113*, 6303–6309.

50. Song M., Lee Y., Kim I., Kim T., Gunjakar J., . Hwang S., porously assembled 2D nanosheets of alkali metal manganese oxides with highly reversible pseudocapacitance behaviors. *J. Phys. Chem. C* **2010,** *114*, 22134-22140.
51. Oyama, S. T.; Gott, T.; Zhao, H.; Lee, Y.K., Transition metal phosphide hydroprocessing catalysts: A review. *Catal. Today* **2009,** *143* (1-2), 94-107.
52. Mirghni, A. A.; Madito, M. J.; Masikhwa, T. M.; Oyedotun, K. O.; Bello, A.; Manyala, N., Hydrothermal synthesis of manganese phosphate/graphene foam composite for electrochemical supercapacitor applications. *J. Colloid Interface Sci.* **2017,** *494*, 325-337.
53. Li, G.; Ji, Y.; Zuo, D.; Xu, J.; Zhang, H., Carbon electrodes with double conductive networks for high-performance electrical double-layer capacitors. *Adv. Compos. Hybrid Mater.* **2019,** *2* (3), 456-461.
54. Zong, Q.; Liu, C.; Yang, H.; Zhang, Q.; Cao, G., Tailoring nanostructured transition metal phosphides for high-performance hybrid supercapacitors. *Nano Today* **2021,** *38*, 101201.
55. Li, X.; Elshahawy, A. M.; Guan, C.; Wang, J., Metal phosphides and phosphates-based electrodes for electrochemical supercapacitors. *Small* **2017,** *13* (39).
56. Zhou, K.; Zhou, W.; Yang, L.; Lu, J.; Cheng, S.; Mai, W.; Tang, Z.; Li, L.; Chen, S., Ultrahigh-performance pseudocapacitor electrodes based on transition metal phosphide nanosheets array via phosphorization: a general and effective approach. *Adv. Funct. Mater.* **2015,** *25* (48), 7530-7538.
57. Jin, Y.; Zhao, C.; Jiang, Q.; Ji, C., Mesoporous NiCoP microflowers as a superior electrode material for supercapacitors. *Appl. Surf. Sci.* **2018,** *450*, 170-179.
58. Lei, X.; Ge, S.; Tan, Y.; Wang, Z.; Li, J.; Li, X.; Hu, G.; Zhu, X.; Huang, M.; Zhu, Y.; Xiang, B., High capacity and energy density of Zn-Ni-Co-P nanowire arrays as an advanced electrode for aqueous asymmetric supercapacitor. *ACS Appl. Mater. Interfaces* **2020,** *12* (8), 9158-9168.
59. Saleh, A. A.; Amer, A.; Sayed, D. M.; Allam, N. K., A facile electrosynthesis approach of Mn-Ni-Co ternary phosphides as binder-free active electrode materials for high-performance electrochemical supercapacitors. *Electrochim.Acta* **2021,** *380*, 138197.
60. Muralee Gopi, C. V. V.; Ravi, S.; Rao, S. S.; Eswar Reddy, A.; Kim, H. J., Carbon nanotube/metal-sulfide composite flexible electrodes for high-performance quantum dot-sensitized solar cells and supercapacitors. *Sci. Rep.* **2017,** *7*, 46519.
61. Sahoo, S.; Rout, C. S., Facile electrochemical synthesis of porous manganese-cobalt-sulfide based ternary transition metal sulfide nanosheets architectures for high performance energy storage applications. *Electrochim. Acta* **2016,** *220*, 57-66.
62. Zhu, C.; Kopold, P.; Li, W.; van Aken, P. A.; Maier, J.; Yu, Y., A general strategy to fabricate carbon-coated 3D porous interconnected metal sulfides: case study of SnS/C nanocomposite for high-performance lithium and sodium ion batteries. *Adv. Sci.* **2015,** *2* (12), 1500200.
63. Wang, T.; Chen, H. C.; Yu, F.; Zhao, X. S.; Wang, H., Boosting the cycling stability of transition metal compounds-based supercapacitors. *Energy Stor. Mater.* **2019,** *16*, 545-573.
64. Acerce, M.; Voiry, D.; Chhowalla, M., Metallic 1T phase MoS_2 nanosheets as supercapacitor electrode materials. *Nat .Nano technol.* **2015,** *10* (4), 313-8.
65. Feng, J.; Sun, X.; Wu, C.; Peng, L.; Lin, C.; Hu, S.; Yang, J.; Xie, Y., Metallic few-layered VS_2 ultrathin nanosheets: high two-dimensional conductivity for in-plane supercapacitors. *J.*

Am. Chem. Soc. **2011,** *133* (44), 17832-8.
66. Tong, H.; Bai, W.; Yue, S.; Gao, Z.; Lu, L.; Shen, L.; Dong, S.; Zhu, J.; He, J.; Zhang, X., Zinc cobalt sulfide nanosheets grown on nitrogen-doped graphene/carbon nanotube film as a high-performance electrode for supercapacitors. *J. Mater. Chem. A* **2016,** *4* (29), 11256-11263.
67. Fan, L.Q.; Pan, F.; Tu, Q.M.; Gu, Y.; Huang, J.L.; Huang, Y.F.; Wu, J.H., Synthesis of $CuCo_2S_4$ nanosheet arrays on Ni foam as binder-free electrode for asymmetric supercapacitor. *Int. J. Hydrog. Energy* **2018,** *43* (52), 23372-23381.
68. Gao, Y. P.; Huang, K. J., $NiCo_2S_4$ materials for supercapacitor applications. *Chem. Asian J.* **2017,** *12* (16), 1969-1984.
69. Geng, P.; Zheng, S.; Tang, H.; Zhu, R.; Zhang, L.; Cao, S.; Xue, H.; Pang, H., Transition metal sulfides based on graphene for electrochemical energy storage. *Adv. Energy Mater.* **2018,** *8* (15), 1703259.
70. Wang, M.; Wang, Y.; Dou, H.; Wei, G.; Wang, X., Enhanced rate capability of nanostructured three-dimensional graphene/Ni_3S_2 composite for supercapacitor electrode. *Ceram. Int.* **2016,** *42* (8), 9858-9865.
71. Yuan, H.; Kong, L.; Li, T.; Zhang, Q., A review of transition metal chalcogenide/graphene nanocomposites for energy storage and conversion. *Chin. Chem. Lett.* **2017,** *28* (12), 2180-2194.
72. Tian, Y.; Du, H.; Zhang, M.; Zheng, Y.; Guo, Q.; Zhang, H.; Luo, J.; Zhang, X., Microwave synthesis of MoS_2/MoO_2@CNT nanocomposites with excellent cycling stability for supercapacitor electrodes. *J. Mater. Chem. C* **2019,** *7* (31), 9545-9555.
73. Wang, Q.; Zhang, D.; Wu, Y.; Li, T.; Zhang, A.; Miao, M., Fabrication of supercapacitors from $NiCo_2O_4$ nanowire/carbon-nanotube yarn for ultraviolet photodetectors and portable electronics. *Energy Technol.* **2017,** *5* (8), 1449-1456.
74. Jin, C.; Cui, Y.; Zhang, G.; Luo, W.; Liu, Y.; Sun, Y.; Tian, Z.; Zheng, W., Synthesis of copper-cobalt hybrid oxide microflowers as electrode material for supercapacitors. *Chem. Eng. J.* **2018,** *343*, 331-339.
75. Lahyani, A.; Venet, P.; Guermazi, A.; Troudi, A., Battery/supercapacitors combination in uninterruptible power supply (UPS). *IEEE Trans. Power Electron.* **2013,** *28* (4), 1509-1522.
76. Wei, M.M.; Li, W.P.; Weng, J.; Liu, Y.Q.; Li, S.R.; Ye, Y.Y.; Wang, M.; Wang, D., Mesopore-dominant porous carbon derived from bio-tars as an electrode material for high-performance supercapacitors. *J. Saudi Chem. Soc.* **2019**.
77. Zhang, Y.; Feng, H.; Wu, X.; Wang, L.; Zhang, A.; Xia, T.; Dong, H.; Li, X.; Zhang, L., Progress of electrochemical capacitor electrode materials: a review. *Int. J. Hydrog. Energy* **2009,** *34* (11), 4889-4899.
78. Xue, D.; Zhu, D.; Duan, H.; Wang, Z.; Lv, Y.; Xiong, W.; Li, L.; Liu, M.; Gan, L., Deep-eutectic-solvent synthesis of N/O self-doped hollow carbon nanorods for efficient energy storage. *Chem. Commun.* **2019,** *55* (75), 11219-11222.
79. Miao, L.; Duan, H.; Wang, Z.; Lv, Y.; Xiong, W.; Zhu, D.; Gan, L.; Li, L.; Liu, M., Improving the pore-ion size compatibility between poly(ionic liquid)-derived carbons and high-voltage electrolytes for high energy-power supercapacitors. *Chem. Engin. J.* **2020,** *382*, 122945.
80. Song, Z.; Duan, H.; Zhu, D.; Lv, Y.; Xiong, W.; Cao, T.; Li, L.; Liu, M.; Gan, L., Ternary-

doped carbon electrodes for advanced aqueous solid-state supercapacitors based on a "water-in-salt" gel electrolyte. *J. Mater. Chem. A* **2019,** *7* (26), 15801-15811.
81. Chen, W.; Tao, X.; Li, Y.; Wang, H.; Wei, D.; Ban, C., Hydrothermal synthesis of graphene-MnO_2-polyaniline composite and its electrochemical performance. *J. Mater. Sci. Mater. Electron.* **2016,** *27* (7), 6816-6822.
82. Dhawale, D. S.; Vinu, A.; Lokhande, C. D., Stable nanostructured polyaniline electrode for supercapacitor application. *Electrochim.Acta* **2011,** *56* (25), 9482-9487.
83. Huang, Y.; Li, H.; Wang, Z.; Zhu, M.; Pei, Z.; Xue, Q.; Huang, Y.; Zhi, C., Nanostructured polypyrrole as a flexible electrode material of supercapacitor. *Nano Energy* **2016,** *22*, 422-438.
84. Zhang, L.; Du, W.; Nautiyal, A.; Liu, Z.; Zhang, X., Recent progress on nanostructured conducting polymers and composites: synthesis, application and future aspects. *Sci. China Mater.* **2018,** *61* (3), 303-352.
85. Nautiyal, A.; Qiao, M.; Cook, J. E.; Zhang, X.; Huang, T.S., High performance polypyrrole coating for corrosion protection and biocidal applications. *Appl. Surf. Sci.* **2018,** *427*, 922-930.
86. Nautiyal, A.; Cook, J. E.; Zhang, X., Tunable electrochemical performance of polyaniline coating via facile ion exchanges. Prog. Org. Coat. **2019,** *136*, 105309.
87. Wang, L.; Zhang, C.; Jiao, X.; Yuan, Z., Polypyrrole-based hybrid nanostructures grown on textile for wearable supercapacitors. *Nano Res.* **2019,** *12* (5), 1129-1137.
88. Fujii, S.; Matsuzawa, S.; Nakamura, Y., One-pot synthesis of conducting polymer-coated latex particles: ammonium persulfate as free radical initiator and chemical oxidant. *Chem. Commun.* **2010,** *46* (38), 7217-9.
89. Wei, H.; Wang, Y.; Guo, J.; Yan, X.; O'Connor, R.; Zhang, X.; Shen, N. Z.; Weeks, B. L.; Huang, X.; Wei, S.; Guo, Z., Electropolymerized Polypyrrole Nanocoatings on Carbon Paper for Electrochemical Energy Storage. *ChemElectroChem* **2015,** *2* (1), 119-126.
90. Rajesh, M.; Raj, C. J.; Kim, B. C.; Cho, B.-B.; Ko, J. M.; Yu, K. H., Supercapacitive studies on electropolymerized natural organic phosphate doped polypyrrole thin films. *Electrochim. Acta* **2016,** *220*, 373-383.
91. Wolfart, F.; Dubal, D. P.; Vidotti, M.; Holze, R.; Gómez-Romero, P., Electrochemical supercapacitive properties of polypyrrole thin films: influence of the electropolymerization methods. *J. Solid State Electrochem.* **2015,** *20* (4), 901-910.
92. Sui, X.; Feng, X.; Hempenius, M. A.; Vancso, G. J., Redox active gels: synthesis, structures and applications. *J. Mater. Chem. B* **2013,** *1* (12), 1658.
93. Li, S.; Qiu, Y.; Guo, X., Influence of doping anions on the ion exchange behavior of polypyrrole. *J. Appl. Polym. Sci.* **2009,** *114* (4), 2307-2314.
94. Chen, Y.; Zhang, X.; Juan Li, J.; Xu, H., Electrodeposition of PPy/HNO_3 film and its capacitive behaviour. *IOP Conference Series: Materials Science and Engineering* **2019,** *484*, 012045.
95. Lang, X.; Wan, Q.; Feng, C.; Yue, X.; Xu, W.; Li, J.; Fan, S., The role of anthraquinone sulfonate dopants in promoting performance of polypyrrole composites as pseudo-capacitive electrode materials. *Synth. Met.* **2010,** *160* (15-16), 1800-1804.
96. Chen, L.; Chen, L.; Ai, Q.; Li, D.; Si, P.; Feng, J.; Zhang, L.; Li, Y.; Lou, J.; Ci, L., Flexible all-solid-state supercapacitors based on freestanding, binder-free carbon nanofibers@polypyrrole@graphene film. *Chem. Eng. Sci.* **2018,** *334*, 184-190.

97. Orangi, J.; Hamade, F.; Davis, V. A.; Beidaghi, M., 3D printing of additive-free 2D $Ti_3C_2T_x$ (MXene) ink for fabrication of micro-supercapacitors with ultra-high energy densities. *ACS Nano* **2020,** *14* (1), 640-650.
98. Xu, J.; Yang, C.; Xue, Y.; Wang, C.; Cao, J.; Chen, Z., Facile synthesis of novel metal-organic nickel hydroxide nanorods for high performance supercapacitor. *Electrochim. Acta* **2016,** *211*, 595-602.
99. Hou, M.; Xu, M.; Hu, Y.; Li, B., Nanocellulose incorporated graphene/polypyrrole film with a sandwich-like architecture for preparing flexible supercapacitor electrodes. *Electrochim. Acta* **2019,** *313*, 245-254.
100. Kausaite-Minkstimiene, A.; Mazeiko, V.; Ramanaviciene, A.; Ramanavicius, A., Evaluation of chemical synthesis of polypyrrole particles. *Colloids and Surfaces A: Physicochem. Eng. Aspects* **2015,** *483*, 224-231.
101. Dhibar, S.; Sahoo, S.; Das, C. K., Fabrication of transition-metal-doped polypyrrole/multiwalled carbon nanotubes nanocomposites for supercapacitor applications. *J. Appl. Polym. Sci.* **2013,** *130* (1), 554-562.
102. P. A. Herrera Herreraa, N. C. S., J. A. Martínezc, Electrosynthesis and DSC characterization of doped polypyrrole films with sodium salicylate and sodium ibuprofen on the Mg alloy AZ31. *ECS Trans.* **2018,** *84* (1), 243-256.
103. Lee, S. H.; Lee, S.; Ryu, H. W.; Park, H.; Kim, Y. S.; Kim, J. H., Synthesis andin situdoping of highly conductive polypyrrole nanocomplexes with binary acids. *J. Polym. Sci. A Polym. Chem.* **2014,** *52* (16), 2329-2336.
104. Cruz-Silva, R.; Amaro, E.; Escamilla, A.; Nicho, M. E.; Sepulveda-Guzman, S.; Arizmendi, L.; Romero-Garcia, J.; Castillon-Barraza, F. F.; Farias, M. H., Biocatalytic synthesis of polypyrrole powder, colloids, and films using horseradish peroxidase. *J. Colloid Interface Sci.* **2008,** *328* (2), 263-9.
105. Ansari, M. O.; Mohammad, F., Thermal stability, electrical conductivity and ammonia sensing studies on p-toluenesulfonic acid doped polyaniline:titanium dioxide (pTSA/Pani:TiO_2) nanocomposites. *Sens. Actuators B Chem.* **2011,** *157* (1), 122-129.
106. Dai, H.; Wang, N.; Wang, D.; Ma, H.; Lin, M., An electrochemical sensor based on phytic acid functionalized polypyrrole/graphene oxide nanocomposites for simultaneous determination of Cd(II) and Pb(II). *Chem. Eng. J.* **2016,** *299*, 150-155.
107. Pan, F.; Yang, X.; Zhang, D., Chemical nature of phytic acid conversion coating on AZ61 magnesium alloy. *Appl. Surf. Sci.* **2009,** *255* (20), 8363-8371.
108. Wang, N.; Dai, H.; Wang, D.; Ma, H.; Lin, M., Determination of copper ions using a phytic acid/polypyrrole nanowires modified glassy carbon electrode. *Mater. Sci. Eng. C Mater. Biol. Appl.* **2017,** *76*, 139-143.
109. Ding, C.; Qian, X.; Yu, G.; An, X., Dopant effect and characterization of polypyrrole-cellulose composites prepared by in situ polymerization process. *Cellulose* **2010,** *17* (6), 1067-1077.
110. Setka, M.; Calavia, R.; Vojkuvka, L.; Llobet, E.; Drbohlavova, J.; Vallejos, S., Raman and XPS studies of ammonia sensitive polypyrrole nanorods and nanoparticles. *Sci. Rep.* **2019,** *9* (1), 8465.
111. Konwar, L. J.; Samikannu, A.; Mäki Arvela, P.; Mikkola, J. P., Efficient C-C coupling of

bio-based furanics and carbonyl compounds to liquid hydrocarbon precursors over lignosulfonate derived acidic carbocatalysts. *Catal. Sci. Technol.* **2018,** *8* (9), 2449-2459.
112. Peng, S.; Fan, L.; Wei, C.; Liu, X.; Zhang, H.; Xu, W.; Xu, J., Flexible polypyrrole/copper sulfide/bacterial cellulose nanofibrous composite membranes as supercapacitor electrodes. *Carbohydr. Polym.* **2017,** *157*, 344-352.
113. Xu, C.; Sun, J.; Gao, L., Synthesis of novel hierarchical graphene/polypyrrole nanosheet composites and their superior electrochemical performance. *J. Mater. Chem.* **2011,** *21* (30), 11253.
114. Shu, K.; Chao, Y.; Chou, S.; Wang, C.; Zheng, T.; Gambhir, S.; Wallace, G. G., A "tandem" strategy to fabricate flexible graphene/polypyrrole nanofiber film using the surfactant-exfoliated graphene for supercapacitors. *ACS Appl. Mater. Interfaces* **2018,** *10* (26), 22031-22041.
115. Yu, M.; Han, Y.; Li, Y.; Li, J.; Wang, L., Polypyrrole-anchored cattail biomass-derived carbon aerogels for high performance binder-free supercapacitors. *Carbohydr. Polym.* **2018,** *199*, 555-562.
116. Jayaramulu, K.; Dubal, D. P.; Nagar, B.; Ranc, V.; Tomanec, O.; Petr, M.; Datta, K. K. R.; Zboril, R.; Gomez Romero, P.; Fischer, R. A., Ultrathin hierarchical porous carbon nanosheets for high-performance supercapacitors and redox electrolyte energy storage. *Adv. Mater.* **2018,** *30* (15), e1705789.
117. Kulandaivalu, S.; Suhaimi, N.; Sulaiman, Y., Unveiling high specific energy supercapacitor from layer-by-layer assembled polypyrrole/graphene oxide|polypyrrole/manganese oxide electrode material. *Sci. Rep.* **2019,** *9* (1), 4884.
118. Recep Yuksel, N. U., Alptekin Aydinli and Husnu Emrah Unalan, Paper Based, Expanded graphite/polypyrrole nanocomposite supercapacitors free from binders and current collectors. *J. Electrochem. Soc.* **2018,** *165* (2) A283 .
119. Scheider, W., Theory of the frequency dispersion of electrode polarization. Topology of networks with fractional power frequency dependence. *J. Phys. Chem.* **1975,** *79* (2), 127-136.
120. Chen, Y.; Zhang, X.; Xu, C.; Xu, H., The fabrication of asymmetry supercapacitor based on MWCNTs/MnO2/PPy composites. *Electrochim. Acta* **2019,** *309*, 424-431.
121. Jin, Y.; Meng, Y.; Fan, W.; Lu, H.; Liu, T.; Wu, S., Free-standing macro-porous nitrogen doped graphene film for high energy density supercapacitor. *Electrochim. Acta* **2019,** *318*, 865-874.
122. Zhuo, H.; Hu, Y.; Chen, Z.; Zhong, L., Cellulose carbon aerogel/PPy composites for high-performance supercapacitor. *Carbohydr. Polym.* **2019,** *215*, 322-329.
123. Tong, L.; Gao, M.; Jiang, C.; Cai, K., Ultra-high performance and flexible polypyrrole coated CNT paper electrodes for all-solid-state supercapacitors. *J. Mater. Chem. A* **2019,** *7* (17), 10751-10760.
124. Liu, Y.; Xu, N.; Chen, W.; Wang, X.; Sun, C.; Su, Z., Supercapacitor with high cycling stability through electrochemical deposition of metal-organic frameworks/polypyrrole positive electrode. *Dalton Trans.* **2018,** *47* (38), 13472-13478.
125. Zhang, Y.; Shang, Z.; Shen, M.; Chowdhury, S. P.; Ignaszak, A.; Sun, S.; Ni, Y., Cellulose nanofibers/reduced graphene oxide/polypyrrole aerogel electrodes for high-capacitance flexible all-solid-state supercapacitors. ACS Sustain. Chem. Eng. **2019,** *7* (13),

11175-11185.
126. Shi, C.; Zhitomirsky, I., Electrodeposition and capacitive behavior of films for electrodes of electrochemical supercapacitors. *Nanoscale Res. Lett.* **2010,** *5* (3), 518-23.
127. Ariyanayagamkumarappa, D. K.; Zhitomirsky, I., Electropolymerization of polypyrrole films on stainless steel substrates for electrodes of electrochemical supercapacitors. *Synth. Met.* **2012,** *162* (9-10), 868-872.
128. Yue, B.; Wang, C.; Ding, X.; Wallace, G. G., Polypyrrole coated nylon lycra fabric as stretchable electrode for supercapacitor applications. *Electrochim. Acta* **2012,** *68*, 18-24.
129. Zhu, L.; Wu, L.; Sun, Y.; Li, M.; Xu, J.; Bai, Z.; Liang, G.; Liu, L.; Fang, D.; Xu, W., Cotton fabrics coated with lignosulfonate-doped polypyrrole for flexible supercapacitor electrodes. *RSC Adv.* **2014,** *4* (12), 6261.
130. Bahloul, A.; Nessark, B.; Briot, E.; Groult, H.; Mauger, A.; Zaghib, K.; Julien, C. M., Polypyrrole-covered MnO_2 as electrode material for supercapacitor. *J. Power Sources* **2013,** *240*, 267-272.
131. Xu, J.; Zhu, L.; Bai, Z.; Liang, G.; Liu, L.; Fang, D.; Xu, W., Conductive polypyrrole-bacterial cellulose nanocomposite membranes as flexible supercapacitor electrode. *Org. Electron.* **2013,** *14* (12), 3331-3338.
132. Y. Su; I. Zhitomirsky, Influence of dopants on performance of polypyrrole coated carbon nanotube electrodes and devices. *J. Electrochem. Soc.* **2015,** *162* (5), A5013-A5019.
133. Northcutt, R. G.; Sundaresan, V. B., Mechanoelectrochemistry of PPy(DBS) from correlated characterization of electrochemical response and extensional strain. *Phys. Chem. Chem. Phys.* **2015,** *17* (48), 32268-75.
134. Sabouraud, G.; Sadki, S.; Brodie, N., The mechanisms of pyrrole electropolymerization. *Chem. Soc. Rev.* **2000,** *29* (5), 283-293.
135. Tian, J.; Zhang, H.; Li, Z., Synthesis of double-layer nitrogen-doped microporous hollow carbon@MoS_2/MoO_2 nanospheres for supercapacitors. *ACS Appl. Mater. Interfaces* **2018,** *10* (35), 29511-29520.
136. Obeidat, A. M.; Gharaibeh, M. A.; Obaidat, M., Solid-state supercapacitors with ionic liquid gel polymer electrolyte and polypyrrole electrodes for electrical energy storage. *J. Energy Storage* **2017,** *13*, 123-128.
137. Bo, J.; Luo, X.; Huang, H.; Li, L.; Lai, W.; Yu, X., Morphology-controlled fabrication of polypyrrole hydrogel for solid-state supercapacitor. *J. Power Sources* **2018,** *407*, 105-111.
138. Razaq, A.; Nyholm, L.; Sjödin, M.; Strømme, M.; Mihranyan, A., Paper-based energy-storage devices comprising carbon fiber-reinforced polypyrrole-cladophora nanocellulose composite electrodes. *Adv. Energy Mater.* **2012,** *2* (4), 445-454.
139. Feng, E.; Ma, G.; Peng, H.; Hua, F.; Tang, W.; Lei, Z., Sponge integrated highly compressible all-solid-state supercapacitor with superior performance. *New J. Chem.* **2017,** *41* (22), 13347-13354.
140. Wang, Z.; Tammela, P.; Stromme, M.; Nyholm, L., Nanocellulose coupled flexible polypyrrole@graphene oxide composite paper electrodes with high volumetric capacitance. *Nanoscale* **2015,** *7* (8), 3418-23.
141. Zhou, H.; Han, G.; Xiao, Y.; Chang, Y.; Zhai, H.-J., Facile preparation of polypyrrole/graphene oxide nanocomposites with large areal capacitance using

electrochemical codeposition for supercapacitors. *J. Power Sources* **2014,** *263*, 259-267.
142. Liu, L.; Lu, Q.; Yang, S.; Guo, J.; Tian, Q.; Yao, W.; Guo, Z.; Roy, V. A. L.; Wu, W., All-printed solid-state microsupercapacitors derived from self-template synthesis of Ag@PPy nanocomposites. *Adv. Mater. Technol.* **2018,** *3* (1), 1700206.
143. Cao, J.; Wang, Y.; Chen, J.; Li, X.; Walsh, F. C.; Ouyang, J.-H.; Jia, D.; Zhou, Y., Three-dimensional graphene oxide/polypyrrole composite electrodes fabricated by one-step electrodeposition for high performance supercapacitors. *J. Mater. Chem. A* **2015,** *3* (27), 14445-14457.
144. Jian, X.; Yang, H.; Li, J.; Zhang, E.; Cao, L.; Liang, Z., Flexible all-solid-state high-performance supercapacitor based on electrochemically synthesized carbon quantum dots/polypyrrole composite electrode. *Electrochim. Acta* **2017,** *228*, 483-493.
145. Zhou, H.; Han, G., One-step fabrication of heterogeneous conducting polymers-coated graphene oxide/carbon nanotubes composite films for high-performance supercapacitors. *Electrochim. Acta* **2016,** *192*, 448-455.
146. Xu, D.; Xuan, C.; Li, X.; Luo, Z.; Wang, Z.; Tang, T.; Wen, J.; Li, M.; Xiao, J., Novel helical carbon nanotubes-embedded reduced graphene oxide in three-dimensional architecture for high-performance flexible supercapacitors. *Electrochim. Acta* **2020,** *339*, 135912.
147. Fu, X.; Li, T.; Qi, F.; Zhang, S.; Wen, J.; Shu, W.; Luo, P.; Zhang, R.; Hu, S.; Liu, Q., Designing high electrochemical surface area between polyaniline and hydrogel polymer electrolyte for flexible supercapacitors. *Appl. Surf. Sci.* **2020,** *507*, 145135.
148. Wang, C.; Xia, K.; Wang, H.; Liang, X.; Yin, Z.; Zhang, Y., Advanced carbon for flexible and wearable electronics. *Adv. Mater.* **2019,** *31* (9), e1801072.
149. Li, Y.; Zhou, M.; Xia, Z.; Gong, Q.; Liu, X.; Yang, Y.; Gao, Q., Facile preparation of polyaniline covalently grafted to isocyanate functionalized reduced graphene oxide nanocomposite for high performance flexible supercapacitors. *Colloids Surf. A Physicochem. Eng. Asp.* **2020,** *602*, 125172.
150. Yang, J.; Yu, X.; Sun, X.; Kang, Q.; Zhu, L.; Qin, G.; Zhou, A.; Sun, G.; Chen, Q., Polyaniline-decorated supramolecular hydrogel with tough, fatigue-resistant, and self-healable performances for all-in-one flexible supercapacitors. *ACS Appl. Mater. Interfaces* **2020,** *12* (8), 9736-9745.
151. Srinivasan, R.; Elaiyappillai, E.; Nixon, E. J.; Sharmila Lydia, I.; Johnson, P. M., Enhanced electrochemical behaviour of Co-MOF/PANI composite electrode for supercapacitors. *Inorganica Chim. Acta* **2020,** *502*, 119393.
152. Payami, E.; Teimuri-Mofrad, R.; Ahadzadeh, I.; Mohammadi, R., A novel composite electrode material derived from bisferrocenyl-functionalized GO and PANI for high performance supercapacitor. *Electrochim. Acta* **2020,** *354*, 136712.
153. Du, P.; Dong, Y.; Kang, H.; Li, J.; Niu, J.; Liu, P., Superior cycle stability carbon layer encapsulated polyaniline nanowire core-shell nanoarray free-standing electrode for high performance flexible solid-state supercapacitors. *J. Power Sources* **2020,** *449*, 227477.
154. Gholami Laelabadi, K.; Moradian, R.; Manouchehri, I., One-step fabrication of flexible, cost/time effective, and high energy storage reduced graphene oxide@PANI supercapacitor. *ACS Appl. Energy Mater.* **2020,** *3* (6), 5301-5312.
155. Yu, S.; Patil, B.; Ahn, H., PANI//MoO_3 fiber-shaped asymmetric supercapacitors with

roll-type configuration. *Fibers Polym.* **2020,** *21* (3), 465-472.
156. Iqbal, M. Z.; Faisal, M. M.; Ali, S. R.; Farid, S.; Afzal, A. M., Co-MOF/polyaniline-based electrode material for high performance supercapattery devices. *Electrochim. Acta* **2020,** *346*, 136039.
157. Zhang, T.; Yue, H.; Gao, X.; Yao, F.; Chen, H.; Lu, X.; Wang, Y.; Guo, X., High-performance supercapacitors based on polyaniline nanowire arrays grown on three-dimensional graphene with small pore sizes. *Dalton Trans.* **2020,** *49* (10), 3304-3311.
158. Awata, R.; Shehab, M.; El Tahan, A.; Soliman, M.; Ebrahim, S., High performance supercapacitor based on camphor sulfonic acid doped polyaniline/multiwall carbon nanotubes nanocomposite. *Electrochim. Acta* **2020,** *347*, 136229.
159. Shen, Y.; Qin, Z.; Hu, S.; Yang, L.; Xu, X.; Ding, L.; Zhang, Y., In-situ hybridization of graphene sheets onto polyaniline nanofiber arrays grown on the surface of carbon cloth under high electric voltage field for high-performance flexible supercapacitor. *Carbon* **2020,** *158*, 711-718.
160. Hou, L.; Zhi, X.; Zhang, W.; Zhou, H., Boosting the electrochemical properties of polyaniline by one-step co-doped electrodeposition for high performance flexible supercapacitor applications. *J. Electroanal. Chem.* **2020,** *863*, 114064.
161. Moradi Golsheikh, A.; Huang, N. M.; Lim, H. N.; Zakaria, R.; Yin, C.Y., One-step electrodeposition synthesis of silver-nanoparticle-decorated graphene on indium-tin-oxide for enzymeless hydrogen peroxide detection. *Carbon* **2013,** *62*, 405-412.
162. Wang, J.; Xu, Y.; Chen, X.; Du, X.; Li, X., Effect of doping ions on electrochemical capacitance properties of polypyrrole films. *Acta. Phys.Chim. Sin.* **2007,** *23* (3), 299-304.
163. Liu, Q.; Wang, Y.; Zhang, Y.; Xu, S.; Wang, J., Effect of dopants on the adsorbing performance of polypyrrole/graphite electrodes for capacitive deionization process. *Synth. Met.* **2012,** *162* (7-8), 655-661.
164. Wu, H. H.; Chang, C. W.; Lu, D.; Maeda, K.; Hu, C., Synergistic effect of hydrochloric acid and phytic acid doping on polyaniline-coupled g-C_3N_4 nanosheets for photocatalytic Cr(VI) reduction and dye degradation. *ACS Appl. Mater. Interfaces* **2019,** *11* (39), 35702-35712.
165. Ruangchuay, L.; Sirivat, A.; Schwank, J., Electrical conductivity response of polypyrrole to acetone vapor: effect of dopant anions and interaction mechanisms. *Synth. Met.* **2004,** *140* (1), 15-21.
166. Wang, Y.; Levon, K., Influence of dopant on electroactivity of polyaniline. *Macromol. Symp.* **2012,** *317-318* (1), 240-247.
167. Zhou, H.; Hou, L.; Zhang, W.; Zhai, H. J., A dual-doped strategy to enhance the electrochemical performances of electropolymerized polyaniline electrodes for flexible energy storage. *Mater. Chem. Phys.* **2020,** *240*, 122259.
168. Kim, S. H.; Oh, K. W.; Kim, T. K., Novel conducting polyaniline blends with cyanoresin. *J. Appl. Polym. Sci.* **2005,** *96* (4), 1035-1042.
169. Abdiryim, T.; Jamal, R.; Nurulla, I., Doping effect of organic sulphonic acids on the solid-state synthesized polyaniline. *J. Appl. Polym. Sci.* **2007,** *105* (2), 576-584.
170. Maqsood R. Waikar, A. S. R., Nitin S. Shinde, Suprimkumar D. Dhas, Annasaheb V. Moholkar, Mahendra D. Shirsat, Shiv K. Chakarvarti, Rajendra G. Sonkawade, Electrochemical performance of polyaniline based symmetrical energy storage device. *Mater.*

Sci. Semicond. Process. **2020,** *120*, 105291.
171. Bortamuly, R.; Konwar, G.; Boruah, P. K.; Das, M. R.; Mahanta, D.; Saikia, P., CeO2-PANI-HCl and CeO_2-PANI-PTSA composites: synthesis, characterization, and utilization as supercapacitor electrode materials. *Ionics* **2020**.
172. Krishnaiah, P.; Prasanna, B. P.; Yogesh Kumar, K.; Asha, P. K.; Nautiyal, P.; Anusuya Devi, V. S.; Alharthi, F. A.; Parashuram, L.; Raghu, M. S., Fabrication of anode material for asymmetric supercapacitor device using polyaniline wrapped boroncarbonitride nanocomposite with enhanced capacitance. *J. Alloys Compd.* **2020,** *848*, 156602.
173. Kim, H. J.; Im, S.; Kim, J. C.; Hong, W. G.; Shin, K.; Jeong, H. Y.; Hong, Y. J., Phytic acid doped polyaniline nanofibers for enhanced aqueous copper(II) adsorption capability. *ACS Sustain. Chem. Eng.* **2017,** *5* (8), 6654-6664.
174. Geethalakshmi, D.; Muthukumarasamy, N.; Balasundaraprabhu, R., Effect of dopant concentration on the properties of HCl-doped PANI thin films prepared at different temperatures. *Optik* **2014,** *125* (3), 1307-1310.
175. Sariciftci, N. S.; Kuzmany, H.; Neugebauer, H.; Neckel, A., Structural and electronic transitions in polyaniline: a fourier transform infrared spectroscopic study. *J. Chem. Phys.* **1990,** *92* (7), 4530-4539.
176. Zhang, Y., Improving ORR activity of nitrogen-doped carbon catalysts via washing PANI-iron coordination precursor with ethanol. *Int. J. Electrochem. Sci.* **2019**, 2476-2488.
177. Mahat, M. M.; Mawad, D.; Nelson, G. W.; Fearn, S.; Palgrave, R. G.; Payne, D. J.; Stevens, M. M., Elucidating the deprotonation of polyaniline films by X-ray photoelectron spectroscopy. *J. Mater. Chem. C* **2015,** *3* (27), 7180-7186.
178. Wang, S.; Lu, S.; Li, X.; Zhang, X.; He, S.; He, T., Study of H_2SO_4 concentration on properties of H_2SO_4 doped polyaniline counter electrodes for dye-sensitized solar cells. *J. Power Sources* **2013,** *242*, 438-446.
179. Alagar, S.; Madhuvilakku, R.; Mariappan, R.; Karuppiah, C.; Yang, C. C.; Piraman, S., Ultra-stable Mn1-xNixCO_3 nano/sub-microspheres positive electrodes for high-performance solid-state asymmetric supercapacitors. *Sci. Rep.* **2020,** *10* (1), 8871.
180. Wang, X.; Sun, T.; Wang, C.; Wang, C.; Zhang, W.; Wei, Y., 1H NMR determination of the doping level of doped polyaniline. *Macromol. Chem. Phys.* **2010,** *211* (16), 1814-1819.
181. Gao, X.; Jing, X.; Li, Y.; Zhu, J.; Zhang, M., Synthesis and characterization of phosphorized polyaniline doped with phytic acid and its anticorrosion properties for Mg-Li alloy. J. Macromol. Sci. A **2017,** *55* (1), 24-35.
182. Zhang, G.Q.; Li, B.; Liu, M.C.; Yuan, S.K.; Niu, L.Y., Liquid phase synthesis of CoP nanoparticles with high electrical conductivity for advanced energy storage. *J. Nanomater.* **2017,** *2017*, 1-8.
183. Kulkarni, M. V.; Viswanath, A. K.; Marimuthu, R.; Seth, T., Spectroscopic, transport, and morphological studies of polyaniline doped with inorganic acids. *Polym. Eng. Sci.* **2004,** *44* (9), 1676-1681.
184. Song, Y.; Guo, Z.; Hu, Z.; Wang, J.; Jiao, S., Electrochemical self-assembly of nano-polyaniline film by forced convection and its capacitive performance. *RSC Adv.* **2017,** *7* (7), 3879-3887.
185. Yoon, S. B.; Yoon, E. H.; Kim, K. B., Electrochemical properties of leucoemeraldine,

emeraldine, and pernigraniline forms of polyaniline/multi-wall carbon nanotube nanocomposites for supercapacitor applications. *J. Power Sources* **2011,** *196* (24), 10791-10797.
186. Pauliukaite, R.; Brett, C. M. A.; Monkman, A. P., Polyaniline fibres as electrodes. *Electrochim. Acta* **2004,** *50* (1), 159-167.
187. Abdiryim, T.; Xiao-Gang, Z.; Jamal, R., Comparative studies of solid-state synthesized polyaniline doped with inorganic acids. *Mater. Chem. Phys.* **2005,** *90* (2-3), 367-372.
188. Bilal, S.; Begum, B.; Gul, S.; Shah, A., PANI/DBSA/H_2SO_4 : A promising and highly efficient electrode material for aqueous supercapacitors. *Synth. Met.* **2018,** *235*, 1-15.
189. Li, J.; Xie, H.; Li, Y.; Liu, J.; Li, Z., Electrochemical properties of graphene nanosheets/polyaniline nanofibers composites as electrode for supercapacitors. *J. Power Sources* **2011,** *196* (24), 10775-10781.
190. Wang, Y. G.; Li, H. Q.; Xia, Y. Y., Ordered whiskerlike polyaniline grown on the surface of mesoporous carbon and its electrochemical capacitance performance. *Adv. Mater.* **2006,** *18* (19), 2619-2623.
191. Boota, M.; Gogotsi, Y., MXene-conducting polymer asymmetric pseudocapacitors. *Adv. Energy Mater.* **2019,** *9* (7), 1802917.
192. Xiong, W.; Hu, X.; Wu, X.; Zeng, Y.; Wang, B.; He, G.; Zhu, Z., A flexible fiber-shaped supercapacitor utilizing hierarchical $NiCo_2O_4$@polypyrrole core–shell nanowires on hemp-derived carbon. *J. Mater. Chem. A* **2015,** *3* (33), 17209-17216.
193. Lv, P.; Tang, X.; Zheng, R.; Ma, X.; Yu, K.; Wei, W., Graphene/polyaniline aerogel with superelasticity and high capacitance as highly compression-tolerant supercapacitor electrode. *Nanoscale Res. Lett.* **2017,** *12* (1), 630.
194. Gülercan, D.; Gergin, İ.; Sarac, A. S., Preparation and electrochemical performances of graphene oxide/PEDOT and reduced graphene oxide/PEDOT nanofibers and nanocomposites. *Fibers Polym.* **2018,** *19* (10), 2178-2187.
195. Zhao, Q.; Jamal, R.; Zhang, L.; Wang, M.; Abdiryim, T., The structure and properties of PEDOT synthesized by template-free solution method. *Nanoscale Res. Lett.* **2014,** *9* (1), 557.
196. Gong, Y.; Li, D.; Fu, Q.; Pan, C., Influence of graphene microstructures on electrochemical performance for supercapacitors. *Pro. Nat. Sci.: Mater. Inter.***2015,** *25* (5), 379-385.
197. Raj, C. J.; Rajesh, M.; Manikandan, R.; Park, S.; Park, J. H.; Yu, K. H.; Kim, B. C., Electrochemical impedance spectroscopic studies on aging-dependent electrochemical degradation of p-toluene sulfonic acid-doped polypyrrole thin film. *Ionics* **2017,** *24* (8), 2335-2342.
198. Mei, B.-A.; Munteshari, O.; Lau, J.; Dunn, B.; Pilon, L., Physical interpretations of nyquist plots for EDLC electrodes and devices. *J. Phys. Chem. C* **2017,** *122* (1), 194-206.
199. Wang, H.; Hao, Q.; Yang, X.; Lu, L.; Wang, X., Effect of graphene oxide on the properties of its composite with polyaniline. *ACS Appl. Mater. Interfaces* **2010,** *2* (3), 821-8.
200. Zhang, M.; Nautiyal, A.; Du, H.; Li, J.; Liu, Z.; Zhang, X.; Wang, R., Polypyrrole film based flexible supercapacitor: mechanistic insight into influence of acid dopants on electrochemical performance. *Electrochim. Acta* **2020,** *357*, 136877.

201. Yan, J.; Wei, T.; Shao, B.; Fan, Z.; Qian, W.; Zhang, M.; Wei, F., Preparation of a graphene nanosheet/polyaniline composite with high specific capacitance. *Carbon* **2010,** *48* (2), 487-493.
202. An, H.; Wang, Y.; Wang, X.; Li, N.; Zheng, L., The preparation of PANI/CA composite electrode material for supercapacitors and its electrochemical performance. *J. Solid State Electrochem.* **2009,** *14* (4), 651-657.
203. Wang, X.; Xu, M.; Fu, Y.; Wang, S.; Yang, T.; Jiao, K., A Highly Conductive and hierarchical PANI micro/nanostructure and its supercapacitor application. *Electrochim. Acta* **2016,** *222*, 701-708.
204. Feng, X.; Chen, N.; Zhou, J.; Li, Y.; Huang, Z.; Zhang, L.; Ma, Y.; Wang, L.; Yan, X., Facile synthesis of shape-controlled graphene-polyaniline composites for high performance supercapacitor electrode materials. *New J. Chem.* **2015,** *39* (3), 2261-2268.
205. Jin, Y.; Huang, S.; Zhang, M.; Jia, M., Preparation of sulfonated graphene-polyaniline nanofiber composites by oil/water interfacial polymerization and their application for supercapacitors. *Synth. Met.* **2013,** *168*, 58-64.
206. Hu, C.; Zhang, X.; Liu, B.; Chen, S.; Liu, X.; Liu, Y.; Liu, J.; Chen, J., Orderly and highly dense polyaniline nanorod arrays fenced on carbon nanofibers for all-solid-state flexible electrochemical energy storage. *Electrochim. Acta* **2020,** *338*, 135846.
207. Oskueyan, G.; Lakouraj, M. M.; Mahyari, M., Nitrogen and sulfur Co-Doped graphene quantum dots decorated CeO_2 nanoparticles/ polyaniline: As high efficient hybrid supercapacitor electrode materials. *Electrochim. Acta* **2019,** *299*, 125-131.
208. Tan, Y.; Zhang, Y.; Kong, L.; Kang, L.; Ran, F., Nano-Au@PANI core-shell nanoparticles via in-situ polymerization as electrode for supercapacitor. *J. Alloys Compd.* **2017,** *722*, 1-7.
209. Zhu, J.; Chen, M.; Qu, H.; Zhang, X.; Wei, H.; Luo, Z.; Colorado, H. A.; Wei, S.; Guo, Z., Interfacial polymerized polyaniline/graphite oxide nanocomposites toward electrochemical energy storage. *Polymer* **2012,** *53* (25), 5953-5964.
210. Kim, M.; Kim, Y. K.; Kim, J.; Cho, S.; Lee, G.; Jang, J., Fabrication of a polyaniline/MoS_2 nanocomposite using self-stabilized dispersion polymerization for supercapacitors with high energy density. *RSC Adv.* **2016,** *6* (33), 27460-27465.
211.Meng, C.; Liu, C.; Chen, L.; Hu, C.; Fan, S., Highly flexible and all-solid-state paperlike polymer supercapacitors. *Nano Lett.* **2010,** *10* (10), 4025-31.
212. Li, K.; Liu, J.; Huang, Y.; Bu, F.; Xu, Y., Integration of ultrathin graphene/polyaniline composite nanosheets with a robust 3D graphene framework for highly flexible all-solid-state supercapacitors with superior energy density and exceptional cycling stability. *J. Mater. Chem. A* **2017,** *5* (11), 5466-5474.
213. Tan, Y.; Liu, Y.; Kong, L.; Kang, L.; Xu, C.; Ran, F., In situ doping of PANI nanocomposites by gold nanoparticles for high-performance electrochemical energy storage. *J. Appl. Polym. Sci.* **2017,** *134* (38), 45309.
214. Zou, B.-X.; Liang, Y.; Liu, X.-X.; Diamond, D.; Lau, K.-T., Electrodeposition and pseudocapacitive properties of tungsten oxide/polyaniline composite. *J. Power Sources* **2011,** *196* (10), 4842-4848.
215. Yang, X.; Tian, Y.; Sarwar, S.; Zhang, M.; Zhang, H.; Luo, J.; Zhang, X., Comparative

evaluation of PPyNF/CoO_x and PPyNT/CoO_x nanocomposites as battery-type supercapacitor materials via a facile and low-cost microwave synthesis approach. *Electrochim. Acta* **2019,** *311*, 230-243.
216. Zhang, M.; Nautiyal, A.; Du, H.; Wei, Z.; Zhang, X.; Wang, R., Electropolymerization of polyaniline as high-performance binder free electrodes for flexible supercapacitor. *Electrochim. Acta* **2021,** *376*, 138037.
217. Ma, M.; Shi, Z.; Li, Y.; Yang, Y.; Zhang, Y.; Wu, Y.; Zhao, H.; Xie, E., High-performance 3 V "water in salt" aqueous asymmetric supercapacitors based on VN nanowire electrodes. *J. Mater. Chem. A* **2020,** *8* (9), 4827-4835.
218. Kuang, M.; Wen, Z. Q.; Guo, X. L.; Zhang, S. M.; Zhang, Y. X., Engineering firecracker-like beta-manganese dioxides@spinel nickel cobaltates nanostructures for high-performance supercapacitors. *J. Power Sources* **2014,** *270*, 426-433.
219. Tian, J.; Zhang, A.; Liu, R.; Huang, W.; Yuan, Z.; Zheng, R.; Wei, D.; Liu, J., Preparation of CoS2 supported flower-like NiFe layered double hydroxides nanospheres for high-performance supercapacitors. *J. Colloid Interface Sci.* **2020,** *579*, 607-618.
220. Liu, H.; Xu, T.; Liu, K.; Zhang, M.; Liu, W.; Li, H.; Du, H.; Si, C., Lignin-based electrodes for energy storage application. *Ind. Crops. Prod.* **2021,** *165*, 113425.
221. Li, B.; Shi, Y.; Huang, K.; Zhao, M.; Qiu, J.; Xue, H.; Pang, H., Cobalt-doped nickel phosphite for high performance of electrochemical energy storage. *Small* **2018,** *14* (13), e1703811.
222. Wan, L.; He, C.; Chen, D.; Liu, J.; Zhang, Y.; Du, C.; Xie, M.; Chen, J., In situ grown NiFeP@$NiCo_2S_4$ nanosheet arrays on carbon cloth for asymmetric supercapacitors. *Chem. Eng. J.* **2020,** *399*, 125778.
223. Zhang, N.; Li, Y.; Xu, J.; Li, J.; Wei, B.; Ding, Y.; Amorim, I.; Thomas, R.; Thalluri, S. M.; Liu, Y.; Yu, G.; Liu, L., High-performance flexible solid-state asymmetric supercapacitors based on bimetallic transition metal phosphide nanocrystals. *ACS Nano* **2019,** *13* (9), 10612-10621.
224. Hou, S.; Xu, X.; Wang, M.; Xu, Y.; Lu, T.; Yao, Y.; Pan, L., Carbon-incorporated Janus-type Ni_2P/Ni hollow spheres for high performance hybrid supercapacitors. *J. Mater. Chem. A* **2017,** *5* (36), 19054-19061.
225. Zhang, X.; Hou, S.; Ding, Z.; Zhu, G.; Tang, H.; Hou, Y.; Lu, T.; Pan, L., Carbon wrapped CoP hollow spheres for high performance hybrid supercapacitor. *J. Alloys Compd.* **2020,** *822*, 153578.
226. Jin, Y.; Zhao, C.; Wang, Y.; Jiang, Q.; Ji, C.; Jia, M., Large-scale production of Cu_3P nanocrystals for ultrahigh-rate supercapacitor. *Ionics* **2017,** *23* (11), 3249-3254.
227. Jiang, A.; Wang, Z.; Li, Q.; Dong, M., Ionic liquid-assisted synthesis of hierarchical one-dimensional MoP/NPC for high-performance supercapacitor and electrocatalysis. *ACS Sustain. Chem. Eng.* **2020,** *8* (16), 6343-6351.
228. Liang, B.; Zheng, Z.; Retana, M.; Lu, K.; Wood, T.; Ai, Y.; Zu, X.; Zhou, W., Synthesis of FeP nanotube arrays as negative electrode for solid-state asymmetric supercapacitor. *Nanotechnology* **2019,** *30* (29), 295401.
229. Wang, W.; Zhang, L.; Xu, G.; Song, H.; Yang, L.; Zhang, C.; Xu, J.; Jia, D., Structure-designed synthesis of CoP microcubes from metal-organic frameworks with enhanced

supercapacitor properties. *Inorg. Chem.* **2018,** *57* (16), 10287-10294.
230. Hu, Y.; Liu, M.; Yang, Q.; Kong, L.; Kang, L., Facile synthesis of high electrical conductive CoP via solid-state synthetic routes for supercapacitors. *J. Energy Chem.* **2017,** *26* (1), 49-55.
231. Lei, X.; Ge, S.; Tan, Y.; Li, J.; Wang, Z.; Liu, P.; Feng, C.; Xiang, B., Bimetallic phosphosulfide Zn-Ni-P-S nanosheets as binder-free electrodes for aqueous asymmetric supercapacitors with impressive performance. *J. Mater. Chem. A* **2019,** *7* (43), 24908-24918.
232. Nguyen, T. T.; Balamurugan, J.; Kim, N. H.; Lee, J. H., Hierarchical 3D Zn-Ni-P nanosheet arrays as an advanced electrode for high-performance all-solid-state asymmetric supercapacitors. *J. Mater. Chem. A* **2018,** *6* (18), 8669-8681.
233. Kong, M.; Wang, Z.; Wang, W.; Ma, M.; Liu, D.; Hao, S.; Kong, R.; Du, G.; Asiri, A. M.; Yao, Y.; Sun, X., NiCoP Nanoarray: A superior pseudocapacitor electrode with high areal capacitance. *Chemistry* **2017,** *23* (18), 4435-4441.
234. Song, S.; Guo, M.; Zhang, S.; Zhan, K.; Yan, Y.; Yang, J.; Zhao, B.; Xu, M., Plasma-assisted synthesis of hierarchical $NiCo_xP_y$ nanosheets as robust and stable electrocatalyst for hydrogen evolution reaction in both acidic and alkaline media. *Electrochim. Acta* **2020,** *331*, 135431.
235. Sahoo, S.; Mondal, R.; Late, D. J.; Rout, C. S., Electrodeposited Nickel Cobalt Manganese based mixed sulfide nanosheets for high performance supercapacitor application. *Microporous Mesoporous Mater.* **2017,** *244*, 101-108.
236. Toghraei, A.; Shahrabi, T.; Barati Darband, G., Electrodeposition of self-supported Ni-Mo-P film on Ni foam as an affordable and high-performance electrocatalyst toward hydrogen evolution reaction. *Electrochim. Acta* **2020,** *335*, 135643.
237. Kan, S.; Xu, M.; Feng, W.; Wu, Y.; Du, C.; Gao, X.; Wu, Y. A.; Liu, H., Tuning overall water splitting on an electrodeposited NiCoFeP films. *ChemElectroChem* **2021,** *8* (3), 539-546.
238. Ilyas, U.; Rawat, R. S.; Roshan, G.; Tan, T. L.; Lee, P.; Springham, S. V.; Zhang, S.; Fengji, L.; Chen, R.; Sun, H. D., Quenching of surface traps in Mn doped ZnO thin films for enhanced optical transparency. *Appl. Surf. Sci.* **2011,** *258* (2), 890-897.
239. Li, Y.; Jia, B.; Chen, B.; Liu, Q.; Cai, M.; Xue, Z.; Fan, Y.; Wang, H. P.; Su, C. Y.; Li, G., MOF-derived Mn doped porous CoP nanosheets as efficient and stable bifunctional electrocatalysts for water splitting. *Dalton Trans.* **2018,** *47* (41), 14679-14685.
240. Deng, B.; Xu, C.; Li, Z.; Huang, W.; Wu, Q.; Zhang, Y.; Ni, M.; Cen, K., Enhanced solar conversion of CO_2 to CO using Mn-doped TiO_2 based on photo-thermochemical cycle. *ChemistrySelect.* **2019,** *4* (1), 236-244.
241. Chu, J.; Bao, Y.; Li, X.; Gao, F.; Wang, M., Characterization of oxidation behavior of Mn fumes generated in the vacuum treatment of melting Mn steels. *Steel Res. Int.* **2020,** *92* (1), 2000333.
242. Wu, H.; Wang, J.; Yan, J.; Wu, Z.; Jin, W., MOF-derived two-dimensional N-doped carbon nanosheets coupled with Co-Fe-P-Se as efficient bifunctional OER/ORR catalysts. *Nanoscale* **2019,** *11* (42), 20144-20150.
243. Yang, S.; Wu, C.; Cai, J.; Zhu, Y.; Zhang, H.; Lu, Y.; Zhang, K., Seed-assisted smart construction of high mass loading Ni-Co-Mn hydroxide nanoflakes for supercapacitor applications. *J. Mater. Chem. A* **2017,** *5* (32), 16776-16785.

244. Tang, G.; Zeng, Y.; Wei, B.; Liang, H.; Wu, J.; Yao, P.; Wang, Z., Rational design of manganese cobalt phosphide with yolk-shell structure for overall water splitting. *Energy Technol.* **2019,** *7* (6), 1900066.
245. Xu, S.; Yu, X.; Liu, X.; Teng, C.; Du, Y.; Wu, Q., Contrallable synthesis of peony-like porous Mn-CoP nanorod electrocatalyst for highly efficient hydrogen evolution in acid and alkaline. *J. Colloid Interface Sci.* **2020,** *577*, 379-387.
246. Chen, X.; Li, Q.; Che, Q.; Chen, Y.; Xu, X., Interface engineering of crystalline/amorphous $Co_2P/CoMoP_x$ nanostructure as efficient electrocatalysts for hydrogen evolution reaction. *ACS Sustain. Chem. Eng.* **2018,** *7* (2), 2437-2445.
247. Zhu, G.; Yang, L.; Wang, W.; Ma, M.; Zhang, J.; Wen, H.; Zheng, D.; Yao, Y., Hierarchical three-dimensional manganese doped cobalt phosphide nanowire decorated nanosheet cluster arrays for high-performance electrochemical pseudocapacitor electrodes. *Chem. Commun.* **2018,** *54* (66), 9234-9237.
248. Andrew P. Grosvenor, S. D. W., Ronald G. Cavell, and Arthur Mar, Examination of the bonding in binary transition-metal monophosphides MP (M = Cr, Mn, Fe, Co) by X-ray photoelectron spectroscopy. *Inorg. Chem.* **2005,** *44* (24), 8989.
249. Tantawy, N. S.; El Taib Heakal, F.; Ahmed, S. Y., Synthesis of worm-like binary metallic active material by electroless deposition approach for high-performance supercapacitor. *J. Energy Storage* **2020,** *31*, 101625.
250. Mu, C.; Song, J.; Zhang, Y.; Liu, L.; Wang, B.; Xiang, J., Three dimensional bimetallic phosphides nanoneedle arrays as electrode materials for symmetric all-solid-state supercapacitor. *J. Alloys Compd.* **2019,** *787*, 618-624.
251. Mei, P.; Pramanik, M.; Young, C.; Huang, Z.; Hossain, M. S. A.; Sugahara, Y.; Yamauchi, Y., Synthesis of mesostructured manganese phosphonate and its promising energy storage application. *J. Mater. Chem. A* **2017,** *5* (44), 23259-23266.
252. Liu, Q.; Hu, R.; Qi, J.; Sui, Y.; He, Y.; Meng, Q.; Wei, F.; Ren, Y., Facile synthesis of NiCoP nanosheets on carbon cloth and their application as positive electrode material in asymmetric supercapacitor. *Ionics* **2019,** *26* (1), 355-366.
253. Tao, K.; Gong, Y.; Lin, J., Epitaxial grown self-supporting $NiSe/Ni_3S_2/Ni_{12}P_5$ vertical nanofiber arrays on Ni foam for high performance supercapacitor: Matched exposed facets and re-distribution of electron density. *Nano Energy* **2019,** *55*, 65-81.
254. Li, S.; Chen, J.; Gong, X.; Wang, J.; Lee, P. S., Holey graphene-wrapped porous TiNb24O62 microparticles as high-performance intercalation pseudocapacitive anode materials for lithium-ion capacitors. *NPG Asia Mater.* **2018,** *10* (5), 406-416.
255. Sankar, K. V.; Selvan, R. K.; Meyrick, D., Electrochemical performances of $CoFe_2O_4$ nanoparticles and a rGO based asymmetric supercapacitor. *RSC Adv.* **2015,** *5* (121), 99959-99967.
256. Zhu, Y.; Zong, Q.; Zhang, Q.; Yang, H.; Wang, Q.; Wang, H., Three-dimensional core-shell NiCoP@NiCoP array on carbon cloth for high performance flexible asymmetric supercapacitor. *Electrochim. Acta* **2019,** *299*, 441-450.
257. Yang, Y.; Pan, Z. Z.; Wang, Y. Y.; Ma, Y. C.; Li, C.; Lu, Y. J.; Wu, X. L., Ionic-liquid-bifunctional wrapping of ultrafine SnO_2 nanocrystals into N-doped graphene networks: high pseudocapacitive sodium storage and high-performance sodium-ion full cells. *Nanoscale* **2019,**

11 (31), 14616-14624.
258. Teli, A. M.; Beknalkar, S. A.; Pawar, S. A.; Dubal, D. P.; Dongale, T. D.; Patil, D. S.; Patil, P. S.; Shin, J. C., Effect of concentration on the charge storage kinetics of nanostructured MnO_2 thin-film supercapacitors synthesized by the hydrothermal method. *Energies* **2020,** *13* (22), 6124.
259. Yang, L.; Li, X.; He, S.; Du, G.; Yu, X.; Liu, J.; Gao, Q.; Hu, R.; Zhu, M., Mesoporous Mo_2C/N-doped carbon heteronanowires as high-rate and long-life anode materials for Li-ion batteries. *J. Mater. Chem. A* **2016,** *4* (28), 10842-10849.
260. Li, L.; Zhang, N.; Zhang, M.; Zhang, X.; Zhang, Z., Flexible $Ti_3C_2T_x$/PEDOT:PSS films with outstanding volumetric capacitance for asymmetric supercapacitors. *Dalton Trans.* **2019,** *48* (5), 1747-1756.
261. Zhu, Y.; Zong, Q.; Zhang, Q.; Yang, H.; Du, W.; Wang, Q.; Zhan, J.; Wang, H., Ultra-long lifespan asymmetrical hybrid supercapacitor device based on hierarchical NiCoP@C@LDHs electrode. *Electrochim. Acta* **2020,** *334*, 135589.
262. Zhou, J.-J.; Han, X.; Tao, K.; Li, Q.; Li, Y.-L.; Chen, C.; Han, L., Shish-kebab type $MnCo_2O_4$@Co_3O_4 nanoneedle arrays derived from MnCo-LDH@ZIF-67 for high-performance supercapacitors and efficient oxygen evolution reaction. *Chem. Eng. J.* **2018,** *354*, 875-884.
263. Surendran, S.; Shanmugapriya, S.; Sivanantham, A.; Shanmugam, S.; Kalai Selvan, R., Electrospun carbon nanofibers encapsulated with NiCoP: a multifunctional electrode for supercapattery and oxygen reduction, oxygen evolution, and hydrogen evolution reactions. *Adv. Energy Mater.* **2018,** *8* (20), 1800555.
264. Song, Y.; Wang, H.; Yan, L., Cobalt-Porphyrin Modified Three-dimensional graphene hydrogel electrode for high performance asymmetric supercapacitors. *Nano* **2019,** *14* (05), 1950062.
265. Pramanik, M.; Salunkhe, R. R.; Imura, M.; Yamauchi, Y., Phosphonate-derived nanoporous metal phosphates and their superior energy storage application. *ACS Appl. Mater. Interfaces* **2016,** *8* (15), 9790-7.
266. Liu, S.; Sarwar, S.; Wang, J.; Zhang, H.; Li, T.; Luo, J.; Zhang, X., The microwave synthesis of porous $CoSe_2$ nanosheets for super cycling performance supercapacitors. *J. Mater. Chem. C* **2021,** *9* (1), 228-237.
267. Li, J.-J.; Liu, M.-C.; Kong, L.-B.; Shi, M.; Han, W.; Kang, L., Facile synthesis of Co3P2O8·8H2O for high-performance electrochemical energy storage. *Mater. Lett.* **2015,** *161*, 404-407.
268. Ding, R.; Qi, L.; Jia, M.; Wang, H., Facile and large-scale chemical synthesis of highly porous secondary submicron/micron-sized $NiCo_2O_4$ materials for high-performance aqueous hybrid AC-NiCo2O4 electrochemical capacitors. *Electrochim. Acta* **2013,** *107*, 494-502.
269. Jagadale, A. D.; Guan, G.; Li, X.; Du, X.; Ma, X.; Hao, X.; Abudula, A., Ultrathin nanoflakes of cobalt-manganese layered double hydroxide with high reversibility for asymmetric supercapacitor. *J. Power Sources* **2016,** *306*, 526-534.
270. Subramani, K.; Sudhan, N.; Divya, R.; Sathish, M., All-solid-state asymmetric supercapacitors based on cobalt hexacyanoferrate-derived CoS and activated carbon. *RSC Adv.* **2017,** *7* (11), 6648-6659.

271. Li, Y.; An, F.; Wu, H.; Zhu, S.; Lin, C.; Xia, M.; Xue, K.; Zhang, D.; Lian, K., A $NiCo_2S_4$/hierarchical porous carbon for high performance asymmetrical supercapacitor. *J. Power Sources* **2019,** *427*, 138-144.
272. Zhang, Y.; Xu, J.; Zheng, Y.; Zhang, Y.; Hu, X.; Xu, T., Construction of $CuCo_2O_4$@$CuCo_2O_4$ hierarchical nanowire arrays grown on Ni foam for high-performance supercapacitors. *RSC Adv.* **2017,** *7* (7), 3983-3991.
273. Wang, Y.; Liu, Y.; Xia, K.; Zhang, Y.; Yang, J., $NiCo_2S_4$ nanoparticles anchoring on polypyrrole nanotubes for high-performance supercapacitor electrodes. *J. Electroanal. Chem.* **2019,** *840*, 242-248.
274. Huang, X.; Gou, L., High performance asymmetric supercapacitor based on hierarchical flower-like $NiCo_2S_4$@polyaniline. *Appl. Surf. Sci.* **2019,** *487*, 68-76.
275. Guo, M.; Gao, H.; Huang, W.; Wang, J.; Liu, Z.; Zhan, C.; Ding, L.; Tu, J., Microwave-assisted rapid synthesis of $NiCo_2S_4$ nanotube arrays on Ni foam for high-cycling-stability supercapacitors. *J. Alloys Compd.* **2019,** *780*, 164-169.
276. Gao, X.; Zhao, Y.; Dai, K.; Wang, J.; Zhang, B.; Shen, X., NiCoP nanowire@NiCo-layered double hydroxides nanosheet heterostructure for flexible asymmetric supercapacitors. *Chem. Eng. Sci.* **2020,** *384*, 123373.
277. Tang, Y.; Chen, S.; Mu, S.; Chen, T.; Qiao, Y.; Yu, S.; Gao, F., Synthesis of capsule-like porous hollow nanonickel cobalt sulfides via cation exchange based on the kirkendall effect for high-performance supercapacitors. *ACS Appl. Mater. Interfaces* **2016,** *8* (15), 9721-32.
278. Zhao, Y.; Ran, W.; He, J.; Huang, Y.; Liu, Z.; Liu, W.; Tang, Y.; Zhang, L.; Gao, D.; Gao, F., High-performance asymmetric supercapacitors based on multilayer MnO_2/graphene oxide nanoflakes and hierarchical porous carbon with enhanced cycling stability. *Small* **2015,** *11* (11), 1310-9.
279. Ma, L.; Chen, T.; Li, S.; Gui, P.; Fang, G., A 3D self-supported coralline-like $CuCo_2S_4$@$NiCo_2S_4$ core-shell nanostructure composite for high-performance solid-state asymmetrical supercapacitors. *Nanotechnology* **2019,** *30* (25), 255603.
280. Hao, L.; Shen, L.; Wang, J.; Xu, Y.; Zhang, X., Hollow $NiCo_2S_4$ nanotube arrays grown on carbon textile as a self-supported electrode for asymmetric supercapacitors. *RSC Adv.* **2016,** *6* (12), 9950-9957.
281. Coromina, H. M.; Adeniran, B.; Mokaya, R.; Walsh, D. A., Bridging the performance gap between electric double-layer capacitors and batteries with high-energy/high-power carbon nanotube-based electrodes. *J. Mater. Chem. A* **2016,** *4* (38), 14586-14594.
282. Salunkhe, R. R.; Lin, J.; Malgras, V.; Dou, S. X.; Kim, J. H.; Yamauchi, Y., Large-scale synthesis of coaxial carbon nanotube/$Ni(OH)_2$ composites for asymmetric supercapacitor application. *Nano Energy* **2015,** *11*, 211-218.
283. Bhagwan, J.; Khaja Hussain, S.; Yu, J. S., Aqueous asymmetric supercapacitors based on $ZnCo_2O_4$ nanoparticles via facile combustion method. *J. Alloys Compd.* **2020,** *815*, 152456.
284. Ren, X.; Du, Y.; Song, M.; Chen, Y.; Zhou, Y.; Ma, F.; Wan, J., Facile preparation of mesoporous $NiCo_2S_4$ microaggregates constructed by nanoparticles via puffing $NiCo_2O_4$ cubes for high performance asymmetric supercapacitors. *J. Alloys Compd.* **2019,** *806*, 1481-1490.
285. Iqbal, M. Z.; Zakar, S.; Haider, S. S.; Afzal, A. M.; Iqbal, M. J.; Kamran, M. A.;

Numan, A., Electrodeposited CuMnS and CoMnS electrodes for high-performance asymmetric supercapacitor devices. *Ceram. Int.* **2020**.
286. Zhao, J.; Hou, S.; Bai, Y.; Lian, Y.; Zhou, Q.; Ban, C.; Wang, Z.; Zhang, H., Multilayer dodecahedrons Zn-Co sulfide for supercapacitors. *Electrochim. Acta* **2020,** *354*, 136714.
287. Kandula, S.; Shrestha, K. R.; Kim, N. H.; Lee, J. H., Fabrication of a 3D hierarchical sandwich Co_9S_8/alpha-MnS@N-C@MoS_2 nanowire architectures as advanced electrode material for high performance hybrid supercapacitors. *Small* **2018,** *14* (23), e1800291.
288. Wang, Y.; Xie, Y., Electroactive FeS_2-modified MoS_2 nanosheet for high-performance supercapacitor. *J. Alloys Compd.* **2020,** *824*, 153936.
289. Liu, Y.; Jiang, G.; Huang, Z.; Lu, Q.; Yu, B.; Evariste, U.; Ma, P., Decoration of hollow mesoporous carbon spheres by $NiCo_2S_4$ nanoparticles as electrode materials for asymmetric supercapacitors. *ACS Appl. Energy Mater.* **2019,** *2* (11), 8079-8089.
290. Liu, Y.; Li, Z.; Yao, L.; Chen, S.; Zhang, P.; Deng, L., Confined growth of $NiCo_2S_4$ nanosheets on carbon flakes derived from eggplant with enhanced performance for asymmetric supercapacitors. *Chem. Eng. J.* **2019,** *366*, 550-559.
291. Zhai, R.; Xiao, Y.; Ding, T.; Wu, Y.; Chen, S.; Wei, W., Construction of $NiCo_2S_4$ heterostructure based on electrochemically exfoliated graphene for high-performance hybrid supercapacitor electrode. *J. Alloys Compd.* **2020,** *845*, 156164.
292. Lu, W.; Yang, M.; Jiang, X.; Yu, Y.; Liu, X.; Xing, Y., Template-assisted synthesis of hierarchically hollow C/$NiCo_2S_4$ nanospheres electrode for high performance supercapacitors. *Chem. Eng. J.* **2020,** *382*, 122943.
293. Bi, T.; Jiang, J.; Lei, Y.; Zheng, X.; Jia, Z.; Wei, Z.; Yang, H., Improving supercapacitive performance of CNTs/$NiCo_2S_4$ composites by interface regulation. *Appl. Surf. Sci.* **2020,** *530*, 147317.
294. Ma, Z.; Sun, Z.; Jiang, H.; Li, F.; Wang, Q.; Qu, F., Nanoporous electrospun $NiCo_2S_4$ embedded in carbon fiber as an excellent electrode for high-rate supercapacitors. *Appl. Surf. Sci.* **2020,** *533*, 147521.
295. Gao, Y.; Lin, Q.; Zhong, G.; Fu, Y.; Ma, X., Novel $NiCo_2S_4$/graphene composites synthesized via a one-step in-situ hydrothermal route for energy storage. *J. Alloys Compd.* **2017,** *704*, 70-78.
296. Wang, F.; Li, G.; Zhou, Q.; Zheng, J.; Yang, C.; Wang, Q., One-step hydrothermal synthesis of sandwich-type $NiCo_2S_4$ @reduced graphene oxide composite as active electrode material for supercapacitors. *Appl. Surf. Sci.* **2017,** *425*, 180-187.
297. Dong, M.; Wang, Z.; Yan, G.; Wang, J.; Guo, H.; Li, X., Confine growth of $NiCo_2S_4$ nanoneedles in graphene framework toward high-performance asymmetric capacitor. *J. Alloys Compd.* **2020,** *822*, 153645.
298. Han, J.K.; Song, H.Y.; Saito, F.; Lee, B.T., Synthesis of high purity nano-sized hydroxyapatite powder by microwave-hydrothermal method. *Mater. Chem. Phys.* **2006,** *99* (2-3), 235-239.
299. Kumar, A.; Kuang, Y.; Liang, Z.; Sun, X., Microwave chemistry, recent advancements, and eco-friendly microwave-assisted synthesis of nanoarchitectures and their applications: a review. *Mater. Today Nano* **2020,** *11*, 100076.
300. Cheng, J. P.; Agrawal, D. K.; Komarneni, S.; Mathis, M.; Roy, R., Microwave

processing of WC-Co composities and ferroic titanates. *Mater. Res. Innov.* **2016,** *1* (1), 44-52.
301. Sarwar, S.; Liu, Z.; Li, J.; Wang, Y.; Wang, R.; Zhang, X., High performance hybrid-capacitor based on $MoTe_2$/graphene through ultra-fast, facile microwave-initiated synthesis. *J. Alloys Compd.* **2020**, 155886.
302. Sarwar, S.; Nautiyal, A.; Cook, J.; Yuan, Y.; Li, J.; Uprety, S.; Shahbazian-Yassar, R.; Wang, R.; Park, M.; Bozack, M. J.; Zhang, X., Facile microwave approach towards high performance MoS_2/graphene nanocomposite for hydrogen evolution reaction. *Sci. China Mater.* **2019**.
303. Chen, H.; Ma, X.; Shen, P. K., $NiCo_2S_4$ nanocores in-situ encapsulated in graphene sheets as anode materials for lithium-ion batteries. *Chem. Eng. J.* **2019,** *364*, 167-176.
304. Raj, S.; Srivastava, S. K.; Kar, P.; Roy, P., Three-dimensional $NiCo_2O_4$/$NiCo_2S_4$ hybrid nanostructure on Ni-foam as a high-performance supercapacitor electrode. *RSC Adv.* **2016,** *6* (98), 95760-95767.
305. Chen, Q.; Miao, J.; Quan, L.; Cai, D.; Zhan, H., Bimetallic $CoNiS_x$ nanocrystallites embedded in nitrogen-doped carbon anchored on reduced graphene oxide for high-performance supercapacitors. *Nanoscale* **2018,** *10* (8), 4051-4060.
306. Jin, R.; Yang, L.; Li, G.; Chen, G., Hierarchical worm-like CoS_2 composed of ultrathin nanosheets as an anode material for lithium-ion batteries. *J. Mater. Chem. A* **2015,** *3* (20), 10677-10680.
307. Li, R.; Wang, S.; Wang, J.; Huang, Z., Ni_3S_2@CoS core-shell nano-triangular pyramid arrays on Ni foam for high-performance supercapacitors. *Phys. Chem. Chem. Phys.* **2015,** *17* (25), 16434-42.
308. Kulurumotlakatla, D. K.; Yedluri, A. K.; Kim, H.-J., Hierarchical $NiCo_2S_4$ nanostructure as highly efficient electrode material for high-performance supercapacitor applications. *J. Energy Storage* **2020,** *31*, 101619.
309. Zheng, Y.; Tian, Y.; Sarwar, S.; Luo, J.; Zhang, X., Carbon nanotubes decorated $NiSe_2$ nanosheets for high-performance supercapacitors. *J. Power Sources* **2020,** *452*, 227793.
310. Huang, T.; Song, X.Z.; Chen, X.; Chen, X. L.; Sun, F.F.; Su, Q.F.; Li, L.D.; Tan, Z., Carbon coated nickel–cobalt bimetallic sulfides hollow dodecahedrons for a supercapacitor with enhanced electrochemical performance. *New J. Chem.* **2018,** *42* (7), 5128-5134.
311. Wang, N.; Wang, Y.; Cui, S.; Hou, H.; Mi, L.; Chen, W., A Hollow tube-on-tube architecture of carbon-tube-supported nickel cobalt sulfide nanotubes for advanced supercapacitors. *ChemNanoMat* **2017,** *3* (4), 269-276.
312. Yu, M.; Han, Y.; Li, Y.; Li, J.; Wang, L., Improving electrochemical activity of activated carbon derived from popcorn by $NiCo_2S_4$ nanoparticle coating. *Appl. Surf. Sci.* **2019,** *463*, 1001-1010.
313. Liu, L., Nano-aggregates of cobalt nickel oxysulfide as a high-performance electrode material for supercapacitors. *Nanoscale* **2013,** *5* (23), 11615-9.
314. Hao, P.; Tian, J.; Sang, Y.; Tuan, C. C.; Cui, G.; Shi, X.; Wong, C. P.; Tang, B.; Liu, H., 1D Ni-Co oxide and sulfide nanoarray/carbon aerogel hybrid nanostructures for asymmetric supercapacitors with high energy density and excellent cycling stability. *Nanoscale* **2016,** *8* (36), 16292-16301.
315. Pu, J.; Cui, F.; Chu, S.; Wang, T.; Sheng, E.; Wang, Z., Preparation and electrochemical

characterization of hollow hexagonal $NiCo_2S_4$ nanoplates as pseudocapacitor materials. *ACS Sustain. Chem. Eng.* **2013,** *2* (4), 809-815.
316. Cheng, J.W.; Lin, L.Y.; Hong, W.L.; Lin, L.Y.; Chen, H.Q.; Lai, H.X., Rational design of nickel cobalt sulfide/cobalt sulfide sheet-on-sheet structure for asymmetric supercapacitors. *Electrochim. Acta* **2018,** *283*, 1245-1252.
317. Huang, Y.; Shi, T.; Zhong, Y.; Cheng, S.; Jiang, S.; Chen, C.; Liao, G.; Tang, Z., Graphene-quantum-dots induced $NiCo_2S_4$ with hierarchical-like hollow nanostructure for supercapacitors with enhanced electrochemical performance. *Electrochim. Acta* **2018,** *269*, 45-54.
318. Teli, A. M.; Beknalkar, S. A.; Pawar, S. A.; Dubal, D. P.; Dongale, T. D.; Patil, D. S.; Patil, P. S.; Shin, J. C., Effect of concentration on the charge storage kinetics of nanostructured MnO_2 thin-film supercapacitors synthesized by the hydrothermal method. *Energies* **2020,** *13* (22).
319. Ensafi, A. A.; Moosavifard, S. E.; Rezaei, B.; Kaverlavani, S. K., Engineering onion-like nanoporous $CuCo_2O_4$ hollow spheres derived from bimetal-organic frameworks for high-performance asymmetric supercapacitors. *J. Mater. Chem. A* **2018,** *6* (22), 10497-10506.
320. Zeng, Z.; Wang, D.; Zhu, J.; Xiao, F.; Li, Y.; Zhu, X., $NiCo_2S_4$ nanoparticles//activated balsam pear pulp for asymmetric hybrid capacitors. *CrystEngComm* **2016,** *18* (13), 2363-2374.
321. Li, Z.; Wu, L.; Wang, L.; Gu, A.; Zhou, Q., Nickel cobalt sulfide nanosheets uniformly anchored on porous graphitic carbon nitride for supercapacitors with high cycling performance. *Electrochim. Acta* **2017,** *231*, 617-625.
322. Kong, W.; Lu, C.; Zhang, W.; Pu, J.; Wang, Z., Homogeneous core–shell $NiCo_2S_4$ nanostructures supported on nickel foam for supercapacitors. *J. Mater. Chem. A* **2015,** *3* (23), 12452-12460.
323. Huang, Y.; Shi, T.; Jiang, S.; Cheng, S.; Tao, X.; Zhong, Y.; Liao, G.; Tang, Z., Enhanced cycling stability of $NiCo_2S_4$@NiO core-shell nanowire arrays for all-solid-state asymmetric supercapacitors. *Sci. Rep.* **2016,** *6*, 38620.